UNIVERSITY OF SOUTHAMPTON

THE VIBROACOUSTIC BEHAVIOUR OF ALUMINIUM EXTRUSIONS USED IN RAILWAY VEHICLES

BY

GANG XIE

Thesis submitted for the degree of Doctor of Philosophy
Faculty of Engineering, Science and Mathematics
Institute of Sound and Vibration Research

February 2004

UNIVERSITY OF SOUTHAMTPON

ABSTRACT

FACULTY OF ENGINEERING, SCIENCE AND MATHEMATICS
INSTITUTE OF SOUND AND VIBRATION RESEARCH
Doctor of Philosophy

THE VIBROACOUSTIC BEHAVIOUR OF ALUMINIUM EXTRUSIONS USED IN RAILWAY VEHICLES

By

Gang Xie

Aluminium extrusions have been used widely as the main structural component of railway passenger trains. To model the interior noise of trains at an early design stage, the vibroacoustic behaviour of aluminium extrusions needs to be modelled. The method of statistical energy analysis (SEA) has been correctly identified by vehicle manufactory as the most appropriate approach for this purpose. The objective of this thesis is to establish a modelling approach for aluminium extrusions which enables an extruded panel to be represented in terms of a small number of subsystems and be incorporated into the overall SEA model for interior noise of vehicles.

To estimate the modal density of extruded panels, the effects of boundary conditions on the mode count and modal density of one- and two-dimensional structural systems, beams and plates respectively, are investigated by using the wavenumber integration method. It is demonstrated, for one-dimensional systems, that the average mode count is reduced by between 0 and 1 for each boundary constraint, depending on the type of boundary conditions. The effects of line constraints on the mode count of two-dimensional systems are similar to the equivalent one-dimensional constraints but they are always frequency-dependent. The modal density is largely independent of boundary conditions for one-dimensional systems, although there are exceptions, while it is dependent on boundary conditions for two-dimensional systems. The results are compared with those from previously published formulae for natural frequencies and with results from finite element (FE) analysis. Inclusion of the effect of the boundary conditions in SEA estimations will result in improved agreements with both analytical and numerical model results.

To model the sound radiation from extruded panels, the average radiation efficiency of point-excited rectangular plates, including those with a very large aspect ratio ('strips'), is investigated by using a modal summation method based on the far-field sound intensity. By taking an average over all possible forcing positions on the plate, the cross-modal contributions average out to zero. The numerical results from the modal summation are compared with established formulae for rectangular plates. For wavenumbers where acoustic circulation takes place, it is shown that the previously published formulae are not applicable for predicting the average radiation efficiency for a strip. Approximate expressions for calculating the average radiation efficiency of the strip are then derived. The maximum radiation efficiency of a rectangular plate around the critical frequency is found to vary less with Helmholtz number $k_c a$, where k_c is the wavenumber at the critical frequency and a is the width, than previously published models suggest.

The vibration behaviour of an extruded panel is dominated by global modes at low frequency while local modes of individual strips are dominant at high frequency. By taking account of the boundary effects, the approximate mode count and modal density are obtained for extruded panels. The result is compared with that from an FE model. The coupling between global and local modes is modelled in terms of the travelling global waves exciting the edges of each strip under the assumption that the local modes of each strip are uncorrelated. The coupling between local modes is modelled using standard expressions for various structural joints. The average radiation efficiency of the extruded panel is developed using a modal summation approach. SEA models for extruded panels are finally assembled using these components.

Experiments are carried out on a sample extruded panel using mechanical excitation to validate the proposed models. The radiation efficiency is also measured using a reciprocity method. The response of the panel is predicted using SEA models for both acoustic and mechanical excitation. The results are compared with measured results with generally good agreement, especially for mechanical excitation.

ACKNOWLEDGEMENT

I would like to thank my supervisors, Prof. Thompson and Dr Jones, for all their inspired instructions and discussions, encouragements and patience through out this project. I would also like to thank Dr. Ferguson and Dr. Mace for their useful suggestions at various stages. Thanks should also be given to Bombardier Transportation Swedish for their kind provision of the sample of the extruded panel and the data of the sound transmission loss measurement.

In addition, I would like to thank Institute of Sound and Vibration Research and University of Southampton for the financial support of my study.

Finally I wish to thank my wife, Yan, and my parent for their love and many sacrifices to support me to pursue the study in England.

List of Contents

List of symbols

a, b	the dimensions of a plate
A	area of cross-section of beam
B	bending stiffness
c	sound speed in air
c_L	longitudinal wave speed
c_B	bending wave speed
E	energy of a system, Young's modulus
F	force
f	frequency
f_c	critical freqeuncy
h, H	thickness of structure
I	second moment of area
k	wavenumber
k_a	wavenumber of acoustic wave
k_c	wavenumber at the critical frequency
k_B	wavenumber of bending wave
l, L	length of beam
L_p	sound pressure level
m, M	mass
M	modal overlap factor
m', m''	mass per unit length and mass per unit area
m, n	integer representing the indices of modes
n	modal density
N	mode count
p	sound pressure
P	perimeter of plate
r	amplitude reflection ratio of wave
R	transmission loss
S	area
t	amplitude transmission ratio of wave
TL	sound transmission loss

u, v	velocity
w	out-of-plane displacement
W	power
Y	mobility
Z	impedance
α	absorption coefficient
δ	boundary effect on mode count
ε	phase change
γ	aspect ratio
η	loss factor
κ	Timoshenko shear coefficient
λ	wavelength
μ	Poisson ratio
μ, σ	non-dimensional mass and stiffness coefficients
ρ	density of air
ρ_s	density of structure
σ	radiation efficiency
τ	transmission coefficient
ω	circular frequency
$\lvert\ \rvert$	modulus of complex value
$\langle\ \rangle$	spatially-averaged response

1 INTRODUCTION

1.1 INTRODUCTION

The passenger travelling environment is always considered to be of prime importance in the design of modern railway vehicles. The provision of acceptable noise levels inside a rail vehicle contributes significantly to the comfort of passengers. There is therefore a commercial pressure to reduce internal noise. In the last thirty years, higher train speeds and the use of lighter rolling stock, both for urban and long distance journeys, have accentuated the need for careful acoustic design. At the same time lightweight extruded aluminium panels have become widely used and these have a poor acoustic performance [1, 2, 3].

The reduction of the interior noise also receives more and more attention in other transport systems such as automobiles and aeroplanes. Consequently, low noise construction becomes one of the major challenges in the engineering community. As computer aided design and vehicle dynamics simulations become increasingly powerful, the development of new vehicle models is carried out at a very fast pace. This requires a validated acoustical prediction model optimising the design at the initial design stage rather than retrospective modification. To find a solution for the reduction of interior noise, a multidisciplinary problem has to be solved. This has attracted numerous efforts in theoretical analysis, numerical simulations and practice. Over the last few decades, structural vibration and structural acoustics, the interaction between structures and acoustics, have been extensively investigated.

It is clearly better to consider noise control when a new vehicle model is being designed rather than to wait until it is built. This can reduce the need for add-on noise control systems later in its life. Applications of numerical methods, mainly the Finite Element Method (FEM) and Boundary Element Method (BEM), have been employed in the improvement of certain acoustic characteristics of structures [4, 5]. Concerning the interior noise inside vehicles, in most cases, the structure is modelled using FEM and the acoustic domain is modelled using either FEM or BEM. Applications of these techniques to study passive noise control are mostly applied on the simplified and idealized structure for aircraft fuselages [6] and cars [7, 8] until now. Many different approaches to the methods of structural-acoustic optimisation have been reviewed by Marburg [9].

Although development of computers has enabled a wide range of applications of such numerical methods by increasing speed and efficiency, the uncertainties of modelling a complex structure at high frequencies using FEM will affect the accuracy of the simulation model. A successful result requires a profound understanding of the underlying physics of the structural dynamics and acoustics. The essence of such passive control therefore still relies on whether or not an accurate predictive model is available. Moreover, high frequency limitations of numerical methods still exist. The computational efficiency using FEM decreases substantially as frequency increases. The main reason for this is due to the fact that the wavelength of the structural deformation reduces with increasing frequency, thereby leading to unfeasibly large models in terms of the number of elements required. This difficulty applies for most of the audible frequency range of noise inside vehicle.

For noise analysis then, it is a challenge for engineers to decide which method might be best suited for a particular purpose because there is not a universal modelling approach for actual complicated structures such as a car or a railway vehicle. As to the present topic, the interior noise of railway passenger trains, very few studies have been carried out compared with those for the aircraft and automotive industries. Consequently, the acoustic environment inside many railway vehicles is not well understood and the effect of noise control measures is limited. A literature review in this field will be given in the next subsection.

In the case of a running train, the possible sources of dynamic excitation cover a very wide frequency range and mainly include the rail-wheel excitation, engine excitation and boundary layer turbulence at high speeds. Eade et al, [10] presented some examples of measured interior sound pressure levels for different types of trains, as shown in Figure 1.1. These cover a very wide frequency range from 20 Hz to about 5 kHz. As well as limiting the application of FEM analysis, which will be too computationally intensive at higher frequencies, FEM requires too much detail to be used at early stage of the design.

Alternatively, Statistical Energy Analysis (SEA) can be considered to be useful to model the interior noise of railway passenger trains.

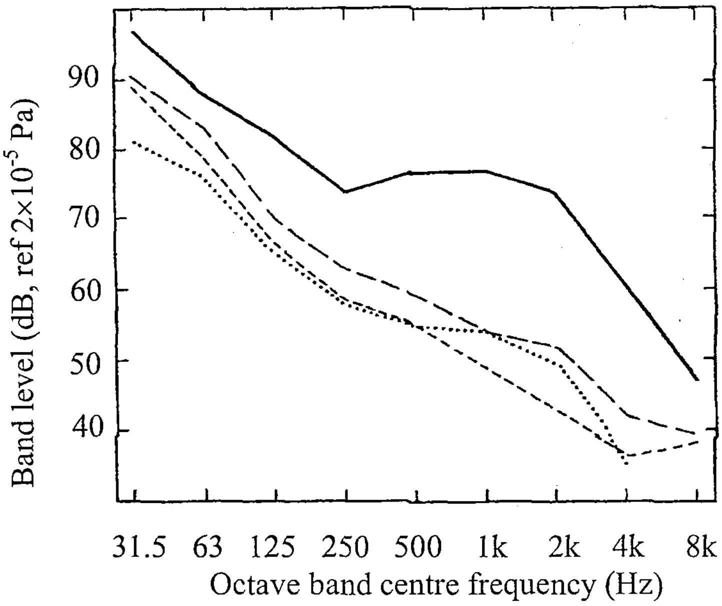

Figure 1.1. A comparison of internal noise levels (from Eade [10] 1977).
—, B.R. Mk. I second class at 145 km/h; – –, B.R. Mk. IID first class at 145 km/h; - - -, B.R. Mk. III second class at 145 km/h; ······, S.N.C.F. 52t coach first class (compartmented) at 140 km/h.

SEA [11] is now one of the most commonly used tools used in the field of the analysis of the response of a coupled structural-acoustic system at high frequencies. It deals with spatially averaged response levels within frequency bands rather than the precise details of mode shapes and resonance frequencies. This enables SEA to bypass the difficulties involved in developing a detailed mathematical model of high-frequency vibration and gives reasonable approximations. In SEA, the system is modelled as a collection of subsystems, each of which is assigned a single response variable corresponding to the vibration energy. By considering the average interaction between the modes of different subsystems, SEA can be used to estimate the response levels for each subsystem at high frequency.

It is obvious that, within the vehicle interior, the passenger listening location varies considerably. Therefore, it would be inappropriate to make any optimisation based on the sound pressure at one or a few specific locations. Prediction of interior noise may therefore be considered based on the power transmitted into the vehicle interior. Moreover, it is inevitable in the production of any type of vehicle that differences will exist between individual vehicles, that can be described by a statistical variance. Ideally, the predictive model should be able to deal with this variance within the ensemble of vehicles. It should not be over-sensitive to detailed features. However, all common control measures should be included; in particular, mass, stiffness, damping and absorption. SEA appears to satisfy all the requirements sought of this predictive model.

This thesis is concerned with a modelling approach for the interior noise of rail vehicles using SEA. An overall SEA model for the interior noise of vehicles will firstly be discussed in Chapter 2, where subsystems will be defined. The essence of this model is to use a small number of subsystems to describe the vibro-acoustics of the vehicle in overall terms rather than a model consisting of many subsystems describing the structure in detail. However, it is not the key issue in this thesis to address how to decompose the whole vehicle into subsystems, to run this SEA model to predict the interior noise, to do any sensitivity analysis, or to implement any design optimisation. Instead, the major work is concentrated on the fundamental study of several specific topics related to modelling extruded panels, which are commonly used to construct the floors and walls in modern rail vehicles. It is believed that a good overall model can only be established once an appropriate model for extruded panels has been obtained in terms of SEA. This must be based on a good understanding of the underlying physics of extruded panel behaviour.

Literature reviews for the studies on the interior noise of railway vehicles and for studies on extruded panels will be presented in sections 1.2 and 1.3. Other literature related to general topics within the fields of acoustics and vibration, which will be involved in modelling extruded panels, will be reviewed in sections 1.4, 1.5 and 1.6.

1.2 REVIEWS OF STUDIES OF THE INTERIOR NOISE OF RAILWAY VEHICLES

The study of the noise inside a railway vehicle can be traced back to the 1970’s. By using experimental methods, the ratio of structure-borne to air-borne noise was determined by Bickerstaffe and Eade [12]. It was found that for passenger vehicles on ‘noisy’ track the structure-borne and air-borne components were comparable but on good ‘quiet’ track structure-borne noise predominated. Still, it is necessary to take account of turbulent boundary-layer noise, the importance of which increases as the running speeds increase.

Eade and Hardy [10] discussed the mechanism by which the noise from various sources reaches the passenger in a rail vehicle. It has been noted that vehicles with quite different suspension systems and bodies have very similar structure-borne noise levels inside them. Through the knowledge of the measured transfer function between the interior level and each external input, the interior noise level was estimated. It was proposed in their study that it is possible to determine how much mass is needed in the various body panels. It was also emphasized that this sort of modification can only be carried out at early stages of the vehicle design.

Hardy and Jones [13] gave an overview of the sources of internal noise and mechanisms by which the sound enters the passenger areas. The measures which can be taken to influence those mechanisms were also discussed with a qualitative analysis. Both the level and the spectrum of the noise should be considered to produce a desirable acoustic environment for vehicle interiors. The criteria for assessing the acoustic comfort of a coach were also discussed by Hardy [14]. Once more, it was emphasised that the improvements to produce quieter vehicles can only be effectively incorporated if the process is started at the very early stages of design. Once the vehicles are built, it is generally too late to achieve much noise reduction. Large costs would be required for only minor improvements. It is therefore important for a manufacturer to have a tool available by which to predict the acoustic behaviour of a new vehicle at an early stage.

In the 1990's, the method of Experimental Statistical Energy Analysis (ESEA) was applied to investigate the vibro-acoustic behaviour of a high-speed train. De Meester and Hermans [15] give a description of ESEA applied to the medium and high frequency range vibro-acoustic behaviour of a high-speed train. The internal, and coupling, loss factors were derived through experiments based on the method given by Lalor [16]. The derived loss factor model was used to determine the power flows of vibration through the structure from the given inputs. The input power was applied on the support beams of the floor. The aim was to understand how the energy could flow to the interior cavity. This SEA model was also used to assess the sensitivities of energies to loss factor changes for a given input power configuration. A similar work was also reported by Lalor [17].

Other recent applications of experimental or theoretical SEA to high-speed train carriages and a driver's cabin are found in references [18, 19, 20].

Experimental SEA is only useful for studying an existing design once a prototype has been built. This would be too late to influence the design significantly. On the other hand, predictive SEA can be used at an early stage in the design. However, little work concerning predictive SEA is reported in the literature. Shaw [1] studied internal noise of railway vehicles using SEA in his MSc project. In his work, he established an SEA model for a complete vehicle (a diesel multiple unit) including a model for extruded panels. Although the dynamic characteristics of extruded panels were not investigated sufficiently to provide an appropriate SEA model for the extruded plate, the potential use of the SEA technique in the prediction of railway vehicle interior noise was shown.

Orrenius [21] presented an acoustic optimisation model for rail vehicles. The objective function in his model that is to be minimized is the total mass of the car body, subject to satisfactory sound pressure levels inside the vehicle. The interior cavity was modelled as a corridor and subdivided into a series of cavities. Based on the assumptions in room acoustics, an SEA power flow formulation was used to calculate the sound level distribution within the vehicle. However, for the airborne transmission of each body component, only mass law behaviour was considered in this simple model. More sophisticated models are required. Orrenius and Stegemann [22] and Stegemann [23]recently presented an SEA model using AutoSEA2 software [24] for a metro vehicle. This model included both the air-borne and structure-borne transmission paths. Their work identified certain modelling tasks, which need to be investigated before using a commercial software package such as AutoSEA2. Such areas include estimation of input powers for structural excitation from measured data, modelling the sound field outside the car body and certain coupling loss factors needed for coupled subsystems typical for rail vehicles. Backstrom and Orrenius [25, 26] studied the transmission loss of train partitions (C20 metro vehicle and Regina intercity train) by comparing measurements with published models for a double wall.

So far, there is generally not a comprehensive predictive model available covering the whole frequency range for the interior noise of railway vehicles. Engineers still rely on the classical approaches and experience to consider this aspect in the early vehicle design stage.

1.3 REVIEW OF THE STUDY ON EXTRUDED PANELS

Extruded aluminium panels are often used in the construction of modern railway vehicles. These consist of two outer skins and an interconnecting plate lattice. Figure 1.2 shows a sketch of a typical extruded panel.

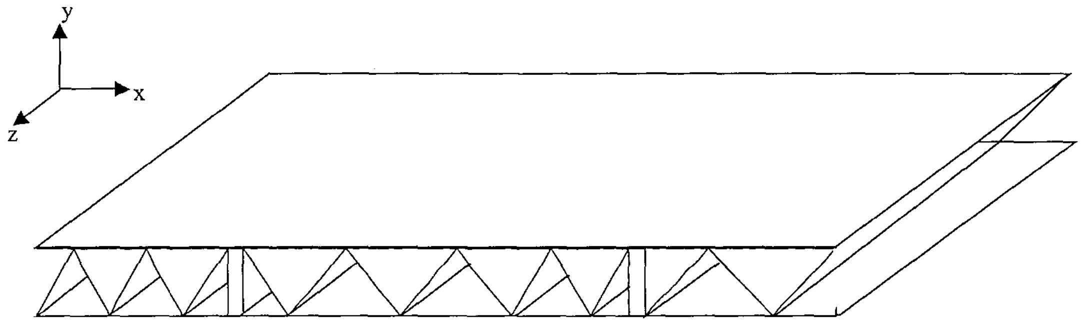

Figure 1.2. Example of an extruded panel.

Shaw [1] first studied the extruded plate in terms of SEA. His work was concentrated on the prediction of both the air-borne transmission loss and the noise radiated by mechanically excited vibrations. In his SEA model, the extruded panel was represented by subsystems composed of two outer skin plates and one tie plate. It was assumed that the tie plate subsystem represents a plate of the same size as the combined area of all interconnecting plates. All the structural connections were considered to be 90° T-type junctions. However, his model cannot take account of the global behaviour of extruded panels at low frequencies. Using different configurations of the SEA model, Shaw made attempts to predict the transmission loss of extruded panels in octave bands between 125 Hz and 4 kHz using his SEA model. It was shown that it is inappropriate to represent the extrusion cavity as a single cavity subsystem because in reality it is series of small cavities. It is plausible to use this reason to ignoring the extrusion cavity in SEA model. More convincingly, it should be taken into account that the stiffness of the tie plates is much greater than the air in the extrusion cavity and therefore dominates the coupling of the vibration of the outer plates. By increasing the damping loss factor of extruded panels, and using the radiation efficiency of a stiffened plate having similar stiffening arrangements to the actual extruded panels, better agreements with measurement results were obtained. Shaw noted that a good estimate of the radiation efficiency for extruded panels is important to develop an SEA model predicting the sound transmission loss.

Geissler and Neumann [2] calculated the transmission loss of extruded panels by using predictive SEA. In their study using AutoSEA, the equivalent sandwich panel and the rib stiffened plate formulations were used to represent extruded panels as subsystems in the SEA model. The calculation results showed considerable deviation from the measured data but the reasons were not fully analysed. Bruhl et al. [27] presented studies on the sound transmission loss and vibrational behaviour of extruded panels using AutoSEA2. It was found that sandwich models fail to predict the vibration response at high frequencies where differences in the vibration levels between the two outer skins occur. This requires further investigations of the basic characteristics of vibrations within an extruded panel to improve the SEA model.

Kohrs [3] presented a hybrid method for transmission loss prediction consisting of FEM calculations of the extruded profile and an analytical transmission loss model for an orthotropic single plate. In his work, the Discrete Fourier Transformation (DFT) technique was used to transform the local velocity distribution from FEM calculations into the wave number domain. By using an analogy with a single orthotropic plate, frequency-dependent bending stiffnesses were extracted. Instead of using the static bending stiffness, these extracted frequency-dependent bending stiffnesses were finally used in the conventional model for the orthotropic plate to predict the transmission loss. The method yielded a good agreement of transmission loss up to about 1000 Hz compared with measurements. The results from FEM calculations were also validated by comparing with mobility measurements made on a narrow sample of an extruded panel. Kohrs observed the wave motions involved within the extruded profile through a two-dimensional FE model and gave a qualitative discussion to explain the possible causes of the behaviour of the transmission loss obtained from measurements. He noted the in-phase deformation of outer plates between adjacent stiffeners at low frequencies and out-phase above certain frequencies, and inferred the requirement of further understanding of the wave motions within extruded panels. However, his model does not distinguish the global behaviour at low frequencies and vibration localisation at high frequencies of extruded panels.

Pezerat et al [28] recently presented an analytical model for extruded panels, in which the motion is decomposed in terms of the assumed mode shapes of the two outer plates. Continuity of displacements and rotations at each connection leads to a system matrix equation. It was claimed that the model permits calculation of intrinsic parameters of the structure (eigen modes, modal density), quantities concerning acoustic radiation for mechanical forces and/or plane wave excitations (mean square velocity, acoustic power, efficiency), and acoustic transmission loss for plane wave or diffuse field excitations. So far, only numerical results for the transmission loss in a diffuse field have been given.

In general, current studies on extruded panels are not sufficient to reveal the underlying physics involved. Consequently, more investigations are required in this area.

1.4 MODE COUNT AND MODAL DENSITY

In order to represent an extruded panel as a single SEA subsystem or a simple SEA model, it is necessary to know its modal densities. The modal density is one of the most important parameters required to define a subsystem within SEA. It is the average number of modes in a unit frequency interval. Related to this is the mode count, the average number of modes occurring below a certain frequency. Investigations of the mode count and modal density of extruded panels therefore form one of the major topics in the present thesis.

The mode count has the form of a 'staircase' function taking integer values that increase by 1 at each resonance frequency. However, it is often more appropriate to work in terms of an average mode count, which is a smooth line which approximates the staircase function (see Figure 3.3). This can also be seen as the average number of modes below a certain frequency occurring within an ensemble of notionally similar structures in terms of SEA. The derivative of this average mode count with respect to frequency is the modal density, which is also a statistical quality.

The evaluation of the mode count and modal density involves the determination of the frequency equation for the structure under consideration from the appropriate equation of motion and then counting the resonance frequencies over all possible modes of vibration. This yields an expression for the mode count in terms of frequency. The differentiation of the expression of the mode count in terms of frequency will then yield the expression for the modal density in terms of frequency. For a simple vibrating rectangular plate, the asymptotic function of the distribution of eigenfrequencies has been analysed by Courant and Hilbert [29] based on the *k*-space integration technique and by Bolotin [30] based on asymptotic methods. However, for a complicated structure, this mathematical solution is usually impractical.

The mode count and modal density of basic structural elements such as beams, plates and shells were investigated several decades ago [31, 32, 33, 34]. Hart and Shah [32] gave a systematic discussion of the modal density of many basic structural elements. Cremer, Heckl and Ungar [35] and Lyon [11] also gave expressions for the mode count and modal density of these basic elements of structures. Langley [36] discussed the modal density of anisotropic structural components. All these results have been used extensively in the applications of SEA for many years. In general, these expressions are based on the forms in which the modal density is taken to be independent of the boundary conditions and is proportional to the size of the system. Hence the mode count of a structural system is proportional to the length for a one-dimensional structure, to the area for a two-dimensional one and to the volume for a three-dimensional one. For more complicated structures, the simple additive property, that the modal density of the complicated system is equal to sum of the modal densities of its components, is utilised in the applications of SEA [32, 37].

The effect of boundary conditions on the mode count and modal density has received comparatively little attention, being seen as of secondary importance. In the expressions for evaluating the mode count of structural SEA subsystems, presented by Lyon and DeJong [37], the effect of boundary conditions on the mode count and modal density was indicated in terms of a coefficient δ_{BC} that is indicated as usually constant for one-dimensional subsystems and usually assumed to be zero for two-dimensional and three-dimensional subsystems. However, for acoustic SEA subsystems, such as, for instance, a cavity with rigid walls, the mode count is given by [38]

$$N(f) = \frac{4\pi V}{3c^3} f^3 + \frac{\pi S}{4c^2} f^2 + \frac{L}{8c} f \tag{1.1}$$

where V is the volume, S is the total surface area, L is the total length of edges, c is the sound speed in air and f is frequency. This expression was first obtained by Maa [39]. For zero pressure boundary conditions the above expression becomes

$$N(f)=\frac{4\pi V}{3c^3}f^3-\frac{\pi S}{4c^2}f^2+\frac{L}{8c}f \tag{1.2}$$

which was given by Roe [40]. This demonstrates that the boundary conditions do have effects on the mode count, and from the derivatives of equation (1.1) and (1.2), also on the modal density although clearly as frequency increases, $N(f)$ becomes dominated by the first term, proportional to the volume. The types of boundary conditions that may be present on structural systems are more diverse and therefore require a more extensive analysis.

More recently, Bogomolny and Hugues [41] and Bertelsen, Ellegaard and Hugues [42] give expressions for the mode count of a rectangular plate under three standard boundary conditions: free, simple support and clamped on all edges, based on the rigorous analysis by Vasil'ev [43]. In their expressions, there is a perimeter term, which corresponds to δ_{BC} as given in reference [37]. However, for one-dimensional systems and the rectangular plate under other combinations of boundary conditions, this perimeter term (or δ_{BC}) is still not generally available.

For complicated structures, it is thought that boundary conditions and intermediate constraints have certain effects on the mode count and modal density of the structures. The determination of these effects quantitatively or qualitatively therefore forms one of the major areas of study in the present thesis. The objective of this study is to enable the modal density of extruded panels, or other complicated structures, to be evaluated based on these investigations.

1.5 SOUND RADIATION

To consider the sound transmission of extruded panels using SEA techniques, the radiation efficiencies of the extruded panels must be known. The radiation efficiency of a structure is essentially a quantity measuring the strength of the coupling between the structure and the surrounding fluid. Before the radiation efficiency of extruded panels can be modelled, the radiation efficiency of rectangular plates is first studied.

The sound radiation from a vibrating rectangular plate is of great practical importance and has been investigated extensively over many years. For a flat plate set in an infinite baffle, the radiated sound field can be calculated by a Rayleigh integral approach [44]. There are two common approaches used to determine the radiation efficiency, or resistance, theoretically. The first is to integrate the far-field acoustic intensity over a hemisphere enclosing the plate. The other approach is to integrate the acoustic intensity over the surface of the vibrating plate. Both approaches require a knowledge of the distribution of vibration velocity over the plate. This is usually obtained by assuming the boundary conditions are simple supports. Since plate vibrations generally involve many superimposed modes, the radiation efficiency of a plate, in principle, can be obtained by summing the effect of all the modes that contribute significantly in the frequency range under consideration.

The radiation efficiency of a single mode of the plate is usually called the modal radiation efficiency. The total radiation efficiency of the plate is called either the 'average radiation efficiency' or the 'weighted radiation efficiency'. In the literature, both the terms 'radiation resistance' and 'radiation efficiency' are used, the latter being the radiation resistance normalised by the surface area and the impedance of air. The radiation efficiency is thus defined by

$$\sigma = \frac{R_{rad}}{\rho c S} = \frac{W_{rad}}{\rho c S \left\langle \overline{v^2} \right\rangle} \tag{1.3}$$

where R_{rad} is radiation resistance, W_{rad} is power radiated by the plate, S is the area of the plate, $\left\langle \overline{v^2} \right\rangle$ is the spatially averaged mean square velocity of the plate, ρ and c are the density of air and the speed of sound in air respectively.

For a detailed study of the radiation it is necessary to derive expressions for the radiation resistance of particular structural mode shapes of the plate. As early as the 1960s, Maidanik [45] first proposed several approximate formulae for calculating the modal radiation resistance in the whole frequency range. Wallace [46] presented exact and approximate expressions for the modal radiation efficiency of rectangular plates at arbitrary frequencies below the critical frequency. He investigated the effects on radiation efficiency of the inter-nodal areas and their aspect ratios. The characteristics of the radiation from a baffled rectangular plate were clearly shown. Gomperts [47, 48] investigated the modal radiation of a rectangular plate under general boundary conditions. It was found by Gomperts that plates with greater edge-constraints do not always have larger radiation efficiencies than less edge-constrained ones, and the radiation efficiencies for two-dimensional vibration patterns differ rather considerably from those for one-dimensional vibration patterns.

In addition to these methods, Heckl [49] analysed sound radiation of planar sources by using a Fourier transform approach in *k*-space (wavenumber space). Leppington [50] later introduced several asymptotic formulae to calculate the modal radiation efficiency for large acoustic wavenumbers, especially in the range close to the critical frequency. Williams [51] proposed a series expansion in ascending powers of the wavenumber *k* for the acoustic power radiated from a planar source. Most recently, Li [52] gave an analytical solution, in the form of a power series of the non-dimensional acoustic wavenumber, to calculate the modal radiation resistance of a rectangular plate for moderate wavenumbers.

As well as modal radiation resistances, the average radiation of a plate has also been an active subject of study because of its practical importance. It was also Maidanik [45] who first applied the concept of power flow and statistical energy analysis to overcome the burdensome calculation at higher frequencies where many modes contribute to the vibration of a plate. He presented a formula for the average radiation resistance based on the assumption of a reverberant vibration field (equal modal energy). A similar modal-average radiation curve was presented in reference [53]. Leppington [50] re-investigated the problem of average radiation efficiency and revised some of Maidanik's work, using the assumption of high modal densities for the plate. His assumption is based on the same principle as Maidanik's. It was found in Leppington's study that Maidanik overestimated the radiation resistance at coincidence, particularly for a plate with a very large aspect ratio. Leppington also gave an equivalent formula to Maidanik's for large acoustic wavenumbers.

However, in the works of both Maidanik and Leppington, the radiation resistance was considered without including the cross-mode contributions. Snyder and Tanaka [54] introduced the contribution of the cross-modal couplings to calculate the total acoustic power at low frequency using modal radiation efficiencies. It was shown that the cross-mode contributions are only non-zero for pairs of modes that are either both odd or both even in a given direction. The mutual radiation resistance was also investigated recently by Li and Gibeling [55, 56]. It was found that the cross-modal coupling could have a significant impact on the radiated power, even at a resonance frequency. The cross-modal contributions were also included in the power series of Li [52].

The radiation of a double-skinned extruded plate has not been sufficiently investigated so far. This problem is far more complicated than that of rectangular plates because of the unavailability of the pattern of the velocity distribution over the surface of the panel. In terms of the modal summation, the average radiation efficiency of extruded panels can be modelled if the natural modes and their modal radiation efficiencies are available. The extruded panel can be considered as a built-up structure composed of a set of strips with their long edges having same length and the short edges having different lengths. At high frequencies, the modes of strips will be dominant in the radiation of extruded panels. Therefore the radiation efficiencies of strips are of great interest for the present purpose.

Although the 'strips' considered here are no more than rectangular plates of large aspect ratio, it will be shown in Chapter 5 that, for a certain frequency range, the classic formulae previously obtained for the rectangular plate are not suitable. Sakagami and Michishita [57, 58] investigated the characteristic of the sound field radiated by a baffled and unbaffled strip with infinite length under different excitation. However, only the sound pressure for certain given positions was studied and the radiation efficiency of the strips was not presented.

1.6 COUPLING BETWEEN MODES OF EXTRUDED PANELS

When an extruded panel is vibrating under certain excitations, the dynamic characteristics of the structure are dominated by the global modes at low frequencies and the local modes at high frequencies. To model extruded panels using SEA techniques, the coupling between global and local modes and the coupling between different local mode subsystems are crucial aspects that govern the applicability of the SEA model.

Due to the low modal density of global modes and the complexity of the structure, it is quite difficult to model the coupling between them and local modes in terms of SEA. Similar problems have been studied to address the dynamic behaviour of complicated or built-up structures over recent decades. In general, these studies were concentrated on beam-plate systems [59, 60], which are commonly used in many industrial structures and, hence, form useful academic examples. Normally, vibration sources are supported by stiff beams. The power injected into and transmitted around structures is controlled by long-wavelength waves generated in these beams. As these long waves propagate along the stiff beams they generate short-wavelength flexural waves in the attached flexible plates. The coupling between global and local modes within extruded panels is physically similar to that between beams and plates within beam-plate systems. In conventional SEA, a stiffening structure, such as a beam or rib, is often not considered as a separate SEA subsystem. Nevertheless, vibration sources are often applied on the stiffeners in the actual structures and, consequently, SEA may not yield satisfactory predictions.

This issue has been recently investigated by several authors. Grice and Pinnington [61, 62] propose a method to analyse the beam-plate system by using a combination of numerical analysis to model the stiff beam and analytical impedances to model the flexible plate. The theoretical foundation of their method relies on there being a significant difference between the wavelengths in the beam and plate. Ji et al. [63] present a mode-based approach to deal with the mid-frequency behaviour of such systems. By introducing a set of basis functions along the interface, the dynamic response of the beam and the power transmitted to the plate can be calculated in a simple and approximate manner.

Langley [64] presents a new method for the analysis of complex dynamic systems which is based on partitioning the system degrees of freedom into a "global" set and a "local" set. The global equations of motion are formulated and solved in a standard deterministic manner, although due account is taken of the presence of the local degrees of freedom via an approach which is analogous to fuzzy structure theory [65, 66, 67]. The local equations of motion are formulated and solved by using statistical energy analysis (SEA) with due account being taken of power input from the global degrees of freedom. This method encompasses a number of existing analysis techniques and forms a flexible framework. However, a number of detailed modelling strategies are required to represent actual structures in practice. Lande et al. [68] recently presented a hybrid modelling strategy for beam-plate structures due to excitation applied through their stiffening members. The power input to the plate subsystems is calculating by adding a power absorbing plate impedance matrix to the regular beam network impedance matrix in the FEM formulation. However, initial investigations were focused on a simple membrane, within which certain numerical difficulties were found.

Although several methods have been proposed to cope with vibrations within built-up structures, they all are derived for and verified on a very simple built-up structure such as a beam attached to a plate. There is not a general approach available to deal with the vibration behaviour within a complicated built-up structure comprising long- and short-wavelength components. The dynamic behaviour of extruded panels can be essentially represented by the combinations of the global motion of the whole structure and the local motion of the part of structure. The interaction between the global and local motion is analogous to that of the beam-plate system. Therefore this problem forms a part of the present work.

1.7 LAYOUT OF THESIS

This thesis is concerned with modelling the interior noise of railway vehicles using the SEA technique with the intention of using a small number of subsystems to enable insight into the sound transmission. An overall SEA model is considered but does not form the main work in this thesis. The major objective is to develop an SEA model for extruded panels. Several aspects relating to this aim are investigated in detail. Ultimately, it is intended that this SEA model can be used to predict the response of extruded panels, under acoustic and mechanical excitations, and can be incorporated into the overall model to predict the interior noise of railway vehicles.

Chapter 2 first introduces SEA, how to use SEA to model a system and the assumptions behind the applications of SEA. A simple three-subsystem SEA model predicting the interior noise of the vehicle is then presented. The aim of this simple SEA model is to introduce the procedures using the SEA technique to model the interior noise for railway vehicles. In particular, it shows how SEA can be used to study the sound transmission of panels. A ten-subsystem overall SEA model is finally established and presented in

Appendix A. The necessary problems associated with the SEA model that need to be solved are identified. Among these problems, modelling extruded panels in terms of SEA is the major interest in the present thesis.

For this reason Chapters 3 and 4 investigate the mode count and modal density of extruded panels. In Chapter 3, a two-dimensional extruded section, i.e. the cross-section of a extruded panel, is considered. This is based on studies on the mode count of one-dimensional subsystems. The mode count of one-dimensional systems is investigated with particular reference to the relationship with the boundary conditions. The effects due to boundary conditions are found for a single one-dimensional element. Then the mode count of a multi-beam system is studied. It is found that an intermediate constraint has the same effect on the average mode count as the same type of constraint applied at an end. The analysis is then extended to the mode count of the cross-section of an extruded panel. An approximate two-dimensional model for the extruded section is developed and the results are compared with those from an FEM analysis. Finally the modal density and driving point mobility of the extruded section are also studied and it is shown that these can be estimated quite well from the above analysis.

In Chapter 4, the relationship between the mode count of two-dimensional systems and their boundary conditions is investigated, with particular reference to rectangular plates. The effects due to line boundary conditions are found using wavenumber space integration. The modal density of two-dimensional systems is hence obtained. Based on these studies, an approximate model for the mode count and modal density of an extruded plate is developed.

The studies of the average radiation efficiency of rectangular plates, strips and extruded panels are the subject of Chapter 5. The radiation of extruded panels is considered in terms of the contributions from global modes and local modes. This involves investigations of the radiation efficiency of rectangular plates and narrow strips. The modal summation approach is first derived and results from it are compared with the classical expressions from the literature. The modal summation approach is able to include both the free field and the near-field radiation from the structure. This allows insight into the effects of large aspect ratio and damping. It is found that the previous formulae are not suitable for strips. A number of analyses are presented to solve this problem. Approximate expressions for strips are then given. This finally leads to an approximate model for the radiation of the extruded panels.

Chapter 6 presents a model for the coupling between global and local modes. A coupling loss factor is derived on the basis of excitation by a travelling global wave under the assumption that the local modes of each strip are uncorrelated.

Experimental results of vibration and sound radiation on a sample double skin aluminium extruded plate are presented in Chapter 7. The panel was forced at points on its surface and the response of the panel was measured using a scanning laser vibrometer. The driving point mobility was measured for excitation positions either on strips or on stiffeners. The distribution of vibration energy over the panel was investigated for different excitation positions. The attenuation of vibration with distance due to the damping effect was measured to derive damping loss factors. The radiation efficiency of the sample panel was measured in a reverberant chamber using a reciprocal technique.

The development of the previous analyses on the vibrational behaviour of the extruded panels leads to their application in Chapter 8. These results are brought together to allow two SEA models for extruded panels to be proposed. The response of the extruded panel is predicted using these SEA models for acoustical and mechanical excitations. Results obtained are compared with experimental data.

Finally, in Chapter 9, the conclusions of this work are summarised and possible future work is suggested.

2 SIMPLE SEA MODELS FOR INTERIOR NOISE

2.1 INTRODUCTION TO SEA MODELLING

The following summary of SEA is largely drawn from [69, 37]. SEA was originally developed, amongst others by Lyon [11], for use in the design of space craft in the 1960s. It is an approach commonly used in the analysis of the response of complex systems in acoustics and vibration at high frequencies. SEA is not concerned with the exact details, such as mode shapes and resonance frequencies, of a specific system. Rather, it is concerned with the average behaviour of a population or ensemble of structures that are nominally identical but in practice have small differences. In SEA, the system is divided into a number of subsystems, normally acoustical and structural, which are coupled together. Broadband stationary random excitations are applied to one or more of them. Each subsystem is represented using its gross physical properties, such as geometric form, dimensions, material properties and loss factors. The primary aim of the analysis is to estimate the distribution of vibration energy among the coupled 'subsystems', and for this purpose energy balance equations are set up which involve expressions for power flowing from one subsystem to another. Each subsystem's energy can be obtained by solving the power balance equation

$$\begin{bmatrix} \sum_{j=1}^{n}\eta_{1j} & -\eta_{21} & \cdots & -\eta_{n1} \\ -\eta_{12} & \sum_{j=1}^{n}\eta_{2j} & \cdots & -\eta_{n2} \\ \vdots & \vdots & \ddots & \vdots \\ -\eta_{1n} & -\eta_{2n} & \cdots & \sum_{j=1}^{n}\eta_{nj} \end{bmatrix} \begin{bmatrix} E_1 \\ E_2 \\ \vdots \\ E_n \end{bmatrix} = \frac{1}{\omega} \begin{bmatrix} W_{in,1} \\ W_{in,2} \\ \vdots \\ W_{in,n} \end{bmatrix} \tag{2.1}$$

where E_i represents the spatially and time-averaged energy of subsystem i, η_{ii} is the internal loss factor of subsystem i and η_{ij} is the coupling loss factor between subsystems i and j, ω is the band centre frequency and $W_{in,i}$ is the power input into subsystem i.

For structural subsystems, which bear bending and longitudinal waves, the subsystem energy is given by

$$E = M\left\langle \overline{v^2} \right\rangle \tag{2.2}$$

where M is the mass of the structure and $\left\langle \overline{v^2} \right\rangle$ is the spatially-averaged mean square velocity.

For acoustic systems, the subsystem energy is given by

$$E = \frac{V\left\langle \overline{p^2} \right\rangle}{\rho c^2} \tag{2.3}$$

where V is the volume of the cavity, ρ is the density of the air, c is the velocity of the sound and $\left\langle \overline{p^2} \right\rangle$ is the spatially-averaged mean square sound pressure. In practice this is expressed via the sound pressure level in decibels, related to $\left\langle \overline{p^2} \right\rangle$ by

$$L_p = 10\log_{10} \frac{\left\langle \overline{p^2} \right\rangle}{p_r^2} \tag{2.4}$$

where p_r is the reference sound pressure, 20μPa.

Much of the literature on SEA is concerned with studies of the fundamentals of coupled resonators and other purely theoretical matters. Although these studies are important for a detailed understanding of SEA, they provide little guidance for its application to complex systems. It should be indicated here that this thesis is not so concerned with the theoretical background of SEA. Rather, the present work is concerned with a set of problems related to the application of SEA, modelling extruded panels, which will be used to consider interior noise of railway vehicles. However, before the main topic is presented, a number of assumptions within the application of SEA have to be mentioned.

In SEA, it is assumed that within a frequency band the vibrational or acoustical energy in each subsystem resides in resonances, each of which has equal energy. This assumption is the so called equipartition of modal energy. This normally demands a high modal density for each subsystem. Usually a minimum of 5 or 6 modes per bandwidth of interest are required [37]. In the point view of waves, this suggests that the wavefield is a diffuse field where waves come from all directions and energy is uniformly distributed. Moreover the coupling loss factors η_{ij} are usually assumed to be related by the consistency relation

$$n_i\eta_{ij} = n_j\eta_{ji} \tag{2.5}$$

where n_i is the modal density. Therefore, the investigation of the modal density of a subsystem always has a high priority during the application of SEA. For homogeneous and simple systems, theoretical expressions for the modal densities are available. However, for complicated built-up structures, analytical expressions are normally not available. This problem forms a main topic and will be addressed in Chapters 3 and 4 of the present thesis.

In addition to the modal density, the modal overlap factor is used to justify the applicability of SEA. The modal overlap factor is the ratio of the average modal damping bandwidth to the average spacing between the modes. It is defined by [37]

$$M = f\eta n(f) \tag{2.6}$$

where f denotes frequency, η is the damping loss factor of the subsystem and $n(f)$ is the modal density per Hz in the subsystem. Values of the modal overlap factor greater than unity indicate a modal response that is suitable for dealing with statistically [70, 71].

Another fundamental assumption in SEA is that subsystems are coupled only weakly. There are no universally agreed criteria to determine whether the coupling is weak. Qualitatively speaking, this assumption requires that subsystems can be considered as separate containers of resonant energy with relatively small flow of energy between them. According to the Smith criterion [72], coupling is weak if the ratio of the coupling loss factor to the internal loss factor of each oscillator is substantially less than unity. Under this condition, the energies of subsystems depend on the dissipation loss factors but not strongly on the coupling loss factors. Weak coupling does not imply that the connections between subsystems are physically weak, e.g. a welded joint between two panels of widely differing thicknesses constitutes a weak coupling due to large impedance discontinuities.

The initial step in the application of SEA to any system is the choice of subsystems. A subsystem is ideally physically uniform and can be simply characterized by its material properties and geometric boundaries. On the boundaries, it is desirable to have a clear impedance mismatch. Normally, the subsystems are finite linear elastic systems which can be described in terms of their modal density and damping. Subsystem modelling for SEA tends to be successful: if the energy density is reasonably uniformly distributed within a subsystem (i.e. fairly homogeneous); if the modal overlap factor of each subsystem is of the order of unity or greater (i.e. subsystems should not be too small); if each subsystem has sufficient modes (>5) in each frequency band of analysis (i.e. subsystems not too small and bandwidth large enough) and if adjacent subsystems are weakly coupled.

There are some difficulties involved in subsystem modelling. In practice, many structures having discontinuities (such as ribs, frames etc.) are highly selective in their reflective properties (strongly dependent on frequency and angle of incidence). Such discontinuities may give widely differing reflection depending on the wave type. Then it is necessary to define different subsystem boundaries for different wave types. Sometimes there is a need to model such complicated structures as a single subsystem or a few subsystems (to ensure a sufficient modal density in the subsystem or to reduce the size of the overall SEA model). This requires an understanding of the wave-propagation behaviours of these types of structure.

On the other hand, difficulties also relate to modelling large subsystems. In a large subsystem, the energy is sometimes not uniformly distributed. This is difficult to divide into several subsystems as there are no obvious discontinuities or boundaries. In these cases it is necessary either to change the coupling loss factors in the SEA model to give increased attenuation or to correct the answer. In the present application, this problem will occur in modelling the interior cavity and the floor of the railway vehicles. This is particularly the case for the decay of sound level along the carriage interior. Craik [73] gives an approach to deal with modelling corridors. This contravenes the weak coupling criterion but at least allows the decay to be taken into account. A convenient limit for the maximum dimension L of a subsystem is also given by Lyon and DeJong [37]

$$L < \frac{c_g}{2\pi f \eta_d} \tag{2.7}$$

where η_d is the damping loss factor and c_g is the energy group speed.

After subsystems are defined, the damping loss factors within subsystems and the coupling loss factor between subsystems have to be evaluated. There are some analytical methods and empirical data available for some common, simple subsystem configurations such as material damping, interface damping and damping treatments [37]. For convenience of analysis, it is sometimes assumed that all modal damping loss factors are equal. This may be sufficient in most cases when the subsystems have similar construction and materials. The damping loss factor can also be measured by experiments. There are two most common methods for experimentally determining the damping loss factor of a subsystem: the decay rate and the half-value bandwidth [35, 74]. In some cases, attenuation of wave propagation with distance can also be used to determine the damping loss factor [35, 75].

The estimation of coupling loss factors between various subsystems is central to SEA. However, there is no universally accepted method for predicting them theoretically or determining them experimentally or numerically. Plentiful literature addressing this problem can be found since the beginning of SEA. The most common theoretical methods are the modal approach [76, 77] and the wave approach [35, 11]. The wave intensity analysis was later introduced to treat cases where the diffuse field assumption no longer holds [78]. FEM can be used to calculate the response of two coupled subsystems and to derive their coupling [79, 80, 81, 82, 83]. Similarly, the dynamic stiffness method can be used to calculate the response of two coupled subsystems in certain special geometric cases [84, 85]. Experiments can be performed on a whole system or pairs of subsystems. By exciting each subsystem in turn and measuring the input powers and the subsystem energies, the loss factor matrix can be determined by matrix inversion [16].

Finally, the input powers are introduced to implement the predictive SEA calculations. In some cases the input power is given independently by experimental measurements. In other cases the excitation is given as a prescribed dynamic variable such as force or velocity at some locations in the system. In these cases the input power can be calculated [37].

2.2 SIMPLIFIED SEA MODEL WITH THREE SUBSYSTEMS

Railway vehicles are large and complicated structures. There is a tendency for SEA models to be made too large initially (i.e. in terms of the number of subsystems) in order to include all the important transmission paths. However, for each subsystem introduced, more coupling loss factors need to be assessed and calculated so that the model can very quickly become unmanageable. Moreover the simplicity of the SEA approach and the insight it gives become lost. Usually, it is better to start with a relatively simple model and add extra subsystems later. This can be difficult since it is not always easy to know in advance which parts of a structure can be ignored.

As a starting-point, a subsystem can be chosen to compare to a physical component of the vehicle. The interior cavity, floor and side walls etc. will be considered as separate subsystems. Ideally, each subsystem in an SEA model should be a group of modes with the same properties that will approximately have the same modal energies. However, in reality, the subsystem itself is of complicated construction and cannot be represented appropriately just using a single and simple subsystem. This causes difficulties in predicting the interior noise of vehicles using an SEA model since subsystems cannot be well defined. For example, the floor and walls are normally built using extruded panels. It will be not possible using bending modes of a single plate to represent extruded panels. Previous studies have also shown that using models of stiffened plates or sandwich plates failed to predict the sound transmission of extruded panels [2].

The difficulties of defining complicated subsystems also limits the use of commercial SEA software such as AutoSEA, which includes most standard subsystems, although it is relatively easy to create an overall model for the interior noise of vehicles. Therefore, more accurate and efficient SEA subsystem models to represent the floor and walls are urgently required. The main work of the present thesis will be focused on this problem. This will be studied in detail in later chapters.

Dividing the system into subsystems should also consider the suitable size for subsystems. The correct choice of the size of subsystems is necessary to prevent too much decay in waves travelling across a length of a subsystem with relatively high damping. This requires an upper limit on subsystem size. In the literature using SEA to model the interior noise [19, 22, 86], the whole vehicle was truncated in a number of sections and only one section was modelled as an SEA model. How the lengths of the section were chosen was not discussed. In reference [21], the interior cavity was modelled as a 'corridor' using the approach given by Craik [73]. The interior cavity was subdivided into N cavities. However, the length of each sub-cavity is not given.

Here, a vehicle is initially considered as a simple SEA model consisting of only 3 subsystems. This three-subsystem model will be discussed as an example to illustrate general features of SEA. It will be used to show that SEA can be used not only for complex problems, such as predicting the overall performance of a whole vehicle, but also for simpler problems, such as estimating the sound transmission of a plate. In addition, this SEA model will be extended to consider the sound transmission of extruded panels in Chapter 8.

A more advanced ten-subsystem SEA model is introduced in Appendix A, where the subsystems are defined and the coupling mechanism between subsystems are identified. However, the results from this ten-subsystem SEA model are not presented since it is beyond the scope of the present thesis.

2.2.1 MODEL DESCRIPTION

This is a very simple SEA model to represent the interior noise of a coach. Under a direct consideration of the obvious source and transmission path, the vehicle is partitioned into only **three** subsystems, as shown in Figure 2.1.

1) An acoustic cavity for the passenger compartment.
2) The floor, represented by a plate sustaining bending waves.
3) The cavity under the floor.

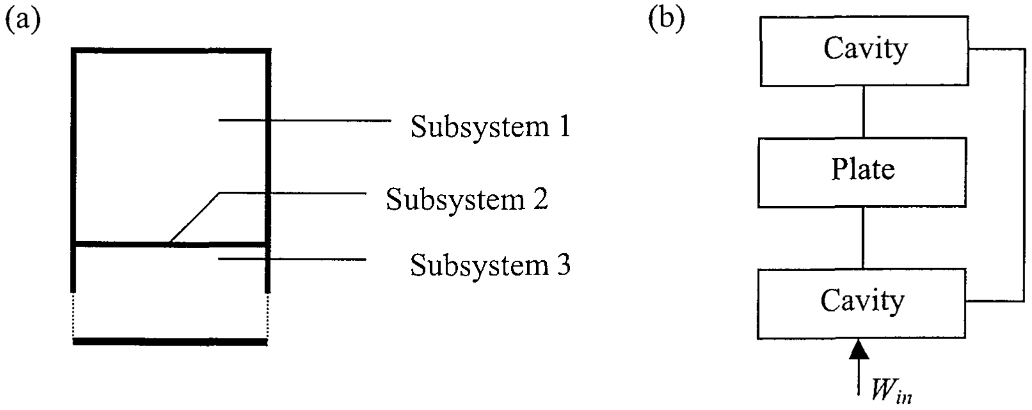

Figure 2.1. Sketch of three-subsystem SEA model for a coach

In order to simplify the model, the mechanical excitation is neglected and the auxiliary equipment or engines under the floor, often present in the real situation, are not considered. Only acoustic excitation under the floor, representing the wheel-rail noise, is considered here as the external excitation. Thus only two kinds of coupling exist in this SEA model, as show in Figure 2.1(b).

- Plate-cavity acoustic coupling
- Non-resonant sound transmission from one cavity to another through a plate.

It should be pointed out that in practice the acoustic transmission from the under-floor cavity to the interior also includes the transmission through the walls, windows and roof (see Appendix A). In this simple model only transmission via the floor is considered.

In Figure 2.1(a) the upper solid lines of subsystem 3 represent the sides of the coach and lower dashed lines are the air gap. The bottom of the cavity represents the surface of the track.

2.2.2 PARAMETERS OF THE MODEL

The geometric dimensions and the physical properties assumed for the three subsystems are presented in Table 2.1. The dimensions are nominally representative of a railway coach. The floor is taken here as a 10 mm thick steel plate whereas in practice it will have a more complex beam-stiffened plate or extruded construction.

Table 2.1. Parameters used to describe 3-subsystem model

No of subsystem	Description of subsystem	Dimensions			Physical properties				
		Length (m)	Width (m)	Height (m)	Material	Density kg/m^3	Young's modulus N/m^2	Poisson ratio	Wave speed m/s
1	Cavity, interior	20	3.0	2.7	Air	1.21			343
2	Plate, floor	20	3.0	0.01	Steel plate	7700	1.95×10^{11}	0.28	
3	Cavity, external	20	3.0	1	Air	1.21			343

2.2.3 LOSS FACTORS

- **Damping loss factor of the plate**

The damping loss factor of the plate is assumed to be constant and equal to 0.03.

- **Internal loss factor of cavity**

The internal loss factor of a cavity can be obtained from the reverberation time of an acoustic field. The relationship is expressed by [37]

$$\eta = \frac{2.2}{fT_R} \tag{2.8}$$

where T_R is the reverberation time. T_R can be estimated from Sabine's formula [37]

$$T_R = 0.161\frac{V}{S\overline{\alpha}} \tag{2.9}$$

where S is the total surface area of the acoustic cavity, V is the volume of the acoustic cavity, and $\overline{\alpha}$ is the average (random incidence) absorption coefficient of the walls of the cavity where parts of the walls S_i have different absorption coefficients α_i,

$$S\overline{\alpha} = \sum S_i\alpha_i \tag{2.10}$$

In the present calculations, a constant absorption coefficient 0.1 is used for the walls of the cavities and 1 for the air gap of the under-floor cavity.

- **Coupling loss factor of plate-cavity**

The power transmitted from the plate (subsystem 2) to the cavity (subsystem 1) is given by

$$W_{21} = \omega\eta_{21}E_2 = \omega\eta_{21}m_2\left\langle\overline{v^2}\right\rangle \tag{2.11}$$

where E_2 is the time-averaged energy of the plate, m_2 is the mass of the plate and $\left\langle\overline{v^2}\right\rangle$ is the spatially-averaged mean-square vibration velocity of the plate.

The energy radiated to the air by the plate is given by

$$W_{rad} = \rho cS_2\sigma_{rad}\left\langle\overline{v^2}\right\rangle \tag{2.12}$$

where ρ is the density of air, c is the velocity of sound, S_2 is the area of the plate and σ_{rad} is the radiation efficiency of the plate and can be calculated as described in Chapter 5 [45].

Because W_{21} is equal to W_{rad} for radiation from one side of the plate, the coupling loss factor from the plate to the cavity is derived and is given by

$$\eta_{21} = \frac{\rho c S_2 \sigma_{rad}}{\omega m_2} = \frac{\rho c \sigma_{rad}}{\omega \rho_s h} \tag{2.13}$$

where ρ_s and h are the density and the thickness of the plate.

The modal density of the plate is given by [37]

$$n_2(f) = \frac{S_2}{2Rc_L} = 2\pi n_2(\omega) \tag{2.14}$$

where $R = h/\sqrt{12}$ is the radius of gyration of the plate cross-section, c_L is the velocity of longitudinal waves in the plate, $c_L = \sqrt{\frac{E}{\rho_s\left(1-\mu^2\right)}}$.

The modal density for the cavity is given by [38]

$$n_1(\omega) = \frac{\omega^2 V_1}{2\pi^2 c^3} + \frac{\omega S_1}{8\pi c^2} + \frac{L_1}{16\pi c} \tag{2.15}$$

where V_1 is the volume of the cavity, S_1 is the total surface area of the cavity and L_1 is the total length of the edges of the cavity. c is the speed of sound in air. This expression is usually dominated by the first term.

The coupling loss factor η_{12} can also be derived according the consistency relationship (equation (2.5)) and expressed by

$$\eta_{12} = \frac{n_2}{n_1}\eta_{21} = \frac{\rho_0 c S_2 \sigma_{rad}}{4\pi\omega\rho_s c_L R h n_1} \tag{2.16}$$

The radiation efficiency of rectangular plates can be calculated from the expressions given by Maidanik [45] or Leppington [50] (see Chapter 5). It can be seen at this stage that the radiation efficiency of the structure is a very important parameter for determining the coupling loss factor between structures and cavities. In Chapter 5, the radiation efficiency will be investigated by the modal summation approach.

- **Non-resonant sound transmission from one cavity to another through a plate**

The coupling loss factor between two cavities through a plate is given by [69]

$$\eta_{31} = \frac{cS_2}{4\omega V_3}\tau_{31} \tag{2.17}$$

where τ_{31} is the transmission coefficient from subsystem 3 through the plate to subsystem 1. It can also be expressed as the sound reduction index R. The relationship between the transmission coefficient and the sound reduction index is expressed by [87]

$$R = 10\log_{10}\left(\frac{1}{\tau}\right) \tag{2.18}$$

The sound reduction index for a uniform panel under random incidence is given approximately by [87]

$$R \approx \begin{cases} R(0) - 5dB\ ; & f < f_c \quad \text{(a)} \\ R(0) + 10\log_{10}\left[f/f_c - 1\right] + 10\log_{10}\eta - 2\ ; & f > f_c \quad \text{(b)} \end{cases} \tag{2.19}$$

where $f_c = \dfrac{c^2}{2\pi}\sqrt{\dfrac{\rho_s h}{B}}$ is the critical frequency of the plate, where B is the bending stiffness of the plate. $R(0)$ is the sound reduction index under normally incident sound waves, which is given by the mass law [87]:

$$R(0) \approx 20\log_{10}\left(\frac{\omega\rho_s h}{2\rho_0 c}\right) \tag{2.20}$$

for frequencies above the first resonance of the panel.

It should be pointed out that, for non-resonant transmission, the transmission coefficient is only dependent on the mass of the panel between two cavities. In other words, the formula for frequencies below the critical frequency is used for all frequencies to calculate the non-resonant transmission. The resonant transmission included in equation (2.19)(b) is included in the SEA model via η_{32} and η_{21}.

2.2.4 CALCULATION RESULTS

The modal densities of the subsystems are presented in Figure 2.2. It can be seen that the modal densities for the two cavity subsystems increase as frequency increases. For the two-dimensional plate subsystem bearing bending waves, the modal density is constant in the present case. It will be shown in Chapters 3 and 4 that the modal density of a plate is frequency-dependent when the effect of the boundaries are taken into account. Figure 2.3 shows the modal overlap factors for each subsystem. The modal overlap factor of the interior cavity is less than unity for frequencies below 70 Hz. Therefore the present SEA model is valid above 70 Hz. For a real passenger coach, the cavity dimension and the damping loss factor should be measured so that a real modal overlap factor can be derived when the SEA model is set up.

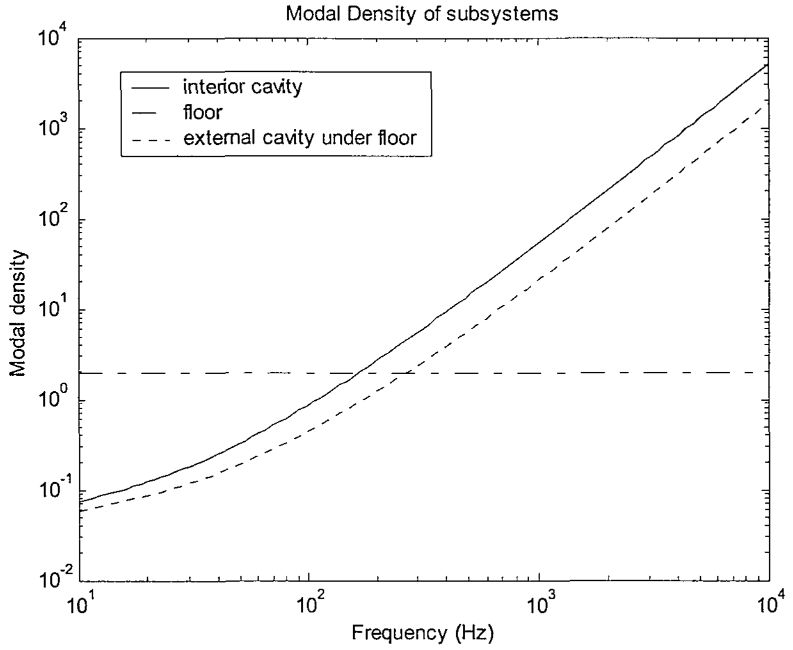

Figure 2.2. The modal densities of subsystems

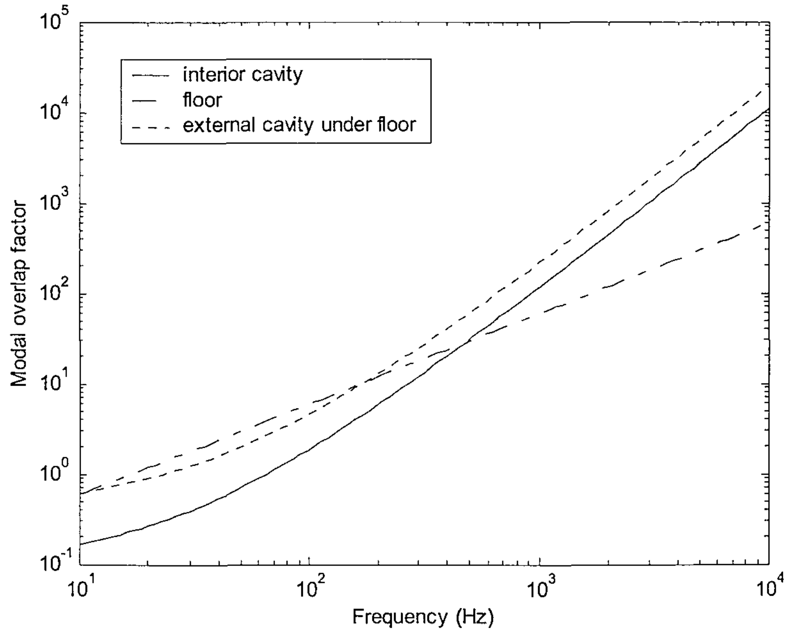

Figure 2.3 Modal overlap factors of subsystems.

The loss factors are presented in Figure 2.4 according to their position in the matrix. Graphs on the diagonal of the grid are the internal loss factors of the subsystems. It can be seen that the coupling loss factors from each subsystem to other subsystems are much smaller than its damping loss factors. This implies that the assumption of weak coupling is satisfied in this three-subsystem model.

The average sound pressure level in the interior cavity due to 1W input power into the under-floor cavity in each one third octave band is presented in Figure 2.5. The peak of the sound pressure in the interior cavity corresponds to the critical frequency of the floor, which is 1250 Hz for the present specification of the floor.

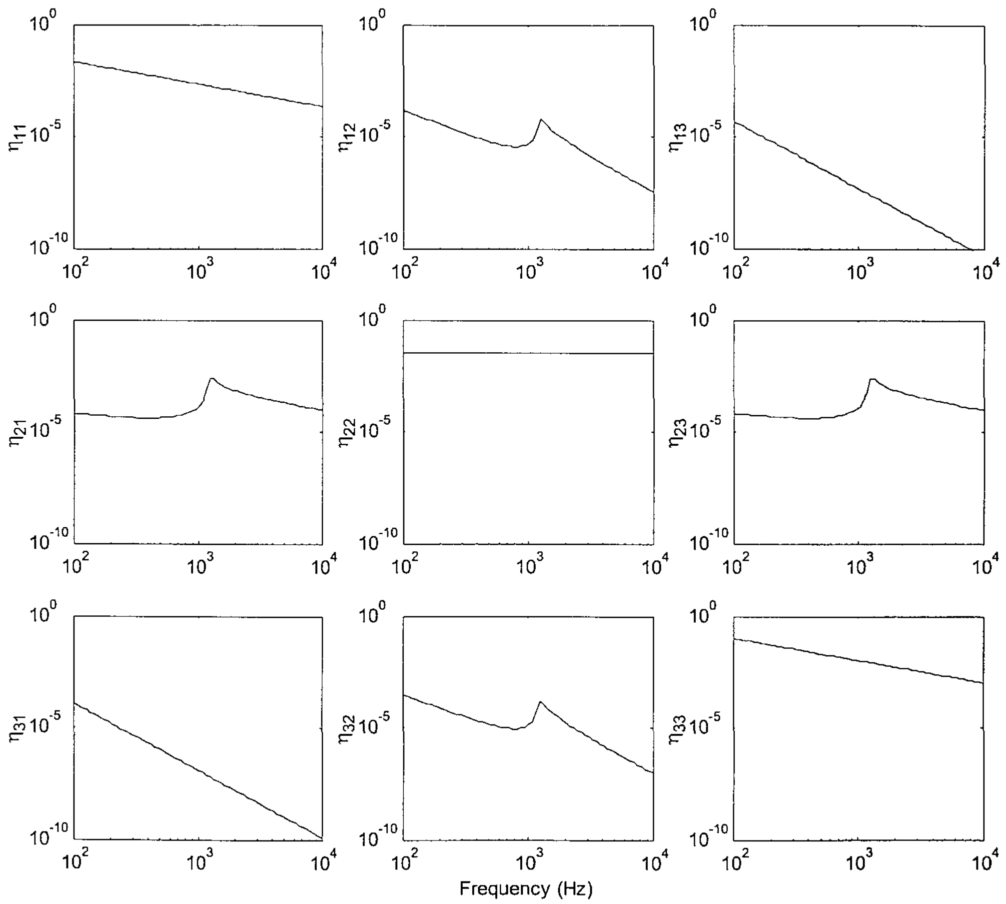

Figure 2.4. The loss factors of subsystems
(subsystem 1=interior cavity, subsystem 2=floor, subsystem 3=underfloor cavity)

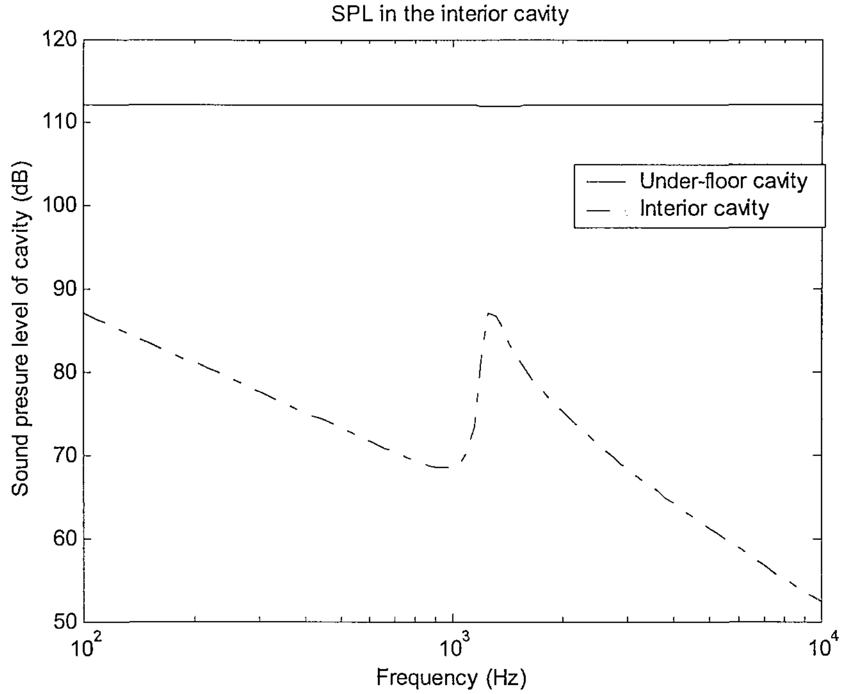

Figure 2.5 The average sound pressure level in the interior cavity

2.2.5 DISCUSSION

It is seen that, from the calculation of the three-subsystem model, the sound pressure level difference across the panel is obtained. This can be related to the sound reduction index of the floor by using the relationship [73, 88]

$$R = L_{p1} - L_{p3} + 10\log_{10}\left(\frac{S_2}{A_1}\right) \tag{2.21}$$

where L_{p1} and L_{p3} are the sound pressure level in the interior cavity and under-floor cavity. S_2 is the area of the floor. A_1 is the total absorption in the interior cavity, which is equal to $\alpha_1 S_1$. This formula is used to derive R experimentally in a transmission suite.

The sound reduction index obtained from the SEA model using this equation is presented in Figure 2.6. The result from equation (2.19) is also presented. The results are basically the same. This shows that the above SEA model can be used to calculate the sound transmission loss of plates, provided the coupling loss factors are known. It can also be seen that, to use this method, the modal density and radiation efficiency of the plates are the central problems to be solved. Some detailed studies related to this method were reported by Crocker and Price [88].

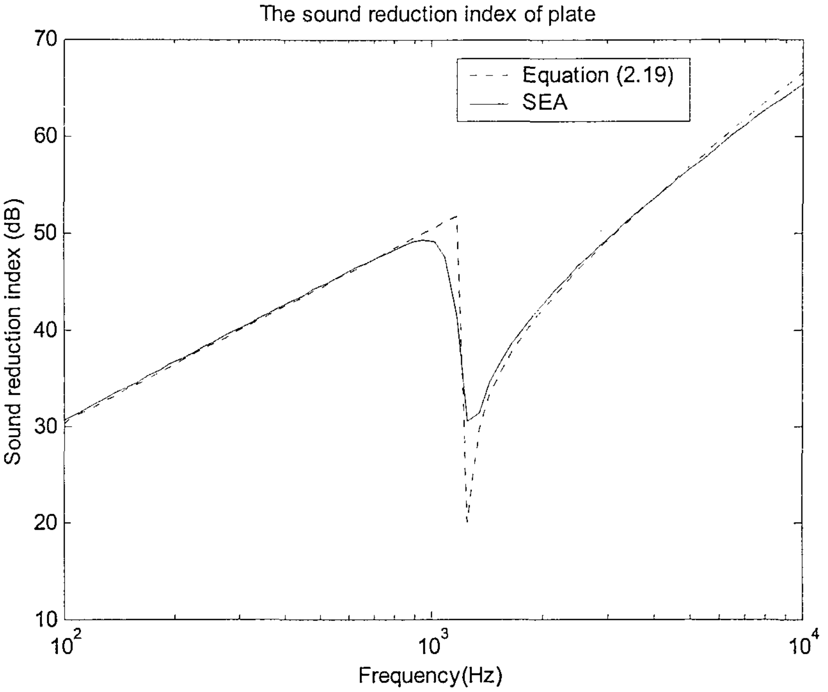

Figure 2.6 Sound reduction index of the floor. —: from SEA, – –: from (2.19).

2.3 CONCLUSIONS

In this chapter, a general introduction of the SEA has been presented. A simple three-subsystem SEA model for predicting the interior noise of the vehicle has been studied. The aim of this simple SEA model is to introduce the procedures using the SEA technique to model the interior noise for railway vehicles. In particular, this shows the use of the SEA technique to study the sound transmission of panels.

3 TWO-DIMENSIONAL MODEL OF EXTRUDED PLATES

3.1 INTRODUCTION

The mode count and modal density of extruded panels are important parameters for modelling them as subsystems in terms of SEA. An extruded panel can be seen as a three-dimensional system composed of series of interconnected two-dimensional plate elements, its cross-section as a two-dimensional system of interconnected one-dimensional beam element. In this chapter, the relationship between the mode count of a single beam and the applied boundary conditions is analysed first. The analysis is then extended to a multi-beam system where the effects on the mode count due to intermediate constraints are investigated. Finally the boundary effects are applied to evaluate the mode count of an extruded section and the results are compared to those from an FEM analysis. These results will be extended to the full three-dimensional extruded panel in the next chapter.

3.2 SINGLE ONE-DIMENSIONAL SYSTEM

3.2.1 NATURAL MODES

It is well known that natural modes of vibration occur in any finite continuous system. The number of modes occurring below a certain frequency f is called the mode count $N(f)$. The theoretical mode count for continuous systems can be obtained by combining boundary information with the dispersion relation relating wavenumber and frequency for free waves in the system. Lyon and DeJong [37] give an expression for the mode count of one-dimensional systems in terms of wavenumber:

$$N(k) = \frac{kL}{\pi} + \delta_{BC} \tag{3.1}$$

where δ_{BC} is dependent on the boundary conditions (and according to Lyon and DeJong is usually a constant of magnitude less than or equal to 1), L is the length of the one-dimensional system and k is the wavenumber which is related to frequency. For the particular wave type being considered, such as bending or longitudinal waves, the dispersion relation defines the frequency dependence of the wavenumber.

3.2.1.1 Longitudinal modes in a rod

The free longitudinal vibration in a bar is governed by the wave equation which is expressed as

$$\frac{\partial^2 u}{\partial x^2} - \frac{1}{c_L^2}\frac{\partial^2 u}{\partial t^2} = 0 \tag{3.2}$$

where c_L is the phase velocity of the longitudinal vibration. ($c_L = \sqrt{\frac{E}{\rho}}$ where E is Young's modulus and ρ is the density).

When the motion is harmonic at circular frequency $\omega=2\pi f$, the above equation can be expressed as the one dimensional *Helmholtz equation*

$$\frac{d^2 u(x)}{dx^2} + k^2 u(x) = 0 \tag{3.3}$$

where k is the wavenumber at the frequency ω ($k = 2\pi / wavelength = \omega / c_L$).

The general solution of the equation (3.3) is

$$u(x) = A_1 e^{jkx} + A_2 e^{-jkx} \tag{3.4}$$

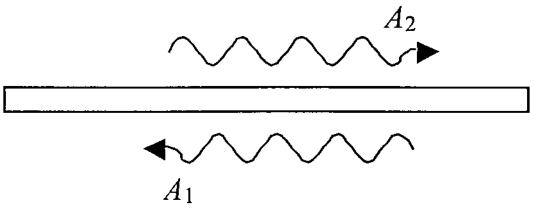

Figure 3.1 Illustration of wave motions in a rod.

To understand this solution physically, the two terms represent opposite-going propagating waves which are superposed, as illustrated in Figure 3.1. The propagating wave is characterized by the wavenumber k. This is the phase difference between two points in the continuous system at a unit distance apart in the direction of wave propagation. As the wave propagates, it can be said that its phase changes by k per unit length. At each of the boundaries, a phase difference is introduced between the incoming and reflected waves. The total phase change as the wave travels one complete circuit around the system can be expressed by

$$\varepsilon = -2kL + \varepsilon_L + \varepsilon_R \tag{3.5}$$

where ε_L and ε_R are the phase change at the left-hand and right-hand ends respectively.

The natural modes occur when the total phase change is equal to an integral number of 2π's. This principle is well known as the *phase-closure* principle (see [89]). From a knowledge of the wavenumber-frequency relationship as well as the phase change when a propagating wave impinges on each end-boundary of the system, the phase-closure principle can be used to find the natural frequencies. It is convenient to begin by considering the reflection coefficient of a propagating wave arriving at the end. Here, the term A_1 in equation (3.4) is supposed to be the incident wave and A_2 is supposed to be the reflected wave. The boundary is taken to lie at $x=0$.

For longitudinal vibrations in a rod, simple boundary conditions are either 'free' or 'rigid' at the two ends.

For free boundary conditions, the force must vanish. So $\left.\frac{du}{dx}\right|_{BC} = 0$, $A_1 = A_2$, and the phase change due to reflection is 0.

For fully fixed conditions, the displacement must vanish. So $u|_{BC} = 0$, $A_1 = -A_2$, and the phase change due to reflection is π.

The frequency equations of natural modes for different boundary conditions are now readily obtained by using the phase-closure principle.

- **Free-free**

The natural modes are governed by

$$-2kL + \varepsilon_L + \varepsilon_R = -2kL = -2(n-1)\pi$$

$$kL = (n-1)\pi \text{ for } n = 1, 2, \cdots \tag{3.6}$$

The result $k=0$ for $n=1$ corresponds to a rigid body mode.

- **Free-fixed**

The natural modes are governed by

$$-2kL+\varepsilon_L+\varepsilon_R=-2kL+\pi=-2(n-1)\pi$$

$$kL=(n-\frac{1}{2})\pi \text{ for } n=1, 2, \cdots \tag{3.7}$$

- **Fixed-fixed**

The natural modes are governed by

$$-2kL+\varepsilon_L+\varepsilon_R=-2kL+\pi+\pi=-2(n-1)\pi$$

$$kL=n\pi \text{ for } n=1,2,\cdots \tag{3.8}$$

3.2.1.2 Bending modes in a beam

The flexural wave equation for the wave displacement w in a uniform Euler-Bernoulli beam is

$$EI\frac{\partial^4 w}{\partial x^4}+\rho A\frac{\partial^2 w}{\partial t^2}=0 \tag{3.9}$$

where EI is the bending stiffness of the beam and ρA is the mass per unit length.

In the usual way, the general solution obtained by the wave method has the form

$$w(x,t)=(A_1e^{kx}+A_2e^{-kx}+A_3e^{jkx}+A_4e^{-jkx})\exp(j\omega t). \tag{3.10}$$

where the four x-dependent terms in equation (3.10) are recognized in order as the positively growing evanescent wave, the decaying evanescent wave, the negatively propagating wave and the positively propagating wave. They will be referred to by their coefficients A_1, A_2, A_3 and A_4 respectively.

Applying the phase-closure principle requires a knowledge of the reflection coefficient at boundaries at which a wave arrives. For the bending vibration of a beam, four basic boundary conditions have to be considered: free, sliding, simple support and fully fixed. Except for the sliding boundary, the results of the other three have been presented by Mead [89]. For an incident propagating wave A_4 arriving at the boundary, this is reflected into an evanescent wave A_1 and a propagating wave A_3. The total motion in the beam is

$$w(x)=A_1e^{kx}+A_3e^{jkx}+A_4e^{-jkx} \tag{3.11}$$

which is illustrated in Figure 3.2.

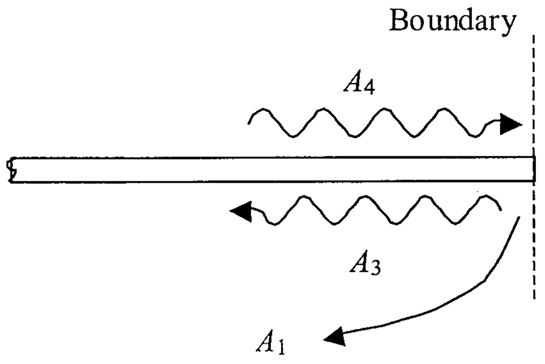

Figure 3.2 Illustration of the wave motion at boundary.

For a free boundary condition, $\left.\frac{\partial^2 w}{\partial x^2}\right|_{BC} = 0$, $\left.\frac{\partial^3 w}{\partial x^3}\right|_{BC} = 0$, $A_3 = -jA_4$, $A_1 = (1-j)A_4$, and the phase change due to reflection is $-\pi/2$.

For a pinned (simple support) boundary condition, $\left.w\right|_{BC} = 0$, $\left.\frac{\partial^2 w}{\partial x^2}\right|_{BC} = 0$, $A_3 = -A_4$, and $A_1 = 0$, the phase change due to reflection is π.

For a fully fixed boundary condition, $\left.w\right|_{BC} = 0$, $\left.\frac{\partial w}{\partial x}\right|_{BC} = 0$, $A_3 = -jA_4$, $A_1 = -(1-j)A_4$, and the phase change due to reflection is $-\pi/2$.

For a sliding boundary condition, $\left.\frac{\partial w}{\partial x}\right|_{BC} = 0$, $\left.\frac{\partial^3 w}{\partial x^3}\right|_{BC} = 0$, $A_3 = A_4$, $A_1 = 0$, and the phase change due to reflection is 0.

The whole process of finding natural modes by using the phase-closure principle is quite simple when the evanescent waves arriving at and reflected from the boundaries are ignored. This is *almost* exact for the third and higher order modes of simple beams and exact for the special case of a beam with simple supports or sliding boundary conditions at both ends [89]. Now the frequency equations for a single beam with different boundary conditions are readily obtained.

- **Free-free**

The natural modes are governed by

$$-2kL+\varepsilon_L+\varepsilon_R=-2kL-\pi/2-\pi/2=-2n\pi$$

$$kL=(n-\frac{1}{2})\pi. \tag{3.12}$$

To include two rigid modes by a rearrangement of n, equation (3.12) should be rewritten as

$$kL=(n-\frac{3}{2})\pi. \tag{3.13}$$

where $n = 3, 4, \cdots$ for the bending modes.

- **Free-sliding**

The natural modes are governed by

$$-2kL+\varepsilon_L+\varepsilon_R=-2kL-\pi/2+0=-2n\pi$$

$$kL=(n-\frac{1}{4})\pi. \tag{3.14}$$

To include one rigid mode by a rearrangement of n, the term in the round bracket in (3.14) should be reduced by 1. The final result is

$$kL=(n-\frac{5}{4})\pi. \tag{3.15}$$

where $n = 2, 3, 4, \cdots$ for bending modes.

- **Free-pinned**

The natural modes are governed by

$$-2kL+\varepsilon_L+\varepsilon_R=-2kL-\pi/2+\pi=-2n\pi$$

$$kL=(n+\frac{1}{4})\pi. \tag{3.16}$$

To include one rigid mode by a rearrangement of n, the term in the round bracket in (3.16) should be reduced by 1. The final result is

$$kL=(n-\frac{3}{4})\pi. \tag{3.17}$$

where $n = 2, 3, 4, \cdots$ for bending modes.

- **Free-fixed**

The natural modes are governed by

$$-2kL + \varepsilon_L + \varepsilon_R = -2kL - \pi/2 - \pi/2 = -2n\pi$$

$$kL = (n - \frac{1}{2})\pi. \tag{3.18}$$

where $n = 1, 2, 3, \cdots$ for bending modes.

The natural modes of other combinations of boundary conditions are given in Appendix B.

3.2.2 AVERAGE MODE COUNT

The mode count is the number of modes below a certain frequency. It consists of discrete numbers in reality. If it is plotted against frequency or wavenumber, a "staircase" curve appears as shown in Figure 3.3. For frequencies just below the n^{th} mode the mode count is n-1, just above the natural frequency it is n. A continuous function that approximates the average of the staircase function is more useful in practice (see Figure 3.3) and represents the average mode count of an ensemble of similar structures. This average function distributes the mode count along the wavenumber axis (or frequency axis). The average mode count can be represented by

$$N = n - \frac{1}{2} \tag{3.19}$$

at the resonance frequencies.

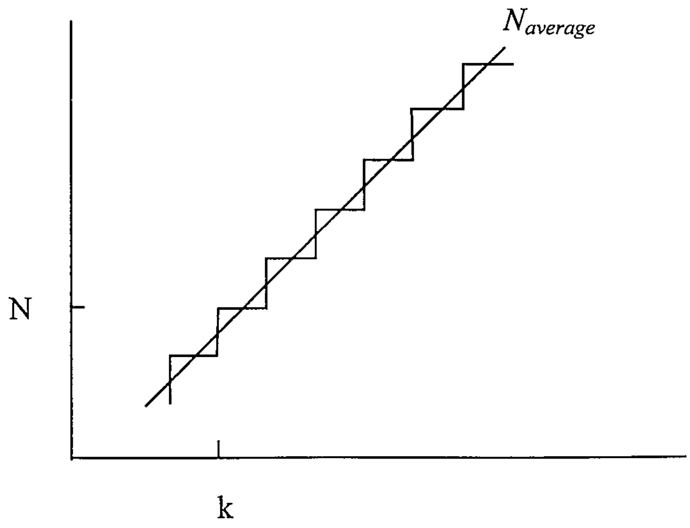

Figure 3.3. The illustration of the average mode count.

The concept of the average mode count will be used in the remainder of this thesis. When a mode count is mentioned, it normally means the average mode count function, not the discrete mode count.

3.2.3 RELATIONSHIP BETWEEN MODE COUNT AND BOUNDARY CONDITIONS

The mode count of natural modes can be easily obtained by rewriting the frequency equations in section 3.2.1 in the form of equation (3.1). Attention is required over the ambiguity in *n*. It is logical to follow the practice adopted above of making *n* start from 1 including the rigid body modes. Now the δ_{BC} in equation (3.1) can be readily obtained.

3.2.3.1 Longitudinal mode count in a rod

By rewriting the frequency equation in section 3.2.1.1 for longitudinal motion in a rod, the average mode count can be expressed in terms of the wavenumber as

$$N = \frac{kL}{\pi} + \frac{1}{2} \qquad \text{for free-free boundary conditions,}$$

$$N = \frac{kL}{\pi} \qquad \text{for free-fixed boundary conditions,}$$

$$N = \frac{kL}{\pi} - \frac{1}{2} \qquad \text{for fixed-fixed boundary conditions.}$$

It can be noted that each fixed boundary constraint adds to the mode count by – ½ for longitudinal vibrations.

3.2.3.2 Bending mode count in a beam

By rewriting the frequency equation in section 3.2.1.2 for bending vibration in a beam, the mode count can be expressed in terms of the wavenumber as

$$N = \frac{kL}{\pi} + 1 \qquad \text{for free-free boundary conditions,}$$

$$N = \frac{kL}{\pi} + \frac{3}{4} \qquad \text{for free-sliding boundary conditions,}$$

$$N = \frac{kL}{\pi} + \frac{1}{4} \qquad \text{for free-pinned boundary conditions.}$$

$$N = \frac{kL}{\pi} \qquad \text{for free-fixed boundary conditions.}$$

Taking a free boundary as the base with which to compare the change of the mode count due to different boundary conditions, sliding adds the mode count by $-\frac{1}{4}$, pinned (simple support) condition by $-\frac{3}{4}$ and fixed boundary constraint by -1 for bending vibrations. This is found to apply to other combinations of boundary conditions as listed in Appendix B.

The mode count of the system can be obtained by considering the mode count of a free-free beam and the boundary conditions at two ends. It is given by

$$N=\frac{kL}{\pi}+1-\delta_L-\delta_R \tag{3.20}$$

where δ_L and δ_R are 0, ¼, ¾, and 1 corresponding to four boundary conditions respectively, as listed in Table 3.1. These values are used to find the constants δ_{BC} described in equation (3.1). δ_{BC} is given by

$$\delta_{BC}=1-\delta_L-\delta_R \tag{3.21}$$

which for the above boundary conditions lies between ± 1 as stated by Lyon and DeJong [37].

Table 3.1 The constants subtracted from the mode count of a beam in bending for different boundary conditions

Boundary conditions	δ
Free	0
Sliding	1/4
Pinned	3/4
Fixed	1

3.2.4 GENERAL BOUNDARY CONDITIONS

Now, more general boundary conditions are considered in which the end of the beam may be connected to a linear spring or a mass.

3.2.4.1 End spring

When the end of a beam is constrained against transverse displacement by an elastic spring K, the resisting force due to this spring is proportional to w (see Figure 3.4). This resisting force is also balanced by the shear force at the end. Thus

$$EI\frac{\partial^3 w}{\partial x^3} = kw \tag{3.22}$$

Equation (3.22) gives

$$EIk^3(A_1 - jA_3 + jA_4) = K(A_1 + A_3 + A_4) \tag{3.23}$$

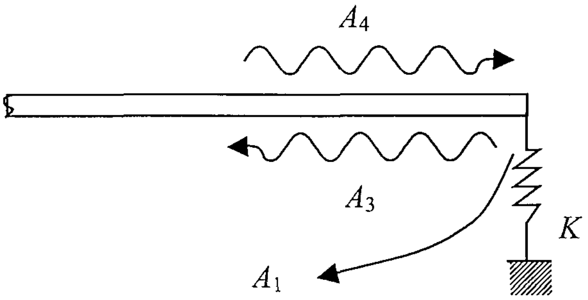

Figure 3.4. Illustration of wave propagations at an end spring.

By introducing the non-dimensional stiffness coefficients $\sigma = K/EIk^3$, equation (3.23) can be rewritten as

$$(1-\sigma)A_1 + (-\sigma - j)A_3 + (-\sigma + j)A_4 = 0 \tag{3.24}$$

In addition, the bending moment must be zero. Hence $\left.\frac{\partial^2 w}{\partial x^2}\right|_{BC} = 0$, which gives

$$A_1 - A_3 - A_4 = 0 \tag{3.25}$$

From equation (3.24) and (3.25), a result can be obtained as follows

$$A_3 = -A_4\left(\frac{1-2\sigma+j}{1-2\sigma-j}\right) \text{ and } A_1 = -A_4\left(\frac{2j}{1-2\sigma-j}\right) \tag{3.26}$$

For the boundary condition of an end spring, the phase change is frequency dependent. When the frequency tends to zero, σ tends to infinity, $A_3 = -A_4$ and $A_1 = 0$. This is a pinned boundary condition. When the frequency becomes very large, σ tends to zero, $A_3 = -jA_4$ and $A_1 = (1-j)A_4$. This corresponds to a free boundary condition. Therefore the phase change due to an end spring would change from π at low frequency to $-\pi/2$ at high frequency. The amplitude reflection ratio can be expressed by

$$r = \frac{A_3}{A_4} = -\left(\frac{1-2\sigma+j}{1-2\sigma-j}\right) = e^{j\theta} \tag{3.27}$$

where $\theta = \tan^{-1}\left(\frac{2\sigma-1}{2\sigma(1-\sigma)}\right)$ and $-\frac{\pi}{2} \leq \theta \leq \pi$.

Consider a beam that is free at left-hand end and with a point spring at right-hand end. The natural modes can be found by

$$\begin{aligned} -2kL - \frac{\pi}{2} + \theta &= -2n\pi \\ kL &= (n-\frac{1}{4})\pi + \frac{\theta}{2} \end{aligned} \tag{3.28}$$

The rigid modes of a free-spring beam will consist of two (especially for $\sigma \to 0$), except one will have non-zero frequency. So in equation (3.28) n should be replaced by $n-1$ and therefore can be rewritten as

$$kL = (n-\frac{5}{4})\pi + \frac{\theta}{2} \tag{3.29}$$

For $\sigma \to \infty$, $\theta \to \pi$ and $kL = (n-3/4)\pi$, this is the case of a free-pinned beam.

For $\sigma \to 0$, $\theta \to -\pi/2$ and $kL = (n-3/2)\pi$, this is the case of a free-free beam.

By comparing equation (3.29) with that of a free-free beam, the effect on the mode count of an end spring can be found as

$$\delta_{spring} = \frac{\theta}{2\pi} + \frac{1}{4} \tag{3.30}$$

δ_{spring} tends ¾ at low frequency and tends zero at high frequency. This is illustrated in Figure 3.5

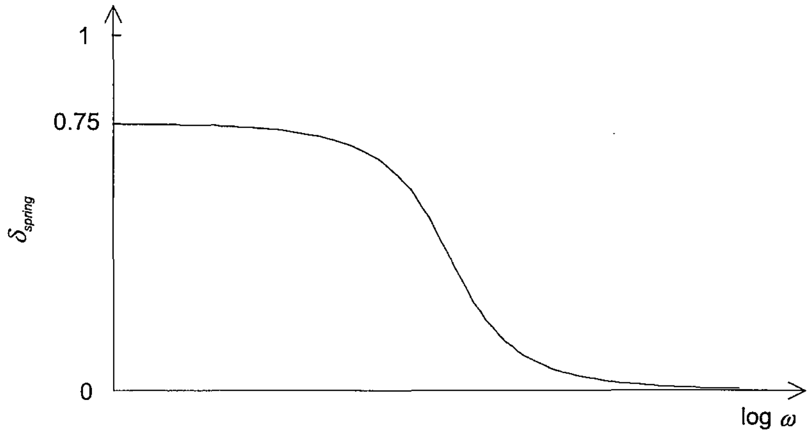

Figure 3.5 Illustration of δ_{spring} against frequency.

3.2.4.2 End mass

Consider now a point mass on the end of a beam. When the end of a beam undergoes a transverse displacement *w*, with acceleration $\partial^2 w/\partial t^2$, the resisting force due to an end mass *m* is proportional to $\partial^2 w/\partial t^2$. This resisting force is balanced by the shear force at the end. Thus

$$EI\frac{\partial^3 w}{\partial x^3} = m\frac{\partial^2 w}{\partial t^2} \tag{3.31}$$

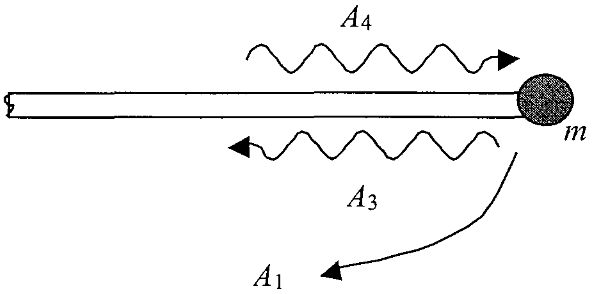

Figure 3.6 Illustration of wave propagations at an end mass.

Again the bending moment is zero. Equation (3.31) gives

$$EIk^3(A_1 - jA_3 + jA_4) = -m\omega^2(A_1 + A_3 + A_4) \tag{3.32}$$

by writing $\mu = m\omega^2/EIk^3 = mk/\rho A$, equation (3.32) is expressed as

$$(\mu+1)A_1+(\mu-j)A_3+(\mu+j)A_4=0 \tag{3.33}$$

From equation (3.25) and (3.33),

$$A_3=-A_4\left(\frac{2\mu+1+j}{2\mu+1-j}\right) \text{ and } A_1=-A_4\left(\frac{2j}{2\mu+1-j}\right) \tag{3.34}$$

From equation (3.34), it can be seen that the phase change due to an end point mass is also dependent on frequency. When the frequency tends to zero, μ tends to zero, $A_3=-jA_4$ and $A_1=(1-j)A_4$. This is a free boundary condition. When the frequency tends to infinity, μ tends to infinity, $A_3=-A_4$ and $A_1=0$. This is a pinned boundary condition. So the phase change due to an end mass would tends to $-\pi/2$ at low frequency and π at high frequency. However, if the reflection ratio is expressed as

$$r=\frac{A_3}{A_4}=-\frac{2\mu+1+j}{2\mu+1-j}=e^{j\theta} \tag{3.35}$$

it is found that θ moves through the third quadrant of the complex plane by $-\pi/2$ as frequency increases. Thus the phase change is actually from $-\pi/2$ to $-\pi$. This is different from the end spring when the total phase change is $-3\pi/2$.

Consider a beam that is free at left-hand end and with a point mass at right-hand end. The natural modes can be found by

$$\begin{gathered}-2kL-\frac{\pi}{2}+\theta=-2n\pi \\ kL=(n-\frac{1}{4})\pi+\frac{\theta}{2}\end{gathered} \tag{3.36}$$

It can be noted that there will always be two rigid body modes, even when the mass is large. So equation (3.36) can be rewritten as

$$kL=(n-\frac{5}{4})\pi+\frac{\theta}{2} \tag{3.37}$$

For $\mu \to 0$, $\theta \to -\pi/2$ and $kL=(n-3/2)\pi$, this is the case of a free-free beam.

For $\mu \to \infty$, $\theta \to -\pi$ and $kL=(n-7/4)\pi$, this is different from the case of a free-pinned beam, which is governed by $kL=(n-3/4)\pi$. The reason is the second rigid body mode.

The effect of an end mass on the mode count can be obtained as

$$\delta_{mass} = \frac{\theta}{2\pi} + \frac{1}{4} \qquad -\pi \le \theta \le -\frac{\pi}{2} \tag{3.38}$$

δ_{mass} tends to zero at low frequency and tends to –¼ at high frequency. This is illustrated in Figure 3.7. It should be noted that δ for an end point mass is less than zero. This means that a mass is able to add to the mode count of a beam because it tends to lower the natural frequencies compared to a free end, whereas a spring lowers the mode count of the beam.

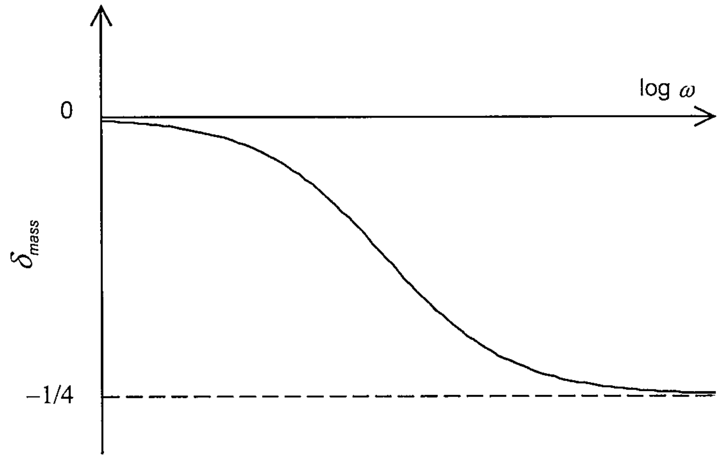

Figure 3.7 Illustration of δ_{mass} against frequency.

3.3 TWO-BEAM SYSTEM

In section 3.2 the relationship between the mode count and boundary conditions for a single one-dimensional system has been discussed and the boundary dependent constants δ_L and δ_R have been obtained. In this section, the corresponding relationship for a one-dimensional system with an intermediate constraint will be considered. In other words, the system discussed is composed of two one-dimensional components, in particular two beams supporting bending vibrations, joined end to end. In the longitudinal case, an extra constraint can only be fully fixed, in which case the mode count becomes that of two uncoupled rods. The longitudinal case will not be discussed further since it is of less interest.

Consider a one-dimensional beam of length $2L$ with simple supports at the two ends. Another constraint is added at some intermediate point, not necessarily the centre (shown in Figure 3.8).

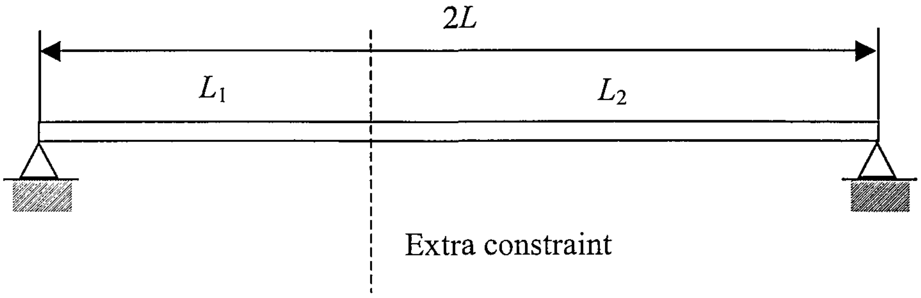

Figure 3.8. A simply supported beam of length $2L$ with an extra constraint.

3.3.1 A BEAM WITH AN INTERMEDIATE FIXED CONSTRAINT

If the extra constraint is a fixed condition, the system is then divided exactly into two independent single beams with pinned-fixed boundary conditions. The mode count for the whole system can be obtained by adding the two mode counts for the single beams

$$N_{total} = N_1 + N_2$$

$$N_{total} = \frac{kL_1}{\pi} - \frac{3}{4} + \frac{kL_2}{\pi} - \frac{3}{4}$$

$$N_{total} = \frac{2kL}{\pi} - \frac{1}{2} - 1 = N - 1 = N - \delta_{fixed} \tag{3.39}$$

where N_{total} is the mode count of the whole system, N_1 and N_2 are the mode counts of the beams L_1 and L_2 respectively and N is the mode count of the original beam of length $2L$ without the extra intermediate constraint.

This shows that the mode count of the whole system can be estimated by taking the mode count of the system without the extra constraint and subtracting the coefficient $\delta = 1$ due to the fixed boundary condition. A similar result is found for the trivial case of a ‘free’ intermediate boundary, for which $\delta_{free} = 0$. In the next section the more interesting case of an intermediate simple support is considered.

3.3.2 A BEAM WITH AN INTERMEDIATE SIMPLE SUPPORT CONSTRAINTS

3.3.2.1 General solution of natural modes

Consider a one-dimensional system of length $2L$ with simple supports at the two ends. Another simple support is applied at an arbitrary position between the two ends of the system (shown in Figure 3.8). The left-hand and right-hand beams support waves represented as

$$w(x) = \begin{cases} Ae^{-jkx} + Be^{jkx} + Ee^{kx} \\ Ce^{-jkx} + De^{jkx} + Fe^{-kx} \end{cases} \tag{3.40}$$

in which the near-field waves at the two ends have been neglected. These component waves are illustrated in Figure 3.9.

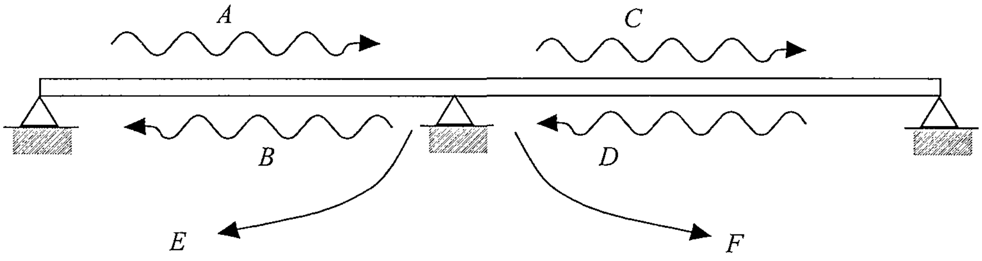

Figure 3.9 Diagram illustrating the component wave motions.

If the near-field waves are neglected for determining the natural modes, the following four equations can be obtained.

$$A = r_L B e^{-2kL_1 j} \tag{3.41}$$

$$D = r_R C e^{-2kL_2 j} \tag{3.42}$$

$$B = Dt_m + Ar_m \tag{3.43}$$

$$C = At_m + Dr_m \tag{3.44}$$

where r_L and r_R are amplitude reflection coefficients at the simple supports at the ends. From section 3.2.1.2, $r_L = -1$ and $r_R = -1$. t_m and r_m are the amplitude transmission and reflection coefficients at the middle simple support.

Substituting (3.41) and (3.42) into (3.43) and (3.44), this gives

$$B(1-r_m r_L e^{-2kL_1 j}) = t_m r_R e^{-2kL_2 j} C \tag{3.45}$$

$$C(1-r_m r_R e^{-2kL_2 j}) = t_m r_L e^{-2kL_1 j} B \tag{3.46}$$

In order to simplify (3.45) and (3.46) mathematically, it is convenient to write $L_1 = L - l$, $L_2 = L + l$, $\alpha = e^{-2kLj}$ and $\beta = e^{-2klj}$. Then multiply the left-hand and right-hand sides of equation (3.45) and (3.46) respectively

$$(1 - r_m r_L \alpha / \beta)(1 - r_m r_R \alpha\beta) = t_m^2 r_R r_L \alpha^2 \tag{3.47}$$

t_m and r_m can be obtained by considering the continuity at the middle constraint. Taking this to be $x = 0$, the following conditions must be satisfied (here all the waves in equation (3.40) must be included).

$$w_-(0) = A + B + E = 0 \tag{3.48}$$

$$w_+(0) = C + D + F = 0 \tag{3.49}$$

$$w'_-(0) = w'_+(0) \qquad -jA + jB + E = -jC + jD - F \tag{3.50}$$

$$w''_-(0) = w''_+(0) \qquad -A - B + E = -C - D + F \tag{3.51}$$

Substitute (3.48) and (3.49) into the two sides of (3.51)

$$E = F \tag{3.52}$$

Substitute (3.48) and (3.49) into the two sides of (3.50)

$$-2jA + (1-j)E = -2jD - (1-j)E \tag{3.53}$$

If the beams were infinite, A can be considered as the incident wave and D would not exist. Then

$$E = F = \frac{-1}{1+j} A \tag{3.54}$$

Substitute (3.54) into (3.49)

$$C = \frac{1}{1+j} A \tag{3.55}$$

Substitute (3.54) into (3.48)

$$B = \frac{-1}{1-j} A \tag{3.56}$$

Thus the amplitude transmission coefficient

$$t_m = \frac{C}{A} = \frac{1}{1+j} \tag{3.57}$$

and the amplitude reflection coefficient

$$r_m = \frac{B}{A} = \frac{-1}{1-j} \tag{3.58}$$

Now substitute r_L, r_R, t_m and r_m into (3.47) and rearrange it to give

$$\alpha^2 - \frac{1-j}{2}\left(\frac{1}{\beta} + \beta\right)\alpha - j = 0 \tag{3.59}$$

Since $\frac{1}{\beta} + \beta = e^{2klj} + e^{-2klj} = 2\cos(2kl)$, equation (3.59) becomes

$$\alpha^2 - (1-j)\cos(2kl)\alpha - j = 0 \tag{3.60}$$

The roots of (3.60) have the form

$$\alpha = \frac{(1-j)\cos(2kl) \pm \sqrt{(1-j)^2\cos^2(2kl) + 4j}}{2} \tag{3.61}$$

Equation (3.61) is an irrational equation in k that gives a general solution for the natural frequencies of the two connected beams with simple support constraints. It can be noted that two sets of modes would occur in the system. A further simplification of equation (3.61) gives

$$e^{-2kLj} = \alpha = \frac{1-j}{2}\sqrt{1-\sin^2(2kl)} \pm \frac{1+j}{2}\sqrt{1+\sin^2(2kl)} \tag{3.62}$$

3.3.2.2 Two identical beams

First, the situation is considered in which the extra constraint is located at the centre. In this case, l would be zero and the roots can be expressed as

$$\alpha_1 = 1 \text{ and } \alpha_2 = -j \tag{3.63}$$

The first root gives

$$e^{-2kLj} = 1 = e^{-2n\pi j}$$

so

$$kL = n\pi \tag{3.64}$$

These are exactly the modes of a pinned-pinned beam. In these modes the two beams vibrate in antiphase, as illustrated in Figure 3.10. This correspondes to a mode count $N_1 = \frac{kL}{\pi} - \frac{1}{2}$.

The second root gives

$$e^{-2kLj} = -j = e^{-(2n\pi+\frac{\pi}{2})j}$$

so

$$kL = (n+\frac{1}{4})\pi \tag{3.65}$$

These are exactly the modes of a fixed-pinned beam. In these modes the two beams vibrate in phase. This correspondes to a mode count $N_1 = \frac{kL}{\pi} - \frac{3}{4}$.

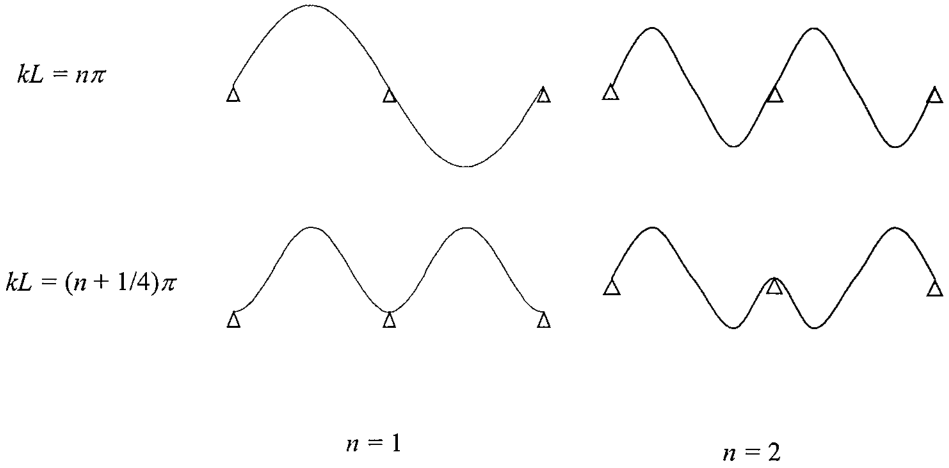

Figure 3.10 Mode shapes of two identical beams joined at a simple support.

The total mode count of the system can be estimated by adding the two sets of modes together

$$N_{total} = N_1 + N_2$$
$$N_{total} = \frac{kL}{\pi} - \frac{1}{2} + \frac{kL}{\pi} - \frac{3}{4}$$
$$N_{total} = \frac{2kL}{\pi} - \frac{1}{2} - \frac{3}{4} = N - \frac{3}{4} = N - \delta_{pinned} \tag{3.66}$$

where N_{total} is the mode count of the whole system, N_1, N_2 are the mode counts of the antisymmetric and symmetric modes respectively and N is the mode count of the beam of length $2L$ without the extra intermediate constraint.

It is thus shown that the mode count of the whole system can be estimated by taking the mode count of the system without the extra constraint and subtracting the coefficient

δ_{pinned} due to the simple support boundary condition. This is in the same as for the case of the fixed support in section 3.3.1.

3.3.2.3 Asymmetrical simple support

An asymmetrical intermediate simple support represents a more general case. By rechecking the general solution described in equation (3.62), the same conclusion is found.

The two roots in (3.62) can be expressed as

$$\begin{aligned} \alpha_1 &= \frac{\sqrt{1-\sin^2(2kl)}+\sqrt{1+\sin^2(2kl)}}{2}+j\left(\frac{-\sqrt{1-\sin^2(2kl)}+\sqrt{1+\sin^2(2kl)}}{2}\right) \\ \alpha_2 &= \frac{\sqrt{1-\sin^2(2kl)}-\sqrt{1+\sin^2(2kl)}}{2}+j\left(\frac{-\sqrt{1-\sin^2(2kl)}-\sqrt{1+\sin^2(2kl)}}{2}\right) \end{aligned} \tag{3.67}$$

It can be noted that there is a relation between the two roots. Writing α_1 as $\alpha_1 = a + jb$, α_2 can be represented as $\alpha_2 = -b - ja$, where a and b are both positive. These two roots have the same modulus but different phase. It can be readily shown that the modulus is 1 in each case. Therefore the two roots can be represented as

$$\alpha_1 = e^{j\phi_1} \quad \alpha_2 = e^{j\phi_2} \tag{3.68}$$

where $0 \le \phi_1 \le \pi/2$ and $-\pi \le \phi_2 \le -\pi/2$. The phases are related by

$$\phi_1 + \phi_2 = -\frac{\pi}{2} \tag{3.69}$$

Similar to the procedure taken in section 3.3.2.2, the first root gives

$$e^{-2kLj} = e^{j\phi_1} = e^{-(2n\pi-\phi_1)j},$$

so

$$kL = n\pi - \frac{\phi_1}{2} \tag{3.70}$$

The second root gives

$$e^{-2kLj} = e^{j\phi_2} = e^{-(2n\pi-\phi_2)j},$$

so

$$kL = n\pi - \frac{\phi_2}{2} \tag{3.71}$$

The total mode count of the system can be estimated by adding the two sets of modes together

$$N_{total} = N_1 + N_2$$

$$N_{total} = \left(\frac{kL}{\pi} - \frac{1}{2} + \frac{\phi_1}{2\pi}\right) + \left(\frac{kL}{\pi} - \frac{1}{2} + \frac{\phi_2}{2\pi}\right)$$

$$N_{total} = \frac{2kL}{\pi} - \frac{1}{2} + \left(\frac{\phi_1 + \phi_2}{2\pi}\right) - \frac{1}{2} = N - \frac{3}{4} = N - \delta_{pinned} \tag{3.72}$$

where N_{total} is the mode count of the whole system, N_1 and N_2 are the mode counts of the two sets of modes and N is the mode count of the beam of length $2L$ without the extra middle constraint.

This shows that the average mode count of the whole system can be estimated in the same way as in section 3.3.2.2. The mode count of the system without the extra constraint is taken and the coefficient due to the simple support boundary condition, δ_{pinned}, is subtracted.

3.3.3 A BEAM WITH AN INTERMEDIATE SLIDING SUPPORT

Another case that could be considered is a two-beam system with a sliding support applied in the middle. The same definitions as in section 3.3.2.1 are used in this section. The free wave solution is represented by equation (3.40).

First, the amplitude transmission and reflection ratios can be found by taking account of the continuity at the sliding support. At $x = 0$, the following conditions must be satisfied.

$$w'_-(0) = -jA + jB + E = 0 \tag{3.73}$$

$$w'_+(0) = -jC + jD - F = 0 \tag{3.74}$$

$$w_-(0) = w_+(0) \qquad A + B + E = C + D + F \tag{3.75}$$

$$w'''_-(0) = w'''_+(0) \qquad jA - jB + E = jC - jD - F \tag{3.76}$$

Substitute (3.73) and (3.74) into the two sides of (3.76)

$$E = -F \tag{3.77}$$

Substitute (3.73) and (3.74) into the two sides of (3.75)

$$2A + (1 + j)E = 2D + (1 + j)F \tag{3.78}$$

If the beams were infinite, A can be considered as the incident wave and D would not exist. Then

$$-E = F = \frac{1}{1+j}A \tag{3.79}$$

Substitute (3.79) into (3.74)

$$-jC = \frac{1}{1+j}A \tag{3.80}$$

Substitute (3.79) into (3.73)

$$B = \frac{1}{1+j}A \tag{3.81}$$

Thus the amplitude transmission coefficient

$$t_m = \frac{C}{A} = \frac{1}{1-j} \tag{3.82}$$

and the amplitude reflection coefficient

$$r_m = \frac{B}{A} = \frac{1}{1+j} \tag{3.83}$$

Substituting (3.82) and (3.83) into equation (3.47) gives

$$\alpha^2 + \frac{1+j}{2}\left(\frac{1}{\beta} + \beta\right)\alpha + j = 0 \tag{3.84}$$

The roots of equation (3.84) have the form

$$\alpha = \frac{-(1+j)\cos(2kl) \pm \sqrt{(1+j)^2\cos^2(2kl) - 4j}}{2} \tag{3.85}$$

Rearranging (3.85)

$$\alpha = \frac{-(1+j)}{2}\sqrt{1-\sin^2(2kl)} \pm \frac{1-j}{2}\sqrt{1+\sin^2(2kl)}\,, \tag{3.86}$$

thus

$$\begin{aligned}
\alpha_1 &= \frac{-\sqrt{1-\sin^2(2kl)} + \sqrt{1+\sin^2(2kl)}}{2} + j\left(\frac{-\sqrt{1-\sin^2(2kl)} - \sqrt{1+\sin^2(2kl)}}{2}\right) \\
\alpha_2 &= \frac{-\sqrt{1-\sin^2(2kl)} - \sqrt{1+\sin^2(2kl)}}{2} + j\left(\frac{-\sqrt{1-\sin^2(2kl)} + \sqrt{1+\sin^2(2kl)}}{2}\right)
\end{aligned} \tag{3.87}$$

If α_1 is written as $\alpha_1 = a - jb$, α_2 can be represented as $\alpha_2 = -b + ja$, where a and b are both positive. These two roots also have the same modulus but different phase in the complex plane. The phases are related by

$$\phi_1 + \phi_2 = \frac{\pi}{2} \tag{3.88}$$

Now the mode count for the system can be estimated.

$$N_{total} = N_1 + N_2 = \frac{kL}{\pi} - \frac{1}{2} + \frac{\phi_1}{2\pi} + \frac{kL}{\pi} - \frac{1}{2} + \frac{\phi_2}{2\pi} \tag{3.89}$$

$$N_{total} = \frac{2kL}{\pi} - \frac{1}{2} + \left(\frac{\phi_1 + \phi_2}{2\pi}\right) - \frac{1}{2} = N - \frac{1}{4} = N - \delta_{sliding} \tag{3.90}$$

This shows a result of the same form as the cases of intermediate simple support or fixed support.

3.3.4 A BEAM WITH A GENERAL INTERMEDIATE CONSTRAINT

Two general intermediate constraints, a point mass and a point spring, are now considered in this section.

3.3.4.1 Intermediate point mass

Suppose that a point mass m is applied at an intermediate position between the two ends of the system. The free wave solutions of the system are still governed by equation (3.40). However, the amplitude transmission and reflection coefficient will become frequency-dependent. They can be obtained by considering the continuity of the position of the point mass. At $x = 0$, the following conditions must be satisfied:

$$w_-(0) = w_+(0) \qquad A + B + E = C + D + F \tag{3.91}$$

$$w'(0) = w'(0) \qquad -jA + jB + E = -jC + jD - F \tag{3.92}$$

$$w_-''(0) = w_+''(0) \qquad -A - B + E = -C - D + F \tag{3.93}$$

$$EI\left[w_-'''(0) - w_+'''(0)\right] = -m\omega^2 w(0) \quad jA - jB + E - jC + jD + F = -\mu(A + B + E) \tag{3.94}$$

where $\mu = m\omega^2 / EIk^3 = mk / \rho A$ is non-dimensional parameter.

From (3.91) and (3.93), $E = F$. Equation (3.92) can be rewritten as

$$-jA + jB + 2E = -jC + jD \tag{3.95}$$

Substitute (3.95) into (3.94)

$$(4+\mu)E = -\mu(A+B) \tag{3.96}$$

If the beams were infinite, A would be the incident wave and D would not exist. Then from (3.91),

$$A+B=C \tag{3.97}$$

Therefore

$$E = \frac{-\mu}{4+\mu}C \tag{3.98}$$

Multiply the two sides of equation (3.93) with j and combine it with (3.92)

$$jA = jC + E \tag{3.99}$$

Substitute (3.98) into (3.99), the transmission ratio t_m can be found as

$$t_m = \frac{C}{A} = \frac{(4+\mu)j}{(4+\mu)j-\mu} \tag{3.100}$$

Then from (3.97) the reflection ratio r_m can be obtained as

$$r_m = \frac{B}{A} = \frac{\mu}{(4+\mu)j-\mu} \tag{3.101}$$

Since μ is a frequency-dependent parameter, the coefficients t_m and r_m are not constant. When frequency is very low, μ tends to zero, $t_m \to 1$ and $r_m \to 0$. This means that there is no constraint applied. Waves will propagate through the mass without reflection. When frequency is very high, μ tends to infinity, $t_m \to \frac{1}{1+j}$ and $r_m \to \frac{1}{j-1}$. This is the case of a simple support constraint (see section 3.3.2).

In order to know the effect of an intermediate mass on the mode count of the whole system, the solution of the natural frequencies must be found. By substituting the transmission and reflection ratio into equation (3.47), the natural frequencies can be found from

$$(r_m^2 - t_m^2)\alpha^2 + r_m(\beta + \frac{1}{\beta})\alpha + 1 = 0 \tag{3.102}$$

Equation (3.102) can be simplified if the two beams are identical in length ($L_1 = L_2$). In this case,

$$(r_m^2 - t_m^2)\alpha^2 + 2r_m\alpha + 1 = 0 \tag{3.103}$$

Thus the roots of (3.103) are

$$\alpha_1 = -\frac{1}{r_m + t_m} \text{ and } \alpha_2 = -\frac{1}{r_m - t_m} \tag{3.104}$$

Substituting (3.100) and (3.101) gives

$$\alpha_1 = \frac{\mu - (4+\mu)j}{\mu + (4+\mu)j} \text{ and } \alpha_2 = 1 \tag{3.105}$$

It may be noted from this that one set of modes (the antisymmetric modes) will always be the modes of a pinned-pinned beam whereas the other set of modes will depend on the mass and on frequency.

The first root gives

$$e^{-2kLj} = \frac{\mu - (4+\mu)j}{\mu + (4+\mu)j} = e^{j\phi_1} = e^{-(2n\pi - \phi_1)j} \tag{3.106}$$

where $\phi_1 = \tan^{-1}\left(\frac{\mu(4+\mu)}{4(\mu+2)}\right)$ and $\pi \le \phi_1 \le \frac{3\pi}{2}$. So the natural modes are governed by

$$kL = n\pi - \frac{\phi_1}{2} \tag{3.107}$$

and the mode count for this set of modes is

$$N_1 = \frac{kL}{\pi} - \frac{1}{2} + \frac{\phi_1}{2\pi} \tag{3.108}$$

The second root gives

$$N_2 = \frac{kL}{\pi} - \frac{1}{2} \tag{3.109}$$

The total mode count of the system can be estimated by adding the two sets of modes together

$$N_{total} = N_1 + N_2 = \frac{kL}{\pi} - \frac{1}{2} + \frac{\phi_1}{2\pi} + \frac{kL}{\pi} - \frac{1}{2}$$

$$N_{total} = \frac{2kL}{\pi} - \frac{1}{2} + \frac{\phi_1}{2\pi} - \frac{1}{2} = N + \frac{\phi_1}{2\pi} - \frac{1}{2} \tag{3.110}$$

Therefore the effect of a midpoint mass on the mode count of the system can be obtained by

$$\delta = \frac{1}{2} - \frac{\phi_1}{2\pi} \qquad \pi \le \phi_1 \le \frac{3\pi}{2} \tag{3.111}$$

For $\mu \to 0$, $\phi_1 \to -\pi$ and $\delta \to 0$; for $\mu \to \infty$, $\phi_1 \to -\pi/2$ and $\delta \to -¼$. This is the same as the case of a mass at the ends of the beams described in section 3.2.4. However, it must be indicated that δ for a mass at the ends of the beams is different from that at a midpoint at a specific frequency, although they have the same trends with frequency. This can be seen when they are plotted against frequency, as shown in Figure 3.11. It can be shown that δ_{mass} for a midpoint mass is equivalent to δ_{mass} for an end mass in which μ is replaced by $\mu/4$. The general intermediate point mass has not been analysed as there is no closed expression for the solution of equation (3.102). But the result is expected as same as the midpoint.

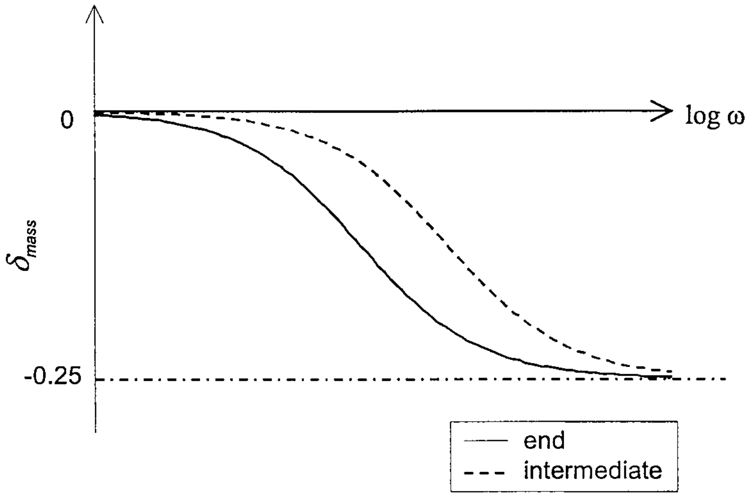

Figure 3.11 Difference between δ_{mass} at ends and midpoint on beams.

It can be seen that the intermediate point mass has a similar effect as that a point mass applied at the end of a beam, which is discussed in section 3.2.4. The difference in the mode count between a beam with and without an intermediate point mass is frequency-dependent, not constant. The mode count of the system with an intermediate point mass can be expressed by

$$N_{total} = N - \delta_{mass} \tag{3.112}$$

where N is the mode count of the beam without the intermediate mass and δ_{mass} is frequency-dependent parameter between zero to – ¼ as described in equation (3.111).

3.3.4.2 Intermediate point spring

When an intermediate point spring K is considered, the continuity conditions are mostly the same as the case of a point mass except for equation (3.94). The continuity of the shear force should be written as

$$EI\left[w_-'''(0)-w_+'''(0)\right]=Kw(0) \qquad jA-jB+E-jC+jD+F=\sigma(A+B+E) \quad (3.113)$$

where $\sigma=K/EIk^3$ is a non-dimensional stiffness coefficient.

The transmission and reflection ratios are now readily obtained by substituting σ into equation (3.100) and (3.101) to replace μ. For this case, t_m and r_m are

$$t_m=\frac{C}{A}=\frac{(4-\sigma)j}{(4-\sigma)j+\sigma} \qquad (3.114)$$

$$r_m=\frac{B}{A}=\frac{-\sigma}{(4-\sigma)j+\sigma} \qquad (3.115)$$

It can be found that an intermediate point spring has the same effect on the wave propagation as the end point spring discussed in section 3.2.4. At very low frequency, σ tends to infinity, $t_m\to\frac{1}{1+j}$ and $r_m\to\frac{1}{j-1}$. This is the case of a simple support constraint. At very high frequency, σ tends to zero, $t_m\to 1$ and $r_m\to 0$. This is the case of a free condition. Waves will propagate past the spring without reflection.

In order to know the effect of an intermediate spring on the mode count of the whole system, the solution of the natural frequencies must be found. By substituting the transmission and reflection ratio into equation (3.47), the natural frequencies can be found from equation (3.102) or, if the beams are identical in length ($L_1=L_2$), equation (3.103). Substituting equations (3.114) and (3.115) into equation (3.104) gives

$$\alpha_1=\frac{\sigma+(4-\sigma)j}{\sigma-(4-\sigma)j} \text{ and } \alpha_2=1 \qquad (3.116)$$

It may be noted from this that one set of modes will always be the modes of a pinned-pinned beam whereas the other set of modes will depend on the stiffness and on frequency.

The first root gives

$$e^{-2kLj}=\frac{\sigma+(4-\sigma)j}{\sigma-(4-\sigma)j}=e^{j\phi_1}=e^{-(2n\pi-\phi_1)j} \qquad (3.117)$$

where $\phi_1=\tan^{-1}\left(\frac{\sigma(4-\sigma)}{4(\sigma-2)}\right)$ and $-\frac{\pi}{2}\le\phi_1\le\pi$. So natural modes are governed by

$$kL = n\pi - \frac{\phi_1}{2} \tag{3.118}$$

and the mode count for this set of modes is

$$N_1 = \frac{kL}{\pi} - \frac{1}{2} + \frac{\phi_1}{2\pi} \tag{3.119}$$

The second root gives

$$N_2 = \frac{kL}{\pi} - \frac{1}{2} \tag{3.120}$$

The total mode count of the system can be estimated by adding the two sets of modes together

$$N_{total} = N_1 + N_2 = \frac{kL}{\pi} - \frac{1}{2} + \frac{\phi_1}{2\pi} + \frac{kL}{\pi} - \frac{1}{2}$$

$$N_{total} = \frac{2kL}{\pi} - \frac{1}{2} + \frac{\phi_1}{2\pi} - \frac{1}{2} = N + \frac{\phi_1}{2\pi} - \frac{1}{2} \tag{3.121}$$

Therefore the effect of a midpoint spring on the mode count of the system can be obtained by

$$\delta = \frac{1}{2} - \frac{\phi_1}{2\pi} \qquad -\frac{\pi}{2} \le \phi_1 \le \pi \tag{3.122}$$

For $\sigma \to \infty$, $\phi_1 \to \pi$ and $\delta \to 3/4$; For $\sigma \to 0$, $\phi_1 \to -\pi/2$ and $\delta \to 0$. This is the same as the case of a spring at the ends of the beams described in section 3.2.4. As for the midpoint mass discussed above, there is some difference for δ between at ends and at intermediate of the beams. This is illustrated in Figure 3.12; the two expressions for δ_{spring} can be shown to the equivalent if K is replaced by $K/4$ in δ_{spring} for the end spring. Again, the result for the midpoint spring has not been analysed but is expected as same as a general intermediate spring.

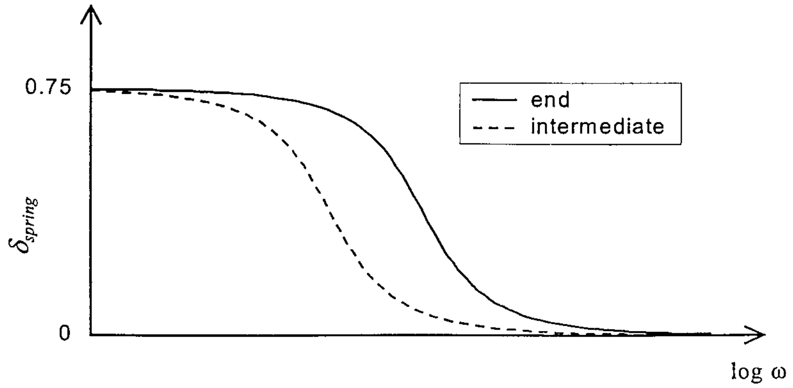

Figure 3.12 Difference between δ_{spring} at ends and midpoint on beams.

The mode count of a beam with an intermediate point spring can thus be expressed by

$$N_{total} = N - \delta_{spring} \tag{3.123}$$

where N is the mode count of the beam without the intermediate spring and δ_{spring} is the frequency-dependent parameter described in (3.122).

Based on the analysis described in section 3.3.1 to 3.3.3, it can be concluded that the mode count of a beam with an extra intermediate constraint is equal to the mode count of this beam without any extra constraint, modified by a constant that depends only on the type of the constraint. These constants are normally the same as those applying for constraints at the ends of the beams described in section 3.2 (Table 3.1). For a mass or a stiffness, the constants have a frequency-dependent effect which is the same as for an end constraint apart from a constant factor.

3.4 MULTI-BEAM SYSTEM

This section will extend the conclusion obtained from two-beam systems to systems consisting of more beams. A finite periodic beam system will be discussed first and then a random multi-beam system will be considered.

3.4.1 FINITE PERIODIC BEAM SYSTEM

The finite periodic beam system discussed here is a finite length beam supported at regular intervals. The mode count of the system will be analysed by treating it as a long beam simply supported at two ends with a number of extra uniform intermediate constraints.

If $m-1$ equally spaced fixed constraints are applied, the system can be regarded as two pinned-fixed beams and $m-2$ fixed-fixed beams. The mode count of the whole system can be calculated by

$$N_{total} = 2N_{pinned-fixed} + (m-2)N_{fixed-fixed} \tag{3.124}$$

with

$$N_{pinned-fixed} = \frac{kL}{\pi} - \frac{3}{4} \tag{3.125}$$

$$N_{fixed-fixed} = \frac{kL}{\pi} - 1 \tag{3.126}$$

where N_{total} is the mode count of the whole system. $N_{pinned\text{-}fixed}$ is the mode count of a pinned-fixed beam. $N_{fixed\text{-}fixed}$ is the mode count of a fixed-fixed beam. m is the number of beam segments of the system. This yields

$$N_{total} = \frac{mkL}{\pi} - \frac{1}{2} - (m-1) = N - (m-1)\delta_{fixed} \tag{3.127}$$

where N is the mode count of the long beam with simple supports at the two ends.

Since fixed constraints separate the system into exactly uncoupled segments, the mode count for the whole system is readily obtained. It can be represented by the mode count of a long beam minus the product of the number of constraints (m – 1) and the constraint constant δ. It can also be noted that the same result could be obtained for the case of random (unequally spaced) constraints.

3.4.2 SIMPLY SUPPORTED FINITE PERIODIC BEAM SYSTEM

3.4.2.1 Natural modes and mode count

In this section a beam with (m – 1) intermediate simple support is considered (Figure 3.13). Mead [90, 91] gives a detailed study of the natural modes of a finite periodic system. The natural modes only occur in propagation bands that are described in terms of "bounding frequencies". The bounding frequencies depend on the natural frequencies of an individual segment of the system, with appropriate boundary conditions. These govern the upper and lower limits of the propagation bands. In the present case, the pinned-pinned and fixed-fixed boundary conditions are appropriate.

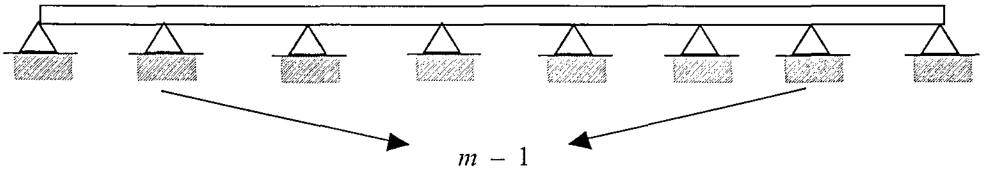

Figure 3.13 Simply supported finite periodic beam system

The natural frequencies for pinned-pinned boundary conditions are obtained from

$$kL = n\pi \tag{3.128}$$

and for fixed-fixed boundary condition from

$$kL \approx (n+\frac{1}{2})\pi . \tag{3.129}$$

The propagation bands thus occur in the ranges $[n\pi, (n+1/2)\pi]$ where n is an integer starting from 1. m modes are available in each propagation band. Hence it can be seen that

between $kL=0$ and π, there are 0 modes,
between $kL=\pi$ and $3\pi/2$, there are m modes,
between $kL=3\pi/2$ and 2π, there are 0 modes,
between $kL=2\pi$ and $5\pi/2$, there are m modes

and so on. Figure 3.14 shows an illustration of the mode count for the finite periodic simply supported beam system.

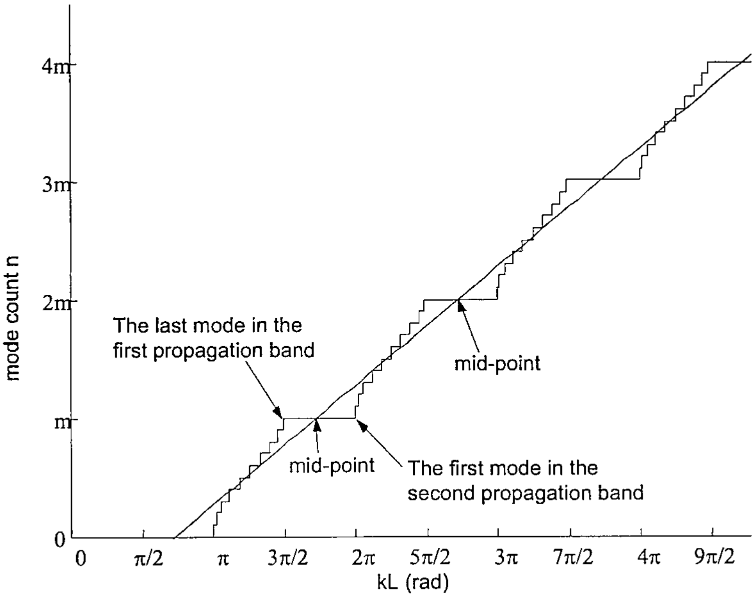

Figure 3.14 Illustration of the mode count of a finite periodic structure.

The average mode count can be obtained by finding the equation of a straight line passing through points that are located midway between the last mode in a propagation band and the first mode in the next propagation band. The physical explanation of these specific points is that the wavenumber at these points should be midway between the two wavenumbers at which two successive modes occur. In fact, these points are located in stop bands.

Clearly this average mode count is only an approximation to the actual mode count, where modes tend to be clustered. More details about the modal density of periodic structures can be found in Reference [92]. The purpose here is not to study the effect of periodicity but the average effect of intermediate constraints.

The last mode in the first propagation band occurs approximately at $kL = \pi + \frac{(m-1)\pi}{2m}$. This is less than the bounding frequency since the end conditions of the whole beam are simple supports. The first mode in the second propagation band occurs at $kL=2\pi$. The mid-point is then located at $kL = \frac{(7-1/m)}{4}\pi$, which corresponds the mode count of m.

The slope of the straight line is m/π. Therefore the average mode count of the finite periodic system can be represented as

$$N_{periodic} = \frac{m}{\pi}\left(kL - \frac{(7-1/m)}{4}\pi\right) + m = \frac{mkL}{\pi} - \frac{3}{4}(m-1) - \frac{1}{2} \tag{3.130}$$

$$N_{periodic} = N - (m-1)\delta_{pinned} \tag{3.131}$$

This shows that the finite periodic beams system has a mode count that can be estimated by the mode count of the long beam minus the product of the number of constraints $m-1$ and the constraint constant δ.

3.4.2.2 Case study

A beam of total length 2m, first with 5 identical segments and then with 10 identical segments, is studied in this section. Simple supports are applied at uniform intervals. The mode counts for the two cases are plotted in Figure 3.15. The mode count of the long beam itself is also plotted in the same figure for comparison.

The staircases plotted in Figure 3.15 are obtained from an FEM model using ANSYS. In the FEM model a number of beam elements are used adequately to approximate the behaviour of each beam segment. The maximum element length is 0.01m. The difference between the results for the periodic case and the average results for the long beam is plotted in Figure 3.16. There are a lot of fluctuations in these difference curves. However, the averaged values for 5 and 10 segments are 3 and 6.8, which are equal to those calculated by equation (3.131).

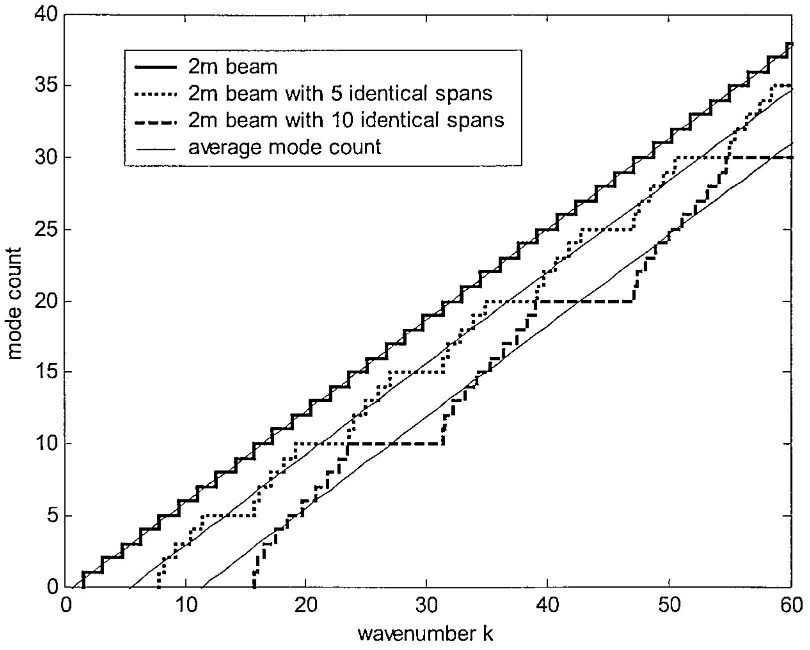

Figure 3.15. Mode count of periodic beams systems.

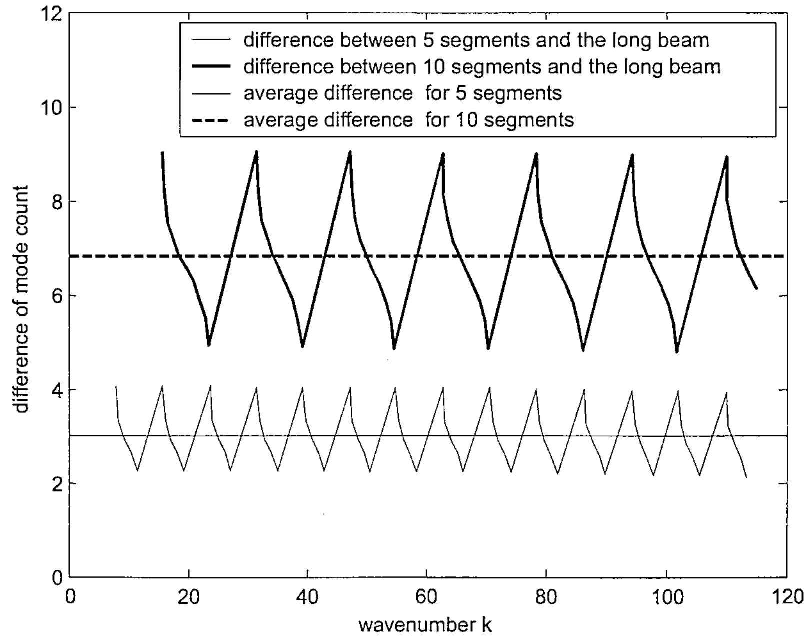

Figure 3.16. Differences of the mode count between the periodic and the long beam.

3.4.3 RANDOMLY SPACED MULTI-BEAM SYSTEM

The periodic structure is an ideal situation suitable to be analysed theoretically. Real structures, however, might not be ideally periodic. Whether or not the conclusion based on the analysis of a finite periodic system can be extended to random multi-beam systems should therefore be considered for practical applications. Since it is nearly impossible to conduct an analytical investigation of the random multi-beam system, numerical tools such as FEM become appropriate. By reusing the example in section 3.4.2.2 a ten segment beam has been generated by perturbing the positions of the simple supports of a periodic system. The modal frequencies have been calculated using the FE method. The length of the segments were 20, 22, 18, 17, 23, 20, 19, 25, 15 and 21cm, giving a total length of 2 m. Figure 3.17 shows the mode count of the system with 10 random segments along with that with 10 periodic segments. This shows that the propagation and stop bands for the periodic system disappear. In fact the modes become local. The mode count difference between the random multi-beam system and the average result for the long beam is calculated and presented in Figure 3.18. The average value is equal to that of the periodic system, with less fluctuations.

This section therefore concludes with an estimated formula for the mode count of a multi-beam system without analytical proof but which has been demonstrated by the example shown. Equation (3.132) gives this estimated formula that has the same form as described in equation (3.131).

$$N_{random} = N-(m-1)\delta_{pinned} \tag{3.132}$$

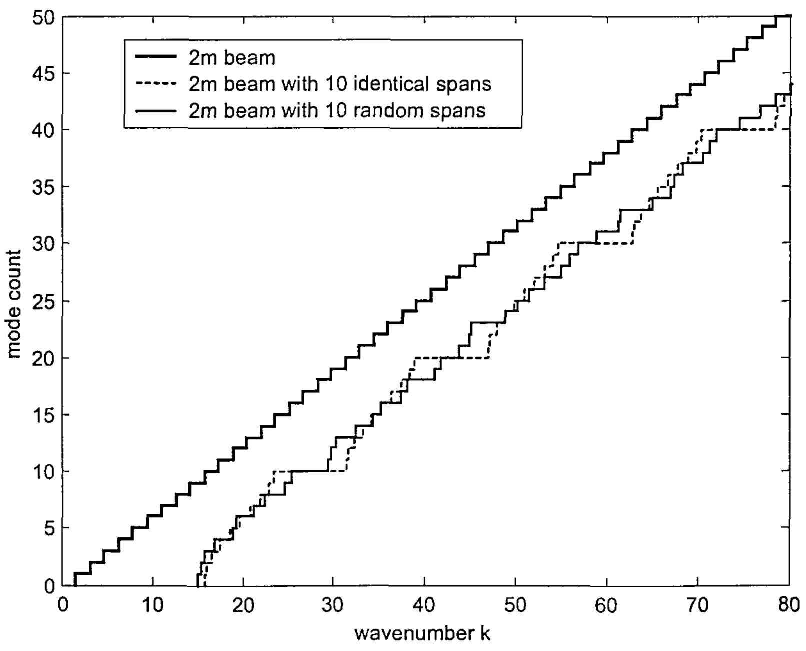

Figure 3.17. Mode counts of multi-beam systems.

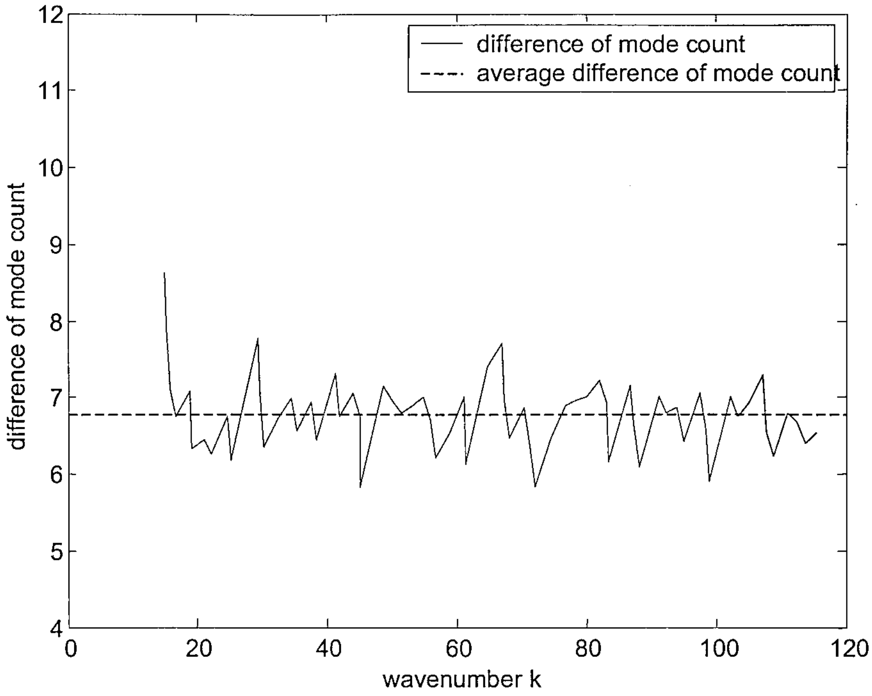

Figure 3.18 Mode count difference between the random multi-beam system and the result for the long beam.

3.5 EXTRUDED SECTION

The mode count and modal density of the cross-section of the extruded plate are studied in this section. The example of an extruded plate used in the present chapter is the floor of a typical railway carriage, which has a length of 2.016 m and a height of 0.070 m. It consists of an upper plate, a lower plate and a set of stiffening plates set at angles between 33° and 49° and some at 90°. The work described here is concentrated on the cross-section in the *x-y* plane as shown in Figure 3.19. This extruded section is composed of a set of one-dimensional segments so that the previous studies on the mode count of 1-D systems can be used to estimate the mode count of the extruded section. The thickness of each segment is 0.003m.

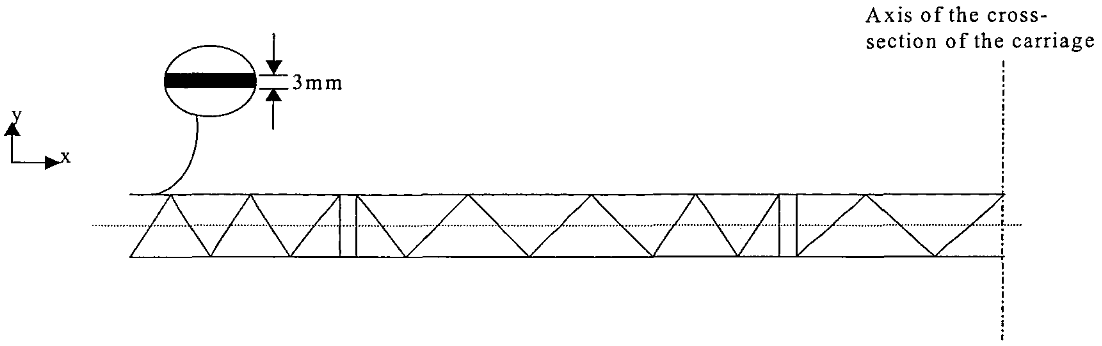

Figure 3.19 Cross-section of the extruded plate (not to scale).

3.5.1 MODAL ANALYSIS OF FEM MODEL

The cross-section of the extruded plate is modelled using FEM with ANSYS. The BEAM 3 element in ANSYS is chosen to represent it. The BEAM 3 element is a uniaxial two node element with tension, compression, and bending capabilities. The element has three degrees of freedom at each node: translations in the nodal x and y directions and rotation about the nodal z-axis. The maximum length of the element used in this FEM model is 0.01m, allowing analysis valid up to 10 kHz.

A modal analysis is carried out by applying certain boundary conditions on the model. In order to obtain more global modes, symmetry and anti-symmetry boundary conditions are separately applied on the two ends of the upper and lower extruded plate. In total, four combinations of boundary conditions are analysed (shown in Figure 3.20).

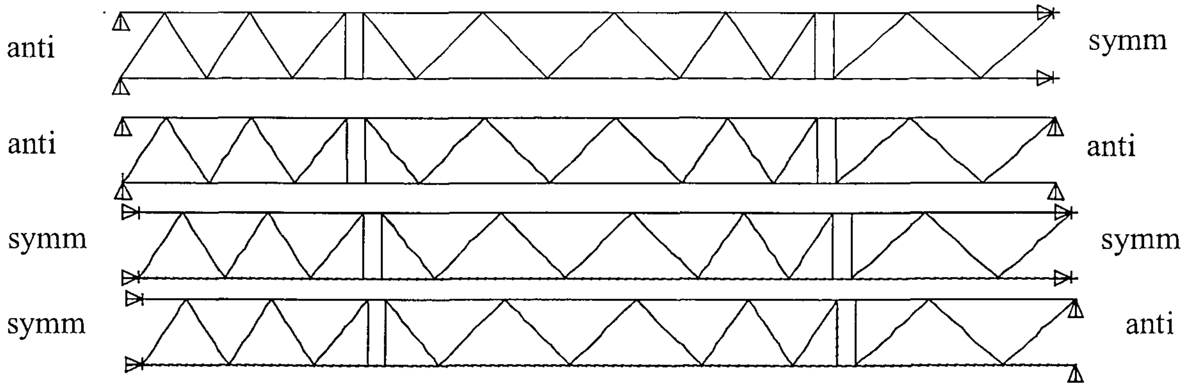

Figure 3.20 Boundary conditions applied in FEM model.

For the present model, to represent the extruded plate in plane bending, the Young's modulus E is replaced by $E/(1-\mu^2)$ where μ is the Poisson's ratio in order to account for the fact that cross-sectional contraction is prevented in one direction ('plane strain' model).

The FEM modal analysis gives the natural frequencies and mode shapes of the extruded section. The first few modes for each boundary condition are presented in Figure 3.21 to Figure 3.24. For each set of boundary conditions, only the first few modes appear to be global behaviour of the structure. For frequencies above 470Hz, the mode shapes become complicated and local motion of a single beam begins to dominate the modes. Global modes may be considered as those in which the energy is distributed over the whole system, involving motion of the whole framework, whereas 'local modes' involve mainly motion of one (or more) members without much motion of the whole framework. Thus, for example, in Figures 3.21 and 3.24 the upper mode is clearly a global mode and the lower mode is clearly a local mode. The middle mode is predominantly a global mode although with strong motion of some members. The frequency above which local modes occur will be denoted by f_{local}. The local modes appear first at the longest beam segment at the right-hand side of the extruded section. For this beam segment, this is its first mode. However, it can be noted that adjacent beams also vibrate to some extent. Then as the frequency increases local modes appear at the shorter beam segments in other locations of the extruded section.

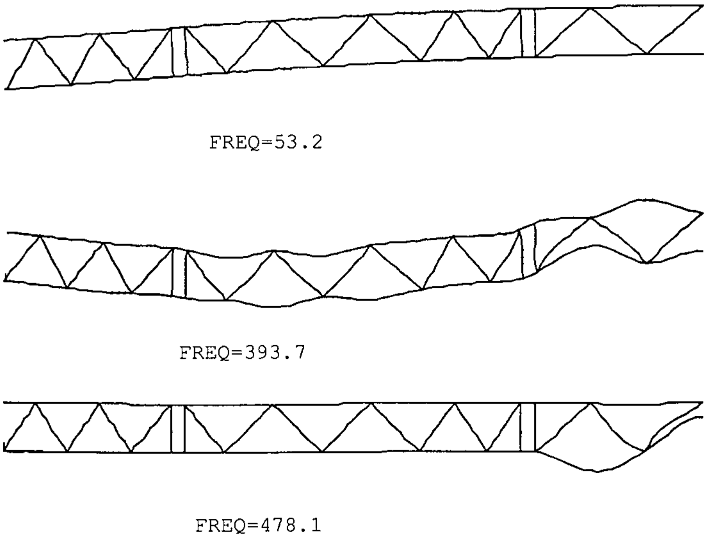

Figure 3.21. Mode shapes for the boundary condition: anti-symmetry and symmetry. (Frequency in Hz).

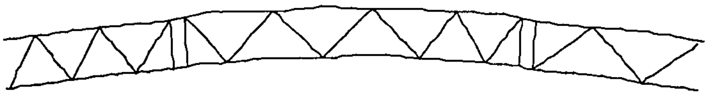

FREQ=197.7

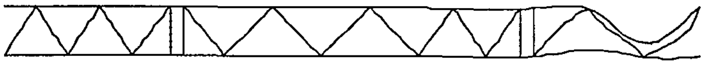

FREQ=477.3

Figure 3.22. Mode shapes for the boundary condition: anti-symmetry and anti-symmetry. (Frequency in Hz).

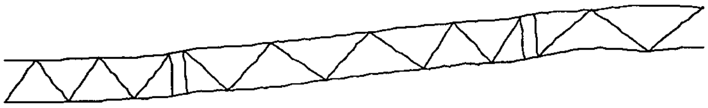

FREQ=199.5

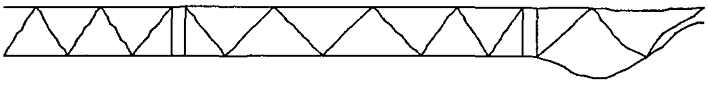

FREQ=488.9

Figure 3.23 Mode shapes for the boundary condition: symmetry and symmetry. (Frequency in Hz).

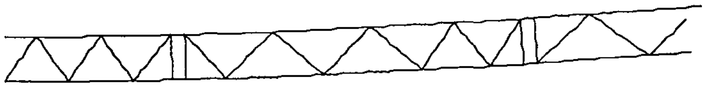

FREQ=52.1

FREQ=399.5

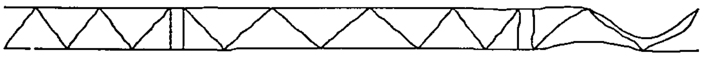

FREQ=490.2

Figure 3.24 Mode shapes for the boundary condition: symmetry and anti-symmetry. (Frequency in Hz).

3.5.2 EVALUATING THE MODE COUNT

To estimate the mode count of the extruded section, account should be taken of the global modes and the local modes. For global modes, the extruded section can be regarded as an equivalent beam. For local modes, the extruded section can be treated as a multi-beam system.

The FEM model represents half the width of the floor. The mode count of the whole floor can be obtained by a combination of the FEM modal analysis under the boundary conditions of antisymmetry-symmetry and antisymmetry-antisymmetry (see Figure 3.20).

3.5.2.1 Global modes

To consider the extruded section as an equivalent beam, the equivalent bending stiffness for the extruded section must be determined. In such global bending motion, the stiffeners are nearly rigid and the bending induces stresses mainly in the upper and lower beams. Supposing the extruded plate is in a state of a pure bending vibration, the upper or lower beams would be either compressed or extended relative to the neutral fibre. This neutral fibre passes through the centre of gravity of the section, and actually is located at the mid-point of the section (see Figure 3.25). It can be assumed that the stiffeners do not bear the tensile and compressive stress under the pure bending condition and behave as rigid spacers that separate the upper and lower beams. Based on the above assumption, the second moment of area about the *z* axis per unit width can be calculated by

$$I_x = 2\times\left(\frac{h^3}{12}+\left(\frac{H}{2}-\frac{h}{2}\right)^2\times h\right) \qquad (3.133)$$

where *h* is the thickness of the upper and lower plates and *H* is the height of the extruded plate. This is illustrated in Figure 3.26.

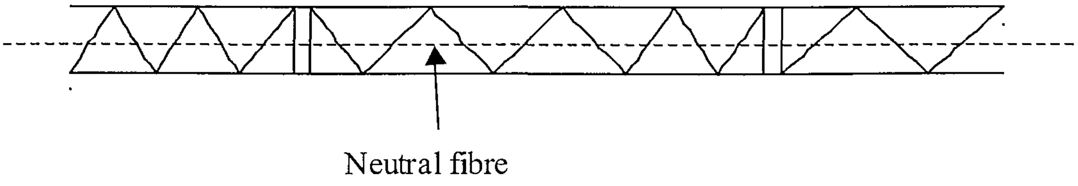

Figure 3.25 Illustration of the neutral fibre of the extruded section.

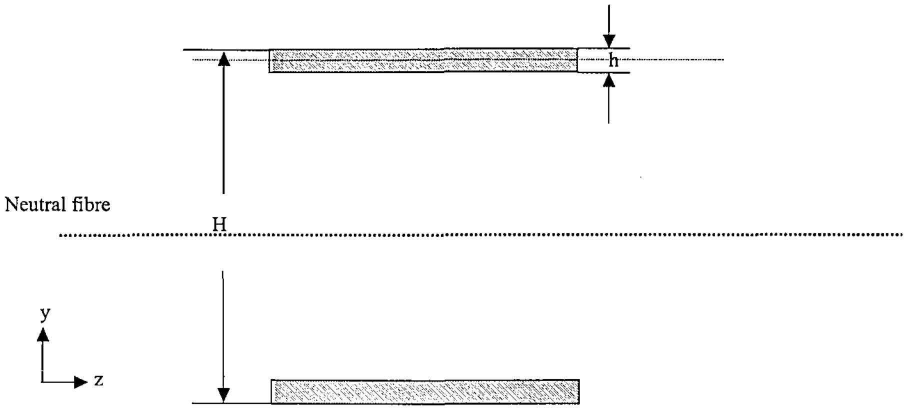

Figure 3.26 The moment of inertia of the area of the cross section.

The equivalent bending stiffness can therefore be calculated by

$$B_x = E'I_x = \frac{EI_x}{1-\mu^2} \tag{3.134}$$

The dispersion relation for the equivalent beam can be expressed by

$$k_{Bg} = \omega^{\frac{1}{2}} \left(\frac{m'}{E'I_x} \right)^{\frac{1}{4}} \tag{3.135}$$

where m' is the mass per unit length, which is given by $m' = \frac{\rho h l_{tot}}{L}$, where l_{tot} is the total length of all the beam segments and L is the length of the section.

To investigate the validity of the above assumption, the bending stiffness can be determined from the FEM model using the dispersion relation of bending vibration and then compared with the result of equation (3.134). The dispersion relation of bending vibration is given by

$$k = \sqrt[4]{\frac{m'}{B}\omega^2} \tag{3.136}$$

where k is the wavenumber, m' is the mass per unit length, B is the bending stiffness of the beam and ω is the radian frequency. Taking the wavelength from the mode shape shown in Figure 3.21 to 3.24, the wavenumber for the global modes can be obtained by

$$k = \frac{2\pi}{\lambda} \tag{3.137}$$

where λ is the wavelength for the global vibration.

By rearranging equation (3.136), and substituting the wavenumber and natural frequencies, the bending stiffness can be calculated. This is shown in Table 3.2. The averaged value from the first mode for each set of boundary conditions from the FEM model is 5.336×10^5 Nm^2. The value calculated by equation (3.134) is 5.369×10^5 Nm^2. The difference between the estimated formula and the FEM results is less than 1%.

Table 3.2 The wave number and bending stiffness derived from FEM analysis

Boundary conditions	Frequency (Hz)	Wavelength (m)	Wave number (rad/m)	Bending stiffness (Nm^2)
anti-symm	53.2	4.032	1.558	5.764×10^5
anti-symm	393.7	3.344	4.675	3.896×10^5
anti-anti	197.7	2.016	3.117	4.974×10^5
symm-symm	199.5	2.016	3.117	5.068×10^5
symm-anti	52.1	4.032	1.558	5.534×10^5
symm-anti	399.5	3.344	4.675	4.013×10^5

Now the mode count of the global modes can be readily obtained by using the approximate formula

$$N_g = \frac{k_{Bg}L}{\pi} - \delta_{BCg} \tag{3.138}$$

where N_g is the mode count of the global modes, k_{Bg} is the wavenumber, which can be obtained from the knowledge of the equivalent bending stiffness for the global modes and δ_{BCg} is the constant due to boundary conditions described in section 3.2. For current case, simple supports are applied on the two ends of the extruded section (full floor) so that δ_{BCg} is 1/2.

Simple *Euler-Bernoulli* beam theory is valid at long wavelengths. At higher frequencies shear deformation and rotational inertia need to be considered. So the beam theory of *Timoshenko* is introduced for evaluation of the global mode count for high frequency. The dispersion relation of the Euler-Bernoulli beam is therefore modified and expressed by [35]

$$E'I_x k_{Timo}^4 - \rho I_x \left(1+\frac{E'}{G\kappa}\right)\omega^2 k_{Timo}^2 - \rho A\omega^2 + \frac{\rho^2 I_x}{G\kappa}\omega^2 = 0 \tag{3.139}$$

where $\beta = ik_{Timo}$, k_{Timo} is the wavenumber, κ is the Timoshenko shear coefficient, I_x is the second moment of area of the equivalent beam, E' is the corrected Young's modulus and G is the shear modulus. The shear modulus is given by $G = \frac{E}{2(1+\mu)}$. The value of κ is partly determined through the analysis of the mobility of joint locations using the FEM model (see section 3.5.3). Here, $\kappa = 0.2$ is used.

The solution of the first propagating wave[1] from equation (3.139) gives the wavenumber of the Timoshenko beam, which is represented by

$$k_{Timo} = \sqrt{\frac{\rho I_x\left(1+\frac{E'}{G\kappa}\right)\omega^2 + \sqrt{\left[\rho I_x\left(1+\frac{E'}{G\kappa}\right)\omega^2\right]^2 - 4E'I_x\left(-\rho A\omega^2 + \frac{\rho^2 I_x}{G\kappa}\omega^2\right)}}{2E'I_x}} \tag{3.140}$$

The global mode count of the Timoshenko beam can be calculated by

$$N_g = \frac{k_{Timo}L}{\pi} - \delta_{BCg} \tag{3.141}$$

The global mode count obtained from both equation (3.138) and (3.141) are presented in Figure 3.27. It can be seen that the Timoshenko beam has a similar result to that of Euler-Bernoulli beam below 200Hz while, above 200Hz, the mode count of the *Timoshenko* beam increases more quickly than *Euler-Bernoulli* beam. It will be shown later in section 3.5.2.4 that the *Timoshenko* beam is a more appropriate model for the global vibration than *Euler-Bernoulli* beam. The beam models give results that are close to the FEM results up to f_{local} which in this case is 470Hz. Above this frequency the FEM results are dominated by the local modes.

---

[1] The solutions of equation (3.139) have two sets of waves. The first is a propagating wave. The second is a near-field wave at low frequency and propagating at higher frequency. Equation (3.140) is the first propagating wave.

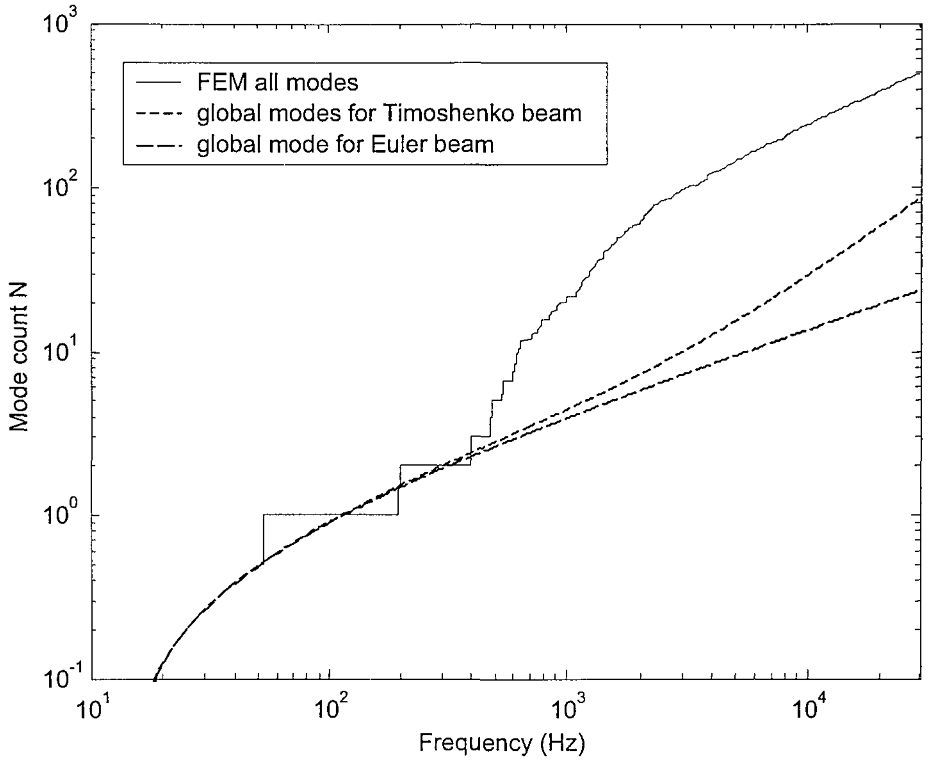

Figure 3.27 Global modes of the extruded section.

3.5.2.2 Local modes

The mode count for local modes can be approximately considered by treating the extruded section as a multi-beam system, that consists only of a single line of segments joined end-to-end. The boundary conditions concerned were also only ideal conditions such as the simple support. For the extruded section, the beam segments are not joined in a single line but multi-coupled and the boundary conditions at the joint points are unknown. However, based on the study described in the previous sections, in which the mode count of a multi-beam system can be estimated by the mode count of a beam with a total length of all the segments, modified to account for the constraints, the mode count for the extruded section can also be evaluated approximately in a similar way.

In order to use this method to predict the mode count for the extruded section, one must first investigate the boundary conditions between the beam segments. This can be done by checking the wavenumber for each beam segment in its local mode. For each local mode, usually only one beam segment dominates the vibration. In other words, the mode of the whole system is determined by this beam segment. The dispersion relation of the bending vibration for this beam segment must satisfy the equation (3.136), where the bending stiffness and mass per unit length refer now to the beam segment. The relation between the wavenumber and the frequency helps to understand the boundary conditions experienced by this beam segment. For example, it is well known (see also Appendix B) that the fixed-fixed boundary condition will give a first mode of a beam which has the largest wavenumber compared with other boundary conditions. Therefore, the natural frequencies of every local mode below 2000Hz directly obtained from the FEM analysis is used to calculate the wavenumber, assuming the beam to be subject to fixed-fixed boundary conditions, by using the frequency equation described in Appendix B. These results are compared with the dispersion relation for free waves in the beam segment. This is plotted in Figure 3.28. For comparison, the wavenumber estimated by assuming a pinned-pinned condition applied to each local mode is also calculated and presented in Figure 3.28. Note that, in Figure 3.28, the wave numbers for fixed-fixed conditions are plotted against the natural frequencies from FEM results, rather than the calculated frequencies for fixed-fixed boundary conditions. This makes the wavenumbers shift to the left so that they appear above the dispersion curve. For the case of pinned-pinned, wavenumbers are shifted to the right and appear below the dispersion curve.

These results show that each beam segment is in a state between the fixed-fixed boundary condition and pinned-pinned. It may be noted from the earlier analysis that intermediate simple supports on a beam lead to local modes with natural frequencies somewhere between pinned-pinned and fixed-fixed (actually between pinned-pinned and pinned-fixed, see section 3.4.2.1). Therefore it is assumed, as a first approximation, that each local beam is simply supported at its ends as well as connected to its neighbours. This leads to an approximate expression for the local modes of the extruded section. It is given by

$$N_l \approx \frac{kl_{tot}}{\pi} - (m-1)\times\frac{3}{4} \tag{3.142}$$

where N_l is the mode count of the local modes, m is the number of the beam segments, l_{tot} is the total length of the beam segments. For this section (whole floor), m= 78, and l_{tot} = 7.41m.

The extruded section is different from the multi-beam system discussed in section 3.4. It includes four simple supports at two ends, the irregularly spaced beam segments and unknown boundary conditions between them. Although these differences exist, the estimation based on equation (3.142) is of a similar form to that for the multi-beam system discussed in section 3.4. This estimation is the simplest one but will give a useful understanding of the dynamics of the extruded section. It also leads to potential estimation errors to some extent. Results will be compared with the FEM mode count in section 3.5.2.4 below.

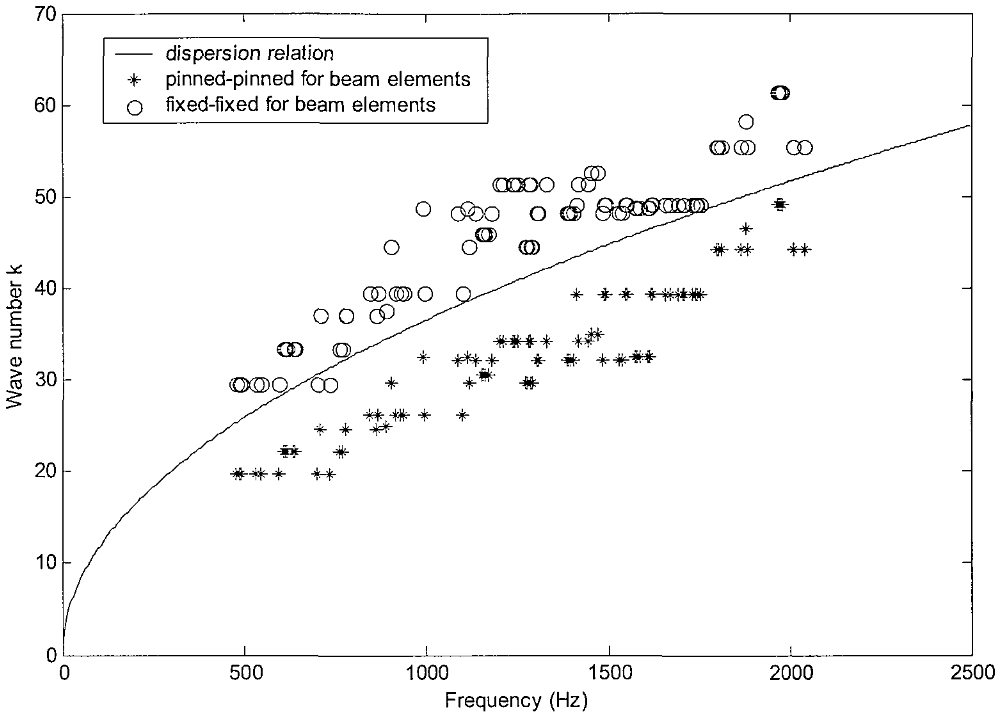

Figure 3.28 Wavenumber of the local modes of the extruded section.

3.5.2.3 Longitudinal modes

In order to estimate the mode count of the extruded section, for comparison with the FEM results, the longitudinal vibration must be also taken into account. The longitudinal modes can also be considered to consist of global and local modes. The local modes occur when a half wavelength would fit within a single beam segment. For the longest beam segment in the extruded section, 0.16m, the first mode would occur at 16250Hz for the wave speed 5200m/s. For shorter beam segments, the first mode would occur at a higher frequency. The local longitudinal modes may therefore be ignored when the mode count for the whole system is considered. The global longitudinal modes may be considered as the modes of a simple rod with the length of the extruded section. The corresponding mode count is given by

$$N_L = \frac{k_L L}{\pi} \tag{3.143}$$

where N_L is the longitudinal mode count, k_L is the wavenumber of the longitudinal vibration and L is the length of the extruded section.

Figure 3.29 shows the longitudinal mode count for the extruded section. It can be seen that the longitudinal mode count has a comparatively small contribution to that of the whole system.

A second set of global longitudinal modes exists in which the two outer beams vibrate in opposite directions on the shear stiffness of the intermediate 'layer'. However, these modes have not been included here as they occur at high frequency and will have even smaller contributions to the mode count than the modes in Figure 3.29.

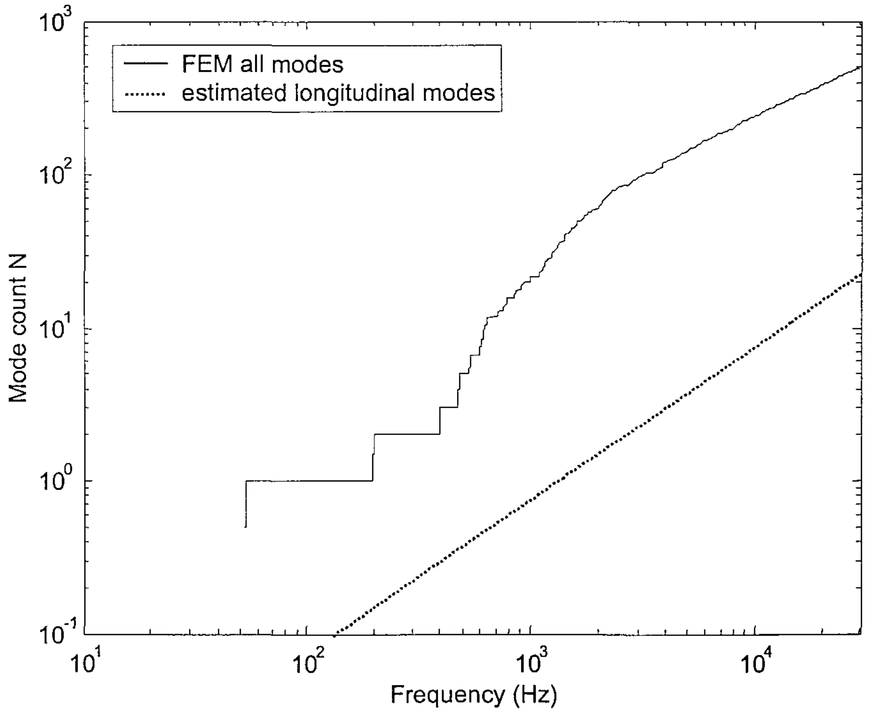

Figure 3.29 The longitudinal mode count of the extruded section.

3.5.2.4 Mode count for extruded section

Now the mode count for the extruded section is estimated and compared with the results of the FEM model. The mode count of the extruded section can be approximately calculated by

$$N = \begin{cases} N_L + N_g & f < f_{local} \\ N_L + N_g + N_l & f \geq f_{local} \end{cases} \tag{3.144}$$

where N_L is the mode count for the longitudinal vibration from equation (3.143), N_g is the mode count for the global bending modes from equation (3.141) and N_l is the mode count for the local bending modes from equation (3.142).

Figure 3.30 presents the mode count estimated by equation (3.144) and that obtained from the FEM model. Figure 3.31 presents the same curves as Figure 3.30 but with logarithmic axes so that the difference at low frequency can be clearly seen. The estimated value is larger than that obtained from FEM above 500Hz. The difference between these two curves is plotted against frequency in Figure 3.32. The average difference is 12.5.

If a fixed boundary condition is considered to exist between the beam segments in the extruded section in place of the pinned boundary condition, the local modes can be predicted by

$$N_l = \frac{kl_{tot}}{\pi} - (m-1) \tag{3.145}$$

The corresponding results are presented in Figure 3.33 to Figure 3.35. The average difference between the estimated and FEM mode count is – 6.2.

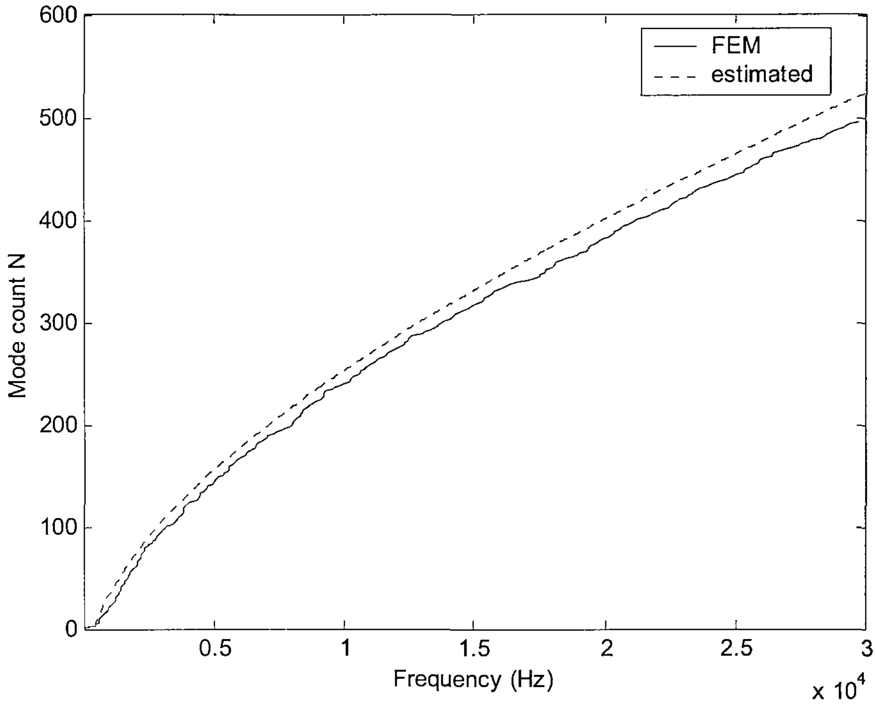

Figure 3.30 Mode count of the extruded section for the whole floor. (simple support condition supposed between beam segments).

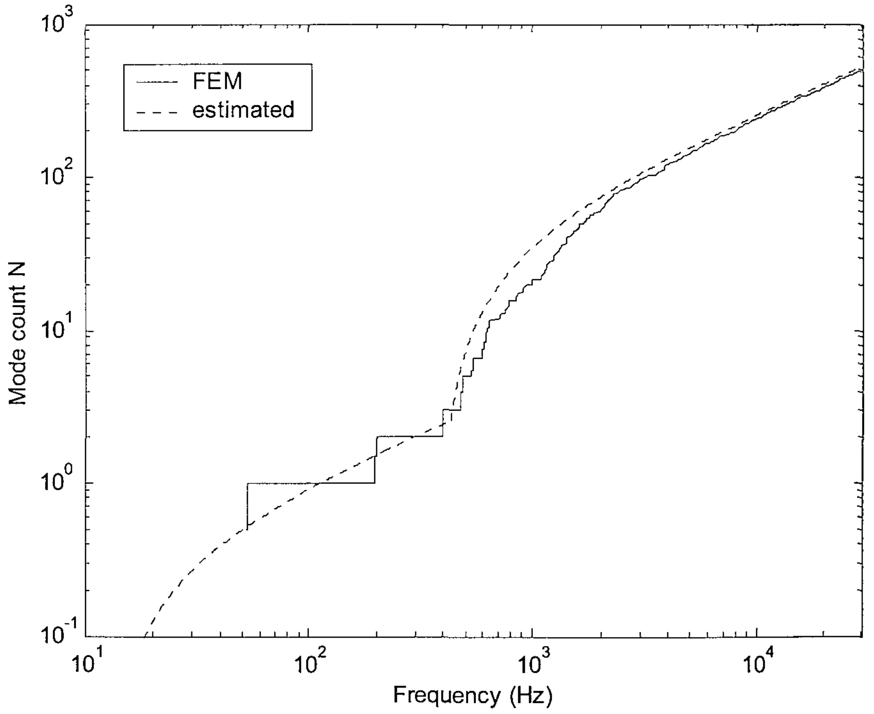

Figure 3.31 Mode count of the extruded section for the whole floor. (simple support condition supposed between beam segments).

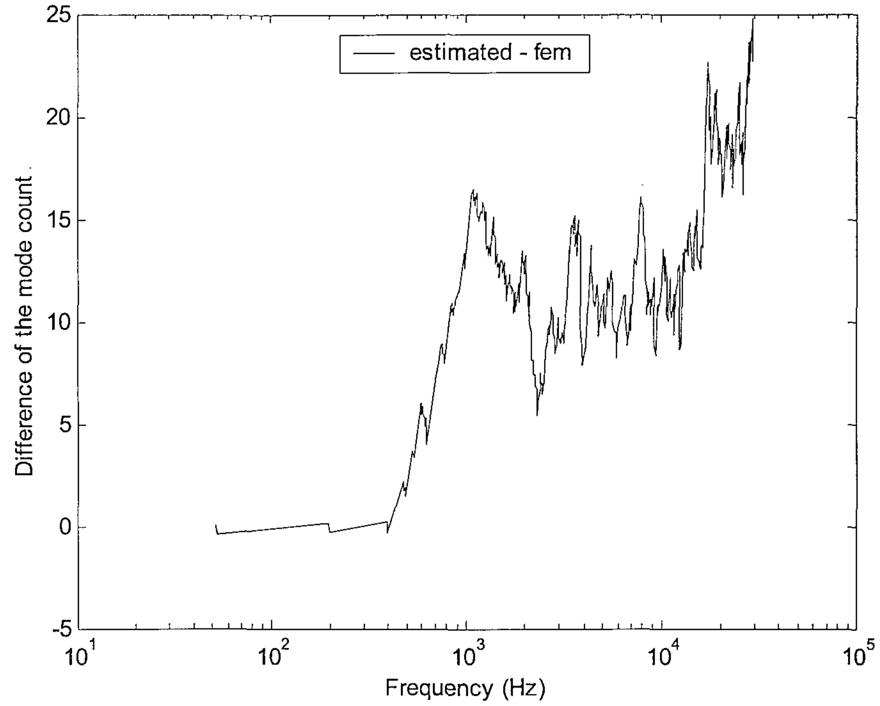

Figure 3.32 The difference between the estimated and FEM mode count. (simple support condition supposed between beam segments).

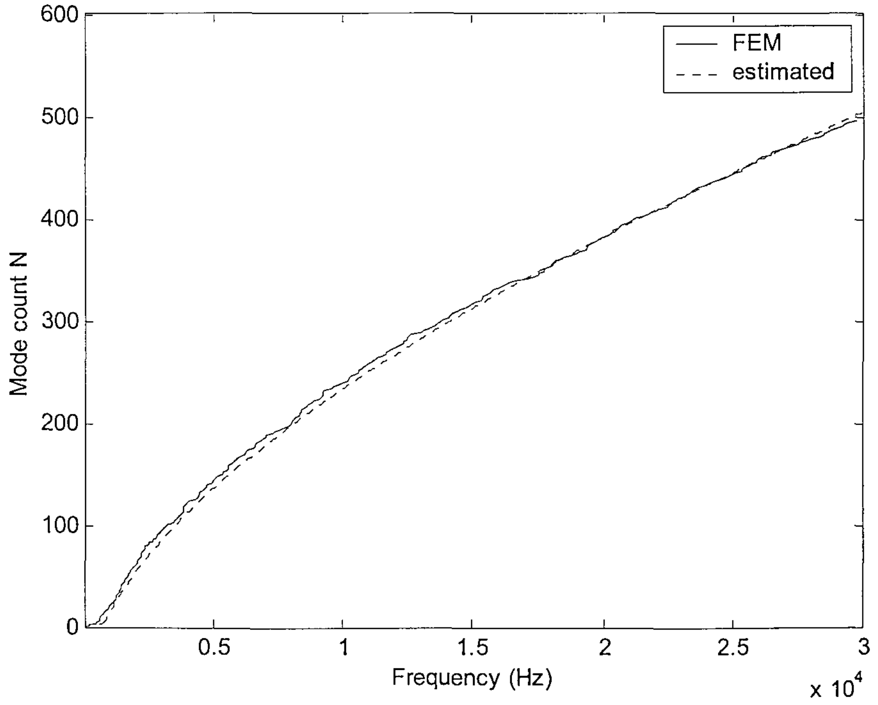

Figure 3.33 Mode count of the extruded section for the whole floor. (fixed conditions supposed between beam segments).

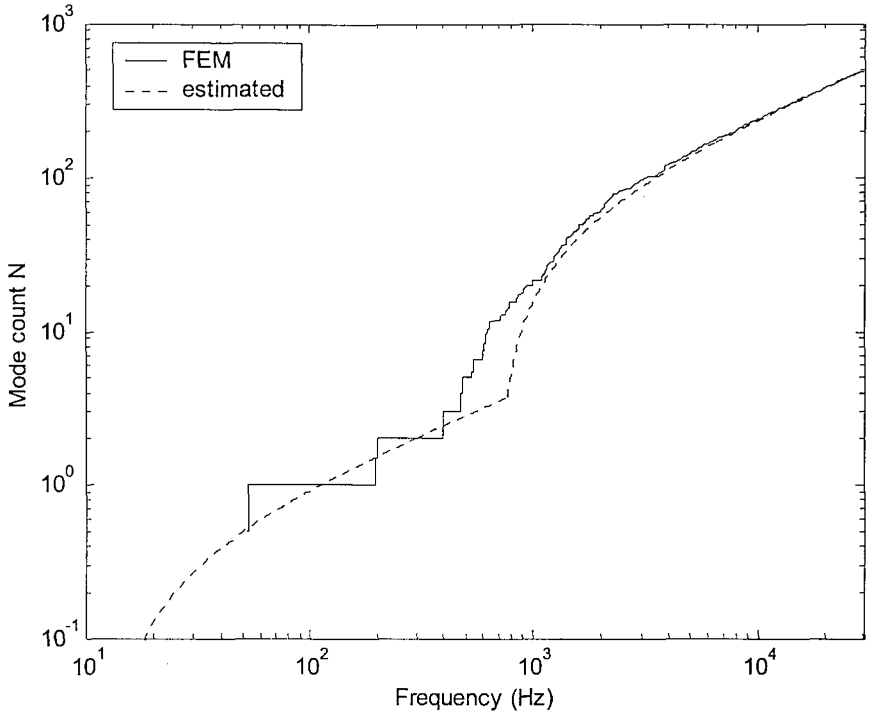

Figure 3.34 Mode count of the extruded section for the whole floor. (fixed conditions supposed between beam segments).

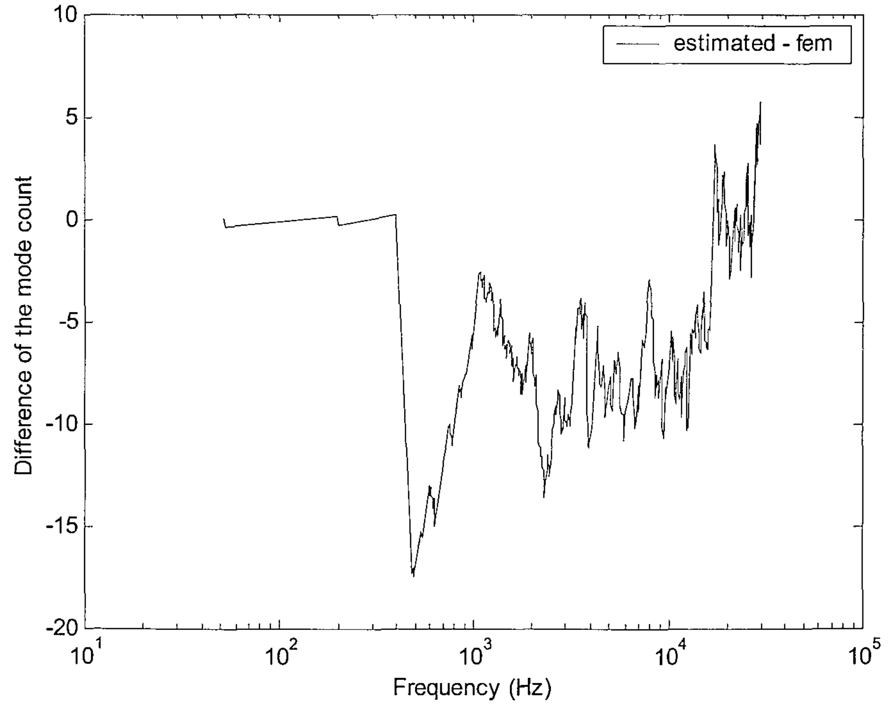

Figure 3.35 The difference between the estimated and FEM mode count. (fixed conditions supposed between beam segments).

It can be concluded that the actual constraint between beam segments of the extruded section is somewhere between simply supported and fixed conditions. From the difference between the estimated value and that from the FEM, the fixed conditions are more appropriate to the real situation than simple supports for frequencies above 1kHz, but at lower frequencies 400 to 700Hz, the simple support is a better approximation. The simple support also gives a better approximation to the frequency f_{local}.

This shows that the conclusion drawn from the one-dimensional system consisting of a single line of segments with either intermediate simple supports or fixed constraints cannot provide a satisfactory agreement when it is applied in a complicated real structure, the extruded section. The extruded section is constructed of a set of beam segments, each of which is coupled with its neighbouring segments. The coupling degrees of freedom include longitudinal and transverse displacement and rotation. For such a multi-coupled system, further separate investigations are really required.

Equations (3.142) and (3.145) is theoretically valid at frequencies which are sufficiently high that the first modes of all beam segments have occurred. At low and mid frequency, the local modes occur only on those relatively wide beam segments. Therefore those relatively narrow strips and their corresponding constraints should not be taken into account for the use of equations (3.142) and (3.145). Alternatively, the mode count for the local modes can be rewritten as

$$N_l = \sum_{i=1}^{m} \max\begin{pmatrix} N_i \\ 0 \end{pmatrix} \tag{3.146}$$

where N_i is the mode count of the ith beam segment. N_i may have a negative value at low frequencies, especially for the relatively narrow strips.

For simple support, $$N_i = \frac{kl_i}{\pi} - \frac{3}{4} + \frac{3}{4m} \tag{3.147}$$

For fixed condition, $$N_i = \frac{kl_i}{\pi} - 1 + \frac{1}{m} \tag{3.148}$$

Figure 3.36 presents the results calculated using equations (3.147) and (3.148). The estimated mode count using fixed conditions between the beam segments gives a better agreement with the FE result for frequencies between 500 and 1k Hz. Using simple support overestimates the mode count in this frequency range due to its overestimate of the cut-on frequencies for the beam segments. The result from the FE model still lies between two predicted curves. This shows again that the actual constraints for the beam segments are somewhere between the simple support and the fixed condition.

The application of equations (3.147) and (3.148) is more complex one as it involves the actual widths of the beam segments. However, it is more important to include this type of analysis for the three-dimensional panel as for each cut-on there is a whole series of modes rather than just one for the beam. This type of analysis will be used in Chapter 4 to consider the mode count of an extruded panel in a three-dimensional model.

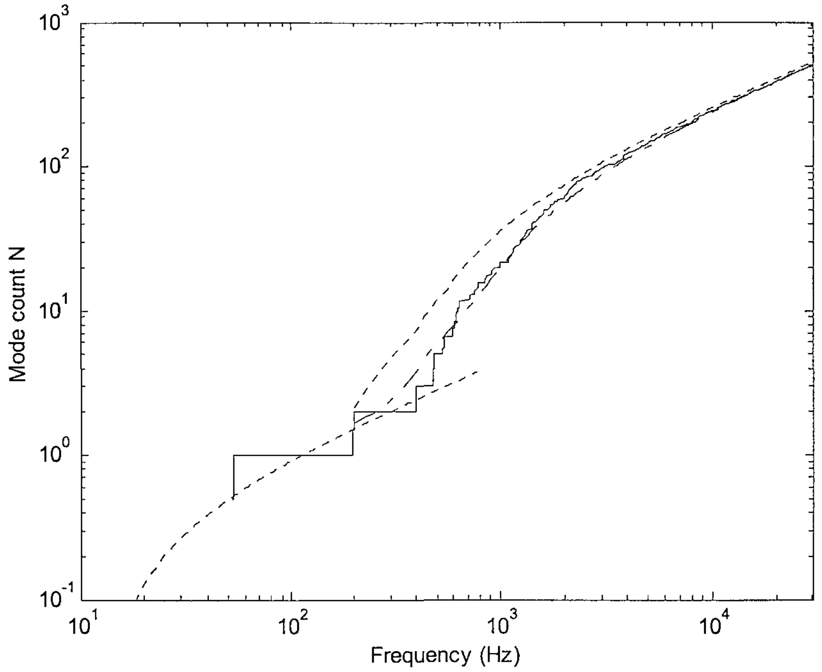

Figure 3.36 Mode count of the extruded section for the whole floor.
(— FEM; – – – using simple supports; ·—· fixed conditions.)

3.5.2.5 Frequency-dependent δ_{BC}

Nevertheless the boundary condition constant δ experienced by the beam segments can be identified through rearranging equation (3.144). The actual mode count is given by

$$N = N_L + N_g + N_l = \frac{k_L l_{tot}}{\pi} + \frac{k_{Bg} L}{\pi} - \delta_{BCg} + \frac{k_B l_{tot}}{\pi} - (m-1) \times \delta_{BC} \qquad f \geq f_{local}$$

If the mode count obtained from the FEM model is substituted into the left-hand of the above equation, the δ_{BC} can be calculated by

$$\delta_{BC} = \frac{\left(N_{FEM} - \frac{k_L l_{tot}}{\pi} - \frac{k_{Bg} L}{\pi} + \delta_{BCg} - \frac{k_B l_{tot}}{\pi} \right)}{(m-1)} \qquad f \geq f_{local} \qquad (3.149)$$

The results of equation (3.149) are presented in Figure 3.37. It can be seen that the constant of the boundary conditions varies with frequency. For frequencies between 500Hz and 1000Hz, δ roughly changes from 0.75 to 0.95. This change might explain the disagreement between 500Hz and 1000Hz in the prediction of the mode count by using fixed or pinned boundary conditions. The pinned boundary conditions have a better agreement in the prediction for the frequencies from 500Hz to 700Hz because δ is close to 0.75 in this frequency range. Both cases give disagreement from 700Hz to 1000Hz because δ is between 0.75 and 1. Above 1000Hz, δ fluctuates around a mean value of about 0.9, which is closer to a fixed boundary condition. Above 16kHz, the estimated value of δ exceeds 1 but it should be noted that at these high frequencies the wavelength of the global modes becomes shorter than twice the length of an individual beam segment, so that the model for global modes becomes inappropriate. This will affect this estimate.

During the study of δ, it has been found that the results are very sensitive at high frequency to the value of κ used for the global modes. It is also noted that the model of an Euler-Bernoulli beam for the global modes is not appropriate. Figure 3.38 shows the result obtained from different values of κ and the Euler-Bernoulli beam. Above 7kHz, the result from $\kappa = 0.1$ would not be appropriate as $\delta > 1$. Between 1kHz to 16kHz, the average result of δ for $\kappa = 0.2$ can be approximated to be 0.9, shown by the solid line.

It may be noted that the concept of a frequency-dependent boundary condition is consistent with the cases of a mass or stiffness considered earlier, although in the present case δ increases with increasing frequency whereas in the previous cases δ decreases with increasing frequency.

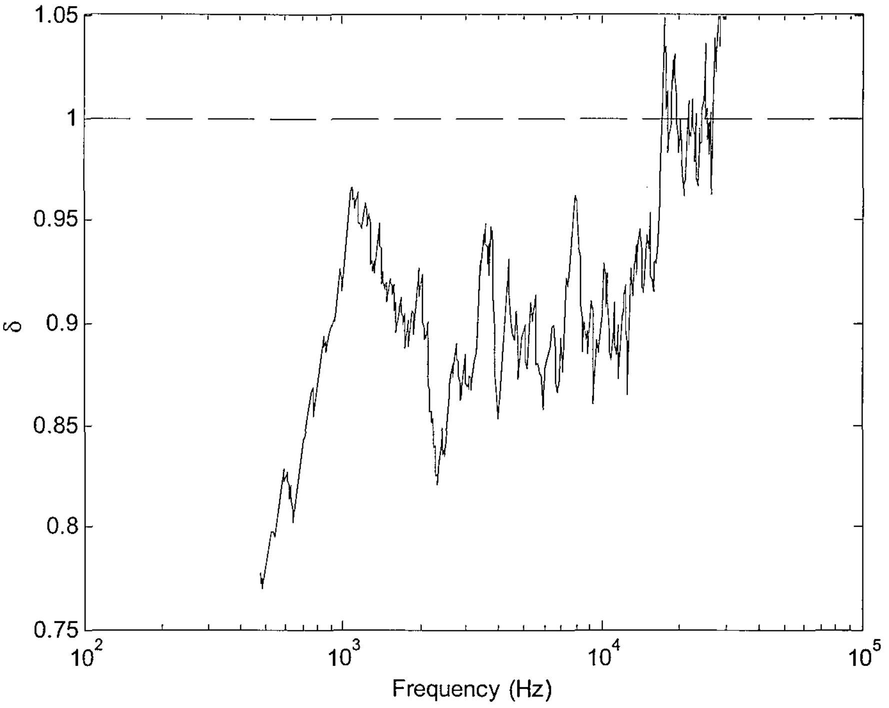

Figure 3.37 Constants of boundary conditions as a function of frequency.

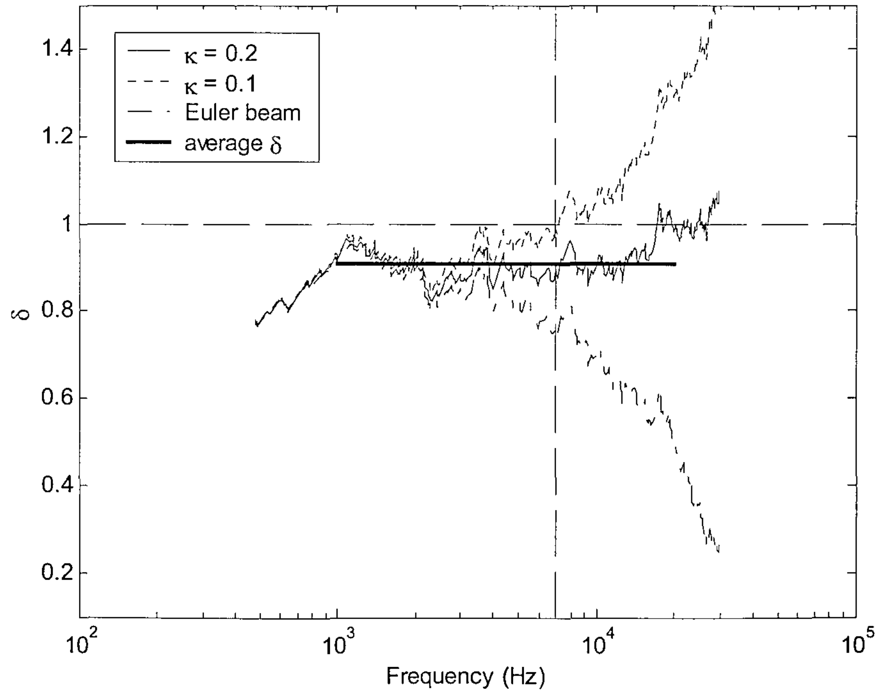

Figure 3.38 The result of δ obtained from different models.

3.5.3 MODAL DENSITY AND DRIVING-POINT MOBILITY

In practice, the spatially averaged driving point mobility for a complicated structure is required since it can be used to calculate the power input to the system. Cremer and Heckl [35] give the following approximate expression to calculate the frequency band averaged real part of the driving point mobility

$$\mathrm{Re}\{Y\} = \frac{\pi}{2m} n(\omega) \tag{3.150}$$

where m is the mass of the system and $n(\omega)$ is the modal density of the system.

The modal density is the slope of the mode count function against frequency. In the case of the extruded section, although the mode count for local modes is different from the single equivalent beam with the same total length as all the beam segments, the slope (modal density) at frequencies above 1kHz is similar. Using this idea, the modal density can be approximately obtained by the differentiation of equation (3.144). Equation (3.144) is given by

$$N = N_L + N_g + N_l = \begin{cases} \dfrac{k_L L}{\pi} + \dfrac{k_{Bg} L}{\pi} - \delta_{BCg} & f < f_{local} \\ \dfrac{k_L L}{\pi} + \dfrac{k_{Bg} L}{\pi} - \delta_{BCg} + \dfrac{k_B l_{tot}}{\pi} - (m-1) \times \delta_{BC} & f \geq f_{local} \end{cases} \tag{3.151}$$

where $k_B = \omega^{\frac{1}{2}} \left(\dfrac{\rho h}{E'I} \right)^{\frac{1}{4}}$ is the wavenumber of bending vibration of the beam segment, k_{Bg} is the wavenumber of the global bending vibration, l_{tot} is the total length of the beam segments of the extruded section and $k_L = \dfrac{\omega}{c_L}$ is the wavenumber of longitudinal vibration.

The modal density of the extruded section now can be given by

$$n(\omega) = \frac{dN}{d\omega} = \begin{cases} \dfrac{L}{c_L \pi} + \dfrac{k_{Bg} L}{2\pi\omega} & f < f_{local} \\ \dfrac{L}{c_L \pi} + \dfrac{k_{Bg} L}{2\pi\omega} + \dfrac{k_B l_{tot}}{2\pi\omega} - (m-1)\dfrac{d\delta_{BC}}{d\omega} & f \geq f_{local} \end{cases} \tag{3.152}$$

which includes four components: longitudinal, global bending, local bending and boundary conditions experienced by all beam segments. The first two items have only a small contribution to the modal density above f_{local} since the local bending dominates the whole system above this frequency. δ_{BC} is represented by a function of frequency as shown in Figure 3.37. From 500Hz to 1kHz, δ_{BC} changes approximately linearly from 0.78 to 0.93. At frequencies above 1kHz, δ_{BC} is approximately constant. Therefore, $\frac{d\delta_{BC}}{d\omega}$ or $\frac{d\delta_{BC}}{df}$ can be approximately expressed by

$$\frac{d\delta_{BC}}{df} = 2\pi \frac{d\delta_{BC}}{d\omega} = \begin{cases} 0.15/500 & 500\text{Hz} < f < 1\text{kHz} \\ 0 & f > 1\text{kHz} \end{cases} \tag{3.153}$$

The result calculated from equation (3.152) is compared with that from the FEM modal analysis, which is obtained by counting the number of the modes in each one-third octave band. This is presented in Figure 3.39. There are actually no modes found in the bands 100, 125, 160, 250 and 315 Hz from the FE results so that the modal density from the FEM for the bands central frequency at 200 and 400 Hz appear higher than the predicted result. The curves presented in Figure 3.39 are in terms of $n(f)$, which is given by

$$n(f) = 2\pi n(\omega) \tag{3.154}$$

Figure 3.39 presents the estimated modal densities by using both the Timoshenko and Euler beam for the global vibration. The estimated results give a good agreement above f_{local} = 470 Hz. It can be noted that only some slight differences occur between the two beam models. This demonstrates that the modal density is not sensitive to which model is chosen for the global vibration. As the modal density above 500Hz is dominated by the local vibration.

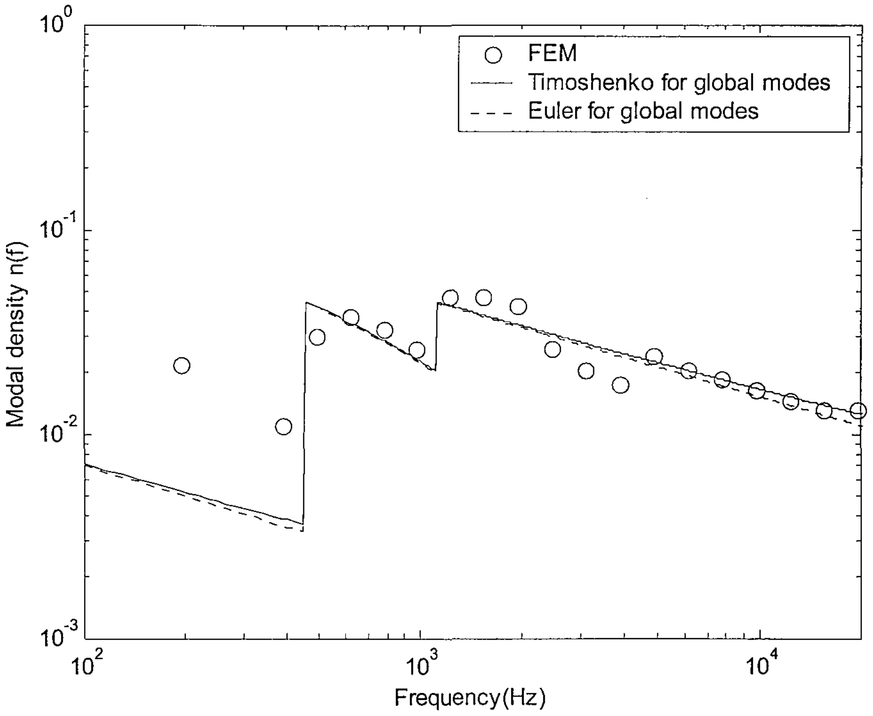

Figure 3.39 The modal density of the extruded section.

The real part of the driving point mobility can thus be calculated approximately from equation (3.150) by using equation (3.152). The estimated result is compared with that from the FEM model in Figure 3.40. The result shows a good agreement in the frequency range above 500Hz where local modes occur. The FEM analysis is based on the average of the real part of the driving point mobility calculated for 27 points on the upper plate of the extruded section, in which 17 points are located on the beam segments away from the joints and the others are at joints. The value of the damping loss factor used is 0.2. There are large variations between the mobilities at these various points, as shown by the range in Figure 3.40. The estimated result based on equation (3.150) is reliable for the mean value. Because of the truncation of the modal summation in the FEM analysis, a small systematic difference occurs at frequencies near to the upper limit. In the analysis of the FEM model, a smaller value of the damping loss factor 0.06 is also calculated. The results do not have too much difference from those obtained using a value of 0.2, as shown in Figure 3.41.

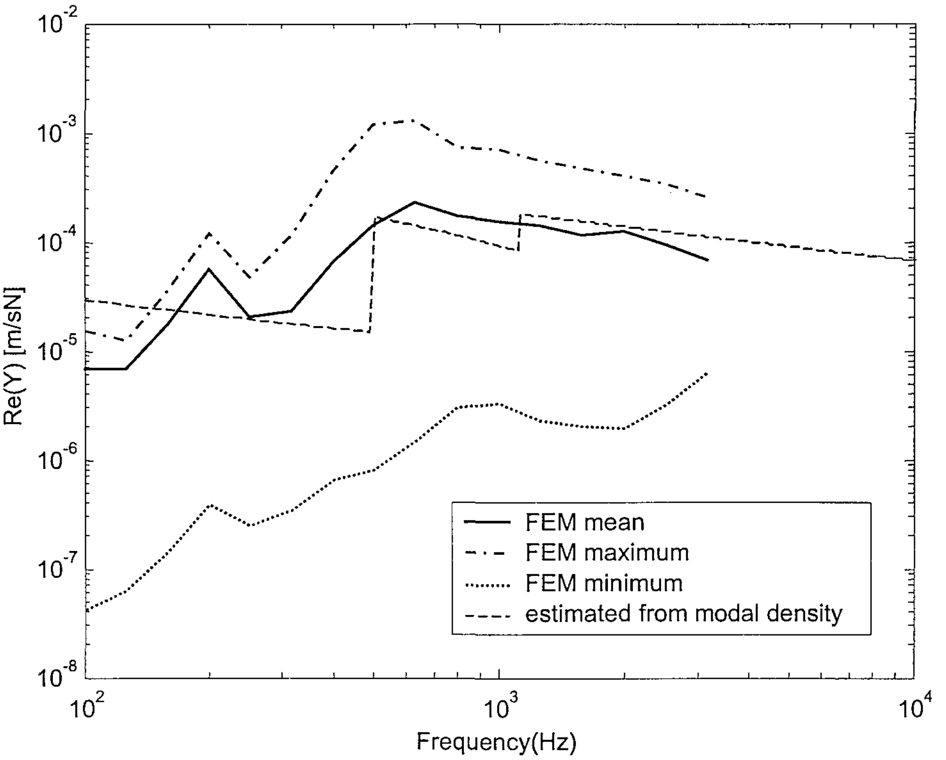

Figure 3.40 Comparison between the estimated mobility of extruded section and result from FEM.

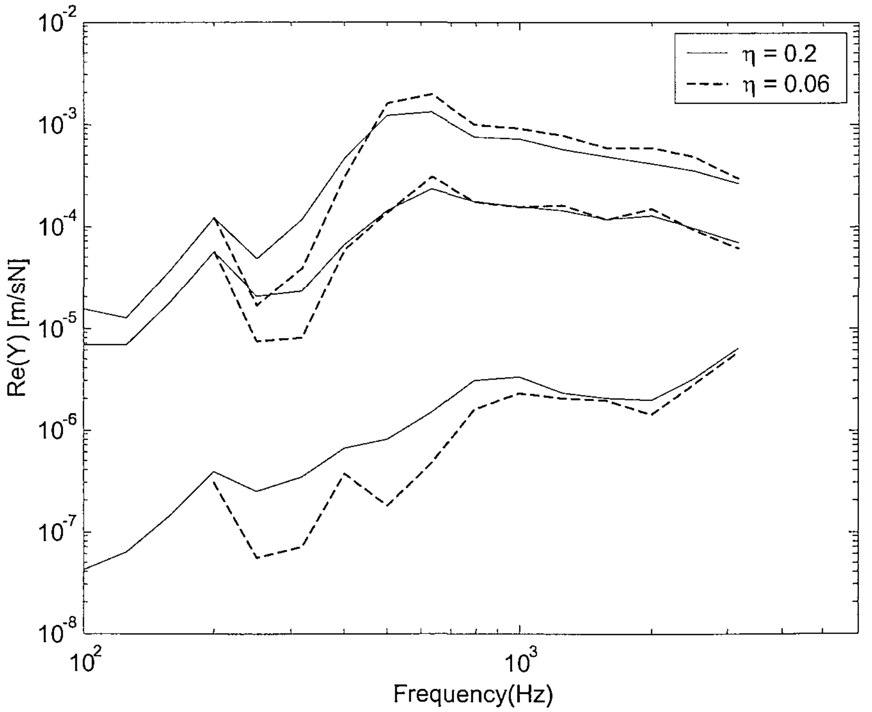

Figure 3.41 Mobility of extruded section obtained from FEM using different damping values.

It may be anticipated that the mobility at the joint points will be much lower than at intermediate points because their responses depend only on the global vibration. Using the equivalent beam for the global modes, the mobility can also be evaluated by [35]

$$\mathrm{Re}\{Y\} = \frac{k_{Bg}}{4m'\omega} \tag{3.155}$$

where k_{Bg} is the wave number of the global bending vibration and m' is the mass per unit length of the equivalent beam.

The results of equation (3.155) are presented in Figure 3.42. Compared with the results obtained from the FEM analysis, the Euler-Bernoulli beam model is not appropriate. Therefore, the Timoshenko thick beam should be introduced at high frequency for global modes. For a thick beam, the mobility can be calculated by the following formula from [35][2]

$$Y = \frac{k_{Bg}}{2\omega m'(1+j)} \frac{\left(\sqrt{1-\frac{E'}{G^*}\left(\frac{{k_{Bg}}^2 I_x}{A}\right)^2} + j\frac{E'}{G^*}\frac{{k_{Bg}}^2 I_x}{A}\right)}{\sqrt{\sqrt{1-\frac{E'}{G^*}\left(\frac{{k_{Bg}}^2 I_x}{A}\right)^2} + j\left(\frac{E'}{G^*}+1\right)\frac{{k_{Bg}}^2 I_x}{2A}}} \tag{3.156}$$

where $G^* = \kappa G$, in which $\kappa = A_e/A$ is the Timoshenko shear coefficient and G is the shear modulus. The shear modulus is given by $G = \dfrac{E}{2(1+\mu)}$. A_e is the cross-sectional area effective in shear and is unknown for the extruded section because of the irregular cross-section. A is the total area of the cross-section. I_x is the second moment of area of the equivalent beam. The wavenumber k_{Bg} in equation (3.156) is that applying to the Euler-Bernoulli beam formulation.

In order to use equation (3.156), a suitable value for κ is needed. Several values of κ have been used in (3.156), and the results are compared with those from the FEM model. Figure 3.42 shows the results. It can be seen that 0.1 gives the closest agreement. In section 3.5.2.4, however, the different values of κ lead to different results in the prediction of the mode count. $\kappa = 0.1$ only gives physically meaningful results below 7kHz. $\kappa = 0.2$

---

[2] Note that a typing error in [35] has been corrected and that $h^2/12$ has been replaced by I_x/A.

gives a more acceptable result for the frequency in the whole audio range and has therefore been adopted. It gives reasonable agreement in Figure 3.42 also.

From Figure 3.42, it can be seen that the mean mobility of the whole system at low frequency is similar to that at the joint locations, as it is governed by global vibration. At high frequency, the vibration of whole system is dominated by local modes and the mobility can be predicted from the local modes. The global modes have only a small contribution to the modal density of the whole system here. The formula for the thick beam with a suitable value of κ gives a better agreement to the mobility at the joint locations. This confirms that the thick beam model is more appropriate than the thin beam model above 200Hz.

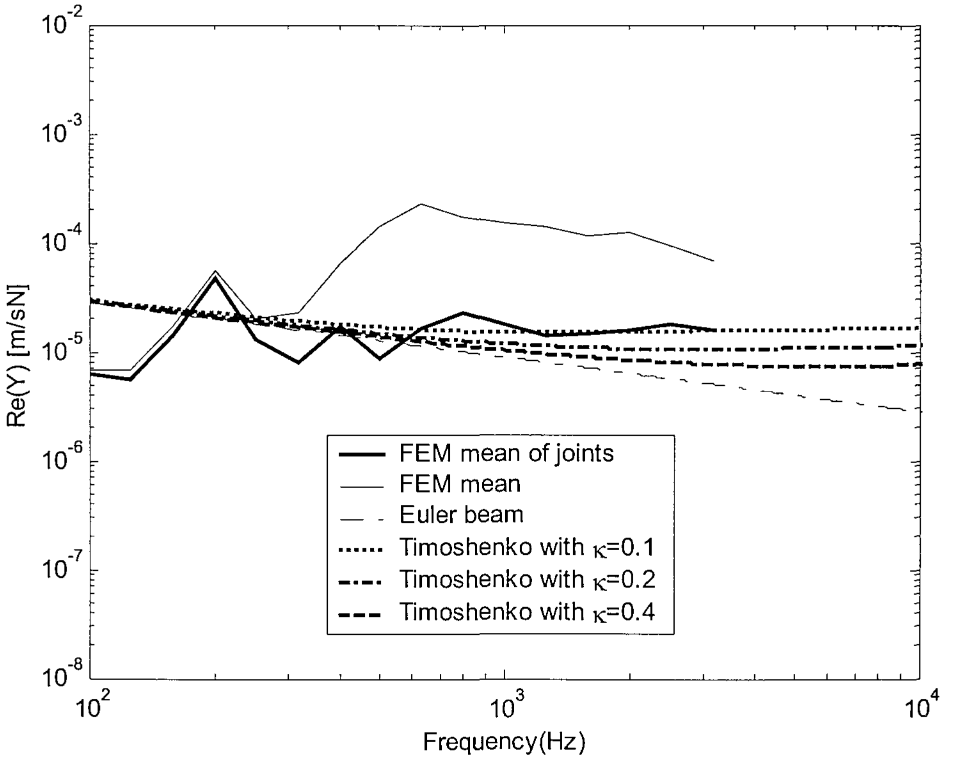

Figure 3.42 Mobility of the joint points from the FEM and estimated values.

3.6 CONCLUSIONS

The mode count of one-dimensional subsystems has been investigated. A simple relationship has been shown between the mode count and the boundary conditions. A free boundary has no effect on the mode count of the system. For longitudinal vibrations, a fixed boundary constraint adds to the mode count by –½. For bending vibrations, which have two coupling degrees of freedom, a sliding constraint adds to the mode count by –¼, a simple support condition by –¾ and a fixed boundary constraint by -1. For more general boundary conditions, here in particular a point mass and a point spring, the boundary effect on the mode count is frequency-dependent. A mass tends to be similar to a free condition at low frequency and to a simple support at high frequency. A spring, conversely, tends to a simple support at low frequency and to a free condition at high frequency.

For multi-beam systems in a single line, the mode count of the system can be estimated by the mode count of a long beam without any extra constraints minus the sum of the constraint constants. This conclusion for the multi-beam system leads to an approximation that can be used for the investigation of an extruded section. Although small errors occur in the prediction of the mode count for the extruded section, as the constraints are neither simple supports nor fully fixed, the modal density and average driving point mobility derived from this model show good agreement with FEM analyses. This demonstrates that the modal density is largely independent of the boundary conditions whereas the mode count is dependent on the boundary conditions for one-dimensional systems.

For complicated structures like the extruded plate at high frequencies, a point source of excitation is likely to be affected very little by the boundary conditions of the whole system on average. The response of the extruded section at high frequency (above f_{local}) can be predicted by the modal character of the beam segment. At low frequency, the global vibration is dominant, which can be represented as an equivalent beam.

The concepts and results developed in this Chapter have been used in investigations into the mode count, modal density and the response of the section of the extruded plate without damping. They may have use in analyses of other complicated structures. The next step will be to extend the analysis to a two-dimensional plate system, which allows the three-dimensional extruded plate to be modelled.

4 THREE-DIMENSIONAL MODEL OF EXTRUDED PLATES

4.1 INTRODUCTION

The relationship between the mode count and boundary conditions for one-dimensional structures has been investigated in the Chapter 3. Based on the results obtained, a two-dimensional model for the mode count and modal density of the extruded section, consisting of one-dimensional elements, has been given. In this Chapter, the effect due to boundary conditions on the mode count for two-dimensional structures, particularly rectangular plates, will be investigated. Then a three-dimensional model, composed of two-dimensional plate elements, for the mode count and modal density of extruded panel will be given.

4.2 MODE COUNT OF RECTANGULAR PLATES

The mode count of a rectangular plate with a wavenumber less than a given value of k is given by Hart and Shah [32] and Cremer, Heckl and Ungar [35] as

$$N = \frac{k^2 S}{4\pi} \tag{4.1}$$

where N is the mode count, k is structural wavenumber and S is the area of the plate under consideration.

Lyon and DeJong [37] give an equivalent expression

$$N \simeq \frac{k^2 S}{4\pi} + \Gamma_{BC} P k \tag{4.2}$$

where S is the area of system, P is the perimeter length and Γ_{BC} depends on the boundary conditions. The first term in equation (4.2) is same as equation (4.1).

The modal density of the system can be obtained by the differentiation of equation (4.2). This yields a term Γ'_{BC} in the expression for the modal density. It is suggested in [37] that although the quantity Γ'_{BC} can often be determined for an isolated system, it is best to assume it to be zero for connected systems because the effective boundary conditions change with frequency. Therefore the modal density of a plate is found to be a constant:

$$n(\omega)=\frac{\partial N}{\partial k}\cdot\frac{1}{c_g}=\frac{kS}{2\pi c_g}+\frac{\Gamma'_{BC}P}{c_g}\approx\frac{kS}{2\pi c_g}=\text{Constant} \tag{4.3}$$

as $k \propto \omega^{1/2}$ and $c_g \propto \omega^{1/2}$.

4.2.1 NATURAL MODES AND MODE COUNT

Before giving a detailed calculation of the mode count of a given rectangular plate, it is instructive to refer to the basic knowledge concerning the flexural vibration of a plate. The equation of motion for flexural waves in an infinite plate is

$$B\left(\frac{\partial^4 w}{\partial x^4}+2\frac{\partial^4 w}{\partial^2 x\partial^2 y}+\frac{\partial^4 w}{\partial y^4}\right)+\rho h\frac{\partial^2 w}{\partial t^2}=0 \tag{4.4}$$

where w is the out-of-plane displacement, B is the flexural rigidity, given by $B=\dfrac{Eh^3}{12\left(1-\mu^2\right)}$, ρ is the density, h is the thickness, E is Young's modulus and μ is the Poisson's ratio.

Harmonic plane wave solutions have the form

$$w(x,y,t)=e^{-jk_x x}e^{-jk_y y}e^{j\omega t} \tag{4.5}$$

where k_x and k_y are the trace wavenumbers in the x and y directions.

Substituting equation (4.5) into (4.4) shows that the free wave solution satisfies

$$B\left(k_x^2+k_y^2\right)^2=\rho h\omega^2 \tag{4.6}$$

The plate free wavenumber can be defined as

$$k=\sqrt{k_x^2+k_y^2}=\left(\frac{\rho h\omega^2}{B}\right)^{1/4} \tag{4.7}$$

For a finite plate, the natural modes will occur due to wave reflections at boundaries. Considering a rectangular plate of dimensions a and b as shown in Figure 4.1, as for the case of a beam, the phase-closure principle can be applied to it to find the natural modes.

By ignoring the effect of near-field waves across the plate, the response of a rectangular plate may be assume to be composed of four free wave components. This is given by

$$w(x,y,t)=\left(A_1e^{-jk_xx}e^{-jk_yy}+A_2e^{jk_xx}e^{-jk_yy}+A_3e^{jk_xx}e^{jk_yy}+A_4e^{-jk_xx}e^{jk_yy}\right)e^{j\omega t} \tag{4.8}$$

where $k_x = k\cos\theta$ and $k_y = k\sin\theta$, with angle θ the heading of the wave, and k wavenumber determined by equation (4.7).

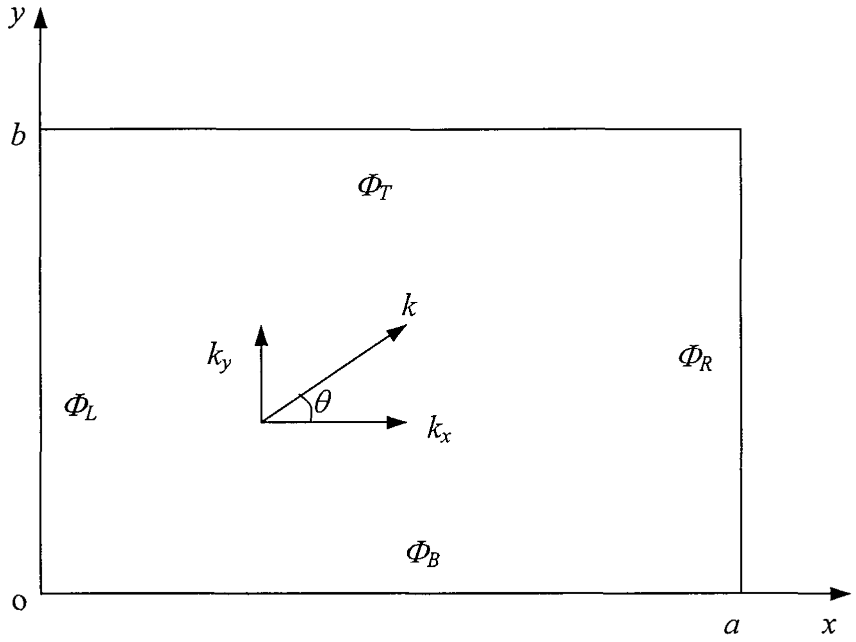

Figure 4.1 Illustration of the rectangular plate under consideration

The phase changes at the boundaries can be defined for each edge: ϕ_L, ϕ_R for reflection in the x direction at the left and right edges and ϕ_T, ϕ_B for reflection in the y direction at the top and bottom edges. The natural modes will occur when

$$2k_xa+\phi_L+\phi_R=2m\pi \tag{4.9}$$

$$2k_yb+\phi_T+\phi_B=2n\pi \tag{4.10}$$

for integer values of m and n. These results are arbitrary to within a multiple of 2π. This corresponds to Bolotin's asymptotic method [30], see also [93].

The natural frequency of the mode (m, n) can be found by substituting these values of k_x and k_y into equation (4.7)

$$\omega_{mn}=\left(\frac{B}{\rho h}\right)^{\frac{1}{2}}\left[k_x^2+k_y^2\right]=\left(\frac{B}{\rho h}\right)^{\frac{1}{2}}\left[\left(\frac{m\pi}{a}-\frac{\phi_L+\phi_R}{2a}\right)^2+\left(\frac{n\pi}{b}-\frac{\phi_T+\phi_B}{2b}\right)^2\right] \tag{4.11}$$

These natural modes can also be plotted in wavenumber *k*-space, as illustrated in Figure 4.2. Every point corresponds to one mode (*m*, *n*). The component wavenumbers in the two directions are given by

$$k_x = \frac{m\pi}{a} - \frac{\phi_L + \phi_R}{2a}, \quad k_y = \frac{n\pi}{b} - \frac{\phi_T + \phi_B}{2b} \tag{4.12}$$

It can be seen that the variation of the wavenumber in each direction from one mode to the next is constant, namely π/a and π/b. The boundary conditions effectively only influence the distance to the axes, not the separation between points. This characteristic is very useful allowing the use of *k*-space integration to calculate the mode count of the rectangular plate.

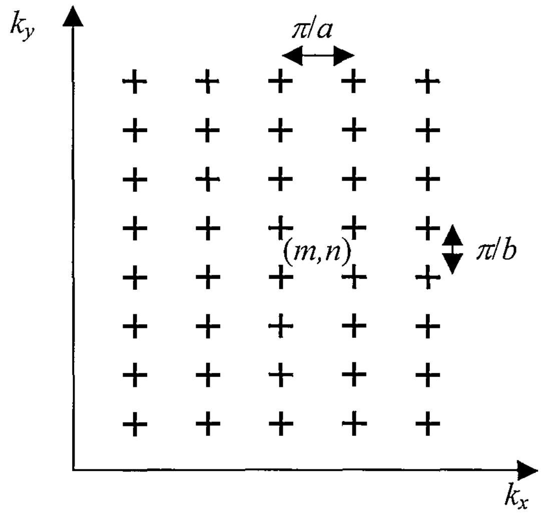

Figure 4.2 Illustration of the *k*-space of the natural modes of a rectangular plate.

4.2.1.1 Simply supported plate

If all four edges of the plate are simply supported, the phase change at each edge is π. The phase-closure principle gives

$$\begin{aligned} k_x a &= m\pi \\ k_y b &= n\pi \end{aligned} \tag{4.13}$$

The natural frequencies are given by

$$\omega_{mn} = \left(\frac{B}{\rho h}\right)^{\frac{1}{2}} \left[\left(\frac{m\pi}{a}\right)^2 + \left(\frac{n\pi}{b}\right)^2\right] \tag{4.14}$$

In this case the phase closure principle gives the exact result as no near-field waves are generated at boundaries due to the wave reflections. The *k*-space plot of the modes is presented in Figure 4.3. The mode count below a particular frequency can be obtained by finding the number of modes located within the quarter circle of radius *k*. This is given by

$$N(k) = \frac{\int_S dk_x dk_y}{\Delta k_x \Delta k_y} \tag{4.15}$$

where S is the area of integration, Δk_x and Δk_y are the changes in component wavenumbers from one mode to the next, ie π/a and π/b.

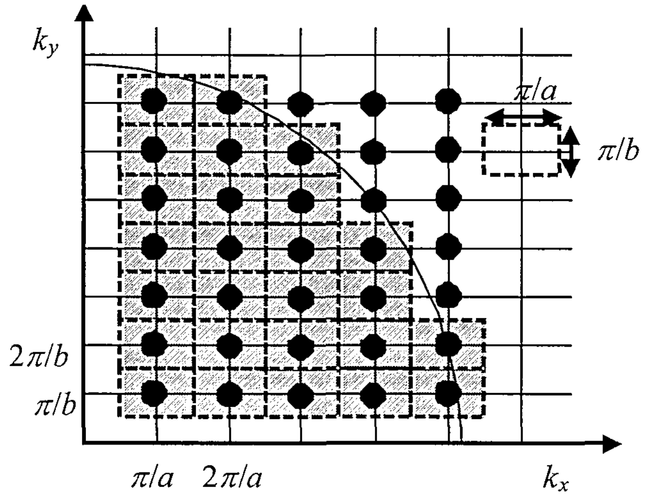

Figure 4.3 The modes of simply supported rectangular plate shown in *k*-space.

Equation (4.15) can be evaluated as

$$N(k) = \frac{\int_0^k \int_0^{\pi/2} k d\theta dk}{\Delta k_x \Delta k_y} = \frac{\frac{1}{4}\pi k^2}{\Delta k_x \Delta k_y} \tag{4.16}$$

In considering the average area occupied by each mode in *k*-space, it can be noted that each mode occupies an area of $\pi/a \times \pi/b$ and the area of two strips along the axes should not be taken into account by integration of equation (4.16). This is illustrated in Figure 4.3. Therefore equation (4.16) should be modified so that the average mode count below wavenumber k is given by

$$N(k) = \frac{\frac{1}{4}\pi k^2 - k(\frac{\pi}{2a} + \frac{\pi}{2b}) + \frac{\pi}{2a}\frac{\pi}{2b}}{\Delta k_x \Delta k_y} \tag{4.17}$$

where Δk_x and Δk_y are given by π/a and π/b.

The final expression for the mode count of a simply supported rectangular plate is

$$N(k) = \frac{k^2 S}{4\pi} - \frac{1}{2}k\left(\frac{a+b}{\pi}\right) + \frac{1}{4} \tag{4.18}$$

or

$$N(k) = \frac{k^2 S}{4\pi} - \frac{kP}{4\pi} + \frac{1}{4} \tag{4.19}$$

where P is the perimeter of the plate.

The first term in equation (4.19) is that is often used in the literature to estimate the mode count for a plate. It can be seen that the result for the mode count of a simply supported plate in equation (4.19) is less than that given by equation (4.1) due to the perimeter term.

Bogomolny and Hugues [41] give this perimeter term as

$$N_p = \beta \frac{P}{4\pi} k \tag{4.20}$$

where $\beta = -1$ for the simple supported plate. It can be seen that the equation (4.19) has the same results as that from equation (4.20) by [41].

To verify the result of equation (4.19), an aluminium plate of dimensions 0.4m×0.3m×0.002m is considered. The natural modes are calculated based on equations from Leissa [94] (see also Appendix C) and then the staircase function of the mode count is plotted. The average mode counts from equation (4.19) and (4.1) are both calculated and plotted for the purpose of comparison. This is presented in Figure 4.4. The differences between the mode count of equations (4.19), and (4.1) and the actual mode count are plotted in Figure 4.5. The values of the actual mode count are given by the top of each stair point minus 0.5 in each case (that is half way between the bottom and top of each vertical line in the staircase function). The average difference between the results from equation (4.19) and the actual average value is only –0.043. However, equation (4.1) has a systematic error increasing as frequency increases although the relative error decreases, which is shown by Figure 4.4.

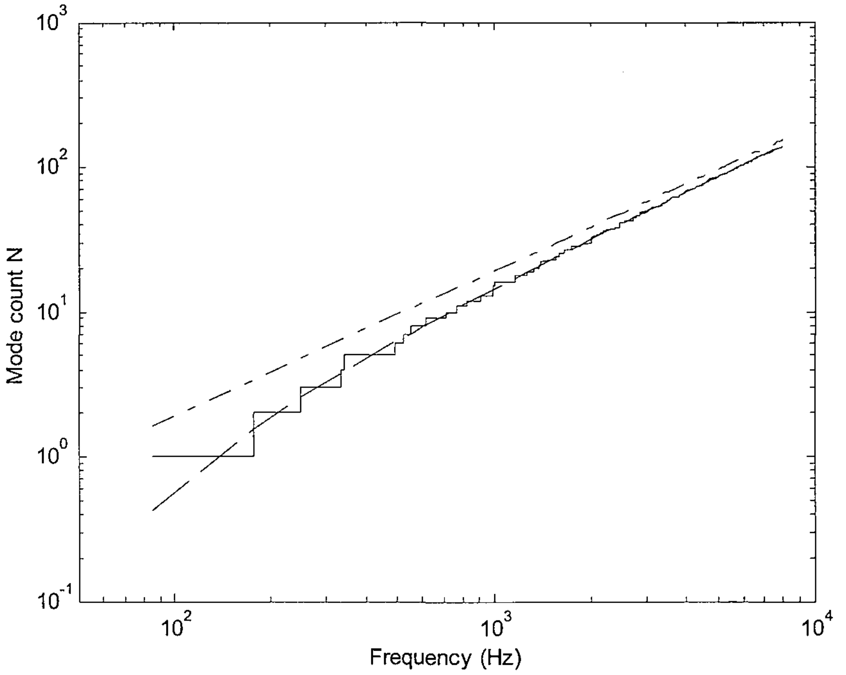

Figure 4.4 Comparison of the mode count for a simply supported aluminium plate 0.4m×0.3m×0.002m. (—, staircase , ---, from (4.19), -·-·-, from (4.1)).

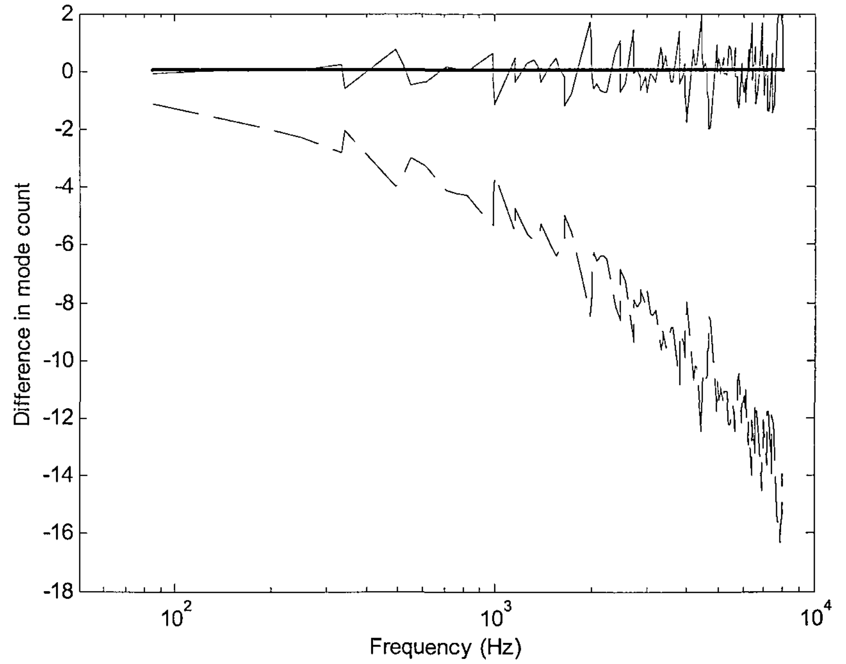

Figure 4.5 Difference between the estimated mode count and the actual result for a simply supported aluminium plate 0.4m×0.3m×0.002m. (—, using (4.19), thick line, average result, -·-·-, using (4.1),)

4.2.1.2 Fully fixed plate

Considering a rectangular plate with fully fixed edges, the natural modes occur approximately when the wavenumbers satisfy

$$k_x a = (m + \frac{1}{2})\pi, \quad k_y b = (n + \frac{1}{2})\pi \tag{4.21}$$

where m, n = 1,2,3, ···. The k-space plot of the natural modes is presented in Figure 4.6.

Based on the equation (4.16) and the concept of the average mode count, the expression for the mode count of a fully fixed rectangular plate can be given by

$$N(k) = \frac{\frac{1}{4}\pi k^2 - k(\frac{\pi}{a} + \frac{\pi}{b}) + \frac{\pi}{a}\frac{\pi}{b}}{\frac{\pi}{a}\frac{\pi}{b}}$$

$$N(k) = \frac{k^2 S}{4\pi} - k\left(\frac{a+b}{\pi}\right) + 1 \tag{4.22}$$

$$N(k) = \frac{k^2 S}{4\pi} - \frac{kP}{2\pi} + 1 \tag{4.23}$$

where P is the perimeter of the plate and S is the area of the plate. In terms of equation (4.20), Bogomolny and Hugues [41] give a more exact value of $\beta = -1.7627598$ for a fully fixed plate. From the present analysis of equation (4.23), β is approximately given as -2.

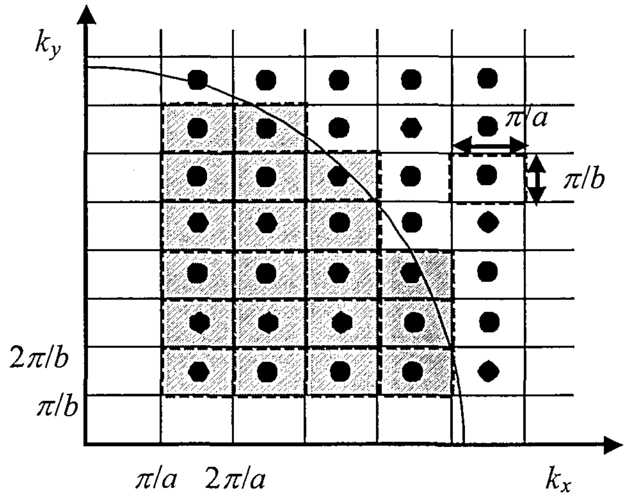

Figure 4.6 The modes of a fully fixed rectangular plate shown in k-space.

Having obtained equation (4.23), it is verified it by comparing it with the analytical solutions. As before an aluminium plate of dimensions 0.4m×0.3m×0.002m is considered. The natural modes can be calculated based on the equation from Leissa [94] (see also Appendix C) and then the staircase function of the mode count can be obtained. Figure 4.7 presents the staircase function and the average mode count from equation (4.23). For comparison, the result from equation (4.1) is also plotted.

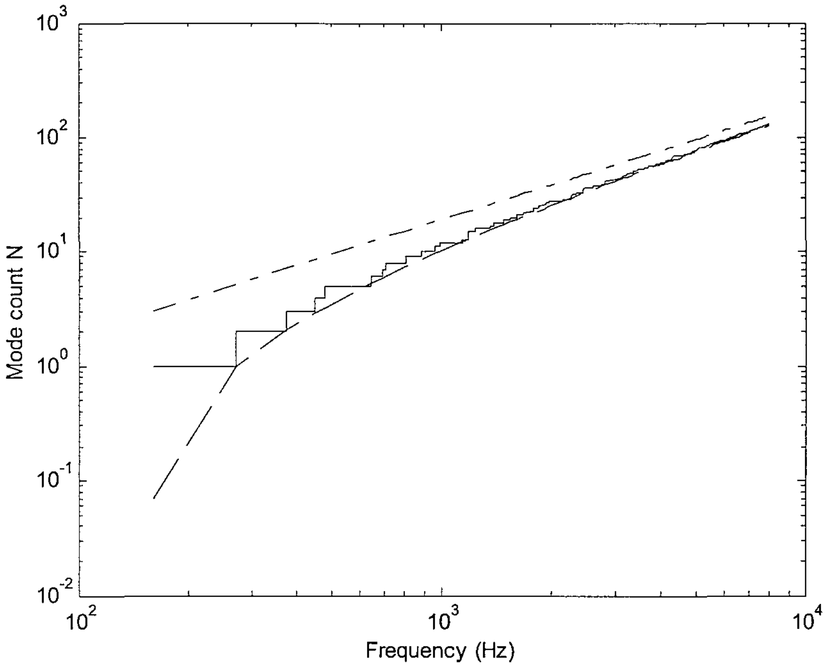

Figure 4.7 Comparison of the mode count for a fully fixed aluminium plate 0.4m×0.3m×0.002m. (—, staircase , ---, from (4.23), -·-·-, from (4.1))

It can be seen that equation (4.23) has a much better agreement with the staircase function than equation (4.1), which results in considerable errors. Figure 4.8 shows the comparison of the difference from the actual result. Compared with the result from equation (4.20) based on $\beta = -1.7627598$ given by Bogomolny and Hugues [41], equation (4.23) has a relatively larger error at high frequencies. The errors from equation (4.23) are caused by approximations made in applying the phase-closure principle from which it is derived. As the near-field waves are neglected in using the phase-closure principle to obtain the natural modes, the solutions for the first few modes and all modes with m=1 or n=1 tend to have larger values than those from the analytical solution. This eventually causes an underestimate of the mode count equation (4.23) by 2 or 3 at high frequencies. Some of the lower natural frequencies derived from the phase-closure principle and the analytical solution are listed in Table 3. These differences are larger than the corresponding difference for one-dimensional systems.

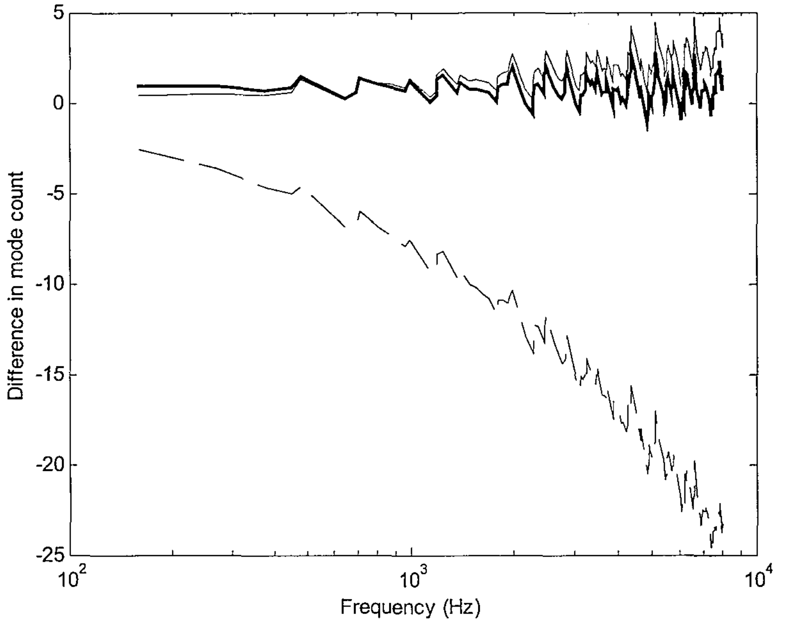

Figure 4.8 Difference between the estimated mode count and the actual result for a fully fixed aluminium plate 0.4m×0.3m×0.002m.

(—, using (4.23), thick line, using (4.20), -·-·-, using (4.1))

Table 3 Comparison of natural frequencies of fully fixed plate from phase-closure and analytical solution

Index of modes (m, n)	Phase-closure	Analytical	Difference (%)
1, 1	192.4	159.7	20.5
2, 1	315.6	269.3	17.2
1, 2	411.4	376.2	9.4
3, 1	500.4	448.5	11.6
2, 2	534.6	476.7	12.1
3, 2	719.3	645.5	11.4
4, 1	739.8	692.7	6.8
1, 3	746.7	704.8	5.9
2, 3	863.0	802.5	7.5
4, 2	965.6	882.5	9.4

4.2.1.3 Free plate

For a plate with four free edges, three rigid body modes should be included. These consist of translation, rotation about the x direction and rotation about y direction. A fourth low frequency mode (not a bending mode) exists in which the plate flexes with opposite corners moving in phase. The natural modes in bending should satisfy approximately

$$k_x a = (m - \frac{3}{2})\pi, \quad k_y b = (n - \frac{3}{2})\pi \tag{4.24}$$

where $m, n = 3, 4, \cdots$.

Corresponding to each rigid mode in one direction (translation or rotation) a set of beam-like modes occur in the other direction. These beam-modes have a similar modal characteristic to a one-dimensional system except that the Poisson ratio effect should be considered. The plate modes, therefore, should include two sets of beam-modes in each direction corresponding to the rigid modes in the other direction. This is shown in a k-space plot in Figure 4.9.

The average mode count hence can be given by

$$N(k) = \frac{\frac{1}{4}\pi k^2 + k(\frac{\pi}{a} + \frac{\pi}{b}) + \frac{\pi}{a}\frac{\pi}{b}}{\frac{\pi}{a}\frac{\pi}{b}} \tag{4.25}$$

$$N(k) = \frac{k^2 S}{4\pi} + k\left(\frac{a+b}{\pi}\right) + 1 \tag{4.26}$$

$$N(k) = \frac{k^2 S}{4\pi} + \frac{kP}{2\pi} + 1 \tag{4.27}$$

In terms of equation (4.20), Bertelsen, Ellegaard and Hugues [42] give $\beta = 1.7125908$ for a free plate. From the present analysis of equation (4.27), β is approximately given as 2.

Equation (4.27) is verified with the analytical solutions from Leissa [94] (see Appendix C). Calculations are performed for the same plate as in previous sections. Figure 4.10 shows the results and Figure 4.11 the differences. It can be seen that equation (4.27) gives a good agreement with the analytical solutions, although there is a small error that increases with frequency. This error is probably also caused by using the phase-closure principle to describe the natural modes of the free plate.

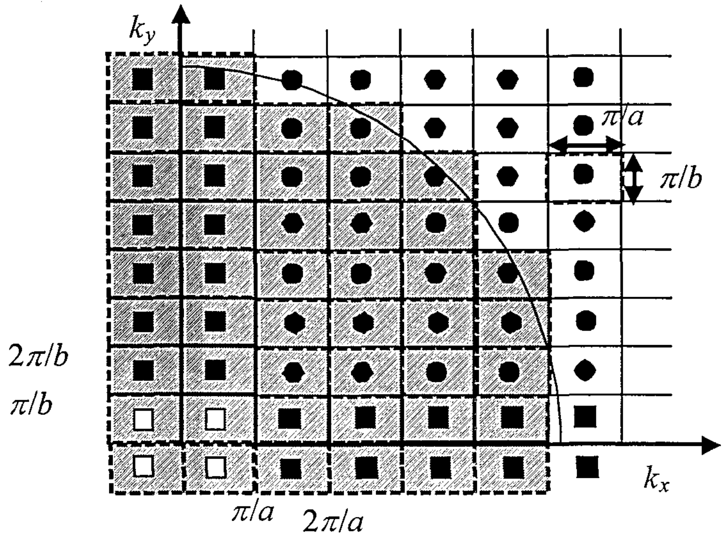

Figure 4.9 The modes of a free plate shown in k-space
(solid square: beam-like mode, square: rigid mode, solid circle: plate mode)

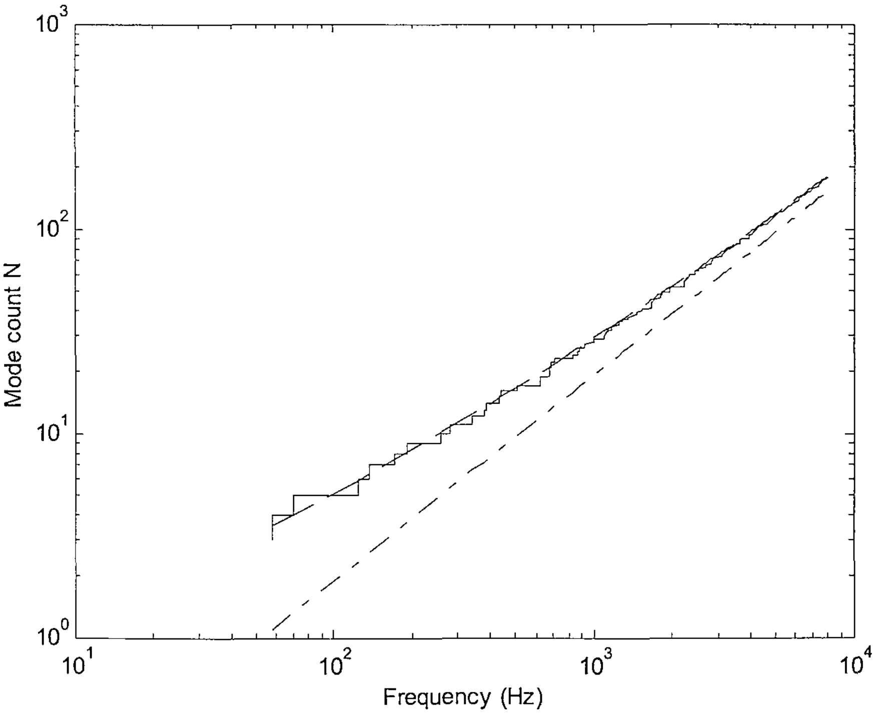

Figure 4.10 Comparison of the mode count for a free aluminium plate 0.4m×0.3m×0.002m
(—, staircase , ---, from (4.27), -·-·-, from (4.1))

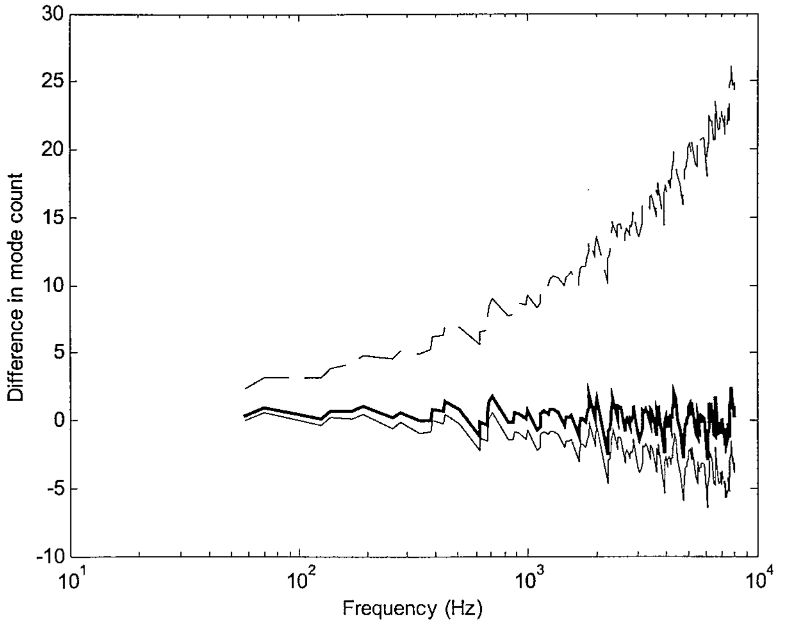

Figure 4.11 Difference between the estimated mode count and the actual result for a free aluminium plate 0.4m×0.3m×0.002m.

(—, using (4.27), thick line, using (4.20), -·-·-, using (4.1))

4.2.1.4 Plate with two opposite edges simply supported

Consider a plate having only two opposite edges in the x-direction with simple supports (x = 0, x= a), the other two edges (y = 0, y = b) being free. Two rigid modes will occur in the y-direction (considering a beam in this direction). These two rigid modes lead to two sets of simply supported beam-like modes in the x-direction of the plate. The natural modes in bending should satisfy approximately

$$k_x a = m\pi, \quad k_y b = (n - \frac{3}{2})\pi \tag{4.28}$$

where m and n are integers starting respectively from 1 and 3, and for n = 1, 2, there are two sets of beam-like modes.

The modes for the plate are shown in a k-space plot in Figure 4.12. All the shaded area must be taken into account for calculating the mode count. The expression of the average mode count is given by

$$N(k) = \frac{\frac{1}{4}\pi k^2 - k\frac{\pi}{2a} + k\frac{\pi}{b} - \frac{\pi}{2a}\frac{\pi}{b}}{\frac{\pi}{a}\frac{\pi}{b}}$$

thus

$$N(k)=\frac{k^2S}{4\pi}-\frac{1}{2}\frac{kb}{\pi}+\frac{ka}{\pi}-\frac{1}{2} \tag{4.29}$$

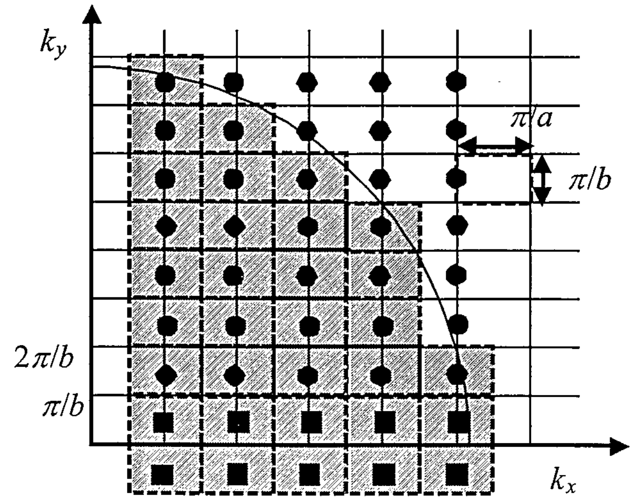

Figure 4.12 The modes of a plate with two opposite edges simply supported shown in *k*-space (solid square: beam-like mode, solid circle: plate mode)

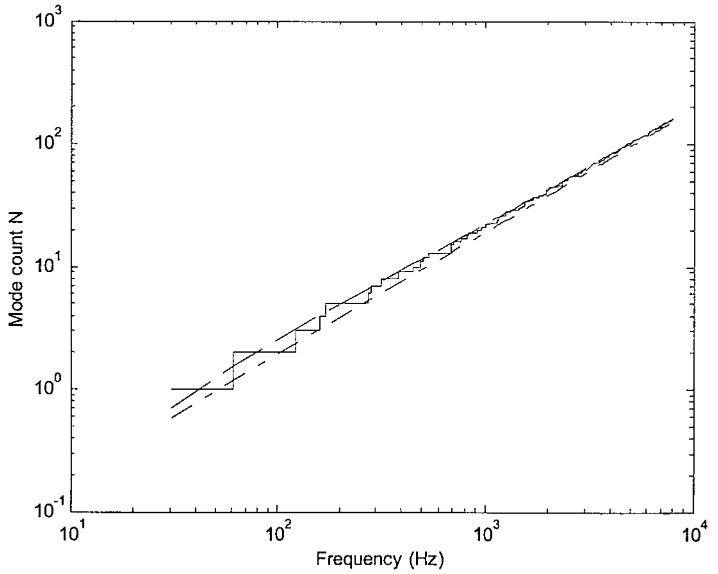

Figure 4.13 Comparison of the mode count for a aluminium plate 0.4m×0.3m×0.002m with two opposite edges free and others simply supported.
(—, staircase , ---, from (4.29), -·-·-, from (4.1))

The result of equation (4.29) is compared with analytical solutions. The same plate dimensions as in previous sections are used. The results are shown in Figure 4.13 and

Figure 4.14. It can be seen that equation (4.29) give a good agreement although there is still a small error, while equation (4.1) has a systematic error as frequency increases.

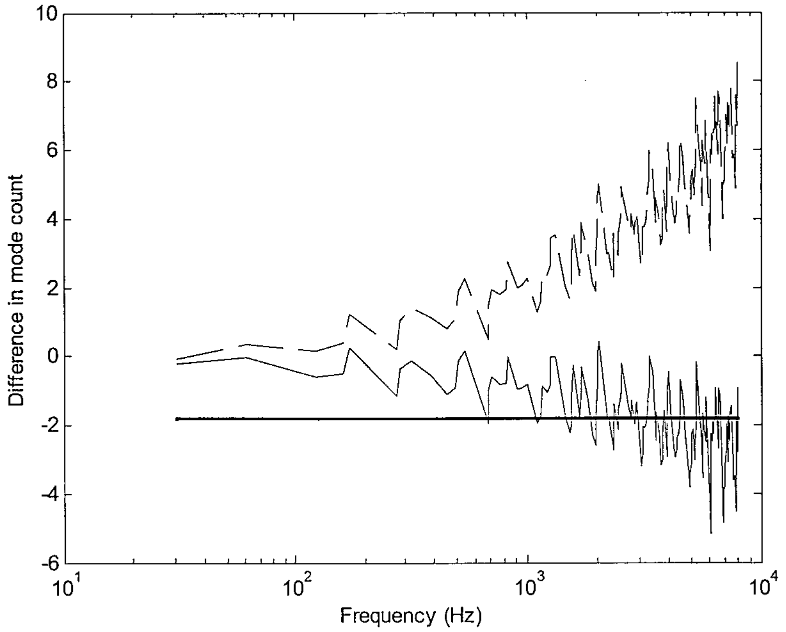

Figure 4.14 Difference between the estimated mode count and the actual result for an aluminium plate 0.4m×0.3m×0.002m with two opposite edges free and others simply supported. (—, using (4.29), thick line, average result, -·-·-, using (4.1))

4.2.2 RELATIONSHIP BETWEEN MODE COUNT AND BOUNDARY CONDITIONS

From sections 4.2.1.1 to 4.2.1.4, it has been seen that the mode count is not independent of the boundary conditions. Using equation (4.1) to evaluate the mode count of a plate will cause a considerable error. The formulae based on the phase-closure principle and *k*-space plot for four combinations of boundary conditions have presented a more correct result. It can also be concluded that in the *k*-space plot for the mode count of a rectangular plate, under any combination of boundary conditions, the mode lattice depends only on the material and dimensions but this is shifted depending on the boundary conditions. By observing equations (4.18), (4.22), (4.26) and (4.29), the general expression for the mode count of a rectangular plate can be written as

$$N(k)=\frac{k^2S}{4\pi}+\delta_x\frac{k}{\Delta k_y}+\delta_y\frac{k}{\Delta k_x}+\Delta \qquad (4.30)$$

where δ_x and δ_y are the boundary effects along the x and y directions and Δ is a constant term.

Actually δ_x and δ_y include the effects from two opposite edges in the corresponding directions. Because all examples used previously are symmetric with respect to their boundaries, it is reasonable to anticipate that half the value of δ_x or δ_y will be the boundary effect of one edge. Considering the free plate as a base for comparison, the effect of each type of boundary can be obtained. The error Δ will be ignored because it is very small. It will be shown later that ignoring Δ is acceptable for calculation of the modal density. The mode count for a free rectangular plate is hence given by

$$N(k)=\frac{k^2S}{4\pi}+\frac{k}{\Delta k_y}+\frac{k}{\Delta k_x} \tag{4.31}$$

Comparing equations (4.29) and (4.31), the effect due to the simple supports on the two edges in the x-direction is given by

$$\delta_x=-\frac{3}{2}\frac{k}{\Delta k_y} \tag{4.32}$$

Therefore the effect due to a simple support on one edge in the x-direction is given by the half of this

$$\delta_{x-pinned}=-\frac{3}{4}\frac{k}{\Delta k_y} \tag{4.33}$$

It is noted that the coefficient in the above expression (3/4) is equal to the constant effect of a simple support on the mode count of one-dimensional systems as discussed in Chapter 3. By further comparing the case of a plate simply supported on four edges with the free plate, the effect due to a simple support on one edge in the y-direction can be given as

$$\delta_{y-pinned}=-\frac{3}{4}\frac{k}{\Delta k_x} \tag{4.34}$$

Similarly, by comparing the case of a fully fixed plate with that of a free plate, the effect of a fixed condition on one edge can be given by

$$\delta_{x-fixed}=-\frac{k}{\Delta k_y} \tag{4.35}$$

$$\delta_{y-fixed}=-\frac{k}{\Delta k_x} \tag{4.36}$$

The constant coefficients (1) in equations (4.35) and (4.36) also correspond with the result of a fixed condition for one-dimensional systems (1).

Based on the above derivations, it is straight forward and reasonable to conclude that the effect of an edge constraint on the mode count of a rectangular plate is equal to the product of the constant effect of the same type of constraint in a one-dimensional beam and a frequency-dependent term, which depends on the dimensions and the dispersion relation of the plate. This can be represented by

$$\delta_{2-D} = \delta_{1-D}\frac{k}{\Delta k_{axis}} \tag{4.37}$$

where δ_{1-D} corresponds to the boundary effect in one-dimensional systems (see Chapter 3) and Δk_{axis} corresponds to the direction parallel to the line constraint and equals $\frac{\pi}{L_{axis}}$ where L_{axis} is the length of the line constraint. (e.g. the edge constraint on $x = a$ has length b).

Hence the mode count of a rectangular plate can be given by

$$N(k) = \frac{k^2 S}{4\pi} + \left(1 - \delta_{x-left} - \delta_{x-right}\right)\frac{k}{\Delta k_y} + \left(1 - \delta_{y-top} - \delta_{y-bottom}\right)\frac{k}{\Delta k_x} + \Delta \tag{4.38}$$

where δ_{x-left}, $\delta_{x-right}$, δ_{y-top} and $\delta_{y-bottom}$ are the one-dimensional boundary effects corresponding to the boundary conditions of the four edges, and Δ is a small constant.

4.2.3 FURTHER EXAMPLES

The effect of boundary conditions on the mode count of a plate has been given in the above section. In this section, this effect will be used to estimate the mode count for a plate with various combinations of boundary conditions. The predicted results will be validated using the analytical solutions from Leissa [94].

4.2.3.1 A plate with simple supports and clamped edges in two directions

Consider a plate with two adjacent edges simply supported and the other two edges clamped. Without considering the k-space plot for the natural modes, the mode count directly obtained from equation (4.38) can be given by

$$N(k)=\frac{k^2S}{4\pi}+\left(1-\delta_{x-pinned}-\delta_{x-clamped}\right)\frac{k}{\Delta k_y}+\left(1-\delta_{y-pinned}-\delta_{y-clamped}\right)\frac{k}{\Delta k_x} \tag{4.39}$$

$$N(k)=\frac{k^2S}{4\pi}+\left(1-\frac{3}{4}-1\right)\frac{k}{\Delta k_y}+\left(1-\frac{3}{4}-1\right)\frac{k}{\Delta k_x} \tag{4.40}$$

$$N(k)=\frac{k^2S}{4\pi}-\frac{3}{4}\frac{k}{\Delta k_y}-\frac{3}{4}\frac{k}{\Delta k_x} \tag{4.41}$$

$$N(k)=\frac{k^2S}{4\pi}-\frac{3}{4}k\frac{a}{\pi}-\frac{3}{4}k\frac{b}{\pi} \tag{4.42}$$

The result from equation (4.42) is compared with the analytical solutions from Leissa [94] in Figure 4.15 and Figure 4.16. It can be seen that equation (4.42) gives a good agreement, although there is still a small error, whereas equation (4.1) has a systematic error as frequency increases.

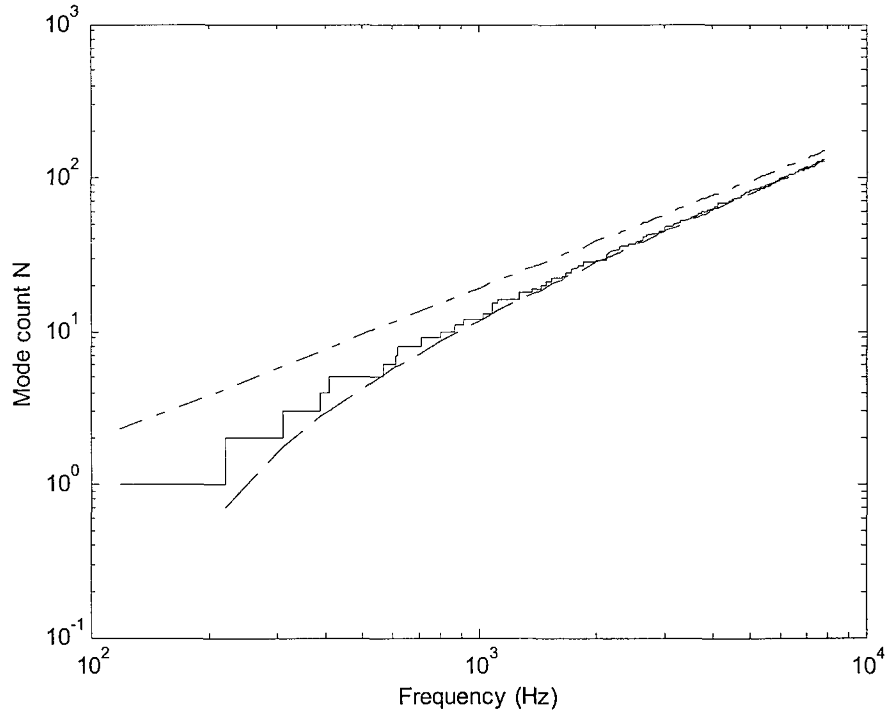

Figure 4.15 Comparison of the mode count for a pinned-pinned-fixed-fixed plate 0.4m×0.3m×0.002m. (—, analytical , ---, from (4.42), -·-·-, from (4.1))

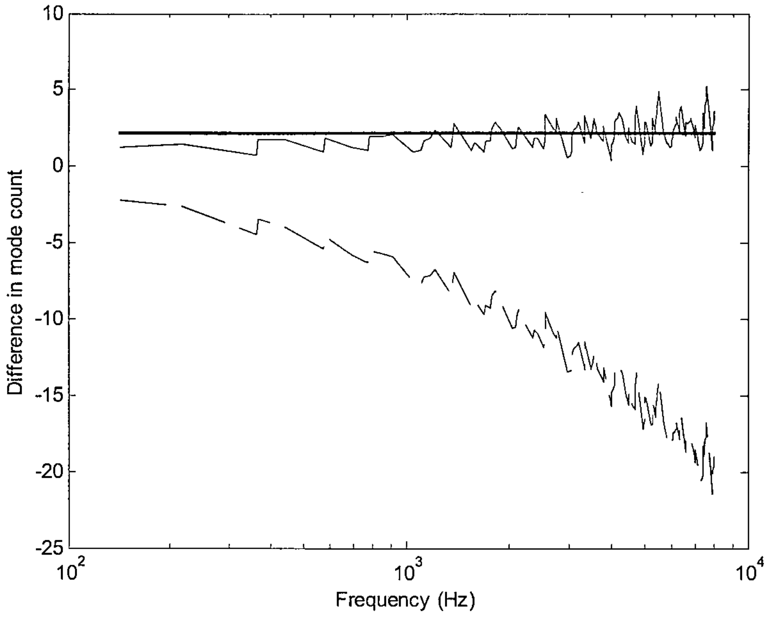

Figure 4.16 Difference between the estimated mode count and the actual result for a pinned-pinned-fixed-fixed aluminium plate 0.4m×0.3m×0.002m..

(—, using (4.42), thick line, average result, -·-·-, using (4.1))

4.2.3.2 A pinned-pinned-pinned-free plate

Consider a plate with one free edge in the y-direction (y = 0) and the others pinned. The mode count is given by

$$N(k)=\frac{k^2S}{4\pi}+\left(1-\delta_{x-pinned}-\delta_{x-pinned}\right)\frac{k}{\Delta k_y}+\left(1-\delta_{y-pinned}-\delta_{y-free}\right)\frac{k}{\Delta k_x} \qquad (4.43)$$

$$N(k)=\frac{k^2S}{4\pi}+\left(1-\frac{3}{4}-\frac{3}{4}\right)\frac{k}{\Delta k_y}+\left(1-\frac{3}{4}-0\right)\frac{k}{\Delta k_x} \qquad (4.44)$$

$$N(k)=\frac{k^2S}{4\pi}-\frac{1}{2}\frac{k}{\Delta k_y}+\frac{1}{4}\frac{k}{\Delta k_x} \qquad (4.45)$$

$$N(k)=\frac{k^2S}{4\pi}-\frac{1}{2}k\frac{b}{\pi}+\frac{1}{4}k\frac{a}{\pi} \qquad (4.46)$$

The comparison of the result from equation (4.45) with the analytical solution is shown in Figure 4.17. Equation (4.45) gives a good agreement with the analytical solution.

Further combinations of boundary conditions for a rectangular plate can be used to verify the applicability of equation (4.38) but these will not be discussed in the present work.

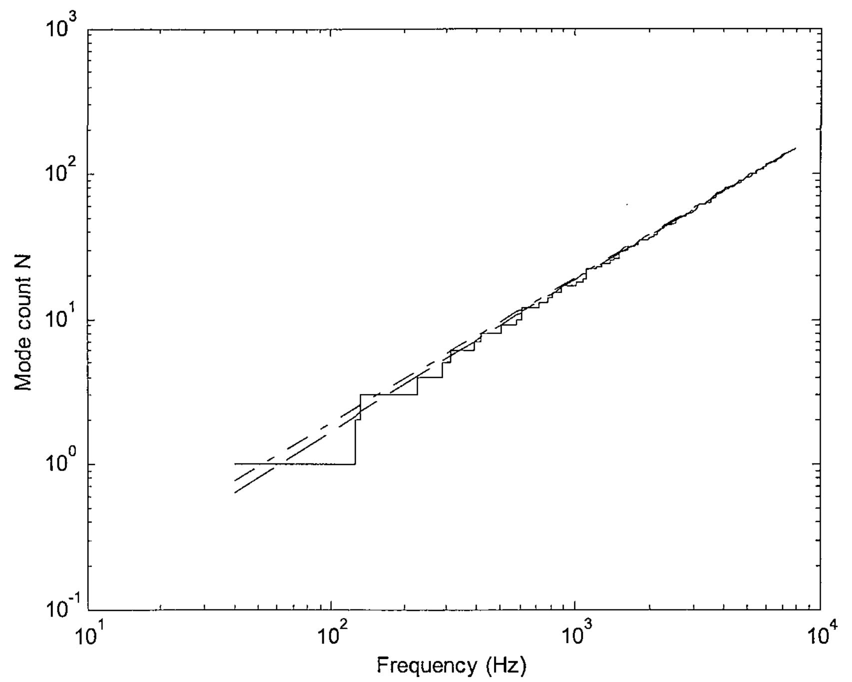

Figure 4.17 Comparison of the mode count for a pinned-pinned-pinned-free plate.

(——, analytical , ---, from (4.46), -·-·-, from (4.1))

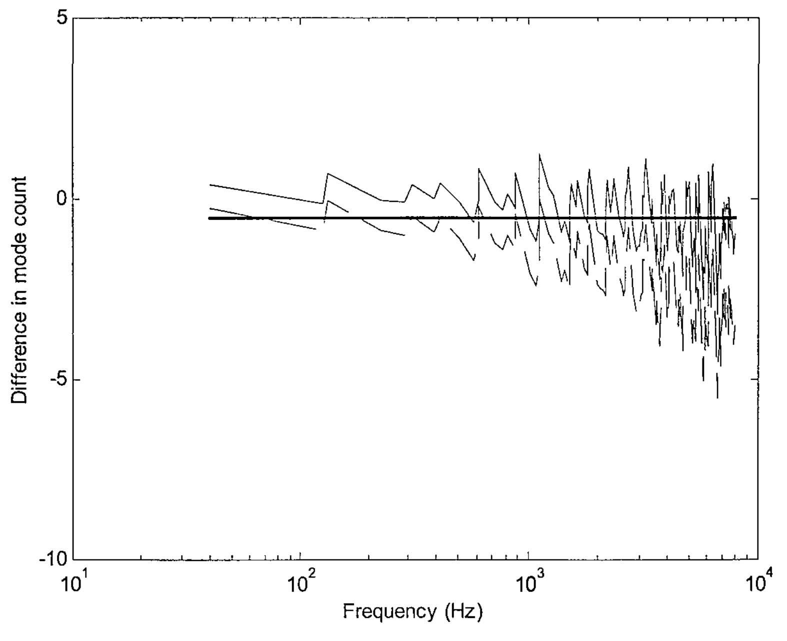

Figure 4.18 Difference between the estimated mode count and the actual result for a pinned-pinned-pinned-free aluminium plate 0.4m×0.3m×0.002m..

(——, using (4.46), thick line, average result, -·-·-, using (4.1))

4.2.4 A PLATE WITH INTERMEDIATE LINE CONSTRAINTS

Following the conclusion from Chapter 3 that, for one-dimensional systems, an intermediate constraint has the same effect on the average mode count as the same type of constraint applied at an end, it can be anticipated that an intermediate line constraint will have the same effect as the same type of line constraint applied at an edge for two-dimensional systems. If a simply supported rectangular plate is considered with one or several intermediate line simple supports applied, the average mode count of such a two-dimensional system can be expected to be given by

$$N_{total}(k) = N(k) - m\delta_{BC} \tag{4.47}$$

where $N_{total}(k)$ is the average mode count of the whole system, $N(k)$ is the average mode count of the system without considering the intermediate constraints, given by equation (4.38), m is the number of applied intermediate constraints and δ_{BC} is the line boundary effect of a simple support on the mode count which is determined by equation (4.37).

To verify equation (4.47), two examples are studied. The first is a simply supported plate of dimension 0.4m×0.3m×0.002m with another line simple support applied at $x_0 = 0.16$m. The second is the same plate with two line simple supports applied at $x_{01} = 0.16$m and $x_{02} = 0.27$m. The position of the line constraint x_0 in both cases is arbitrarily chosen. The expected average mode count of the first example is given by

$$N_{total}(k) = N(k) - \delta_{x-pinned} \tag{4.48}$$

where $N(k)$ is given by equation (4.18) and $\delta_{x-pinned} = -\frac{3}{4}\frac{kb}{\pi}$.

The expected average mode count of the second example is given by

$$N_{total}(k) = N(k) - 2\delta_{x-pinned} \tag{4.49}$$

Since the analytical solutions of natural frequencies for such systems are not available, an FEM modal analysis is used to obtain numerical results. The ANSYS SHELL 63 elements (4 nodes) of dimensions 0.01 × 0.01 m^2 are used. This allows analysis valid up to 8kHz, based on six nodes per wavelength. Then the estimated results from equations (4.48) and (4.49) are compared with those from the FEM analysis, as shown in Figure 4.19 and Figure 4.20. It can be seen that the estimated values have a good agreement with the result from the FEM analysis. The mode counts obtained differ more significantly from the result of equation (4.1) as intermediate constraints are added.

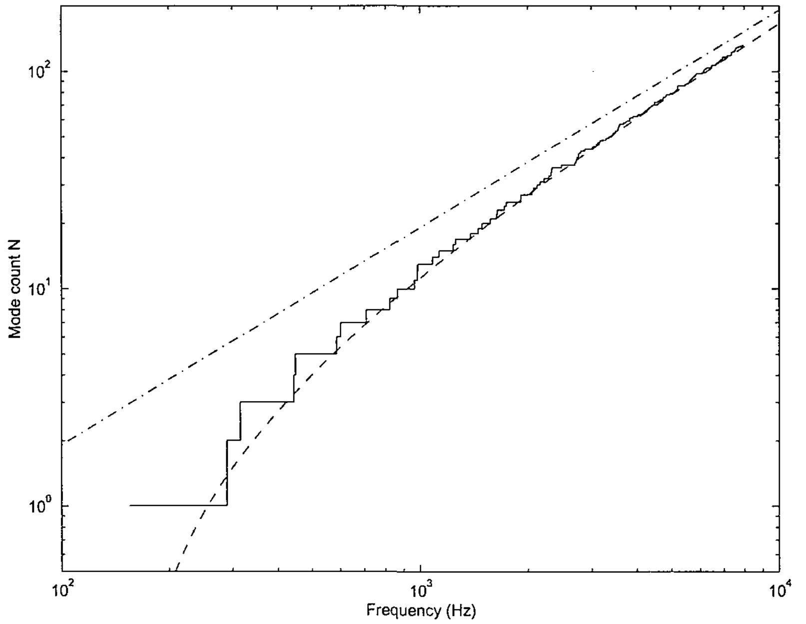

Figure 4.19 Comparison of the estimated mode count and FEM result for a plate 0.4m×0.3m×0.002m with a line intermediate simple support at x_0 = 0.16m.

(stair-case: FEM, ---: equation (4.48), -·-·-: equation (4.1))

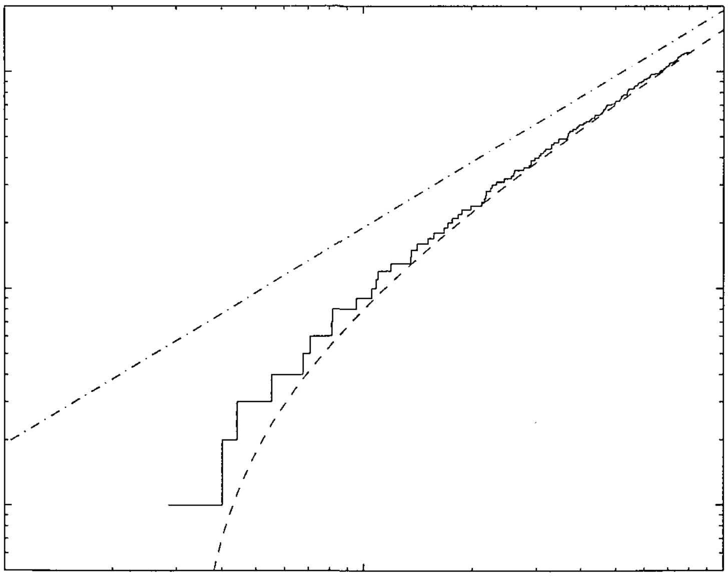

Figure 4.20 Comparison of the estimated mode count and FEM result for a plate 0.4m×0.3m×0.002m with two intermediate simple support at x_{01} = 0.16m and x_{02} = 0.27m.

(stair-case: FEM, --- : equation (4.49), -·-·-: equation (4.1))

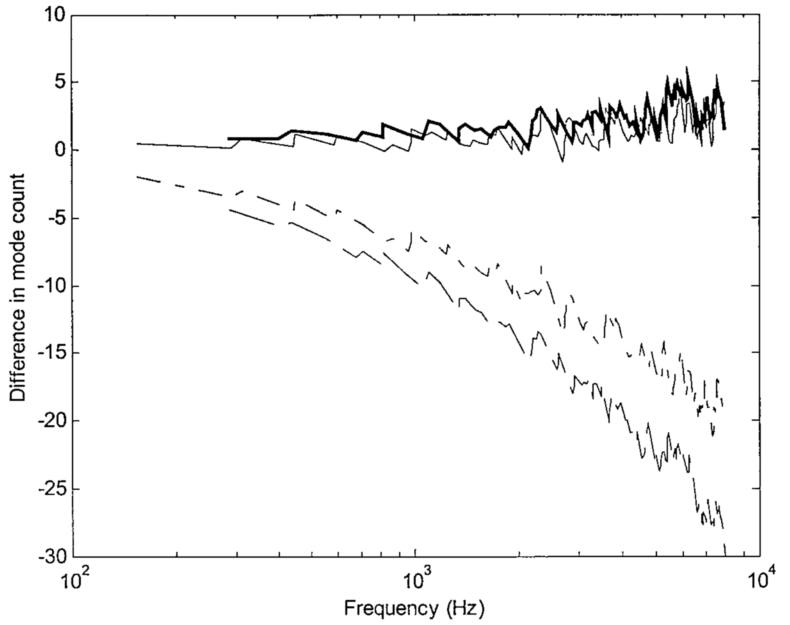

Figure 4.21 Difference between the estimated mode count and the FEM results. (solid line: using (4.48) for one intermediate constraint, thick solid line: using (4.49) for two intermediate constraints, -·---: using (4.1) for one intermediate constraints, ----: using (2.1) for two intermediate constraints)

4.3 MODAL DENSITY OF RECTANGULAR PLATES

4.3.1 MODAL DENSITY

Having obtained the expression for the mode count of the rectangular plate with various boundary conditions, the modal density can be readily derived through the derivative of the mode count. In terms of frequency, the expression (4.38) of the mode count for a rectangular plate can be rewritten as

$$N(\omega)=\frac{S}{4\pi}\sqrt{\frac{m''}{B}}\omega+\left(\frac{m''}{B}\right)^{\frac{1}{4}}\left[\frac{\left(1-\delta_{x\text{-}left}-\delta_{x\text{-}right}\right)b}{\pi}+\frac{\left(1-\delta_{y\text{-}top}-\delta_{y\text{-}bottom}\right)a}{\pi}\right]\omega^{\frac{1}{2}}+\Delta \tag{4.50}$$

It should be noted that there is a small constant term Δ in equation (4.50). The derivative of the mode count will eventually eliminate the effect of this term in the modal density. The modal density of a rectangular plate is hence given by

$$n(\omega)=\frac{\partial N(\omega)}{\partial\omega}=\frac{S}{4\pi}\sqrt{\frac{m''}{B}}+\frac{1}{2}\left(\frac{m''}{B}\right)^{\frac{1}{4}}\left[\frac{\left(1-\delta_{x-left}-\delta_{x-right}\right)b}{\pi}+\frac{\left(1-\delta_{y-top}-\delta_{y-bottom}\right)a}{\pi}\right]\omega^{-\frac{1}{2}} \tag{4.51}$$

It can be seen from equation (4.51) that the modal density of the plate is frequency-dependent. The first term in equation (4.51) is equivalent to equation (4.52) that is given in most literature (see [35, 32, 37]).

$$n(\omega)=\frac{S}{4\pi}\sqrt{\frac{m''}{B}} \tag{4.52}$$

This first term is constant for a specific plate and depends only on the material, thickness and area of the plate under consideration. The second term in equation (4.51) is frequency dependent and contains information on the geometric characteristics of the plate. It becomes relatively smaller and less important as frequency increases so that the modal density tends to a constant only at high frequency.

4.3.2 CASE STUDY OF MODAL DENSITY

Substituting $\delta_x=3/4$ and $\delta_y=3/4$ in equation (4.51), the modal density of a simply supported plate can be given by

$$n(\omega)=\frac{S}{4\pi}\sqrt{\frac{m''}{B}}-\frac{1}{4}\left(\frac{m''}{B}\right)^{\frac{1}{4}}\left(\frac{a+b}{\pi}\right)\omega^{-\frac{1}{2}} \tag{4.53}$$

Similarly using $\delta_{1D}=0$, the modal density of a free plate can be given by

$$n(\omega)=\frac{S}{4\pi}\sqrt{\frac{m''}{B}}+\frac{1}{2}\left(\frac{m''}{B}\right)^{\frac{1}{4}}\left(\frac{a+b}{\pi}\right)\omega^{-\frac{1}{2}} \tag{4.54}$$

and using $\delta_{1D}=1$, the modal density of a fully fixed plate can be given by

$$n(\omega)=\frac{S}{4\pi}\sqrt{\frac{m''}{B}}-\frac{1}{2}\left(\frac{m''}{B}\right)^{\frac{1}{4}}\left(\frac{a+b}{\pi}\right)\omega^{-\frac{1}{2}} \tag{4.55}$$

From the above three equations it can be noted that the modal density of the plate can be either larger or smaller than the constant value from equation (4.52). Taking the plate investigated in section 4.2 as an example, the result of the modal densities of a simply supported, a fully fixed and a free plate are shown in Figure 4.22 (NB results are plotted as $n(f) = 2\pi n(\omega)$). It can be seen that equation (4.52) can only represent the true modal density well at high frequencies. The first mode of this simply supported plate occurs at 85 Hz. The error can be as much as 14% at frequency 850 Hz (ten times the fundamental frequency). For the cases of the free and fully fixed plate, the errors are 35% and 20% at a frequency ten times the natural frequency of the first mode.

The modal density can also be obtained directly by counting the number of modes in a band (it is actually impractical in applications). Figure 4.23 shows the results counted in one-third octave bands for a simply supported plate. It can be seen that the result from one-third octave bands agrees better with the curve from equation (4.53) and converges to the constant determined by equation (4.52) at high frequencies. However, for frequencies below 630Hz, the result counted in one-third octave bands has a quite large error as only a small number of modes is presented in each band. This error can be decreased by expanding the bandwidth of the frequency interval into overlapping octave bands, as shown in Figure 4.24. Figure 4.25 and 4.26 present the results for the free plate. The same phenomenon as the simply supported plate can be observed.

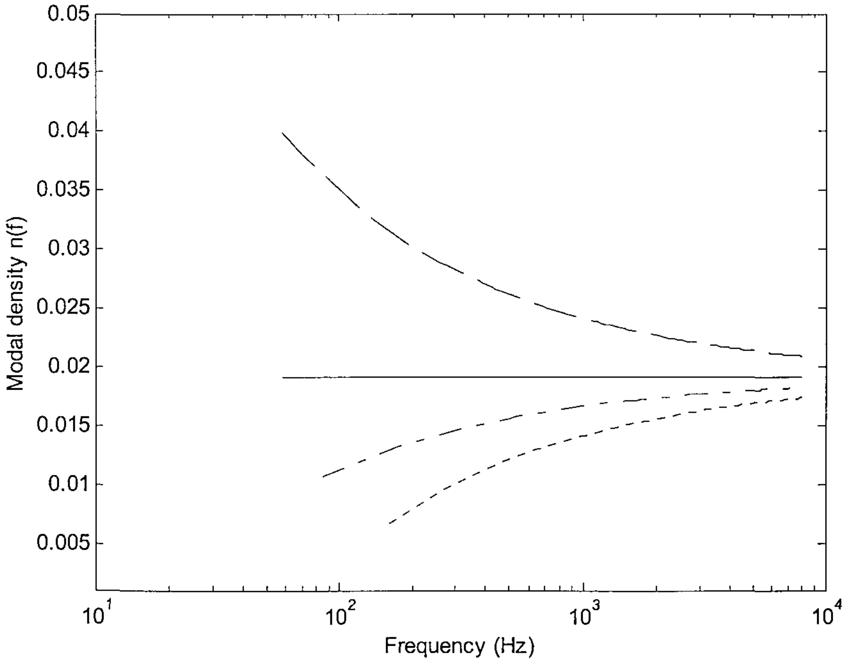

Figure 4.22 Modal density of the plate 0.4m×0.3m×0.002m.

(—, equation (4.52); -·-, simple support; —, free; ······, fixed.)

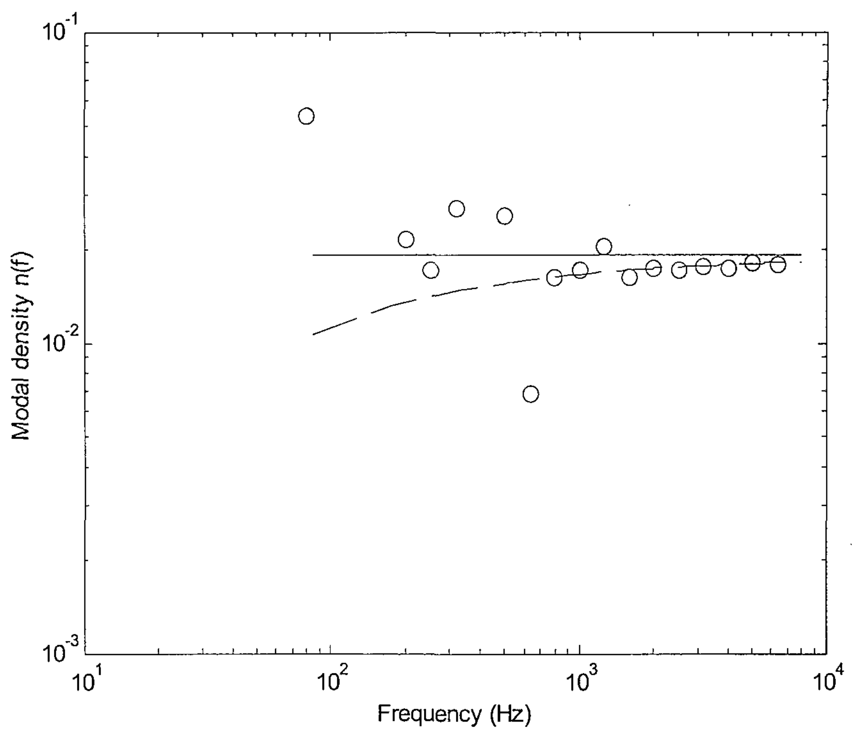

Figure 4.23 Modal density of the simply supported plate 0.4m×0.3m×0.002m.

(—, equation (4.52); ---, equation (4.53); o, 1/3 octave bands.)

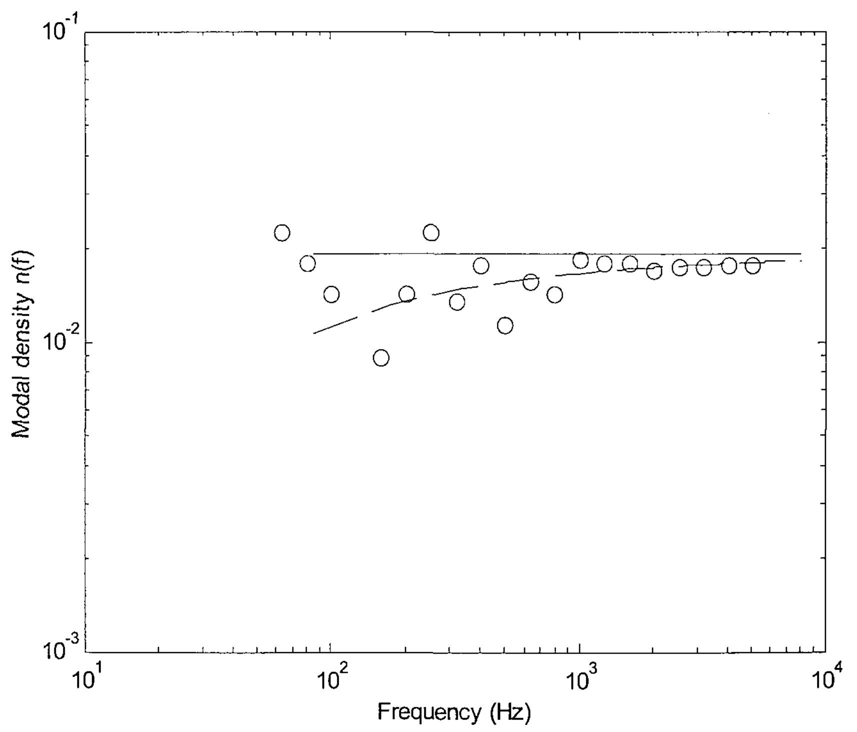

Figure 4.24 Modal density of the simply supported plate 0.4m×0.3m×0.002m.

(—, equation (4.52); ---, equation (4.53); o, counted in overlapping octave bands.)

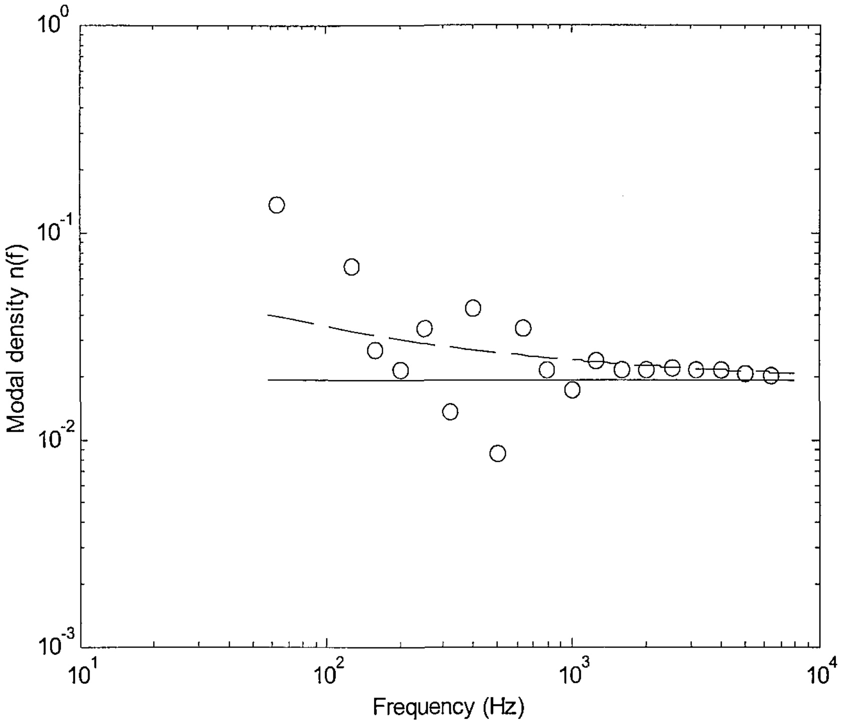

Figure 4.25 Modal density of the free plate 0.4m×0.3m×0.002m.

(—, equation (4.52); ·—·, equation (4.54); o, 1/3 octave bands.)

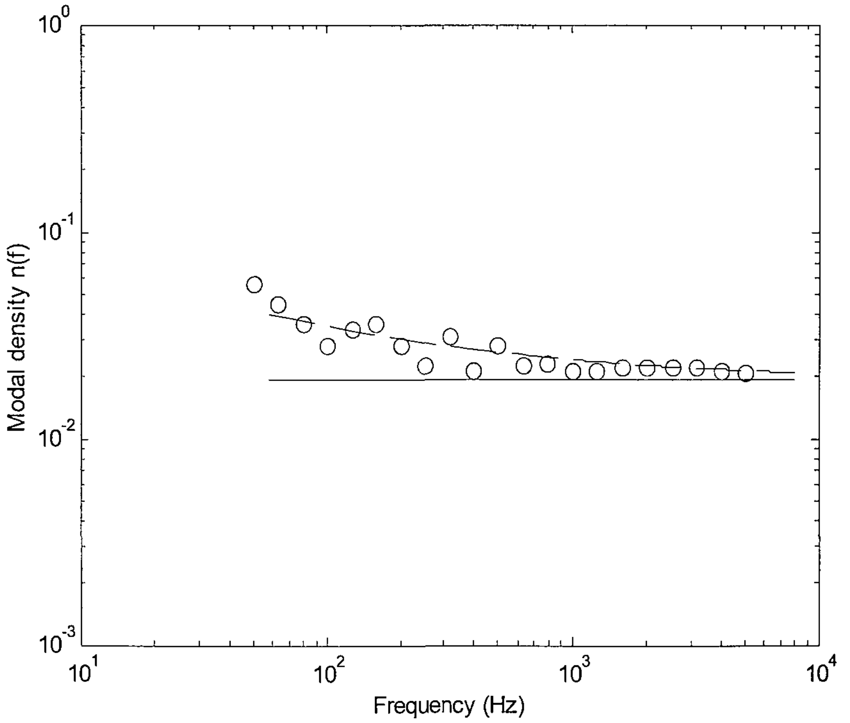

Figure 4.26 Modal density of the free plate 0.4m×0.3m×0.002m.

(—, equation (4.52); ·—·, equation (4.53); o, counted in overlapping octave bands.)

4.4 MODE COUNT AND MODAL DENSITY OF AN EXTRUDED PLATE

For complicated structures, there is no analytical result available for the modal density. When using SEA, however, it is desirable to estimate their modal density using theoretical expressions rather than rely on experimental methods or numerical methods such as FEM. Based on the conclusions drawn in this Chapter, the modal density of extruded panels can be estimated theoretically through including the effect of the boundary conditions and constraints applied. The vibration of the extruded plate involves global motion and local motion. At low frequencies the extruded plate behaves as a whole plate while the local vibration dominates at high frequencies. The modal density of the extruded plate is a combination of the modal densities of global modes and local modes.

4.4.1 MODEL FOR GLOBAL MODES

Consider the extruded plate as an equivalent plate in bending vibration, namely global bending motion. For such motion, the stiffeners are nearly rigid and the bending induces stresses mainly in the upper and lower plates, which are either compressed or extended relative to the neutral fibre. This neutral fibre passes through the centre of gravity of the section, and is actually located at the mid-point of the section (see Figure 3.26). It may be assumed that the stiffeners do not bear the tensile and compressive stress under the pure bending condition but behave as rigid spacers that separate the upper and lower plates.

The equivalent bending stiffness along the x axis has already derived in Chapter 3 (see equation (3.134)). For bending along the z axis, the second moment of area about the y axis based on the above assumption can be considered as an equivalent counterpart of a II section [95], as shown in Figure 4.27. This gives

$$I_y = 2\times\left[\left[\frac{ah^3}{12} + ah\times\left(\frac{H}{2}-\frac{h}{2}\right)^2\right] + \frac{h(H-2h)^3}{12\sin\alpha}\right] \tag{4.56}$$

where a is the average spacing between the stiffeners.

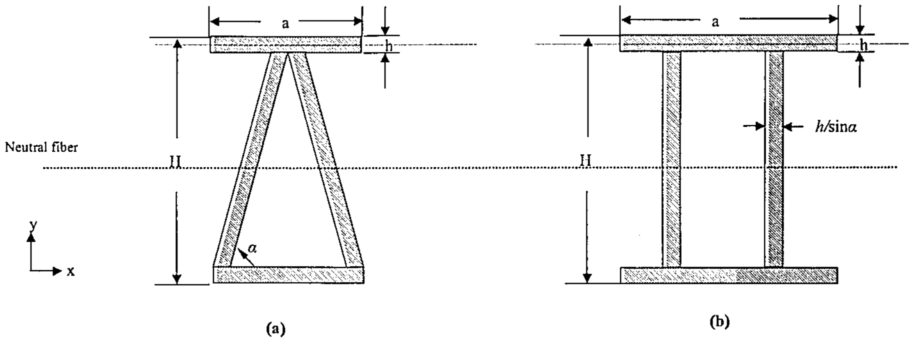

Figure 4.27 (a) Cross section of part of the extruded plate. (b) The cross-section of the equivalent II section

The equivalent bending stiffness along the y axis is given by

$$B_y = E'I_y = \frac{EI_y}{1-\mu^2} \tag{4.57}$$

The bending stiffnesses B_x and B_y from equations (3.137) and (4.57) have very similar values since the second moment of area is dominated by the cross-section of the top and bottom plates. B_x is calculated as 5.369×10^5 m^4 and B_y is 5.715×10^5 m^4 for a typical section. In spite of this similarity, the extruded plate behaves as an orthotropic plate because its bending stiffness varies with direction. For orthotropic plates, if the bending wavelength is considerably greater than the stiffener spacing, it can be approximated as an equivalent isotropic plate by introducing an equivalent bending stiffness B_{xy} [35]. This equivalent bending stiffness B_{xy} is equal to the geometric mean of the bending stiffness in the two directions. It is given by

$$B_{xy} \approx \sqrt{B_x B_y} \tag{4.58}$$

4.4.2 MODE COUNT AND MODAL DENSITY OF GLOBAL MODES

It is assumed that the boundary conditions of the extruded plate are simple supports. The mode count for global modes of the extruded plate can thus be given by

$$N_g(\omega) = \frac{S}{4\pi}\sqrt{\frac{M''}{B_g}}\omega - \frac{1}{2}\left(\frac{M''}{B_g}\right)^{\frac{1}{4}}\left(\frac{L_x+L_y}{\pi}\right)\omega^{\frac{1}{2}} \tag{4.59}$$

where L_x and L_y are the dimensions of the extruded plate, S is its surface area (L_xL_y), M'' is the equivalent mass per unit area, and B_g is the equivalent bending stiffness for the global modes, i.e. B_{xy}.

The modal density of the global modes is therefore given by the derivative of equation (4.59) as

$$n_g(\omega)=\frac{S}{4\pi}\sqrt{\frac{M''}{B_g}}-\frac{1}{4}\left(\frac{M''}{B_g}\right)^{\frac{1}{4}}\left(\frac{L_x+L_y}{\pi}\right)\omega^{-\frac{1}{2}} \tag{4.60}$$

4.4.2.1 Mindlin thick plate

In the same way as Timoshenko beam theory should be used for beams at high frequencies, Mindlin's thick plate theory should be considered for global plate modes at high frequencies. The two-dimensional equation of motion for free vibration of a thick plate is given by [96]

$$\left(\nabla^2-\frac{\rho}{G\kappa}\frac{\partial^2}{\partial t^2}\right)\left(D\nabla^2-I\frac{\partial^2}{\partial t^2}\right)w+\rho h\frac{\partial^2 w}{\partial t^2}=0 \tag{4.61}$$

where ρ is the density of plate, G is the shear modulus, κ is the Timoshenko shear coefficient, I is the second moment of area per unit width, h is the thickness of the plate, D is the bending stiffness and ∇^2 is Laplace's two-dimensional operator.

The dispersion relation of the thick plate has a similar form to that for a thick beam. This is given by

$$Dk_t^4+\left(\frac{\rho D}{G'}+I\right)\omega^2k_t^2+\frac{\rho^2 I}{G'}\omega^4-\rho h\omega^2=0 \tag{4.62}$$

where k_t is the wavenumber.

The solution of the first propagating wave from equation (4.62) is given by

$$k_t=\sqrt{\frac{\rho\left(I+\frac{D}{G\kappa}\right)\omega^2+\sqrt{\left[\rho\left(I+\frac{D}{G\kappa}\right)\omega^2\right]^2-4D\left(-\rho h\omega^2+\frac{\rho^2 I}{G\kappa}\omega^4\right)}}{2D}} \tag{4.63}$$

The mode count of global modes of the thick plate can be calculated by

$$N_t=\frac{Sk_t^2}{4\pi}-\frac{1}{2}\left(\frac{L_x+L_y}{\pi}\right)k_t \tag{4.64}$$

The modal density of global modes of the thick plate can hence be given by

$$n_t(\omega)=\left[\frac{Sk_t}{2\pi}-\frac{1}{2}\left(\frac{L_x+L_y}{\pi}\right)\right]\frac{dk_t}{d\omega} \tag{4.65}$$

where $dk_t/d\omega$ is given by the derivative of equation (4.63). Here this is evaluated numerically.

4.4.3 LOCAL MODES

4.4.3.1 Mode count of local modes

The local modes occur above the first cut-on frequency of the widest strip. This behaviour was studied using a two-dimensional FEM model of the cross-section of an extruded plate in Chapter 3.

To consider the modal density of the local modes, the extruded plate can be treated as a large plate with a number of line constraints applied. The area of this large plate S_{total} is equivalent to the combined area of all the strips. These line constraints can be approximated as simple supports or a value between the simple support and clamped according to the results in Chapter 3. The mode count of local modes can be approximately given by

$$N_l(\omega)=N(\omega)-p\delta\frac{L_y}{\pi}\left(\frac{m''}{B}\right)^{\frac{1}{4}}\omega^{\frac{1}{2}} \tag{4.66}$$

where N is the mode count of the plate having area S_{total}, p is the number of intermediate constraints, which is the number of strips minus 1, δ is the boundary effect of the intermediate constraints between strips, L_y is the length of the extruded plate in the y-direction, m'' is the mass per unit area and B is the bending stiffness of the strip.

$N(\omega)$ is given by

$$N(\omega)=\frac{S_{total}}{4\pi}\sqrt{\frac{m''}{B}}\omega-\frac{1}{2}\left(\frac{m''}{B}\right)^{\frac{1}{4}}\left(\frac{L_y+\sum l_i}{\pi}\right)\omega^{\frac{1}{2}} \tag{4.67}$$

where S_{total} is the total area of all strips and l_i is the length of the shorter edge of each strip.

Theoretically, equation (4.66) is valid at frequencies which are sufficiently high that the first modes of all strips have occurred. At low and mid frequency, the term containing the information relating to the constraints in equation (4.66) will become significant to the result. It may cause a negative value for the mode count at low and mid frequencies. This does not actually happen in reality, as the mode count must be positive. In practice, at low frequencies, the local modes occur only on those relatively wide strips. Therefore those relatively narrow strips and their corresponding constraints should not be taken into account for the application of equation (4.66). Therefore equation (4.66) can be rewritten as the sum of the local modes occurring on each strip

$$N_l(\omega) = \sum_{i=1}^{p+1}\left[\max\begin{pmatrix} N_i \\ 0 \end{pmatrix}\right] \tag{4.68}$$

where N_i is given by

$$N_i = \frac{l_i L_y}{4\pi}\sqrt{\frac{m''}{B}}\omega - \frac{1}{2}\frac{l_i}{\pi}\left(\frac{m''}{B}\right)^{\frac{1}{4}}\omega^{\frac{1}{2}} - \frac{1}{p+1}\left(p\delta_{pinned} + \frac{1}{2}\right)\frac{L_y}{\pi}\left(\frac{m''}{B}\right)^{\frac{1}{4}}\omega^{\frac{1}{2}} \tag{4.69}$$

This is equivalent to treating each strip as simply supported parallel to the x-axis and with the assumed constraints defined by δ parallel to the y-axis. A negative N_i at one frequency is physically meaningless. For such a case, this strip only contributes zero to the local modes of the extruded plate. Note that $N_l = 0$ if the mode count of all strips is zero. It becomes non-zero as soon as local modes occur in the widest strip.

4.4.3.2 Modal density of local modes

The modal density of the local modes of the extruded plate can hence given by

$$n_l(\omega) = \sum_{i}^{p+1} n_i \tag{4.70}$$

where n_i is given by

$$n_i = \begin{cases} \frac{l_i L_y}{4\pi}\sqrt{\frac{m''}{B}} - \frac{1}{4}\frac{l_i}{\pi}\left(\frac{m''}{B}\right)^{\frac{1}{4}}\omega^{-\frac{1}{2}} - \frac{1}{2(p+1)}\left(p\delta_{pinned} + \frac{1}{2}\right)\frac{L_y}{\pi}\left(\frac{m''}{B}\right)^{\frac{1}{4}}\omega^{-\frac{1}{2}} & \text{for } N_i > 0 \\ 0 & \text{for } N_i < 0 \end{cases} \tag{4.71}$$

4.4.4 MODE COUNT AND MODAL DENSITY OF EXTRUDED PLATES

The mode count and modal density of the extruded plate can be obtained by combining the expressions for global and local modes. The mode count of an extruded plate is given by

$$N(\omega) = N_g(\omega) + N_l(\omega) \tag{4.72}$$

where N_g can be obtained by equation (4.59) or (4.64) and N_l by equation (4.68).

The modal density of an extruded plate is given by

$$n(\omega) = n_g(\omega) + n_l(\omega) \tag{4.73}$$

where n_g is given by equation (4.60) or (4.65) and n_l is given by equation (4.70).

4.4.5 RESULTS

The example of the extruded panel used in the present chapter is of aluminium and of dimensions 2.016×1.0×0.07m. The model is based on the geometry of the beam model from chapter 3, expanded to a length of 1 m. It is composed of 77 strips. The thickness of each strip is 0.003m. The widest strip is 0.16m wide while the narrowest strip is 0.046m wide.

An FEM model has been established using ANSYS for this example. A modal analysis is implemented to obtain the natural modes of the structure. The SHELL 93 element (8 nodes) is chosen with maximum dimension $0.03\times0.03\text{m}^2$. This allows valid analysis up to 3000Hz, based on six nodes per wavelength.

Figure 4.28 presents the results of the mode count from equation (4.72) and from the FEM model. Simple supports are assumed for the line constraints between strips in these calculations, i.e. $\delta = 3/4$. The result by assuming the fixed constraints ($\delta = 1$) is also presented in Figure 4.28. The estimated result based on the assumption of simple supports constraints has a good agreement with that from the FEM model above about 700Hz. However, it appears that the first local modes occur at a higher frequency in the FEM model (500Hz) than predicted using simple supports (300Hz). This indicates that the line constraints vary between the simple support and fixed conditions for frequencies below 700Hz, and tend to simple supports at high frequencies.

The global modes are estimated using thin plate theory as well as thick plate theory. The Timoshenko shear coefficient $\kappa = 0.2$ is used here for the thick plate as in Chapter 3. Figure 4.29 gives curves for the dispersion relation of the thin and thick plate theory used for the global modes of the extruded plate. It can be seen that the thick plate has a similar wavenumber to that of thin plate below 200Hz. The divergence above 200Hz causes the difference between the estimated global mode count of two models, shown in Figure 4.28.

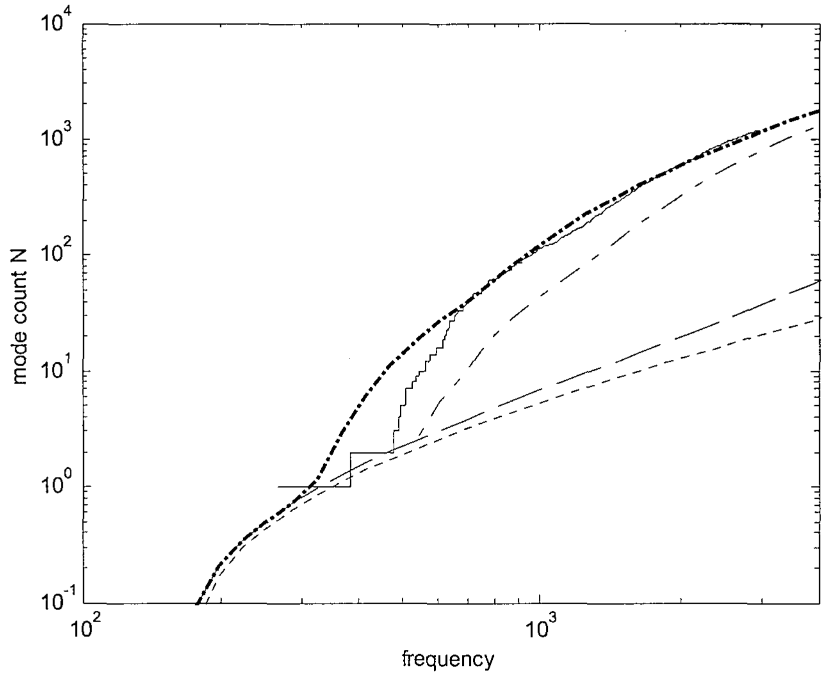

Figure 4.28 Mode count of the example extruded plate.

Thick line·—·, estimated with simple supports; —, FEM; – – global modes with thin plate model; ·····, global modes with thick plate model; ·—·, estimated with fixed boundaries.

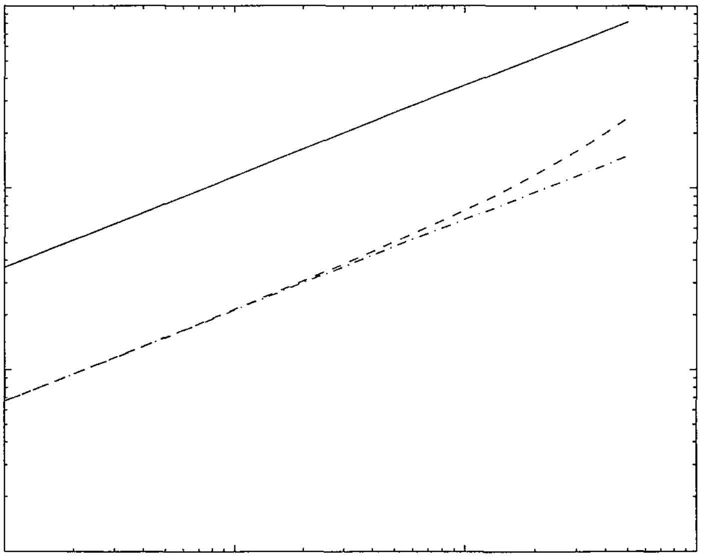

Figure 4.29 Dispersion relations of thin and thick plate theory used for global modes.

—, local modes; – –, thin plate model; ·—·, thick plate model.

Figure 4.30 shows the estimated modal density of the extruded plate based on equation (4.73), compared with the result from the FEM modal analysis, expressed in overlapping octave bands. The result generally agrees well with that from the FEM model. It should be noted that there are no modes below 200Hz in the FEM results.

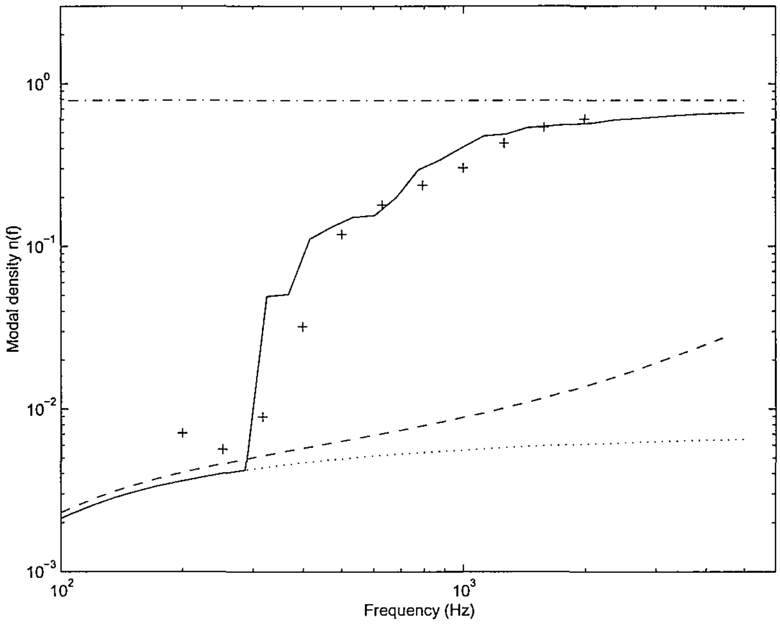

Figure 4.30 Modal density of the extruded plate. —, estimated; +, FEM in overlapping octave bands; ·—·, simple additive; – –, global modes by thick plate model; ·····, global modes by thin plate model.

The global modal density based on thin plate theory is calculated from equation (4.60). Equation (4.65), based on thick plate theory, is calculated numerically since the expression in terms of frequency is unavailable. The modal density for the global modes using thick plate theory is about four times higher than that using thin plate theory at 3 kHz.

The estimated result is also compared with that from the simple additive methods, which actually is equivalent to equation (4.3). The simple additive method is not able to consider the global behaviour and the effects due to intermediate constraints between strips. Therefore its result shows quite a large difference to that from the FEM, especially at low frequencies.

4.5 CONCLUSIONS

The mode count and modal density of bending vibrations of two-dimensional systems have been investigated in this chapter. A relation has been shown between the mode count and the boundary conditions, in particular for rectangular plates. Line constraints have systematic effects on the mode count of a system. The effect depends on the type of the boundary condition, as well as the geometric and material properties of the system. The effect is an extension of that found for the same type of boundary in one-dimensional systems. Theoretical expressions that can be used to estimate the mode count of a two-dimensional system have been obtained. The results from these estimated formulae have shown the limitation of the common formula used previously, which is based a form that neglects boundary effects. For a composite two-dimensional system, an intermediate line constraint has the same effect on the mode count as the equivalent constraint applied on an edge. The average mode count of such a composite system can be estimated by that of the system without intermediate constraints minus the product of the number of the constraints, the constraint effect δ_{BC} and the term kL/π, where k is the wavenumber and L is the length of the constrained edges.

Theoretical expressions for the modal density of a two-dimensional system have been obtained including boundary effects. The modal density of the rectangular plate is frequency-dependent and depends on the geometric information and dispersion relation of the plate under consideration. However, at high enough frequency, the modal density tends to a constant value, which is determined only by the area of the plate and dispersion relation and is independent of the boundary conditions.

The conclusion drawn from the multi-plate system leads to an approximation that can be used for the investigation of the extruded plate. The mode count of an extruded plate is predicted based on assuming simple supports between the strips. Although differences occur between the predicted results and those from the FEM analysis, the modal density shows a good agreement.

5 SOUND RADIATION FROM EXTRUDED PANELS

5.1 INTRODUCTION

To analyse the sound transmission of extruded panels using SEA techniques, it is required to model the sound radiation of extruded panels. As seen in Chapter 2, the radiation efficiency of the structure is central to considering the coupling between the structure and fluid around. The extruded panels can be considered as a built-up structure composed of a set of strips with their long edges having same length and the short edges having different lengths. From the studies described in Chapters 3 and 4, the natural modes of the extruded plate can be separated into the global modes of the whole plate, particularly at low frequency, and the local modes of the various strips at high frequency. The local modes are dominated by the dynamic behaviour of a single strip. The consideration of the sound radiation of the strip essentially involves the sound radiation of a rectangular plate of a high aspect ratio.

This Chapter will investigate this problem. The average radiation efficiency of a rectangular plate is considered first in terms of the summation of its normal modes. The average radiation efficiency of a strip is then investigated. An approximate formula applicable at frequencies below the critical frequency is developed and compared with the results from a numerical integration. Finally an analytical method for the radiation efficiency of a double-walled extruded plate is given.

5.2 MODAL RADIATION EFFICIENCY

The subject of sound radiation from vibrating structures is of great practical importance. Many structures of practical interest may be modelled sufficiently accurately by rectangular, uniform flat plates. Although they are generally dynamically coupled in real systems to contiguous structures, the isolated rectangular panel is useful to illustrate the radiation from bending waves. This subject has been investigated extensively over the last few decades.

The modal radiation efficiency of a rectangular plate can be obtained by the integral of the far-field acoustic intensity [46]. It can also be obtained by integration of the intensity over the plate surface but this is less usual in the literature. The plate is assumed to vibrate in one of its natural frequencies with simple supports and to be set in an infinite baffle. It is well known that, below the critical frequency, the odd-odd modes (modes with an odd number of half wavelengths in both directions) have a higher radiation efficiency than odd-even and even-even modes because the latter suffer more cancellation of radiation [46]. Above the critical frequency, the radiation efficiency approaches unity, provided that the plate is also large compared with the acoustic wavelength. For plates with different aspect ratios, these conclusions are always valid.

Before the radiation of the strip is considered, it should be indicated that the boundary conditions of the strip edges are supposed here to be simple supports. There are two reasons for this choice. Based on the investigation of the mode count of the extruded plate in Chapters 3 and 4, the boundary conditions between strips were found to be between simple supports and clamped. The two short edges of the strips could be considered as simple supports and the other two as between simple supports and clamped. However, Gomperts [48] showed that the radiation efficiency of a hinged-clamped plate is almost equal to that of the hinged-hinged (simply supported) plate. Therefore it is reasonable to assume that the strips of an extruded plate are simply supported for the purpose of calculating the sound radiation of the strips. Secondly, as the modes of such a plate are simple sine functions this considerably simplifies calculations.

The plate is assumed to be flat and lie in an infinite baffle in order that the Rayleigh integral technique may be used.

Considering a simply supported plate in an infinite baffle, the expression for the modal radiation obtained by integrating the far-field acoustic intensity is given by Wallace [46] as

$$\sigma_{mn} = \frac{64k^2ab}{\pi^6 m^2 n^2} \int_0^{\pi/2}\int_0^{\pi/2} \left\{ \frac{\begin{matrix}\cos\\ \sin\end{matrix}\left(\frac{\alpha}{2}\right) \begin{matrix}\cos\\ \sin\end{matrix}\left(\frac{\beta}{2}\right)}{\left[\left(\frac{\alpha}{m\pi}\right)^2 - 1\right]\left[\left(\frac{\beta}{n\pi}\right)^2 - 1\right]} \right\}^2 \sin\theta \, d\theta \, d\phi \qquad (5.1)$$

where a and b are the dimensions of the plate, m and n are the indices of modes (number of half sine waves across the length and width directions), k is the acoustic wavenumber, and $\alpha = ka\sin\theta\cos\phi$ and $\beta = kb\sin\theta\cos\phi$. The cosine terms apply when m or n are odd and sine terms when m or n are even.

Approximate expressions for the modal radiation efficiency at arbitrary frequencies below the critical frequency were also given by Wallace [46] as

$$\sigma_{mn} \simeq \frac{32(ka)(kb)}{m^2n^2\pi^5}\left\{1-\frac{k^2ab}{12}\left[\left(1-\frac{8}{(m\pi)^2}\right)\frac{a}{b}+\left(1-\frac{8}{(n\pi)^2}\right)\frac{b}{a}\right]\right\} \quad m,n \text{ odd} \qquad (5.2)$$

$$\sigma_{mn} \simeq \frac{8(ka)(kb)^3}{3m^2n^2\pi^5}\left\{1-\frac{k^2ab}{20}\left[\left(1-\frac{8}{(m\pi)^2}\right)\frac{a}{b}+\left(1-\frac{24}{(n\pi)^2}\right)\frac{b}{a}\right]\right\} \quad m \text{ odd, } n \text{ even} \qquad (5.3)$$

$$\sigma_{mn} \simeq \frac{2(ka)^3(kb)^3}{15m^2n^2\pi^5}\left\{1-\frac{5k^2ab}{64}\left[\left(1-\frac{24}{(m\pi)^2}\right)\frac{a}{b}+\left(1-\frac{24}{(n\pi)^2}\right)\frac{b}{a}\right]\right\} \quad m,n \text{ even} \qquad (5.4)$$

From the power of k in these expressions, it can be seen that odd-odd modes are most effective in radiation and even-even modes are least effective.

Figure 5.1 presents the radiation efficiency calculated using equation (5.1) of the first few modes of an aluminium strip of dimension 0.16×3m. The thickness of the strip is arbitrary. It can be seen that the odd-odd modes have the highest radiation efficiency. Moreover, the lowest order modes have the highest radiation efficiency at low frequency. In each case the radiation efficiency reaches unity at high frequencies.

Note that some results at high frequencies become unreliable due to the integration of a strongly oscillating function.

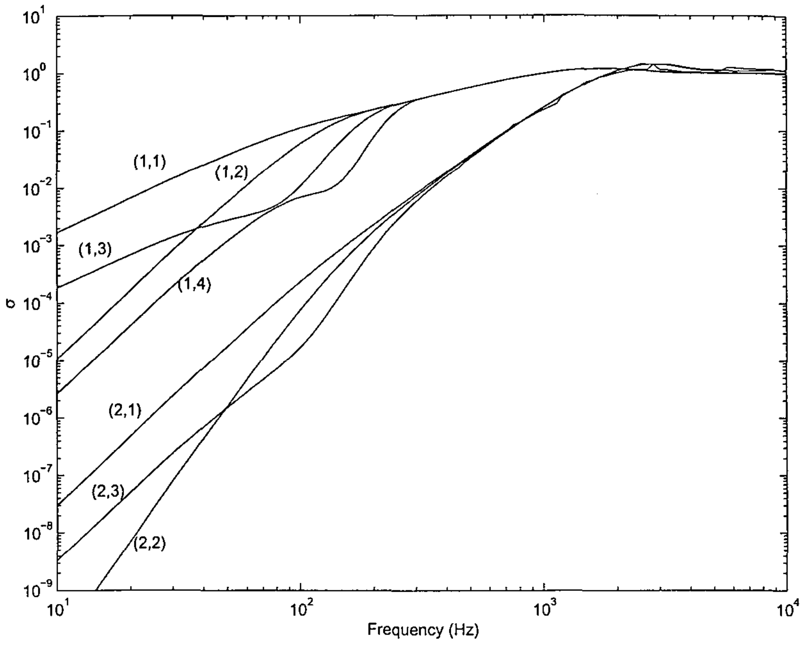

Figure 5.1 Modal radiation efficiency of a strip 0.16×3m.

5.3 AVERAGE RADIATION EFFICIENCY

In actual engineering applications, the modal radiation efficiency is not really useful because the plate vibrations generally involve many superposed modes. The average radiation efficiency is of greater importance. In principle, the average radiation efficiency of a plate can be determined if the velocity at every point on the plate is known as a function of frequency. It is also possible to evaluate the average radiation efficiency from the velocity amplitudes and the radiation efficiency of all participating modes. Since the amplitude of each mode depends not only on the ratio of the excitation frequency to the resonance frequency of the mode, but also on the spatial distribution of the excitation, it is almost impossible to know the total radiation efficiency in practice. However, if the uncertainties are accepted to some extent, a statistical result can be obtained from general considerations, such as the use of a rain on the roof excitation, and this can be useful in practice. Such an approach is considered here.

5.3.1 RADIATED POWER IN TERMS OF PLATE MODES

Consider a rectangular plate, simply supported on four edges and set in an infinite rigid baffle as shown in Figure 5.2. For harmonic motion at frequency ω, the total acoustic power radiated from the plate can be obtained by integrating the far-field acoustic intensity over a hemisphere of radius r to give

$$W = \int_0^{2\pi}\int_0^{\pi/2} \frac{|p(\mathbf{r})|^2}{2\rho c} r^2 \sin\theta d\theta d\phi \tag{5.5}$$

where $p(\mathbf{r})$ is the complex acoustic pressure amplitude at a location in space expressed in spherical coordinates, $\mathbf{r} = (r, \theta, \phi)$ at frequency ω.

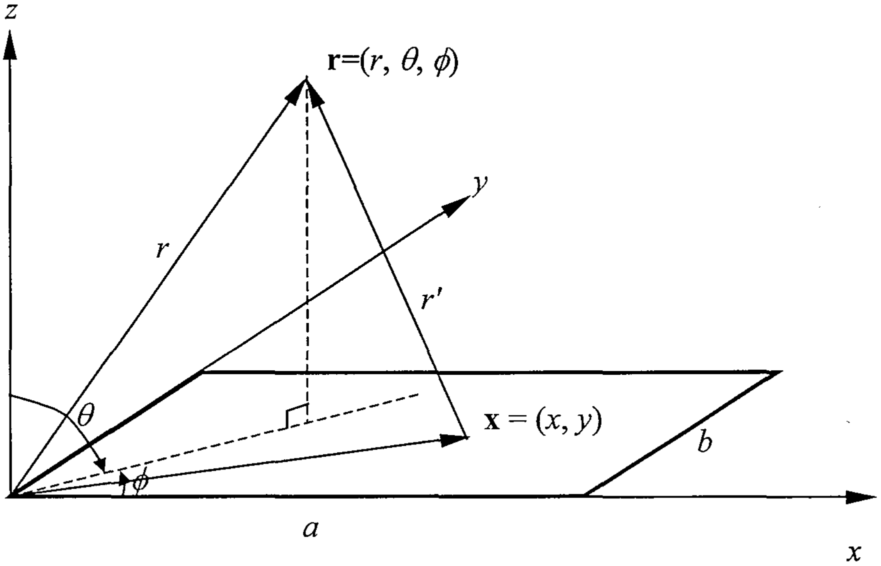

Figure 5.2. Coordinate system of a vibrating rectangular plate.

The complex acoustic pressure amplitude $p(\mathbf{r})$ can be written in terms of the plate surface velocity using the Rayleigh integral [44],

$$p(\mathbf{r}) = \frac{jk\rho c}{2\pi} \int_s v(\mathbf{x}) \frac{e^{-jkr'}}{r'} d\mathbf{x} \tag{5.6}$$

where $v(\mathbf{x})$ is the complex surface normal velocity amplitude at location $\mathbf{x} = (x, y)$, $k = \omega/c$ is the acoustic wavenumber and the integral is evaluated over the plate surface S. The distance $r' = |\mathbf{r} - \mathbf{x}|$.

The velocity $v(\mathbf{x})$ at any location $\mathbf{x}$ on the structure can be found by superposing the modal contributions from each mode of structural vibration of the plate as

$$v(\mathbf{x}) = \sum_{m=1}^{\infty}\sum_{n=1}^{\infty} u_{mn}\varphi_{mn}(\mathbf{x}) \tag{5.7}$$

where u_{mn} is the complex velocity amplitude of the mode (m, n), $\varphi_{mn}(\mathbf{x})$ is the value of the associated mode shape function at the location $\mathbf{x}$, and m, n are the indices of the modes. u_{mn} depends on the form of the excitation and on frequency. The mode shape function $\varphi_{mn}(\mathbf{x})$ for the simply supported rectangular plate can be expressed as

$$\varphi_{mn}(x, y) = \sin\left(\frac{m\pi x}{a}\right)\sin\left(\frac{n\pi y}{b}\right) \tag{5.8}$$

Substituting equations (5.7) and (5.8) into (5.6), and rearranging the order of summation and integral, the sound pressure is given by

$$p(\mathbf{r}) = \sum_{m=1}^{\infty}\sum_{n=1}^{\infty} u_{mn}\left\{\frac{jk\rho c}{2\pi}\int_{s}\varphi_{mn}(\mathbf{x})\frac{e^{-jkr'}}{r'}d\mathbf{x}\right\} = \sum_{m=1}^{\infty}\sum_{n=1}^{\infty} u_{mn}A_{mn}(\mathbf{r}) \tag{5.9}$$

From Wallace [46], the term in the brackets, called $A_{mn}(\mathbf{r})$ here, is given by

$$A_{mn}(\mathbf{r}) = jk\rho c\frac{e^{-jkr}}{2\pi r}\frac{ab}{\pi^2 mn}\left[\frac{(-1)^m e^{j\alpha}-1}{\left(\frac{\alpha}{m\pi}\right)^2-1}\right]\left[\frac{(-1)^n e^{j\beta}-1}{\left(\frac{\beta}{n\pi}\right)^2-1}\right] \tag{5.10}$$

where $\alpha = ka\sin\theta\cos\phi$ and $\beta = kb\sin\theta\sin\phi$, and $r = |\mathbf{r}|$.

The substitution of equation (5.9) into equation (5.5) gives the total radiated power of the plate as

$$W = \sum_{m=1}^{\infty}\sum_{n=1}^{\infty}\sum_{m'=1}^{\infty}\sum_{n'=1}^{\infty}\left\{u_{mn}u_{m'n'}^{*}\int_{0}^{2\pi}\int_{0}^{\pi/2}\frac{A_{mn}(\mathbf{r})A_{m'n'}^{*}(\mathbf{r})}{2\rho c}r^2\sin\theta d\theta d\phi\right\} \tag{5.11}$$

where m' and n' are used to distinguish m and n in the conjugate. From this equation, it can be seen that the total radiated power depends on the contribution of combinations of modes. The contribution is usually referred to as the self-modal radiation for $m = m'$ and $n = n'$, and cross-modal radiation for either $m \neq m'$ or $n \neq n'$.

Equation (5.11) can also be expressed in a matrix form,

$$W = \mathbf{u}^{\mathrm{T}}\mathbf{D}\mathbf{u} \tag{5.12}$$

where $\mathbf{u}$ is a column vector of terms u_{mn} and $\mathbf{D}$ is a matrix of integral terms. The diagonal elements of $\mathbf{D}$ are the self-modal terms and the off-diagonal elements are the mutual radiation terms. According to Snyder and Tanaka [54], cross-modal radiation only occurs between a pair of modes with a similar index-type (i.e. either both odd or both even in each direction). Hence, many off-diagonal terms are zero and only a quarter of the matrix elements are non-zero.

It is clear that the calculation of total radiation efficiency requires the calculation of both self- and cross-modal radiation terms described in equation (5.11). At the same time, a knowledge of the excitation is also required to determine **u**.

5.3.2 RESPONSE TO POINT FORCE

Consider a point force applied on the plate at location (x_0, y_0). The modal velocity amplitude is given by [35]

$$u_{mn} = \frac{j\omega F \varphi_{mn}(x_0, y_0)}{\left[\omega_{mn}^2(1+j\eta) - \omega^2\right] M_{mn}} \tag{5.13}$$

where F is the force amplitude, ω_{mn} is the natural frequency, η is the damping loss factor, assuming hysteretic damping, and M_{mn} is the modal mass that is given by

$$M_{mn} = \int_S \rho_s h \varphi_{mn}^2(x, y)\, dS = \frac{1}{4}\rho_s hab = \frac{M}{4} \tag{5.14}$$

where ρ_s and h are the density and thickness of the plate, M is the mass the plate and use is made of the form of φ_{mn} from equation (5.8). The natural frequencies ω_{mn} are given by

$$\omega_{mn} = \left(\frac{B}{\rho_s h}\right)^{\frac{1}{2}} \left[\left(\frac{m\pi}{a}\right)^2 + \left(\frac{n\pi}{b}\right)^2\right] \tag{5.15}$$

where B is the bending stiffness of the plate.

5.3.3 AVERAGE OVER FORCING POINTS

For the purpose of obtaining a general result for the total radiated power, the average of all possible locations of the uncorrelated point forces on the plate is considered. This averaged radiated power can be written as

$$\overline{W} = \frac{1}{ab}\int_0^a\int_0^b W\, dx_0 dy_0 = \sum_{m=1}^{\infty}\sum_{n=1}^{\infty}\sum_{m'=1}^{\infty}\sum_{n'=1}^{\infty}\left\{\frac{1}{ab}\int_0^a\int_0^b u_{mn}u_{m'n'}^{*}\, dx_0 dy_0 \int_0^{2\pi}\int_0^{\pi/2}\frac{A_{mn}(\mathbf{r})A_{m'n'}^{*}(\mathbf{r})}{2\rho c} r^2 \sin\theta\, d\theta\, d\phi\right\} \tag{5.16}$$

where $\int_0^a\int_0^b u_{mn}u^*_{m'n'}dx_0dy_0 = \int_0^a\int_0^b \left[\frac{j\omega F\varphi_{mn}\left(x_0,y_0\right)}{\left[\omega^2_{mn}\left(1+j\eta\right)-\omega^2\right]M_{mn}}\frac{-j\omega F^*\varphi_{m'n'}\left(x_0,y_0\right)}{\left[\omega^2_{m'n'}\left(1-j\eta\right)-\omega^2\right]M_{m'n'}}\right]dx_0dy_0$

(5.17)

Because of the orthogonality of the eigenfunctions, it can be seen from equation (5.17) that equation (5.16) can be simplified to

$$\overline{W} = \sum_{m=1}^{\infty}\sum_{n=1}^{\infty}\left\{\frac{1}{ab}\int_0^a\int_0^b u_{mn}u^*_{mn}dx_0dy_0\int_0^{2\pi}\int_0^{\pi/2}\frac{A_{mn}\left(\mathbf{r}\right)A^*_{mn}\left(\mathbf{r}\right)}{2\rho c}r^2\sin\theta d\theta d\phi\right\} \tag{5.18}$$

where each term in the sum is the power radiated by a single mode. Hence the cross-modal terms have been eliminated. After some algebraic manipulations, equation (5.18) can also be written as

$$\overline{W} = \sum_{m=1}^{\infty}\sum_{n=1}^{\infty}\overline{W}_{mn} \tag{5.19}$$

where $\overline{W}_{mn}$ is given by

$$\overline{W}_{mn} = \overline{\left|u_{mn}\right|^2}\int_0^{2\pi}\int_0^{\pi/2}\frac{A_{mn}\left(\mathbf{r}\right)A^*_{mn}\left(\mathbf{r}\right)}{2\rho c}r^2d\theta d\phi \tag{5.20}$$

and $\overline{\left|u_{mn}\right|^2}$ represents the modulus squared of the modal velocity amplitude u_{mn}, averaged over all force positions. This is given by

$$\overline{\left|u_{mn}\right|^2} = \frac{1}{ab}\int_0^a\int_0^b u_{mn}u^*_{mn}dx_0dy_0 = \frac{4\omega^2\left|F\right|^2}{M^2\left[\left(\omega^2_{mn}-\omega^2\right)^2+\eta^2\omega^4_{mn}\right]} \tag{5.21}$$

The modal radiation efficiency σ_{mn} is hence given by

$$\sigma_{mn} = \frac{\overline{W}_{mn}}{\rho cab\overline{\left\langle\overline{v^2_{mn}}\right\rangle}} = \frac{4\int_0^{2\pi}\int_0^{\pi/2}A_{mn}\left(\mathbf{r}\right)A^*_{mn}\left(\mathbf{r}\right)r^2d\theta d\phi}{\left(\rho c\right)^2ab} \tag{5.22}$$

where $\overline{\left\langle\overline{v^2_{mn}}\right\rangle}$ represents the spatially-averaged mean square velocity in mode (m, n) averaged over all possible force positions, which is given by

$$\overline{\left\langle\overline{v^2_{mn}}\right\rangle} = \frac{1}{S}\int_S\left\langle\overline{v^2_{mn}}\right\rangle dx_0dy_0 = \frac{1}{2M^2}\frac{\omega^2\left|F\right|^2}{\left[\left(\omega^2_{mn}-\omega^2\right)^2+\eta^2\omega^4_{mn}\right]} = \frac{\overline{\left|u_{mn}\right|^2}}{8} \tag{5.23}$$

After some algebraic manipulations to equation (5.22), the modal radiation efficiency σ_{mn} can be given by

$$\sigma_{mn} = \frac{64k^2ab}{\pi^6 m^2 n^2}\int_0^{\pi/2}\int_0^{\pi/2}\left\{\frac{\substack{\cos\\ \sin}\left(\frac{\alpha}{2}\right)\substack{\cos\\ \sin}\left(\frac{\beta}{2}\right)}{\left[\left(\frac{\alpha}{m\pi}\right)^2-1\right]\left[\left(\frac{\beta}{n\pi}\right)^2-1\right]}\right\}^2 \sin\theta d\theta d\phi \tag{5.24}$$

which corresponds to the expression given by Wallace [46].

Having obtained the total radiated power in terms of a summation of modal radiated power, the average radiation efficiency considering all possible point force locations is readily given by

$$\sigma = \frac{\sum_{m=1}^{\infty}\sum_{n=1}^{\infty}\overline{W}_{mn}}{\rho cab\overline{\left\langle v^2\right\rangle}} = \frac{\sum_{m=1}^{\infty}\sum_{n=1}^{\infty}\rho cab\sigma_{mn}\overline{\left\langle v_{mn}^2\right\rangle}}{\rho cab\overline{\left\langle v^2\right\rangle}} = \frac{\sum_{m=1}^{\infty}\sum_{n=1}^{\infty}\sigma_{mn}\overline{\left\langle v_{mn}^2\right\rangle}}{\overline{\left\langle v^2\right\rangle}} \tag{5.25}$$

where $\overline{\left\langle v^2\right\rangle}$ is the spatially-averaged mean square velocity averaged over all possible force locations. This is given by [35]

$$\overline{\left\langle v^2\right\rangle} = \frac{\omega^2|F|^2}{2M^2}\sum_{m=1}^{\infty}\sum_{n=1}^{\infty}\frac{1}{\left[\left(\omega_{mn}^2-\omega^2\right)^2+\eta^2\omega_{mn}^4\right]} = \sum_{m=1}^{\infty}\sum_{n=1}^{\infty}\overline{\left\langle v_{mn}^2\right\rangle} \tag{5.26}$$

Hence,

$$\sigma = \frac{\sum_{m=1}^{\infty}\sum_{n=1}^{\infty}\sigma_{mn}\left[\left(\omega_{mn}^2-\omega^2\right)^2+\eta^2\omega_{mn}^4\right]^{-1}}{\sum_{m=1}^{\infty}\sum_{n=1}^{\infty}\left[\left(\omega_{mn}^2-\omega^2\right)^2+\eta^2\omega_{mn}^4\right]^{-1}} \tag{5.27}$$

It is noted that this average radiation efficiency depends only on the self-modal radiation due to the averaging over all possible force locations. Equation (5.25) is stated by Cremer and Heckl [35], who analysed the radiated power using a wavenumber transform but without explicitly averaging over excitation points. However, as shown here, it is only strictly valid when such averaging is included.

Using the modal summation approach, based on equation (5.25), various values of the damping of the plate can be taken into account.

5.4 COMPARISON WITH CONVENTIONAL MODAL AVERAGE RESULTS

5.4.1 EXAMPLE RESULTS

Based on equation (5.25), the average radiation efficiency of a rectangular plate of dimensions 0.5 × 0.6 × 0.003 m is calculated as an example. The plate is chosen as aluminium with Young's modulus 7.1 × 10^{10} N/m^2, density 2700 kg/m^3 and a damping loss factor $\eta = 0.1$. This level of damping is used here for clarity although other values of damping are considered later. Calculations are implemented using 40 frequency points per decade that ensure 3 points within the half-power bandwidth of resonances.

Figure 5.3 presents the spatially-averaged mean square velocity from equation (5.26) and the spatially-averaged mean square velocity for each mode from equation (5.23) for the rectangular plate with a unit force amplitude. The infinite numbers of modes in these two equations are truncated to a finite number. For this example rectangular plate, all modes with natural frequencies below 10 kHz are included in the calculation.

Figure 5.4 presents the modal and average radiation efficiency of the above rectangular plate. It can be seen that below 70 Hz the radiation efficiency of the first mode determines the overall result. This is due to the dominance of this mode in the response, see Figure 5.3, and its high value of σ_{mn}. Above this frequency the average result drops, only rising to 1 at the critical frequency (see below) of about 4 kHz.

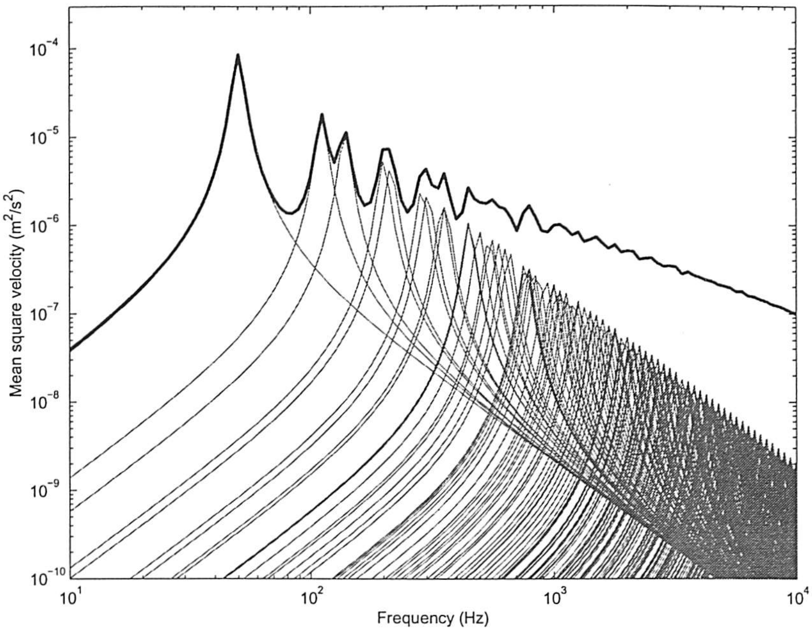

Figure 5.3. Average mean square velocity of a rectangular plate showing contribution from modes (0.6 × 0.5 × 0.003 m aluminium plate with $\eta = 0.1$) —: modal mean square velocity, thick line: total mean square velocity.

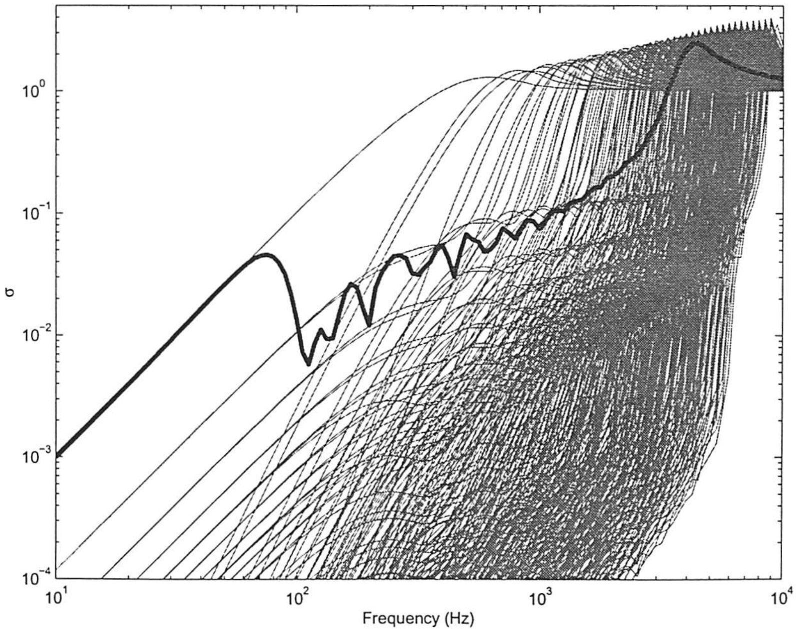

Figure 5.4. Modal and average radiation efficiency of a rectangular plate (0.6 × 0.5 × 0.003 m aluminium plate with $\eta = 0.1$) —: modal radiation efficiency, thick line: average radiation efficiency.

5.4.2 CONVENTIONAL MODAL AVERAGE RESULTS

Based on the assumption of a diffuse field in the plate, Maidanik [45] has produced formulae for the modal-average radiation of a lightly damped plate. These can be written as [53]

$$\sigma = \begin{cases} \dfrac{4S}{c^2} f^2 & \text{for } f < f_{1,1} \quad \text{(a)} \\ \dfrac{4\pi^2}{c^2 S} \dfrac{B}{m''} & \text{for } f_{1,1} < f < f_e, \quad f_e = \dfrac{3c}{P} \quad \text{(b)} \\ \dfrac{Pc}{4\pi^2 S f_c} \times \dfrac{\left(1-\alpha^2\right)\ln\left(\dfrac{1+\alpha}{1-\alpha}\right) + 2\alpha}{\left(1-\alpha^2\right)^{3/2}} & \text{for } f_e < f < f_c, \quad \alpha = \sqrt{\dfrac{f}{f_c}} \quad \text{(c)} \\ 0.45\sqrt{\dfrac{P f_c}{c}} & \text{for } f = f_c \quad \text{(d)} \\ \left(1 - \dfrac{f_c}{f}\right)^{-1/2} & \text{for } f > f_c \quad \text{(e)} \end{cases} \tag{5.28}$$

where c is speed of sound, f is frequency, P is the perimeter of the plate, S is the area of the plate, $f_{1,1}$ is the first resonance frequency of the plate, B is the bending stiffness, m'' is the mass per unit area of the plate and f_c is the critical frequency, $f_c = (m''/B)^{1/2} c^2 / 2\pi$. The first and second terms have been added here from [53] to represent the monopole radiation from the motion below the first resonance frequency and radiation in the so-called corner mode region. NB, an additional term in the third expression is presented in [45] but is often omitted, see also [50].

Figure 5.5 presents a comparison of the results from equation (5.28) and the modal summation approach. The same plate is used as above but now has a damping loss factor 0.0005. The calculation is carried out using 4000 points per decade. The curve shown in Figure 5.5 has been converted into one-third octave bands for clarity. The comparison shows that equation (5.28) gives a good agreement with the numerical result at almost all frequencies. There is some fluctuation of the numerical result between the fundamental natural frequency (at 50 Hz) and about 500 Hz. It is well known that this frequency range is dominated by 'corner' modes (modes with $ka \ll 1$ and $kb \ll 1$). For these modes sound radiation is effectively limited to the corners of the plate and the radiation efficiency is approximately constant with frequency. As frequency increases, the radiation efficiency increases until the critical frequency. This increasing region corresponds to the occurrence of 'edge' modes ($ka < 1, kb > 1$ or $ka > 1, kb < 1$) where radiation is from two opposite edges [87].

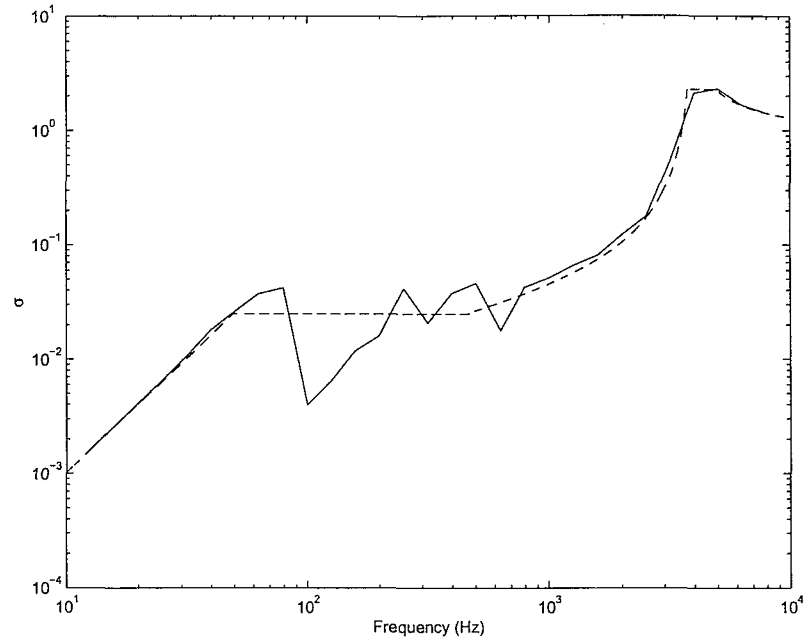

Figure 5.5. Average radiation efficiency of a rectangular plate (0.6 × 0.5 × 0.003 m aluminium plate with $\eta = 0.0005$) —: average radiation efficiency from the modal summation approach, – –: equation (5.28).

5.4.3 INCLUSION OF NEAR-FIELD EFFECTS

Cremer, Heckl and Ungar [35] and Fahy [87] have given analyses for the sound radiation from the vibration near-field around the forcing point for a damped rectangular plate. From this, the equivalent radiation efficiency from the near-field of a point force, that is normalised by the mean square velocity of the plate, can be expressed as

$$\sigma_n = \frac{4}{\pi}\frac{f}{f_c}\eta \qquad \text{for } f < f_c \qquad (5.29)$$

It is also noted from Cremer et al. [35] that, when the radiated power is studied, the power radiated by the near-field does not depend on the damping loss factor whereas the modal response does. The increase in radiation efficiency with increase in damping is, in effect, due to the reduction in the modal response and thus the greater importance of the near-field.

The power radiated is obtained using this value of σ with the mean square velocity of the whole plate. The overall radiation efficiency of a damped point-excited plate can thus be given by [87]

$$\sigma = \sigma_0 + \sigma_n \qquad \text{for } f < f_c \tag{5.30}$$

where σ_0 is the radiation efficiency for very lightly damped plates, which is given by equation (5.28).

The result from equation (5.30) agrees well with that from the modal summation approach. Figure 5.6 presents the results for three values of the damping loss factor. It can be seen that the radiation efficiency is independent of the damping loss factor for frequencies below the fundamental natural frequency and above the critical frequency, but depends on the loss factor in the corner and edge mode region. This increase in radiation efficiency is proportional to the damping loss factor and can also be understood qualitatively in terms of the modal summation approach. Due to the increase in the damping, the amplitude of the modal response at resonance to a point force decreases. So does the spatially averaged mean square velocity. Hence relatively more modes will contribute significantly to the response in this frequency range so that the average radiation efficiency increases.

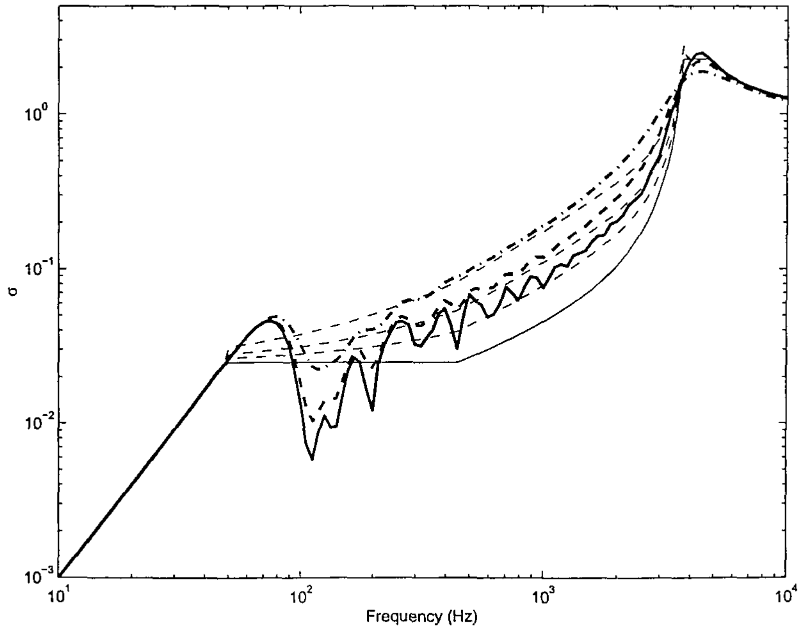

Figure 5.6. The average radiation efficiency from the modal summation and equation (5.30). Thick line: $\eta = 0.1$, thick dashed: $\eta = 0.2$, thick dash-dot: $\eta = 0.4$, — formula by Maidanik, – – equation (5.30).

5.4.4 RADIATION EFFICIENCY AT THE CRITICAL FREQUENCY

The radiation efficiency at the critical frequency, given in equation (5.28), can also be represented in terms of the non-dimensional parameter $k_c a$ as

$$\sigma = 0.45\left(k_c a\right)^{\frac{1}{2}}\left(\frac{\gamma+1}{\gamma\pi}\right)^{\frac{1}{2}} \tag{5.31}$$

where k_c is the wavenumber at the critical frequency, a is the length of the shorter edges of the plate (i.e. $a \le b$), γ denotes the ratio of the lengths of shorter edges to longer edges $\gamma = a/b$.

Leppington [50] found that equation (5.31) overestimates the radiation efficiency for plates with large aspect ratios and presented a modified formula as

$$\sigma = \left(k_c a\right)^{\frac{1}{2}} H(\gamma) \tag{5.32}$$

where k_c, a and γ have the same meaning as in equation (5.31) and the function $H(\gamma)$ is given by

$$H(x) = \frac{4}{15\pi^{\frac{3}{2}}} x^{\frac{1}{2}} \int_0^1 (5-t)\left\{\left(t^2+x^2\right)^{-\frac{3}{4}} + \left(1+x^2t^2\right)^{-\frac{3}{4}}\right\} dt \tag{5.33}$$

For $0.2 < x < 1$, a good approximation of $H(x)$ is given by $H(x) = 0.5 - 0.15x$.

It can be noted that, for a given aspect ratio, both equations (5.31) and (5.32) will give a value of radiation efficiency for the critical frequency smaller than unity for $k_c a$ smaller than a certain value. For instance, equation (5.31) gives results less than unity for $k_c a \le 7.6$ for $\gamma = 1$ and $k_c a \le 2.6$ for $\gamma = 0.2$ while equation (5.32) for $k_c a \le 7.6$ for $\gamma = 1$, $k_c a \le 4.2$ for $\gamma = 0.2$. Thick, stiff (or small) plates can have a critical frequency near to, or lower than, their first natural frequency, corresponding to a small value of $k_c a$. In this case, equations (5.31) and (5.32) are not appropriate to estimate the radiation efficiency. At their 'critical frequency' these plates vibrate as piston which is small compared with the acoustic wavelength and therefore radiate inefficiently. The concept of critical frequency is not meaningful in this context.

Using the modal summation approach of Section 5.3, the radiation efficiencies at the critical frequency have been reinvestigated. Figure 5.7 presents a comparison of the results from modal summation and according to equations (5.31) and (5.32) for square plates ($\gamma = 1$). For square plates, equations (5.31) and (5.32) give similar results to each other. Results are given for two values of damping loss factor for the plate. The results presented from the modal summation are the maximum radiation efficiency, which occurs around, or just above, the critical frequency. Both narrow-band (300 frequency points per decade) and one-third octave band results from the modal summation are plotted. The latter are included since predictions are often made in one-third octave bands, in which case the precise details of a narrow peak are less important than the frequency average behaviour. The one-third octave band here is centred about the frequency at which the maximum radiation efficiency occurs.

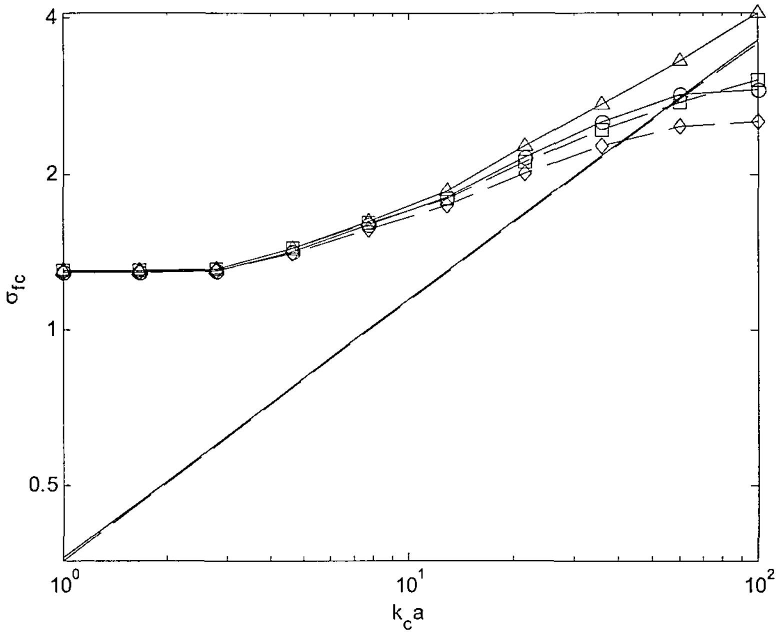

Figure 5.7. Maximum radiation efficiencies from modal summation.
$\gamma = 1$, damping loss factor 0.01, –o–: 1/3 octave, –Δ–: narrow band, —: equation (5.32), – –: equation (5.31), –◊–: 1/3 octave $\eta = 0.1$, –□–: narrow $\eta = 0.1$.

For large values of $k_c a$, the maximum value from the narrow-band results is larger than that from 1/3 octave bands. The narrow-band results for $\eta = 0.01$ appear to tend towards the approximate results for very large values of $k_c a$, but the result from one-third octave bands is lower than this at large $k_c a$. Damping does have certain effects on the results from the modal summation approach. Figure 5.7 includes corresponding results for a damping loss factor of 0.1. The radiation efficiency at the critical frequency will decrease as the damping loss factor increases for large values of $k_c a$. As damping increases, the response differs increasingly from a free wave of wavelength equal to the acoustic wavelength, and the coincidence effect will reduce. For $k_c a$ smaller than 10, the radiation efficiency at the critical frequency is largely independent of damping loss factor as here the boundaries disturb the coincidence phenomenon to a greater extent.

For $k_c a$ smaller than 3, the maximum radiation efficiency tends to a constant value of 1.3 that is actually determined by the maximum modal radiation efficiency of the fundamental mode (see Figure 5.4) rather than the result at the critical frequency. Figure 5.8 presents examples of the average radiation efficiencies of square plates with different thickness and $\eta = 0.01$ calculated using the modal summation approach. In each case the critical frequency is also marked. For the thickest plate shown, the maximum radiation efficiency is not associated with the critical frequency. As the thickness reduces the maximum value occurs at frequencies that are progressively closer to the corresponding critical frequency.

Corresponding investigations have been carried out for a plate with $\gamma = 0.2$. Figure 5.9 presents the comparison of the results from modal summation and equations (5.31) and (5.32). Damping loss factors of 0.01 and 0.1 again are used in these calculations. For large $k_c a$, equation (5.32) slightly overestimates the radiation efficiency at the critical frequency compared with the result from the modal summation. The result from equation (5.31) is higher still. For $k_c a$ smaller than 2, the maximum radiation efficiency tends to a constant value (1.2) as before. Results were not produced for larger values of $k_c a$ due to the very long computation times required, but it can be anticipated that they will drop below the lines corresponding to the approximate formula.

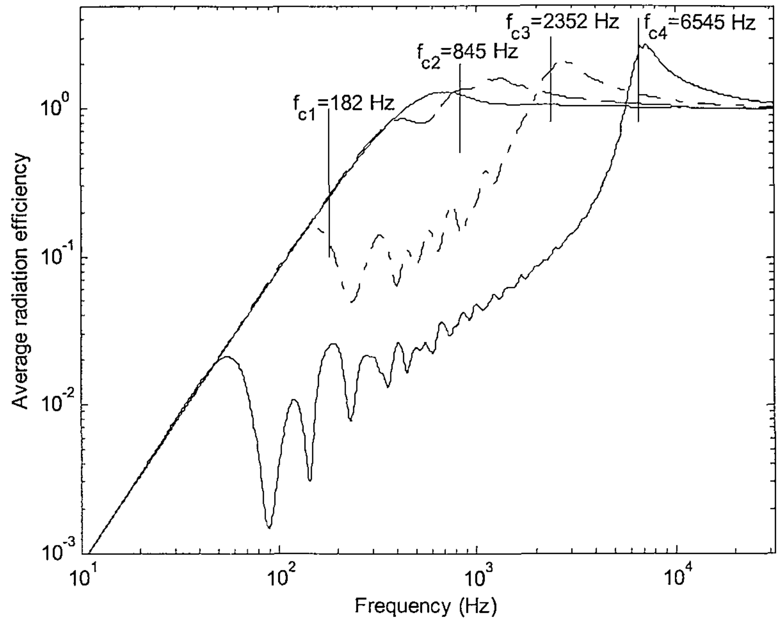

Figure 5.8. Average radiation efficiency of plate 0.5 × 0.5m with several different thickness, η = 0.01.
(— h = 1.8 mm, ka = 60.0, · – · h = 5.1 mm, ka = 21.5,
– – h = 14 mm, ka = 7.74, thick line: h = 66 mm, ka = 1.67).

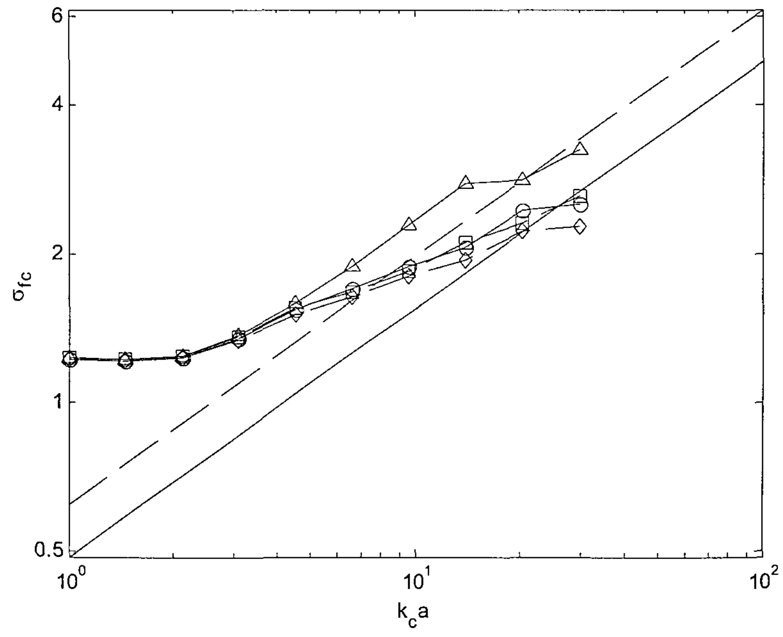

Figure 5.9. Maximum radiation efficiencies from modal summation (γ = 0.2)
–o–1/3 octave η = 0.01, –Δ–: narrow band, η = 0.01 —: equation (5.32),
– –: equation (5.31), –◇–: 1/3 octave band η = 0.1, –□–: narrow η = 0.1.

In order to find a general relation between the maximum average radiation efficiency and the value of $k_c a$, the analysis has been extended to include plates with different values of

γ. Figure 5.10 shows the results for seven different aspect ratios obtained from the modal summation. All the results are given in one-third octave bands. For $k_c a < 3$, the radiation efficiency tends to a constant value between 1.2 and 1.3 for different aspect ratios, determined by the modal radiation efficiency of the fundamental mode. For $k_c a > 3$, the radiation efficiency increases approximately in proportion to $(k_c a)^{1/4}$, rather than $(k_c a)^{1/2}$ as given in equation (5.31) and (5.32). Moreover the result appears to be only weakly dependent on the aspect ratio as Figure 5.11 shows. These results can be summarised by an approximate expression as

$$\sigma_c \approx \begin{cases} 1.2-1.3 & \text{for } k_c a \le 3 \\ (k_c a)^{1/4} & \text{for } k_c a > 3 \end{cases} \tag{5.34}$$

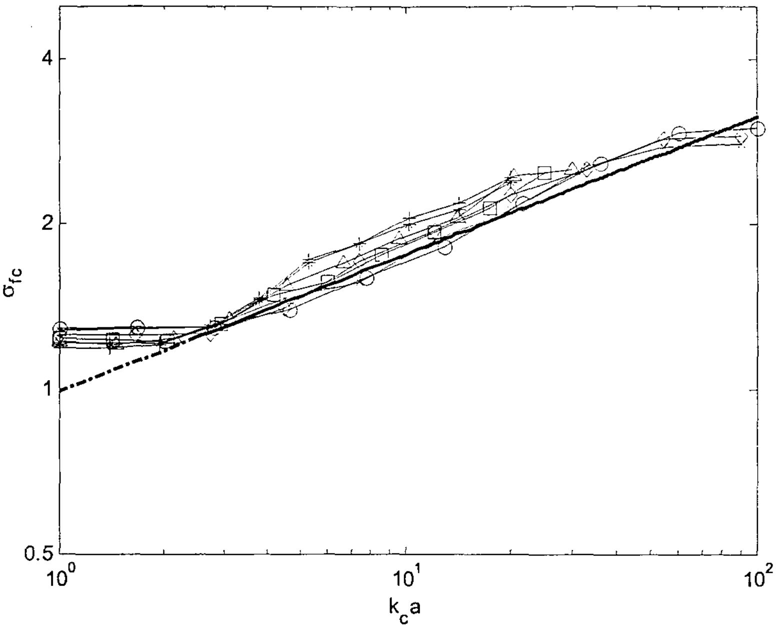

Figure 5.10. Radiation efficiencies at the critical frequencies from modal summation for different aspect ratios in 1/3 octave band for $\eta = 0.01$ (thick line: equation (5.34), –o– : $\gamma = 1$, –x– : $\gamma = 0.8$, –◇– : $\gamma = 0.6$, –□– : $\gamma = 0.4$, –△–: $\gamma = 0.2$, –*– : $\gamma = 0.1$, –+– : $\gamma = 0.16/3$).

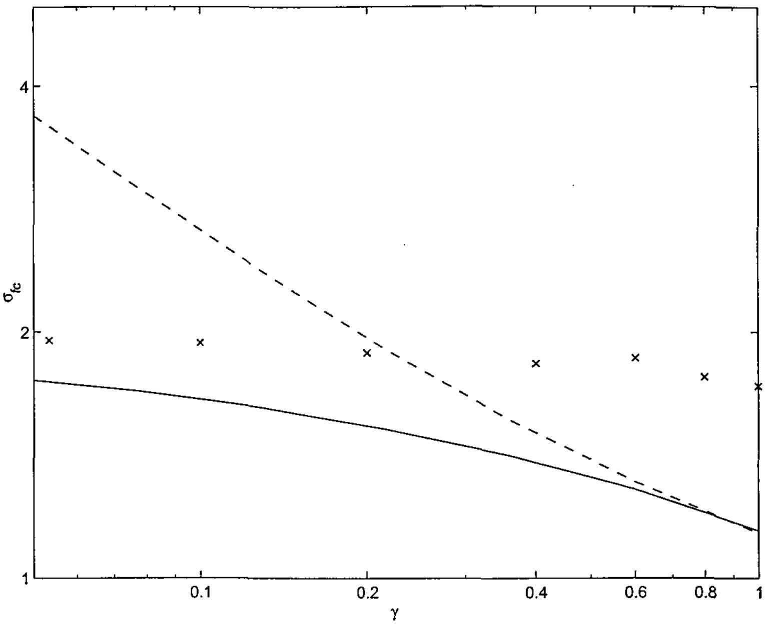

Figure 5.11. Maximum radiation efficiencies from modal summation for $k_c a = 10$.
× : modal summation, —: equation (5.32), – –: equation (5.31),

5.5 RADIATION EFFICIENCY OF STRIPS

5.5.1 RESULTS FROM THE MODAL SUMMATION APPROACH

Next the modal summation approach technique, described in Section 5.3, is used to study the radiation from a strip, that is a plate with a large aspect ratio, or small value of γ.

Figure 5.12 presents the average mean square velocity for a unit force amplitude of a plate with dimensions 0.16 × 3.0 × 0.003 m as a sum of the individual modal contributions in a manner similar to Figure 5.3. A damping loss factor $\eta = 0.1$ is used. This plate has an aspect ratio $\gamma = 0.053$. The natural frequencies of the strip can be seen as the peaks of the modal amplitudes in Figure 5.12. At about 290 Hz, the first mode corresponding to a half-wavelength of bending along the strip occurs (the fundamental mode, in which $m = 1$, $n = 1$). Above this frequency, modes of higher order (index n) bending waves along the strip occur close together in frequency. Just above 1.1 kHz, the first mode corresponding to a whole wavelength of bending across the strip occurs ($m = 2$). Above this 'cut-on' frequency of order $m = 2$, modes with $n = 1, 2, 3 \cdots$ occur closely spaced. At about 2.6 kHz, modes of order $m = 3$ can be seen to cut-on.

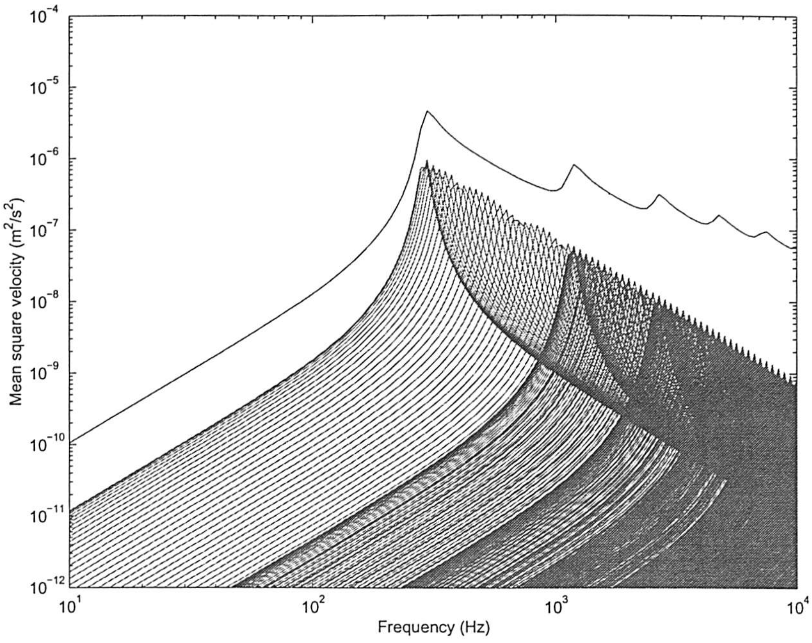

Figure 5.12. Average mean square velocity of the strip showing contributions from modes. 0.16 × 3 × 0.003 m aluminium strip with $\eta = 0.1$, —: modal mean square velocity, thick line: total mean square velocity.

Figure 5.13 presents both the modal radiation efficiency and average radiation efficiency calculated using the modal summation approach. The curve of average radiation efficiency of the strip has two broad peaks, which occur close to the fundamental mode (1, 1) and close to the second mode along the short edge (2, 1). If equation (5.28) is used to evaluate the average radiation efficiency for the strip, a significant underprediction is made above the first mode. This is shown in Figure 5.14. Even including the effect of damping using equation (5.30) does not account for the behaviour correctly. Moreover, below the fundamental mode, the radiation efficiency is considerably lower than given by equation (5.28). Only at frequencies well above the critical frequency is the formula able to predict the radiation efficiency well for the strip. Clearly, further investigation is required into the radiation behaviour of such a very narrow rectangular plate.

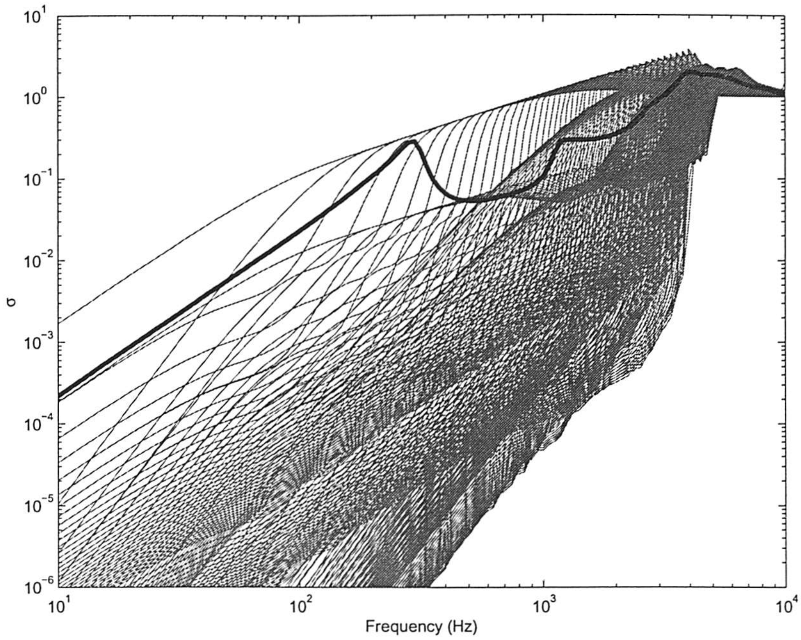

Figure 5.13. Modal and average radiation efficiency of the 0.16 × 3 × 0.003 m aluminium strip with $\eta = 0.1$, —: modal radiation efficiency, thick line: average radiation efficiency.

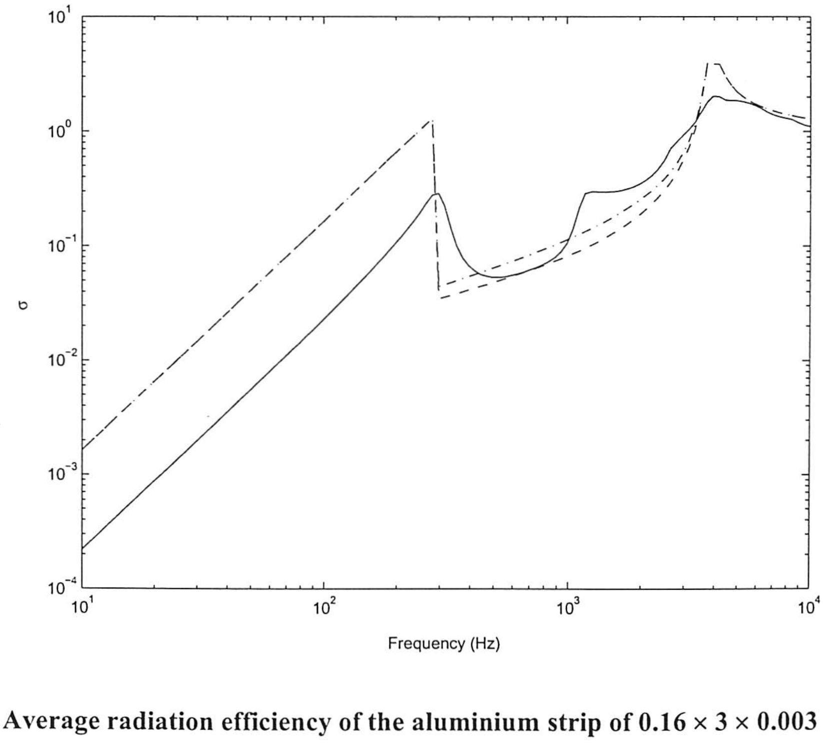

Figure 5.14. Average radiation efficiency of the aluminium strip of 0.16 × 3 × 0.003 m with $\eta = 0.1$. —: modal summation approach, – –: equation (5.28), · – ·: equation (5.30).

5.5.2 BELOW THE FUNDAMENTAL FREQUENCY

As seen in Section 5.2, the modes with odd indices (both *m* and *n*) are the most effective radiators for a rectangular plate when *ka, kb* << 1 [46, 45]. For frequencies well below the fundamental natural frequency, the average radiation efficiency of a plate with moderate aspect ratio is dominated by the fundamental mode (see Figure 5.4). This is not only because the radiation of the fundamental mode is most effective but also because its velocity amplitude is dominant (see equation (5.23) and Figure 5.3). The summation in both the denominator and numerator of equation (5.25) is dominated by the term corresponding to the fundamental mode. Therefore the average radiation efficiency of this plate below the fundamental natural frequency can be given by

$$\sigma \approx \frac{\sigma_{1,1}\overline{\left\langle v_{1,1}^2 \right\rangle}}{\overline{\left\langle v_{1,1}^2 \right\rangle}} = \sigma_{1,1} \tag{5.35}$$

The physical explanation of equation (5.35) is that the whole surface of the plate vibrates in phase in the form of the first mode and the plate motion radiates sound as a monopole.

However, the case of a strip differs from this because of its large aspect ratio. As a result of the large aspect ratio, many modes are distributed closely just above the fundamental frequency (see Figure 5.12). From equation (5.23), it can be seen that the mean square velocity of these modes will have very similar amplitude since ω_{mn} is similar in each case. As a result, the approximation of equation (5.35) will no longer be valid. Suppose *p* modes have significant values that contribute to the average radiation efficiency below the fundamental frequency. Then equation (5.25) should be rewritten as

$$\sigma \approx \frac{\sum_{n=1}^{p} \sigma_{1,n}\overline{\left\langle v_{1,n}^2 \right\rangle}}{\sum_{n=1}^{p} \overline{\left\langle v_{1,n}^2 \right\rangle}} \tag{5.36}$$

Since the fundamental mode is the most effective in sound radiation, the numerator of equation (5.36) is still dominated by the term corresponding to the fundamental mode. Thus equation (5.36) can be simplified as

$$\sigma \approx \frac{\sigma_{1,1}\overline{\left\langle v_{1,1}^2 \right\rangle}}{\sum_{n=1}^{p}\overline{\left\langle v_{1,n}^2 \right\rangle}} \tag{5.37}$$

It is now necessary to determine which modes of the strip will contribute to the average radiation efficiency. The mean square velocity of the mode (*m*, *n*) (equation (5.23))can be approximated by

$$\overline{\left\langle v_{m,n}^2 \right\rangle}(\omega) \approx \frac{\omega^2 |F|^2}{2M^2\omega_{m,n}^4\left(1+\eta^2\right)} \qquad \text{for } \omega \ll \omega_{mn} \tag{5.38}$$

The ratio of the mean square velocity of mode (1, *n*) to that of the fundamental mode is given by

$$\frac{\overline{\left\langle v_{1,n}^2 \right\rangle}}{\overline{\left\langle v_{1,1}^2 \right\rangle}} = \left(\frac{\omega_{1,1}}{\omega_{1,n}}\right)^4 \tag{5.39}$$

where $\omega_{1,1} = \sqrt{\frac{B}{m''}}\left[\left(\frac{\pi}{a}\right)^2 + \left(\frac{\pi}{b}\right)^2\right]$, $\omega_{1,n} = \sqrt{\frac{B}{m''}}\left[\left(\frac{\pi}{a}\right)^2 + \left(\frac{n\pi}{b}\right)^2\right]$. Writing $\Delta k_x = \pi/a$ and $\Delta k_y = \pi/b$, equation (5.39) can be rewritten as

$$\frac{\overline{\left\langle v_{1,n}^2 \right\rangle}}{\overline{\left\langle v_{1,1}^2 \right\rangle}} = \left(\frac{\Delta k_x^2 + \Delta k_y^2}{\Delta k_x^2 + n^2\Delta k_y^2}\right)^4 \tag{5.40}$$

For the case of a strip with $a << b$, $\Delta k_y << \Delta k_x$ and writing $\gamma = a/b$, gives

$$\frac{\overline{\left\langle v_{1,n}^2 \right\rangle}}{\overline{\left\langle v_{1,1}^2 \right\rangle}} \approx \left(\frac{\Delta k_x^2}{\Delta k_x^2\left(1+\gamma^2 n^2\right)}\right)^4 \approx \left(1+\gamma^2 n^2\right)^{-4} \tag{5.41}$$

The average radiation efficiency of the strip below the fundamental natural frequency can be rewritten as

$$\sigma = \frac{\sigma_{1,1}\overline{\left\langle v_{1,1}^2 \right\rangle}}{\sum_{n=1}^{p}\overline{\left\langle v_{1,1}^2 \right\rangle}\left(1+\gamma^2 n^2\right)^{-4}} = \frac{\sigma_{1,1}}{\sum_{n=1}^{p}\left(1+\gamma^2 n^2\right)^{-4}} \tag{5.42}$$

It has been found by numerical evaluation that $\sum_{n=1}^{p}\left(1+\gamma^2 n^2\right)^{-4}$ can be approximated as

$$\sum_{n=1}^{p}\left(1+\gamma^2 n^2\right)^{-4} \approx 0.485\left(\frac{1}{\gamma}-1\right) \qquad \text{for } p \text{ large and } \gamma \le 0.5 \tag{5.43}$$

Then the substitution of equation (5.43) into equation (5.42) gives

$$\sigma \approx \frac{\sigma_{1,1}}{0.485\left(\frac{1}{\gamma}-1\right)} \tag{5.44}$$

It can be noted that the average radiation efficiency of the strip depends on the aspect ratio and the radiation efficiency of the fundamental mode. Compared with the rectangular plate of the same area, the strip radiates less sound. In order to understand the characteristics of the strip radiation physically, it is instructive to simplify equation (5.44) further as

$$\sigma \approx \frac{\gamma}{0.485}\sigma_{1,1} \qquad \text{for } \gamma \le 0.1 \tag{5.45}$$

According to Wallace [46], the radiation efficiency of the fundamental mode for frequencies well below the fundamental natural frequency can be approximately given by

$$\sigma_{1,1} = \frac{32(ka)(kb)}{\pi^5} = \frac{128}{\pi^3 c^2} abf^2 \tag{5.46}$$

This is proportional to the area of the plate. For the case of the strip, equation (5.45) gives

$$\sigma \approx \frac{1}{0.485}\frac{a}{b}\frac{128}{\pi^3 c^2} abf^2 \approx \frac{264}{\pi^3 c^2} a^2 f^2 \approx \frac{8.5}{c^2} a^2 f^2 \tag{5.47}$$

The average radiation efficiency of the strip at frequencies well below the first natural frequency is thus found to be approximately proportional to the square of the short-edge length of the strip and is independent of the long-edge length.

In order to verify this conclusion, strips with different aspect ratios have been investigated using the numerical evaluation of equation (5.25) and the modal radiation efficiency from the numerical integration of equation (5.24). Example calculations have been carried out for strips with a short edge length of 0.16 m and long edge lengths of 1.5 m, 2.5 m and 3 m and two additional strips with long edge length 3 m having short edge lengths of 0.08 m and 0.32 m. The results are presented in Figure 5.15. It is seen that the three strips with the same width, 0.16 m, have very similar average radiation efficiencies and are indistinguishable at low frequency. The results also verify that the average radiation efficiency below the fundamental natural frequency is proportional to the square of the short-edge length of the strip. Equation (5.47) underestimates the average radiation efficiency slightly at low frequency if compared with the results from numerical calculations. This is because of the simplification from equation (5.36) to (5.37) by ignoring the contributions of other modes in the numerator. Actually, mode (1, 3) still has a significant contribution to the frequencies below the fundamental frequency.

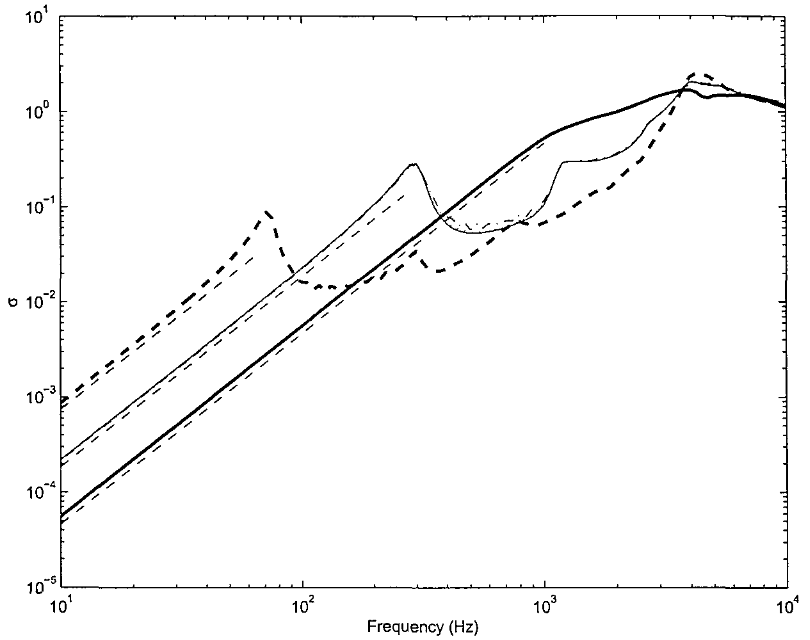

Figure 5.15. Average radiation efficiency of aluminium strips h = 0.003 m, η = 0.1, —: 0.16 × 3 m, · – ·: 0.16 × 1.5 m, · · ·: 0.16 × 2.5 m, thick solid line: 0.08 × 3 m, thick – –: 0.32 × 3 m, – –: from equation (5.47).

5.5.3 EFFECTS OF DAMPING

The average radiation efficiencies of the strip have been calculated for various damping values using the modal summation approach. These results are presented as one-third octave band spectra in Figure 5.16. (The narrow band results vary too rapidly with frequency for clear observations to be made). The average radiation efficiency is largely independent of the damping for frequencies below the fundamental natural frequency and above the critical frequency. However, the average radiation efficiency between the fundamental natural frequency and the critical frequency increases with an increase of damping. A quite large change occurs for the frequencies between the first two cut-on frequencies, where the radiation efficiency appears to be proportional to the damping loss factor. Figure 5.17 shows the variation of the average radiation efficiency with loss factor for the example 0.16 × 3.0 × 0.003 m strip. Corresponding results for the rectangular plate considered previously with 0.6 × 0.5 m are shown for comparison. It can be seen that the radiation efficiency of the strip is much more strongly dependent on damping than that of the plate considered previously. The results calculated using equation (5.30) for the plate and strip are also presented in Figure 5.17. It can be noted that equation (5.30) give better agreements with the result from the modal summation approach for the rectangular plate, especially for large damping. However, for the case of the strip, the damping effect on the near-field radiation cannot be estimated approximately.

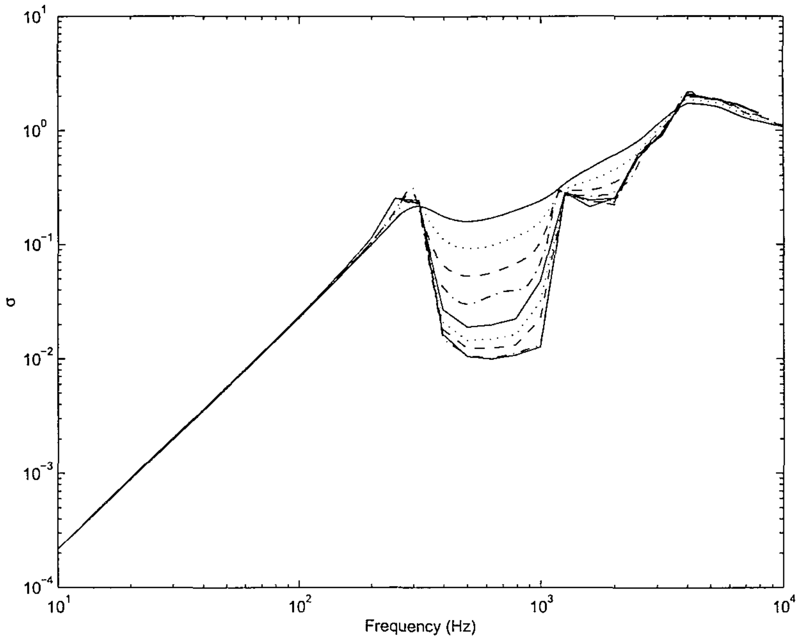

Figure 5.16. Average radiation efficiency of an aluminium strip (0.16 × 3 × 0.003 m) with different damping values, 0.4, 0.2, 0.1, 0.05, 0.02, 0.01, 0.005, 0.001, 0.0005 (from top to bottom).

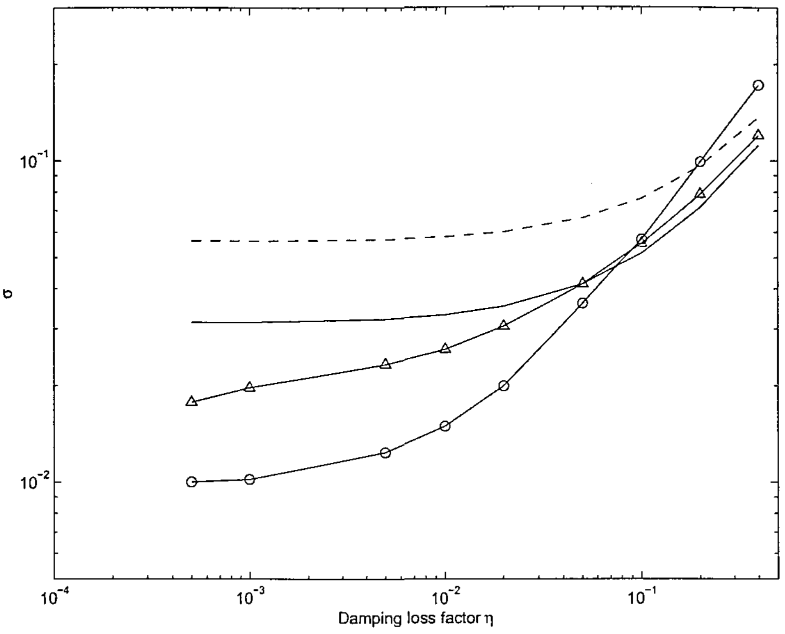

Figure 5.17. Radiation efficiency in 630 Hz one-third octave band as a function of loss factor –○– strip 0.16 × 3 × 0.003 m by modal summation, –Δ–: rectangular plate 0.6 × 0.5 × 0.003 m by modal summation, —: equation (5.30) for rectangular plate 0.6 × 0.5 ×0.003 m, – –: equation (5.30) for strip.

Figure 5.18 shows the effect of damping on the approximated radiation efficiency using equation (5.30). The average radiation efficiency of the strip is shown for damping loss factors of 0.1, 0.2 and 0.4. These results are compared with the corresponding results from the modal summation. Not surprisingly, poor agreement is obtained. The cause of this disagreement can be attributed qualitatively to an overprediction in the modal radiation and an underprediction of the near-field radiation.

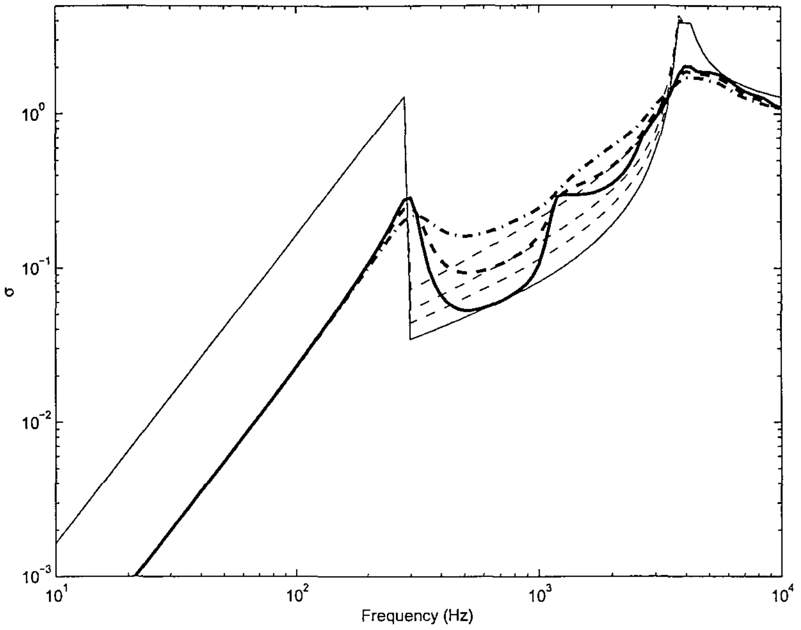

Figure 5.18. Comparison of the average radiation efficiency for the strip between the modal summation and equation (5.30). Thick line: $\eta = 0.1$, thick dash line: $\eta = 0.2$, thick dot-dash line: $\eta = 0.4$,—: equation (5.28), – –: equation (5.30).

The sparse distribution of the modes in k-space means that the assumption of a high modal density is not applicable and so Maidanik's formulae for calculating the average radiation efficiency for low damping may no longer be appropriate. This can be demonstrated in a comparison of the acoustic and structural wavenumbers, shown in Figure 5.19. At the fundamental natural frequency, the wavenumber in the plate is k_{b1} while that in air is k_{a1}, which is much smaller. The first few structural modes with $m = 1$ are 'edge' modes ($k_y < k_{a1}$), so the radiation at and just above the cut-on frequency is quite large. For a frequency between the first and second cut-on frequencies, k_{b2} is the wavenumber in the plate and k_{a2} is that in air. The radiation is now dominated by 'corner' modes ($k_y > k_{a2}$) and thus it is fairly low. For frequencies close to the second cut-on frequency, corresponding to k_{a3} for the acoustical wavenumber and k_{b3} for the structural one, the radiation is again controlled mainly by 'edge' modes. This causes another broad peak around this frequency. For frequencies above the second cut-on frequency, the distribution of modes becomes more even so that the average radiation efficiency formulae gradually become more appropriate with increasing frequency.

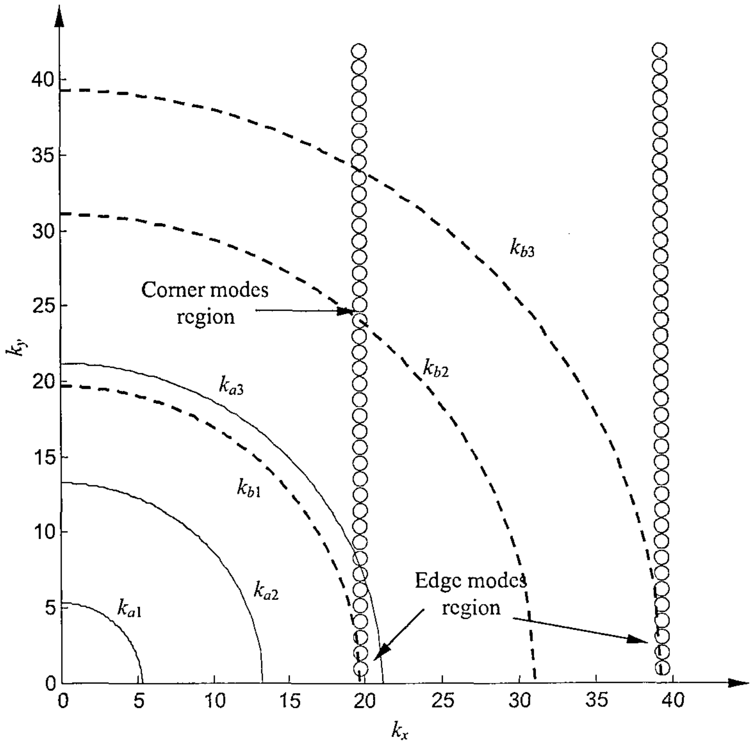

Figure 5.19. Comparison of acoustical and structural wavenumber showing the characteristic of the modal radiation of the strip for frequencies between the fundamental and second cut-on natural frequencies. o: wavenumber at structural modes, —: acoustic wavenumber at three frequencies, – –: structural wavenumber at corresponding frequencies.

For the frequencies between the fundamental natural frequency and the second cut-on frequency, provided k_x, $k_y > k_a$, although the region has been called the 'corner mode region', the radiation from the strip can be considered to be equivalent to the radiation of two monopoles, each of size $a \times \lambda_y/4$ where λ_y is the wavelength along the length of the strip. Thus the 'corner' is spread over the whole width of the strip. The power radiated by the strip in this region is given by

$$W = 2\rho c S_m \left\langle \overline{v_m^2} \right\rangle \sigma_m \tag{5.48}$$

where $\sigma_m = \dfrac{4f^2 S_m}{c^2}$ is the radiation efficiency of a monopole with the velocity distribution of a simply supported plate (equation (5.28)). $S_m = a\lambda_y / 4$ is the area of each monopole, and $\left\langle \overline{v_m^2} \right\rangle$ is the mean square velocity within these monopole regions. The radiation efficiency of the whole strip with light damping can thus be given by

$$\sigma_{0s} = \frac{W}{\rho cab\left\langle \overline{v^2} \right\rangle} = \frac{2\sigma_m S_m}{ab} = \frac{8S_m^2 f^2}{abc^2} \tag{5.49}$$

since $\left\langle \overline{v_m^2} \right\rangle = \left\langle \overline{v^2} \right\rangle$. Substituting $\lambda_y = 2b/n$, equation (5.49) becomes

$$\sigma_{0s} = \frac{2abf^2}{c^2 n^2} \qquad \text{for } f_{1,1} < f < f_{2,1},\ k_y > k_a \tag{5.50}$$

where n is the index of modes in the y-direction, i.e., along the length.

Equation (5.50) will not be appropriate for a very small value of γ. For those cases, the 'corner' modes will not appear and only 'edge' modes will dominate this frequency range. This can be seen from the radiation efficiency of the strip 0.08 × 3 × 0.003 m, as shown in Figure 5.15. The absence of 'corner' modes occur if

$$\gamma \le \frac{2\pi}{bc}\left(\frac{B}{\rho h}\right)^{\frac{1}{2}} \tag{5.51}$$

For the current case, a strip with $b = 3$ m and $h = 0.003$ m, this limiting value of γ is 0.0287.

The characteristics of the near-field radiation also appear to be different from the case of moderate aspect ratio. The radiation efficiency at 630 Hz for different values of the damping loss factor was presented in Figure 5.17 for plates with large and moderate aspect ratios. It is found for the strip that the dependence of the radiation efficiency on the damping loss factor is approximately twice that for the rectangular plate. So the near-field radiation efficiency for the strip in this region can be approximated as

$$\sigma_{ns} = \frac{8}{\pi}\frac{f}{f_c}\eta \qquad \text{for } f_{1,1} < f < f_{2,1},\ k_y > k_a \tag{5.52}$$

Combining these two expressions, the radiation efficiency of the damped strip in this region is therefore approximately given by

$$\sigma = \sigma_{0s} + \sigma_{ns} \approx \frac{2abf^2}{c^2 n^2} + \frac{8}{\pi}\frac{f}{f_c}\eta \qquad \text{for } f_{1,1} < f < f_{2,1},\ k_y > k_a \tag{5.53}$$

Results calculated using equation (5.53) are compared with the results from the modal summation. Figure 5.20 shows the results for the strip of dimensions 0.16 × 3.0 m with values of damping loss factor of 0.0005 and 0.1. Although small differences exist, equation (5.53) gives a fairly good approximation for this region. For the strip of dimensions 0.32 × 3.0 m, the comparison is presented in Figure 5.21. The model represented by equation (5.53) is also shown to be a good approximation for the radiation efficiency in this region, in this case 100 to 250 Hz.

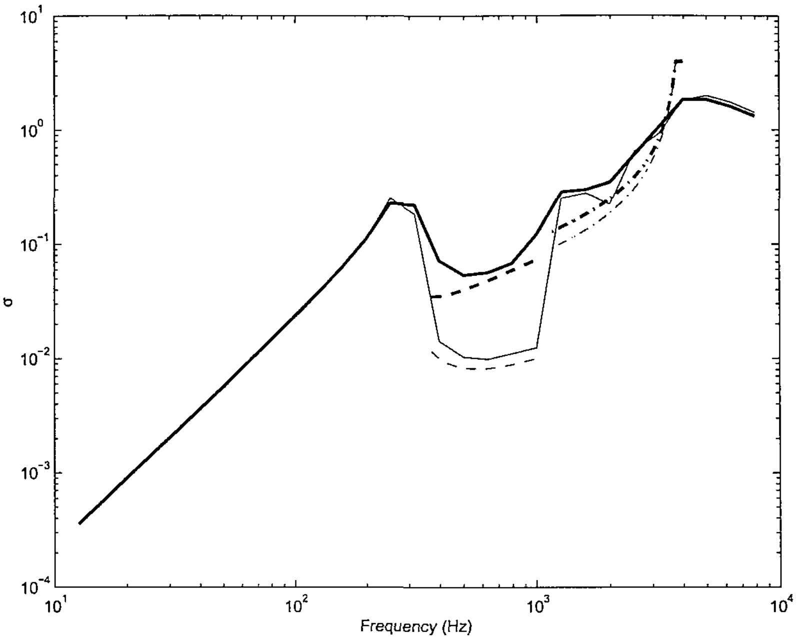

Figure 5.20. Estimation of the radiation efficiency of the strip 0.16 × 3m for the frequencies between the fundamental and second cut-on natural frequency. — : modal summation with η = 0.0005, thick line : modal summation with η = 0.1, – –: η = 0.0005 by equation (5.53), thick – –: η = 0.1 by equation (5.53), · – · : η = 0.0005 by equation (5.30), thick · – · : η = 0.1 by equation (5.30).

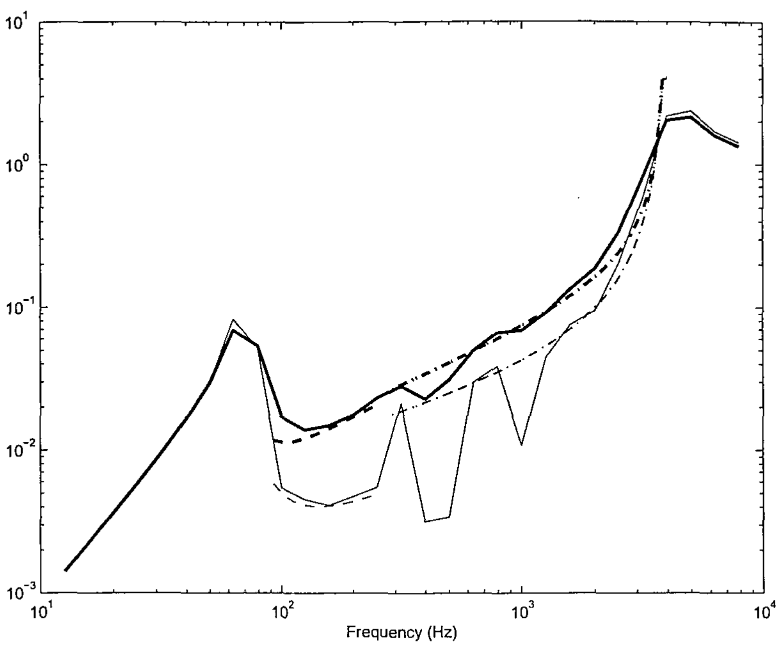

Figure 5.21. Estimation of the radiation efficiency of the strip 0.32 × 3m for the frequencies between the fundamental and second cut-on natural frequency. — : modal summation with η = 0.0005, thick line : modal summation with η = 0.1, – –: η = 0.0005 by equation (5.53), thick – –: η = 0.1 by equation (5.53), · – · : η = 0.0005 by equation (5.30), thick · – · : η = 0.1 by equation (5.30).

5.5.4 SUMMARY OF APPROXIMATION FORMULAE FOR STRIPS

For a rectangular plate with a large aspect ratio (γ smaller than 0.1), equation (5.47) can be used to replace the corresponding part of equation (5.28) for frequencies below the fundamental natural frequency. For frequencies between the fundamental natural frequency and the second cut-on frequency, the radiation efficiency of the strip can be estimated by using equation (5.53). For frequencies between the second cut-on frequency and the critical frequency, the radiation efficiency of the strip can also be approximated with the third expression in equation (5.28) since the mode distribution in this region becomes more evenly spaced the wavenumber domain. This is seen from the comparisons given in Figure 5.20 and 5.21. For frequencies around the critical frequency the results discussed in Section 5.4.4 apply while above the critical frequency the conventional results of equation (5.28) remains valid. All these formulae are combined as below

$$\sigma \approx \begin{cases} \dfrac{8.5}{c^2} a^2 f^2 & \text{for } f < f_{1,1} \\ \dfrac{2abf^2}{c^2 n^2} + \dfrac{8}{\pi}\dfrac{f}{f_c}\eta & \text{for } f_{1,1} < f < f_{2,1},\ k_y > k_a \text{ and } \dfrac{2\pi}{bc}\left(\dfrac{B}{\rho h}\right)^{\frac{1}{2}} \le \gamma \le 0.1 \\ \dfrac{Pc}{4\pi^2 S f_c} \times \dfrac{\left(1-\alpha^2\right)\ln\left(\dfrac{1+\alpha}{1-\alpha}\right) + 2\alpha}{\left(1-\alpha^2\right)^{3/2}} + \dfrac{4}{\pi}\dfrac{f}{f_c}\eta & \text{for } f_{2,1} < f < f_c,\quad \alpha = \sqrt{\dfrac{f}{f_c}} \\ \sigma_c \approx \begin{cases} 1.2 - 1.3 & \text{for } k_c a \le 3 \\ \left(k_c a\right)^{1/4} & \text{for } k_c a > 3 \end{cases} & \text{for } f = f_c \\ \left(1 - \dfrac{f_c}{f}\right)^{-1/2} & \text{for } f > f_c \end{cases} \qquad (5.54)$$

5.6 RADIATION OF EXTRUDED PLATES

The radiation of a double-skinned extruded plate is far more complicated than the foregoing discussion of a rectangular plate. Calculation of the radiation efficiency requires a knowledge of the velocity distribution over the surface of the structure which, in the case of the extruded plate, becomes unwieldy because of the complexity of the structure. The vibration of the extruded plate can be considered to involve global motion and local motion. At low frequencies it behaves as a whole plate while the local vibration of individual strips dominates at high frequencies. The radiation of the extruded plate can therefore be treated in terms of the contributions from both global modes and local modes. By following the foregoing analysis, where an average over all point force excitations over the plate is considered, these global and local modes may be assumed to radiate sound independently of each other by orthogonality of the mode shapes (strictly speaking they are only orthogonal if normalised and integrated over the whole plate, but the forces are only applied on the outer skin). Therefore, an average radiated power for the extruded plate can be given by

$$\overline{W} = \overline{W}_{global} + \overline{W}_{local} \qquad (5.55)$$

where $\overline{W}_{global}$ and $\overline{W}_{local}$ represent the power radiated by global modes and local modes respectively.

The radiation efficiency of the extruded plate can be thus given by

$$\sigma = \frac{\overline{W}_{global} + \overline{W}_{local}}{\rho c S \langle \overline{u^2} \rangle} \tag{5.56}$$

where S is the surface area of the extruded plate, $\langle \overline{u^2} \rangle$ is the spatially averaged mean square velocity over one side of the extruded plate and $\overline{W}_{global}$ and $\overline{W}_{local}$ refer to radiation from that side.

In the following sections, the radiation from global modes and local modes of the extruded plate will be discussed under certain assumptions. These will be combined to give an expression for the total radiation efficiency.

5.6.1 RADIATION FROM GLOBAL MODES

A model of equivalent isotropic plate for the global modes of extruded panels has been given previously in Chapters 3 and 4. The problem of the radiation from the global modes of the extruded panels can be treated in the same way as that of a rectangular plate discussed in section 5.3. It should be indicated that the critical frequency behaviour of orthotropic plates, whose bending stiffness in two directions are largely different, is somewhat more complicated. The bending wavenumbers and thus the wavelengths of such plates depends on the direction of propagation along the plate. In the direction of the greatest stiffness, the corresponding critical frequency is lower than that of the smallest stiffness. There are rather complicated relations between the two critical frequencies [97]. For the present extruded panels under consideration, the critical frequencies in the two directions are very similar due to the similarity of the bending stiffness in the two directions (see Section 4.4.1). Hence, the model of the equivalent isotropic plate is accurate enough to be used to study the radiation from the global modes of the extruded plates.

Considering all possible point force locations over the surface of the extruded plate, the average radiation efficiency from global modes can be predicted by using equation (5.25). The modal radiation efficiencies are obtained by using numerical integration. The spatially averaged mean square velocity is given by equation (5.26) based on assuming simply supported boundary conditions.

The example of the extruded plate used in the present chapter is of aluminium and of dimensions 2.016×3.0×0.07m (i.e. similar to that studied in Chapter 4 but now 3 m long). The critical frequency for the global modes is 139Hz.

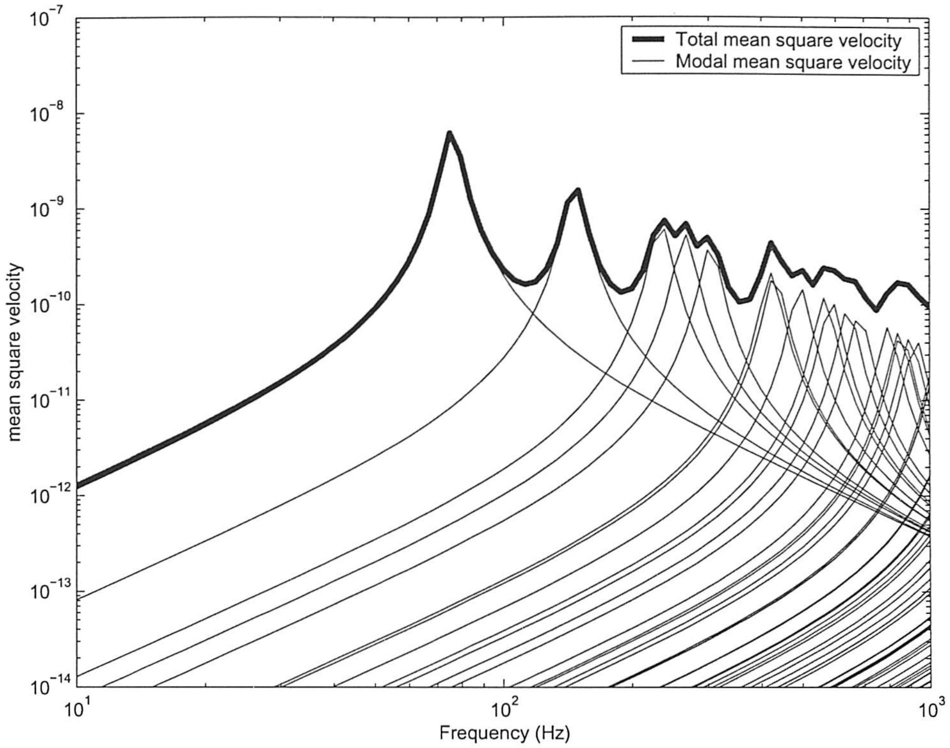

Figure 5.22 Average mean square velocity of the extruded plate showing contributions from global modes. (2.016 × 3.0 × 0.07m aluminium extruded plate with strip thickness 0.003m and $\eta = 0.1$)

The calculation results are presented in Figures 5.22, 5.23 and 5.24. It can be seen that the first mode at 76Hz is the only mode below the critical frequency. This anticipates that, for frequencies below the critical frequency, Leppington's formula might not give a good agreement with the results from the summation of all mode contributions because it is based on a high modal density. This disagreement is confirmed by the comparison of results, as shown in Figure 5.24. The comparison shows that Maidanik's formula has a good agreement at frequencies below the first global mode of the extruded plate. However, from both Leppington's and Maidanik's formulae the limiting values around the critical frequency are less than unity because f_c is low. The values calculated are 0.90 and 0.91 respectively (see section 5.4.4 for details). These have therefore not been applied in Figure 5.24. According to equation (5.34), as $k_c a = 5.17$, the maximum radiation efficiency for global modes is therefore found to be 1.5.

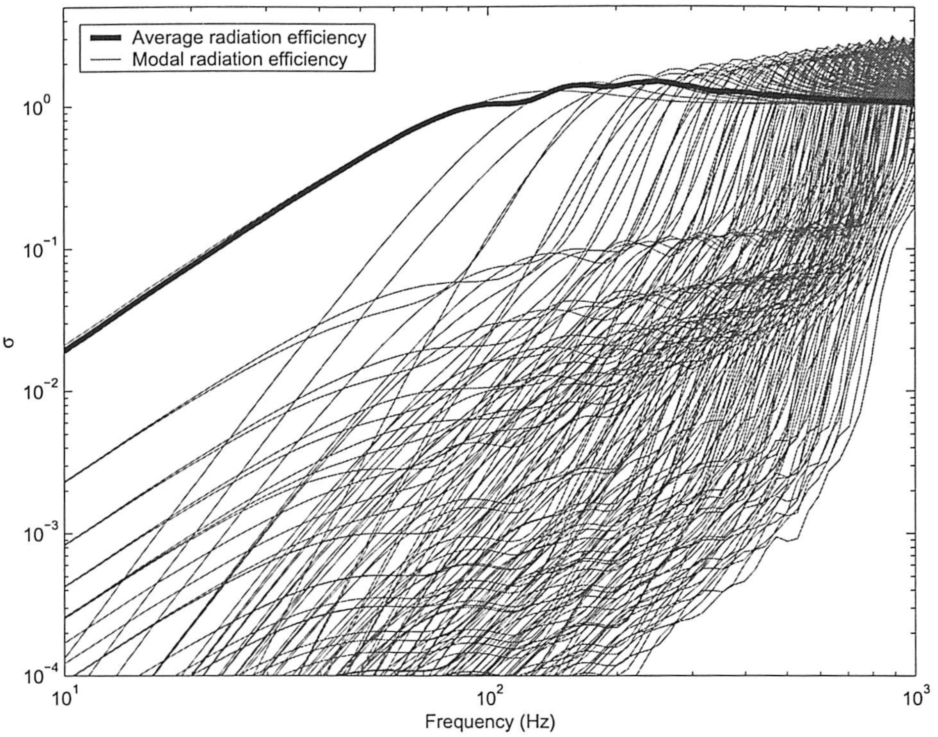

Figure 5.23 Modal and average radiation efficiency of the global modes of the extruded plate.

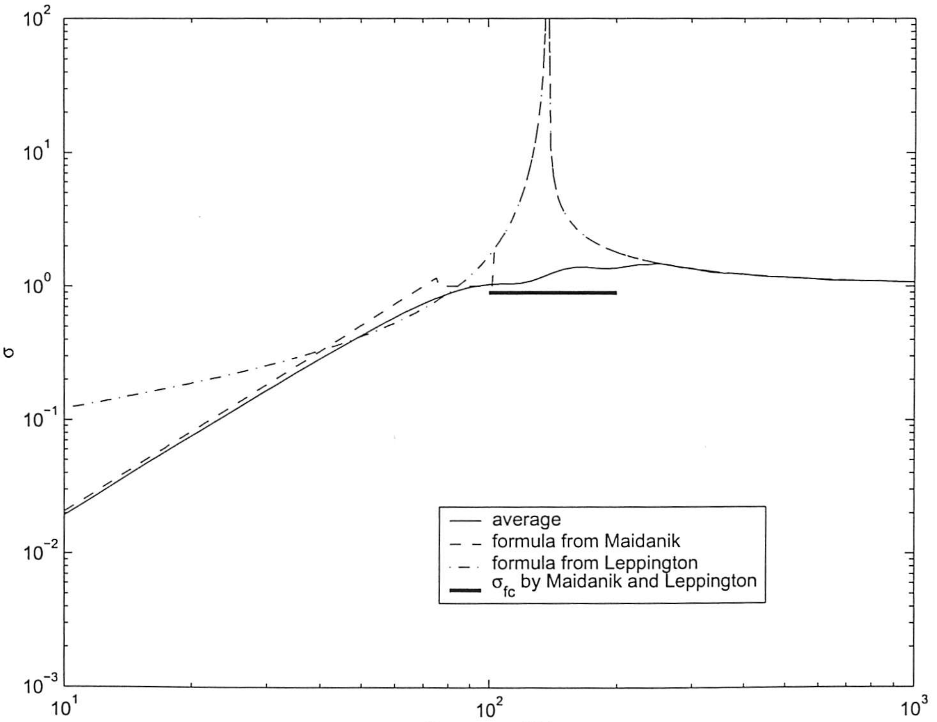

Figure 5.24 Average radiation efficiency of the global modes of the extruded plate.

5.6.2 RADIATION FROM LOCAL MODES

The radiation efficiency from local modes can be analysed by considering each strip independently. Each strip vibrates with a certain velocity amplitude in a baffled plane. The distribution of velocity over the strip is similar to that under the boundary conditions of simple supports. Then each strip can be treated by following the procedure carried out for the strips described in Section 5.5.

However, the amplitude distribution of the velocity of the local modes over all strips due to a point force applied on the surface of the extruded plate is unknown at present. The simplest approximation is to assume that the vibration is localised to the strip excited directly by the point force due to the modal localization, provided that the dimensions of strips are different from each other, and thus only that strip radiates sound. This means that the term for local modes in equation (5.55) depends on a 'single' strip and should be weighted over the entire surface depending on the excitation point. The averaged radiated power from local modes for all possible excitation point can hence be given by

$$\overline{W}_{local} = \sum_i \frac{S_i}{S} \overline{W}_i \tag{5.57}$$

where S is the area of the surface of the extruded plate, i under the summation indicates the ith strip on the surface of the extruded plate, S_i is the area of the ith strip, and W_i is the averaged power radiated by the ith strip, which is given by

$$\overline{W}_i = \rho c S_i \sigma_i \overline{\left\langle u_i^2 \right\rangle} \tag{5.58}$$

where σ_i and $\overline{\left\langle u_i^2 \right\rangle}$ are the radiation efficiency and spatially averaged mean square velocity corresponding to ith strip respectively.

For a system with many modes of vibration, the mean square velocity is approximately given by

$$\overline{\left\langle u_i^2 \right\rangle} = \frac{W_{in}}{\omega \eta \rho_s h S_i} \tag{5.59}$$

where $\overline{W_{in}} = \frac{1}{2} |F|^2 \overline{\mathrm{Re}(Y)}$ is the input power averaged over forcing positions on plate i with the force F. For an average over forcing locations $\overline{\mathrm{Re}(Y)}$ is similar on each strip.

Thus the average square velocity on each strip is proportional to $1/S_i$. But the likelihood of a point force occurring on a given strip is proportional to S_i (equation (5.57)).

The spatially averaged mean square velocity of the whole plate for excitation on plate A_i is

$$\overline{\langle u_l^2 \rangle} = \frac{S_i}{S}\overline{\langle u_i^2 \rangle} = \frac{W_{in}}{\omega\eta\rho_s hS} \tag{5.60}$$

which is the same for excitation on any strip.

The radiated power for excitation on the ith strip can be rewritten as

$$W_i = \rho c S_i \sigma_i \overline{\langle u_i^2 \rangle} = \rho c \sigma_i \frac{W_{in}}{\omega\eta\rho_s h} = \rho c \sigma_i S \overline{\langle u_l^2 \rangle} \tag{5.61}$$

Hence equation (5.57) can be rewritten as

$$\overline{W}_{local} = \overline{\langle u_l^2 \rangle} \sum_i \rho c S_i \sigma_i \tag{5.62}$$

where u_l is the spatially averaged velocity due to local modes.

5.6.3 OVERALL RADIATION FROM EXTRUDED PLATES

The averaged radiation efficiency of the extruded plate over all possible forcing points on one side can be now considered through equation (5.56). This gives

$$\sigma = \frac{\overline{W}_{global} + \overline{W}_{local}}{\rho c S \overline{\langle u^2 \rangle}} = \frac{\sigma_g \overline{\langle u_g^2 \rangle} + \overline{\langle u_l^2 \rangle} \sum_i \frac{S_i}{S}\sigma_i}{\overline{\langle u_g^2 \rangle} + \overline{\langle u_l^2 \rangle}} \tag{5.63}$$

where u_g is the velocity due to global modes, u_l is the velocity due to local modes. Here, use has been made of orthogonality of the modes and hence (approximately) of the local and global motions. Note that due to the assumed uniform thickness the mass density can be taken outside the orthogonality expressions. However, although the modes are orthogonal, these do not correspond to purely global and local motions (see Figures 3.21-24), so the expression in (5.63) is an approximation.

Obviously, the calculation of equation (5.63) requires the knowledge of the spatially averaged mean square velocity for global modes and local modes, radiation efficiencies for global modes and for each strip. In the present chapter, the radiation efficiency for global modes and each strip have been modelled. However, the prediction of the velocities of global and local modes needs further work. One approach is to find the modal density of the extruded plate. For a structure, the mean square velocity can be given in terms of modal density by [35]

$$\left\langle \overline{u^2} \right\rangle = \overline{F}^2 \frac{\pi n(\omega)}{2\eta m^2 \omega} \tag{5.64}$$

where $\overline{F}$ is the r.m.s value of the force applied, $n(\omega)$ is the modal density of the structure under consideration, η is the damping loss factor and m is the mass of the structure.

If the modal densities of the global modes and local modes are found using the models of Chapter 4, the mean square responses of the two sets of modes can be estimated.

5.7 CONCLUSIONS

The radiation efficiency of plates has been investigated by using the modal summation approach. The radiation efficiency is calculated by considering the average over all possible point force excitation positions. Cross-modal terms do not arise in this averaged radiation efficiency. This averaged radiation efficiency shows the limitations of previous formulae by Maidanik [45] for a strip, a plate with a large aspect ratio. It has been shown that its radiation efficiency below the fundamental frequency is proportional to the square of the shortest edge length rather than the area of the plate. For frequencies between the fundamental natural frequency and the cut-on of modes involving a whole wavelength deformation across the strip, the radiation from the strip can be considered to be equivalent to the radiation of two monopoles each of size $a \times \lambda_y/4$ where λ_y is the wavelength along the length of the strip. The near-field radiation from the forcing point in this frequency region is proportional to the damping loss factor. It is found that the dependence on the damping loss factor of the near-field radiation efficiency for the strip is approximately twice that for the rectangular plate with moderate aspect ratio. Finally, an approximate model for calculating the radiation efficiency of a strip has been presented.

Based on the results from the modal summation approach, it is found that the maximum average radiation efficiency expressed in one-third octave bands increases in proportion to $(k_c a)^{1/4}$ for $k_c a > 3$, not $(k_c a)^{1/2}$ as given by Leppington and Maidanik, where k_c is the wavenumber at the critical frequency and a is the shorter edge of the plate. For $k_c a < 3$, the maximum radiation efficiency tends to a constant value between 1.2 and 1.3, depending on the aspect ratio.

The radiation efficiency of extruded plates has been considered in terms of global modes and local modes. The characteristics of the radiation of the global modes are equivalent to that of a rectangular plate which has a low critical frequency. The radiation of the local modes is treated as strips. An approximation for the calculation of the radiation efficiency of extruded plates has been given.

6 COUPLING BETWEEN GLOBAL AND LOCAL MODES

6.1 INTRODUCTION

The coupling between global and local modes within the proposed model for extruded panels will be discussed in this Chapter. There is not a general approach available to deal with the vibration behaviour within a complicated built-up structure comprising long- and short-wavelength components. However, investigations of beam-plate systems provide some insights to understand the behaviour of other similar structures. One important conclusion of these is that the short wave components, or plates, act to introduce damping [59, 60] and present a locally reacting impedance to the long waves at the structural joints [61], provided the difference between the wavelengths of beams and plates is large. Also, apart from this damping effect, the dynamic behaviour of the beams is not greatly affected by the presence of the attached plates. For extruded panels, the local modes within strips can be considered to be driven by the global modes. This can form an analogue to beam-plate systems. Here, global modes are equivalent to beams and local modes to plates. Therefore, for the case of excitations applied on the stiffeners of the extruded panels, the power balance equation for local modes can be expressed by

$$-\omega E_g \eta_{gl} + \omega E_l \left(\eta_{lg} + \eta_l \right) = 0 \tag{6.1}$$

where the first term represents the power injected into the local modes of the strips, the second term represents the power dissipated by damping and re-injected back to global modes. E_g and E_l are the energy of global and local mode subsystems, η_{gl} and η_{lg} are the coupling loss factors from global modes to local modes and from local to global modes respectively, and η_l is the damping loss factor of the local modes.

For the purpose of simplification, by considering that a weak coupling holds for the system, the effects of the local modes on the global modes can be neglected in the present analysis, namely $\eta_{lg} << \eta_l$. Then equation (6.1) reduces to

$$W_{g \to l} = \omega E_g \eta_{gl} = \omega E_l \eta_l \tag{6.2}$$

The response of the global modes can be initially calculated without including the effects from local modes. This is given by

$$W_{in} = \omega E_g \left(\eta_g + \eta_{gl} \right) - \omega E_l \eta_{lg} \simeq \omega E_g \eta_{g,tot} \tag{6.3}$$

where $\eta_{g,tot} = \eta_g + \eta_{gl}$ is the total loss factor of the global modes.

The power injected into the local modes can be calculated by considering a set of strips driven by global modes along the stiffeners. Due to the large difference of the wavelength between global modes and local modes (see Figure 4.29), waves are radiated from the global modes into the local modes at an angle which is almost normal to the axis of the stiffeners [61]. The problem of the three-dimensional extruded panels is hence simplified further into that of the two-dimensional extruded section, which consists of a set of beam components. Also, investigations of beam-plate systems show that the beam acts as a kinetic source to excite the plate. For the extruded section, the vibration of all joints is controlled by the global modes. The local vibration of each beam component (strip) is then driven by the kinetic source at its two ends (joints). Therefore, a finite beam driven by kinetic excitations at its two ends is firstly studied in the following sections.

6.2 FINITE BEAM DRIVEN BY KINETIC EXCITATIONS AT TWO ENDS

Consider a beam driven by two velocity excitations v_1 and v_2 at its ends, as illustrated in Figure 6.1. The transverse displacement w is represented by

$$w(x) = Ae^{-jkx} + Be^{jkx} + Ce^{-kx} + De^{kx} \tag{6.4}$$

where A and C are coefficients of the positively propagating and growing evanescent wave, B and D are coefficients of the negatively propagating and decaying evanescent waves, and k is the complex wavenumber.

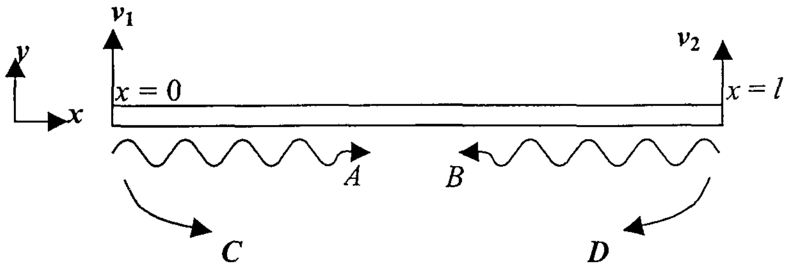

Figure 6.1. A beam driven by kinetic excitations at two ends.

To obtain the above four amplitude coefficients, four boundary conditions are needed. In real extruded panels, each stiffener may act as a rotation stiffness at the joint point. Here, a free rotation is used for the purpose of simplification. This gives

$$w''(0) = w''(l) = 0 \tag{6.5}$$

After manipulations, *A, B, C* and *D* can be given by

$$A = \frac{1}{2j\omega}\frac{v_2 - v_1 e^{jkl}}{e^{-jkl} - e^{jkl}} \tag{6.6}$$

$$B = \frac{1}{2j\omega}\frac{v_1 e^{-jkl} - v_2}{e^{-jkl} - e^{jkl}} \tag{6.7}$$

$$C = \frac{1}{2j\omega}\frac{v_2 - v_1 e^{kl}}{e^{-kl} - e^{kl}} \tag{6.8}$$

$$D = \frac{1}{2j\omega}\frac{v_1 e^{-kl} - v_2}{e^{-kl} - e^{kl}} \tag{6.9}$$

The forces acting at the two ends can be found by

$$\begin{aligned} F_1 &= EIw'''(0) \\ F_2 &= -EIw'''(l) \end{aligned} \tag{6.10}$$

where

$$w'''(0) = \frac{k^3}{2\omega}\left[\frac{v_1\cos(kl) - v_2}{j\sin(kl)} + j\frac{v_1\cosh(kl) - v_2}{\sinh(kl)}\right] \tag{6.11}$$

$$w'''(l) = \frac{k^3}{2\omega}\left[\frac{v_1 - v_2\cos(kl)}{j\sin(kl)} + j\frac{v_1 - v_2\cosh(kl)}{\sinh(kl)}\right] \tag{6.12}$$

The power input into the beam can be given by

$$W_{in} = \frac{1}{2}\mathrm{Re}\left\{F_1^* v_1 + F_2^* v_2\right\} \tag{6.13}$$

For a highly damped beam or at high frequencies, the power input into the beam can be approximated by using the impedance of semi-infinite beam. This is given by

$$W_{in,0} = \frac{1}{2}\mathrm{Re}(Z_0)\left[|v_1|^2 + |v_2|^2\right] \tag{6.14}$$

where z_0 is the impedance of semi-infinite beam, which is given by

$$z_0 = \frac{1}{2}m'c_B(1+j) \tag{6.15}$$

where m' is the mass per unit length and c_B is the phase velocity of bending waves.

It can also be shown that equation (6.14) holds for other boundary conditions, provided the beam is highly damped or at high frequencies.

6.3 FINITE BEAMS DRIVEN BY TRAVELLING GLOBAL WAVE

Consider a travelling global wave with wavenumber k_g driving a segment beam to generate local vibrations, which have wavenumber k. This is illustrated in Figure 6.2. v_1 and v_2 are related by

$$v_2 = v_1 e^{-jk_g l} \tag{6.16}$$

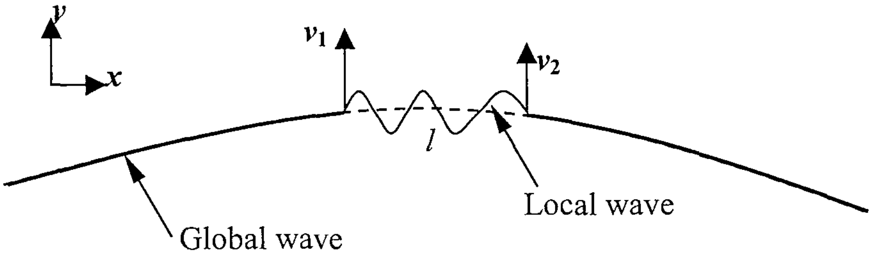

Figure 6.2. Illustration of a beam driven by global travelling waves.

According to the model previously described for the global modes and local modes of an extruded panel, $k = 5.5k_g$ (see Figure 4.29). The power input to the strip from the travelling global wave with unit velocity amplitude is calculated for a strip of width 0.15 m. The damping loss factor for the beam η_l is assumed as 0.01. Figure 6.3 presents the calculated results from the exact solution given by equation (6.13) and the approximate one by equation (6.14). It is seen that using the impedance of a semi-infinite beam gives a result that approximates the average input power. By increasing the damping within the beam, it can be anticipated that the agreement between this approximation and the exact result will be improved. The result corresponding to $\eta_l = 0.1$ is presented in Figure 6.4 which verifies this.

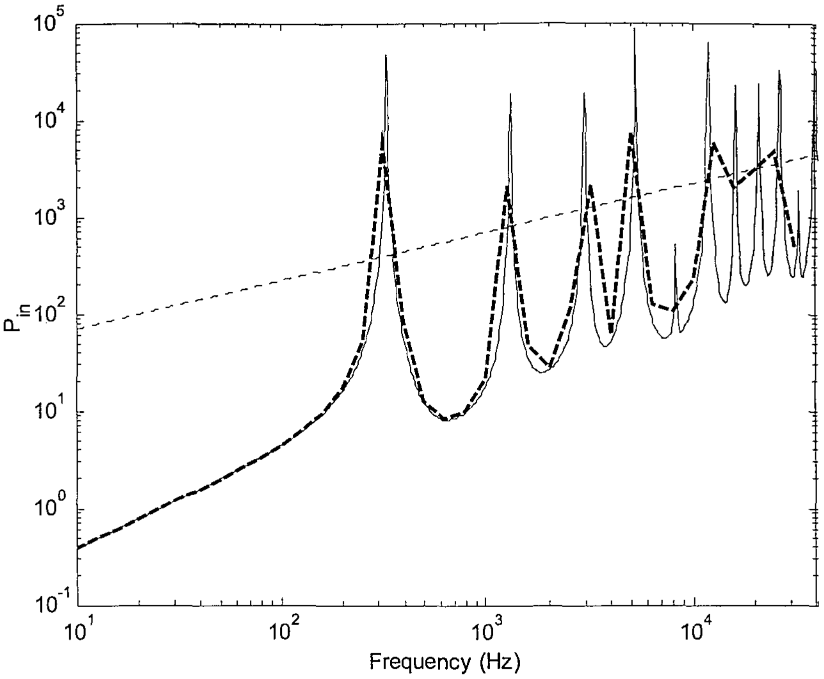

Figure 6.3. Power input into a beam from a travelling global wave. ($\eta_l = 0.01$)

— equation (6.13), – – 1/3 octave bands, ···· equation (6.14)

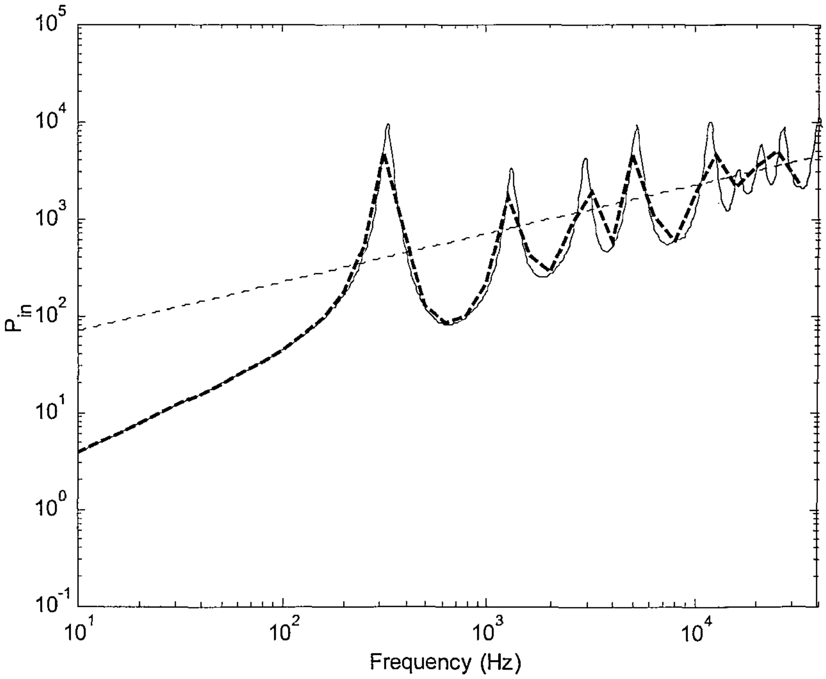

Figure 6.4. Power input into a beam from a travelling global wave. ($\eta_l = 0.1$)

— equation (6.13), – – 1/3 octave bands, ···· equation (6.14)

Consider next a set of beams driven by a travelling global wave, illustrated Figure 6.5. All joints vibrate with the global velocity and are related by the phase change $e^{-jk_g x}$. Each beam segment is assumed to vibrate independently from the others and is excited by the velocity source at its two ends. The power input into all beam segments can be obtained by the summation of power input into each beam segment from equation (6.13). This total power can also be approximated using the impedance of a semi-infinite beam, given by

$$P_{in,0} = \frac{1}{2}\mathrm{Re}\left(Z_0\right)\left|v_1\right|^2 \times 2 \times \text{number of strips} \tag{6.17}$$

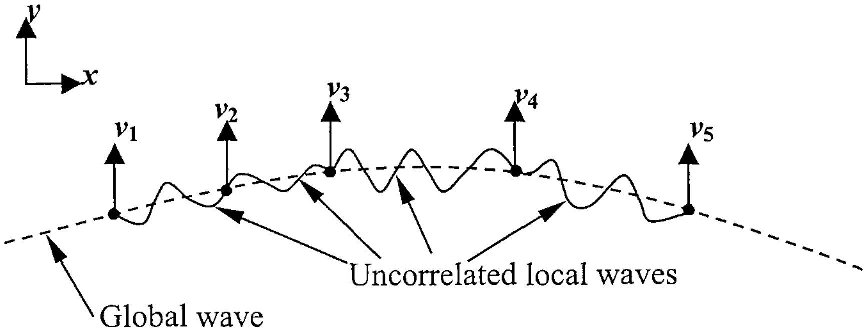

Figure 6.5. Illustration of a set of beams driven by a travelling global wave.

An example of such a system is calculated. The beam segments have irregular lengths of 0.145, 0.16, 0.15, 0.14, 0.155, 0.137, 0.153, 0.148, 0.12, 0.09 and 0.10 m. Figure 6.6 presents the result for the case of $\eta_l = 0.01$. The result approximated with the impedance of a semi-infinite beam still gives a good approximation to the average input power. Compared with Figure 6.3, the variance of the exact results decreases due to the irregularity of the length of beam segments.

Figure 6.7 presents the corresponding result for the damping loss factor $\eta_l = 0.1$. In this case, the approximation using the impedance of semi-infinite beam gives a very good agreement with the exact results for frequencies above the first resonance frequency of beam segments. This shows the potential for using this simplification to the calculation of the power input into such systems.

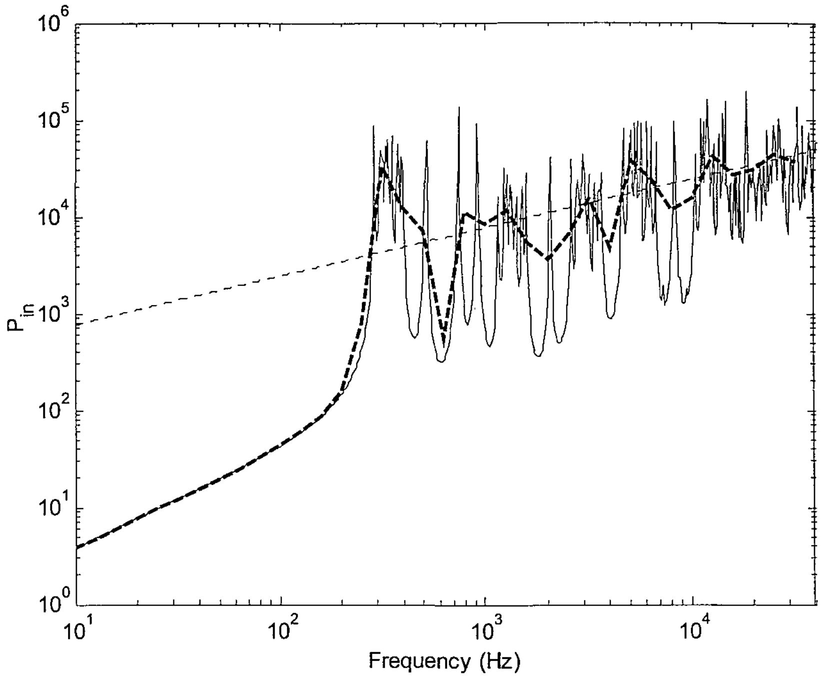

Figure 6.6. Power input into a set of uncorrelated beams from travelling global waves. ($\eta_l = 0.01$)

— equation (6.13), – – 1/3 octave bands, ···· equation (6.17)

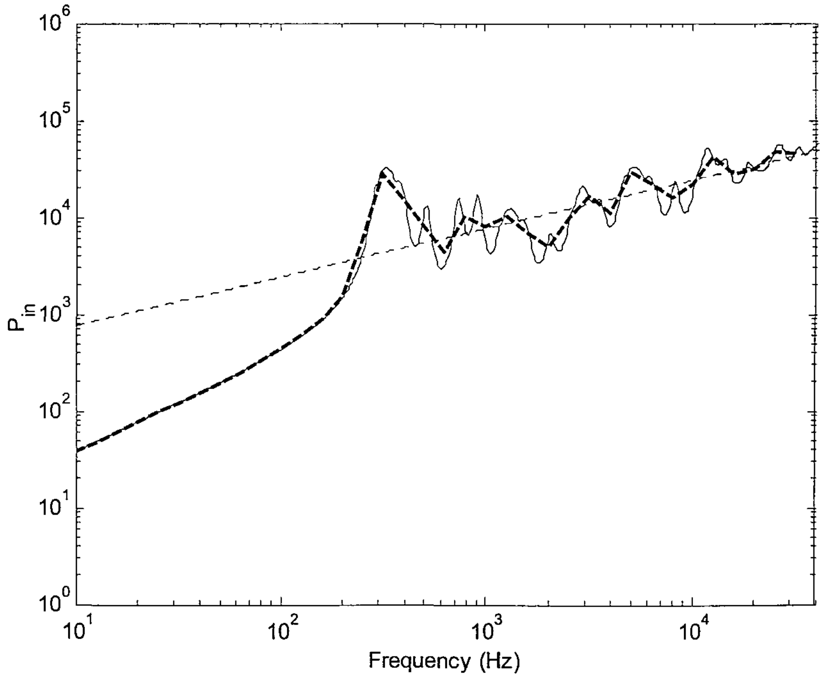

Figure 6.7. Power input into a set of uncorrelated beams from travelling global waves. ($\eta_l = 0.1$)

— equation (6.13), – – 1/3 octave bands, ···· equation (6.17)

6.4 COUPLING LOSS FACTOR

Consider the power input into p beam segments by the global wave travelling over the total length of beams L. The coupling loss factor is defined as related to the total energy of the global wave in L

$$W_{g\to l} = E_{tot}\omega\eta_{gl} \tag{6.18}$$

where $E_{tot} = \frac{1}{2}m_g'|v_1|^2$ is the total energy per unit length of the travelling global wave.

Since the input power can be approximated using equation (6.17), the coupling loss factor is given by

$$\eta_{gl} = \frac{P_{g\to l}}{E_{tot}\omega} \tag{6.19}$$

$$\eta_{gl} \approx \frac{P_{g\to l}}{E_{tot}\omega} \approx \frac{2p\,\mathrm{Re}\{Z_0\}}{m_g'L\omega} \approx \frac{m'c_B p}{m_g'\omega L} \approx \frac{m'p}{m_g'kL} \tag{6.20}$$

It can be noted that this coupling loss factor only includes the mass unit per length of global and local systems, the wavenumber of local systems and number of beams per unit length p/L (or average length of beams L/p). It is similar to a result given by Grice and Pinnington for a beam-plate system [61].

For the example of a set of beams used above, the coupling loss factor can be calculated from equations (6.19) and (6.20). Figure 6.8 presents the results for the damping loss factor $\eta_l = 0.01$. Equation (6.20) gives an approximation of the average result by equation (6.19) for frequencies above the first resonance of the beams. Below the first resonance of the beams, equation (6.20) cannot give a reasonable estimation as the local subsystem is not resonant. Figure 6.9 presents the results corresponding to a damping loss factor $\eta_l = 0.1$. It can be seen that equation (6.20) gives a good agreement with the coupling loss factor calculated using equation (6.19).

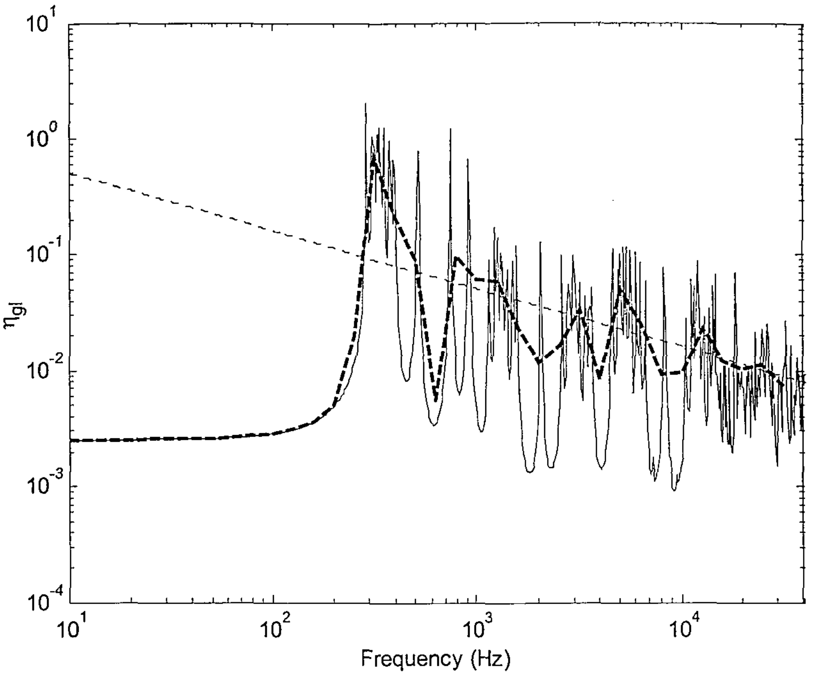

Figure 6.8. Coupling loss factor from global to local systems. ($\eta_l = 0.01$)

— equation (6.19), – – 1/3 octave bands, ···· equation (6.20).

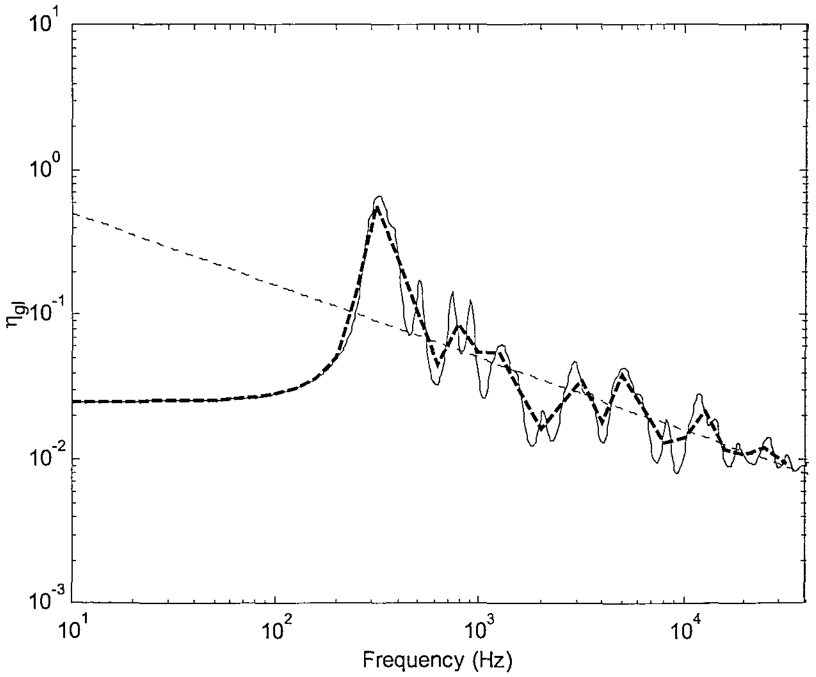

Figure 6.9. Coupling loss factor from global to local systems. ($\eta_l = 0.1$)

— equation (6.19), – – 1/3 octave bands, ···· equation (6.20).

6.5 FINITE BEAM DRIVEN BY FINITE GLOBAL MODES

The above coupling loss factor is actually obtained for the travelling global wave under an assumption that the local modes of each beam are uncorrelated. For a finite global system, however, this condition will be challenged because the global system will be controlled by natural modes. For the present interest, consider a finite extruded panel.

There are a number of difficulties involved to justify the use of this coupling loss factor for the analysis of extruded panel. In conventional SEA, the responses of two subsystems can be obtained from an analytical model or from experiments. These responses are then used to compare with the results obtained from SEA prediction. Thereby the validity of the coupling loss factors can be justified. For extruded panels, however, there is no analytical solution for the response of the system. Moreover, even from experiments, it will be difficult to distinguish which part of the response comes from global modes and which from local modes.

Numerical methods such as FEM can be used to evaluate the coupling loss factor. Using FE models in the study of SEA has some advantages. In FE models, the details of the structure can be easily varied to investigate how the SEA parameters will vary. In most cases, computer experiments can be done on FE models. It may consume less time and be more controllable than experiments carried out on the real complicated structures. Evaluations of coupling loss factors using FEM have been reported by Steel et al [83] for building structures and Shankar et al [82] for ship structures. The power injection method can be carried out using FEM.

6.5.1 FEM MODEL

An FE model for an extruded section (as in Section 3.5) is used to investigate the coupling between the global and local modes. In FE models the structure is modelled as a number of elements connected at nodes. By applying a sinusoidal load at each frequency of interest the response at each node in the structure can be calculated. Note that the total energy is equal to

$$E = m\left\langle \overline{v^2} \right\rangle \qquad (6.21)$$

where m is the mass and $\left\langle \overline{v^2} \right\rangle$ is the spatially averaged mean square velocity. From FE data, the total energy in the structure, or part of the structure, can therefore be calculated by

$$E = \sum_{i}^{n} m_i \overline{v_i^2} \tag{6.22}$$

where n is the node number and m_i is the mass attributed to each node and $\overline{v_i^2}$ is the mean square velocity at each node. If the mass is evenly distributed in the structure, the above equation can be written as

$$E = \frac{m}{n} \sum_{i}^{n} \overline{v_i^2} \tag{6.23}$$

A point force is applied on a node corresponding to a joint position on the extruded section. The total energy of global modes is calculated from the response of all joint nodes. The energy of global modes can be approximated by

$$E_g = m_g \left\langle \overline{v_g^2} \right\rangle = \frac{m_g}{n_{\text{joint}}} \sum_{i}^{n_{\text{joint}}} \overline{v_{\text{i,joint}}^2} \tag{6.24}$$

where m_g is the mass associated with the global modes (equal to the mass of the extruded panel), $\left\langle \overline{v_g^2} \right\rangle$ is spatially-averaged mean square velocity of the global modes, n_{joint} is the number of joint nodes and $\overline{v_{\text{i,joint}}^2}$ is the mean square velocity of each joint node.

All nodes on the structure represent the subsystem of local modes. For instance, all nodes on the upper plate can be considered as a local mode subsystem. The FE results on these nodes are the total response including the contributions from global modes and local modes. Therefore the energy of the local subsystem is equal to the difference between the total energy and the contribution from global modes. This is given by

$$E_l = m_l \left\langle \overline{v_l^2} \right\rangle = m_l \left(\left\langle \overline{v_{tot}^2} \right\rangle - \left\langle \overline{v_g^2} \right\rangle \right) \tag{6.25}$$

where m_l is the mass of the subsystem of local modes (e.g. the mass of the upper plate) and spatially-averaged mean square velocity $\left\langle \overline{v_{tot}^2} \right\rangle$ is averaged from all nodes on the upper plate using equation

$$\left\langle \overline{v_{tot}^2} \right\rangle = \frac{1}{n_{all}} \sum_i^{n_{all}} \overline{v_i^2} \tag{6.26}$$

where n_{all} is the number of nodes on the upper plate and $\overline{v_i^2}$ is the mean square velocity of each node.

From equation (6.2), the coupling loss factor is given by

$$\eta_{gl} = \frac{E_l \eta_l}{E_g} = \frac{m_l \left\langle \overline{v_l^2} \right\rangle \eta_l}{m_g \left\langle \overline{v_g^2} \right\rangle} \tag{6.27}$$

It should be noted that FE analysis is essentially a deterministic tool, while SEA is concerned with average results. Thus, to apply FEM to traditional SEA, some kind of averaging is required. Formally, SEA is concerned with an average over ensembles of similar but not identical systems carried out frequency by frequency. It is, however, commonly applied to averages over frequency on a single system. Here, this can be achieved conveniently by averaging over one-third octave bands for results from a single FEA run.

Also, it should be considered that it is common practice in SEA to average results over a range of forcing points when deducing CLFs. Therefore the above procedures should be carried out for a number of excitation points. Note that, in the present case, only joint points can be used since any excitation on nodes between joints will excite both global and local modes. In another words, two subsystems will be excited simultaneously. Consequently, it will not be straight forward to deduce the CLFs. The joint nodes on the upper plate are used in the analysis.

6.5.2 RESULTS FROM FEM MODEL

The FE model of the cross-section of an extruded panel used in Chapter 3 is used again here, shown in Figure 6.10. In the present case, all joint nodes on the upper plate are used to represent the response of the global modes. The upper plate has 9 strips. A number of harmonic analyses are implemented for a frequency range from 0 to 13 kHz. A constant damping loss factor of 0.06 is used. Figure 6.11 presents a comparison of the results for the coupling loss factor obtained from FE analysis and that from equation (6.20). The result from FE analysis is averaged from three point force positions, as shown in Figure 6.10. The result from FE analysis can be used for the frequencies above 500 Hz. This is because the local modes only occur above about 500 Hz. It is seen that the result from FE analysis tends to converge to that from equation (6.20) at high frequencies. For frequencies below 4 kHz, there are quite large variances in the coupling loss factor. This is due to the modal behaviour of the global modes. There are only about four global modes below 4 kHz. It has also been noted, in this FE analysis, that the spatially-averaged total response of all nodes at certain frequencies is lower than the averaged response of joint nodes for the cases in which the positions of the point force is applied on the nodes close to the two ends of the extruded panels. Therefore the data from these excitation positions have been ignored for the present purpose.

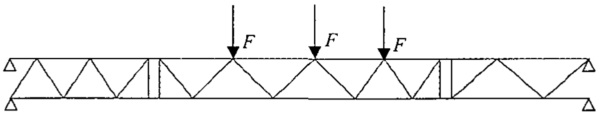

Figure 6.10 Positions of the point force in FE model.

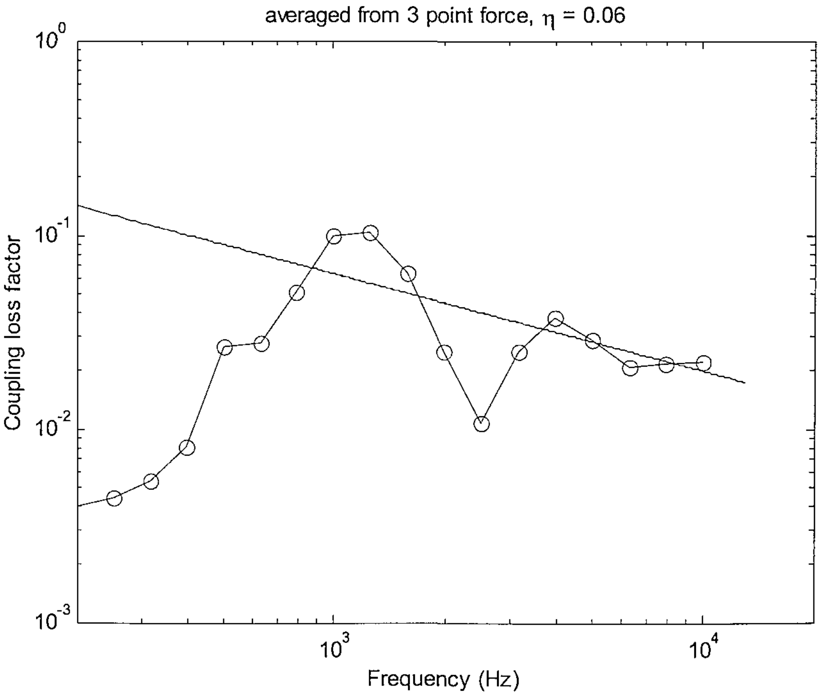

Figure 6.11 Comparison of the coupling loss factors from global modes to local modes. —, from equation (6.20); –o–, from FEM (averaged of 3 force positions).

The results from FEM analysis have shown that the model of the coupling loss factor given by equation (6.20) is encouraging. The spatially-averaged mean square velocity of the local modes can be predicted using this coupling loss factor and the spatially-averaged response of joint points. This predicted $\left\langle \overline{v_l^2} \right\rangle$ can be expressed as

$$\left\langle \overline{v_l^2} \right\rangle = \frac{m_g \left\langle \overline{v_g^2} \right\rangle \eta_{gl}}{m_l \eta_l} \tag{6.28}$$

Figure 6.12 presents the results from equation (6.28) and FEM model. It can be seen that two curves agree with each other reasonably well for frequencies above 800 Hz, which is the applicable frequency range of the coupling loss factor. This shows that the average response of the extruded panels, for the case of excitation applied on the joints, can be predicted if the response of the global modes is known.

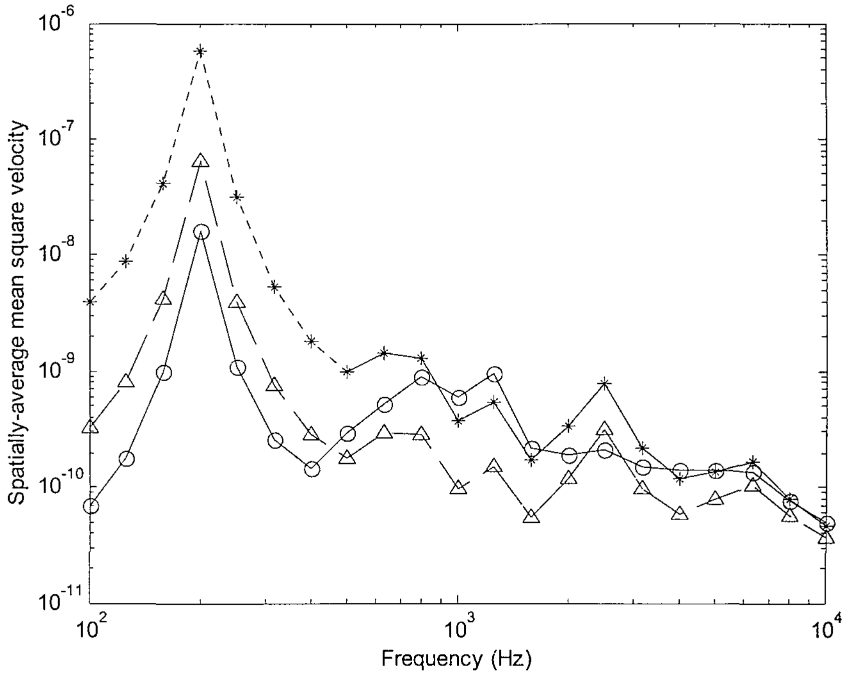

Figure 6.12. Comparison of the predicted response for local modes and FEM result. –*–, predicted local (dotted part corresponds absence of local modes); –o–, FEM local; –Δ–, FEM global.

6.6 CONCLUSIONS

The coupling between the global and local modes has been modelled based on analysing the input power of a set of uncorrelated finite beams driven by kinetic excitations at their two ends. Here, the local modes in each strip of the extruded panel are assumed to be uncorrelated which is reasonable if they are not too similar in width. An expression of the coupling loss factor from global modes to local modes has been given. An FE model for the cross-section of the extruded panel has been used to verify this coupling loss factor. The comparison has shown the good agreement for the applicable frequency range.

7 MEASUREMENTS OF VIBRATION AND SOUND RADIATION OF EXTRUDED PANELS

7.1 INTRODUCTION

Models have been established for the modal density and radiation efficiency for extruded plates in previous chapters. A set of experiments has been carried out to investigate the validity of these models. In these experiments, a sample extruded plate was forced at a point on its surface using an electrodynamic shaker. The response of the plate was measured using a scanning laser vibrometer. The spatially-averaged transfer mobility obtained from vibration measurements has then been used with sound power measurements in a reverberant chamber to derive the radiation efficiency. These measurements have been carried out using a reciprocal technique.

7.2 VIBRATION MEASUREMENTS

7.2.1 EXPERIMENTAL SET-UP

The sample extruded panel used in the vibration measurements is aluminium of overall dimensions 1.0 × 1.5 × 0.07 m taken from a large sample corresponding to a railway carriage floor section. The thickness of each strip member of the panel is 2.6 mm. On one surface a layer of stiff rubber was attached and in the gaps of the extrusion foam was inserted. There are 9 strips on the side of the rubber layer, 6 strips on the bare metal side and 18 strips between the two outer skins. The panel was suspended vertically from a steel frame using elastic rope to give free boundary conditions on all edges. Figure 7.1 shows the appearance of the sample panel and the experimental setting.

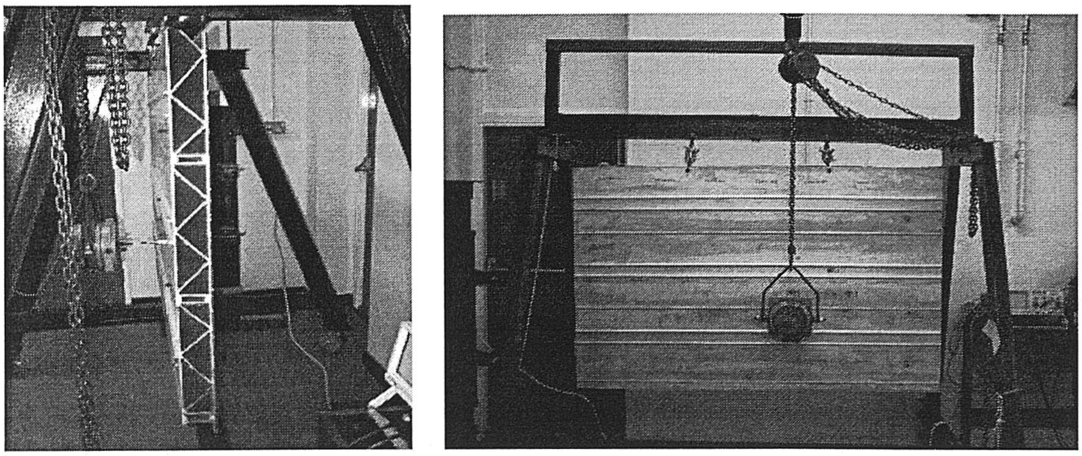

Figure 7.1. Experimental setting for the sample extruded plate.

7.2.2 ARRANGEMENT FOR MOBILITY MEASUREMENTS

The excitation was applied by connecting the shaker to the plate via a slender rod stinger and a B&K type 8200 force gauge was used to measure the force. The response was measured at a large number of positions over the two outer plates using a Polytec Scanning Laser Vibrometer. In addition, the response was measured at a number of locations close to the driving point using B&K type 4374 accelerometers attached using beeswax. This was necessary because the area close to the driving point behind the shaker could not be scanned by the Scanning Laser Vibrometer. Force gauge and accelerometer signals were amplified using B&K charge amplifiers, type 2635. A broad-band random excitation signal generated by the Laser Vibrometer, covering the frequency range from 0 to 6.4 kHz, was used. Transfer mobilities were measured with a frequency resolution of 2 Hz, using a Hanning window.

Measurement locations over the two outer plates were intentionally divided into two groups, one group at the joints between strips ('stiffeners') and the other at general positions on the strips. The overall spatially-averaged transfer mobility was obtained by combining the measurements made of both groups of locations, provided results were weighted by the ratio of the areas of the surface they represent. The strips and stiffeners represent 85% and 15% of the surface area respectively. The excitation points were chosen arbitrarily with 3 on strips and 3 on joints, shown in Figure 7.2. For convenience, the strips were named strip 1, strip 2 and so on from top of the panel to the bottom while the stiffeners were named as stiffener 1, stiffener 2 and so on. The locations of the excitation points are listed in Table 7.1.

Table 7.1 Locations of excitation points in measurements.

Number	Locations	Coordinate	
		x (m)	y
1	Strip 2	1.32	52% of strip width
2	Strip 4	1.1	52% of strip width
3	Strip 4	0.78	51% of strip width
4	Stiffener 3	1.05	_
5	Stiffener 4	1.35	_
6	Stiffener 4	0.78	_

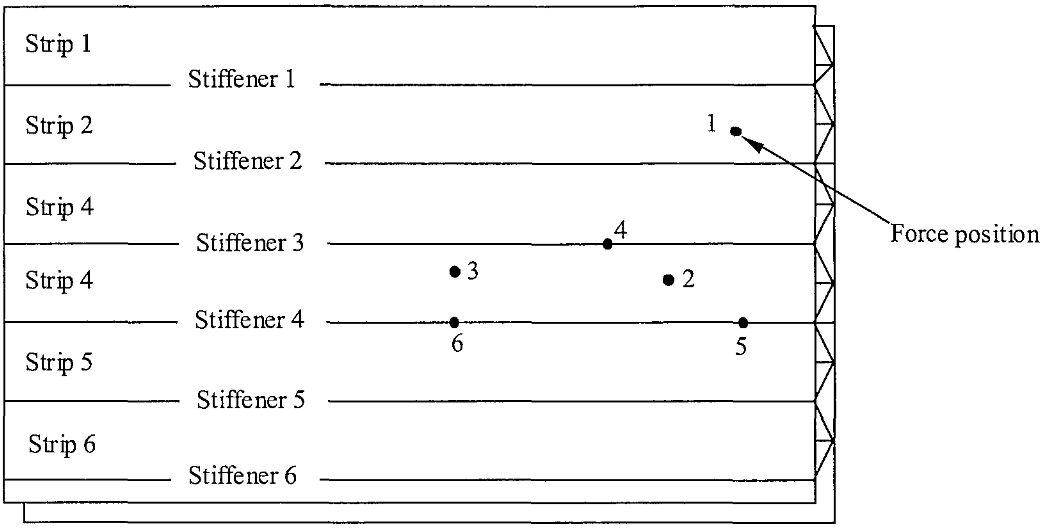

Figure 7.2. Sketch showing the positions of excitations applied in experiments.

The measurements have been carried out for these 6 excitation locations. The results will show the variance of responses due to different force positions although this is not enough to give statistical characteristics. On average, 60 to 70 response points on each strip and 30 to 40 points on each stiffener were measured.

7.2.3 EXCITATION ON STRIPS

The vibration levels of the extruded plate are first investigated for the driving points on strips (between stiffeners). There are three main aspects to present. First, results of the measured driving point mobility are compared with equation (7.1), which is based on the modal density for extruded plates developed in Chapter 4.

$$\mathrm{Re}\{Y\} = \frac{\pi}{2M} n(\omega) \tag{7.1}$$

where Y is the driving point mobility, M is the mass of the structure and the modal density $n(\omega)$ is given in Chapter 4. However, the real part of mobility in the above equation is defined as averaged over all excitation positions. Evaluation for a large number of excitation points would therefore be preferred, but was not carried out due to time constraints.

The second issue concerns the vibration energy distribution in the plate. The spatially-averaged transfer mobility for each strip on the excitation side is examined. This shows that the response is 'localized', i.e. the vibration of the driven strip is much higher than other strips. The word 'local' is used in this sense in what follows.

The third aspect is to examine the difference of the response of the two outer plates and develop a method to predict the energy transfer between the two outer plates of the panel.

The magnitude and phase of the driving point mobility for excitation point 3 on strip 4 is presented as a narrow-band spectrum in Figure 7.3. For frequencies below 400 Hz, the magnitude of the mobility increases with frequency and the phase of the response is 90° ahead of the force. This shows that the plate behaves as a stiffness in this frequency range. The real part of the measured driving point mobility and that calculated from equation (7.1) are presented in Figure 7.4. The discrepancy between the two curves is not surprising because the measured result is not averaged for all excitation positions. This also suggests that it is fairly difficult in practice to measure the modal density based on the frequency-averaged value of the real part of the driving point mobility for non-uniformly distributed systems because of uncertainties regarding suitable points of application and total effective masses. This point has been indicated in [69].

It is believed that the measured driving point mobility at this location is determined by the particular dynamic characteristics of strip 4. A mode of the whole plate around 175 Hz is also present which affects the real part of the mobility. It can also be seen as a ripple in the stiffness characteristic in Figure 7.3. Nevertheless, the general agreement is quite reasonable.

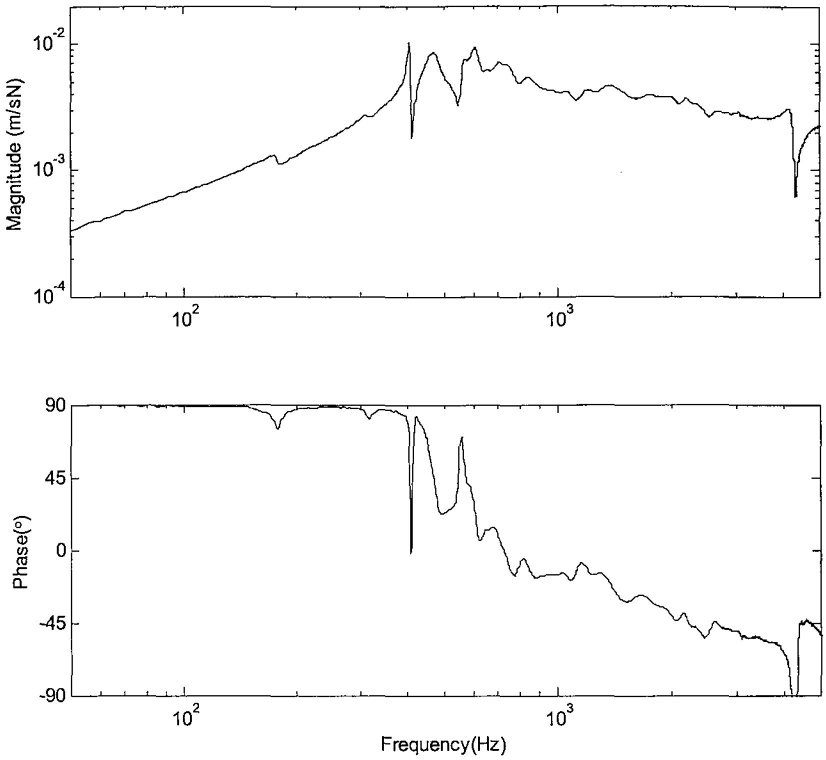

Figure 7.3. Driving point mobility of extruded plate at point 3 on strip 4.

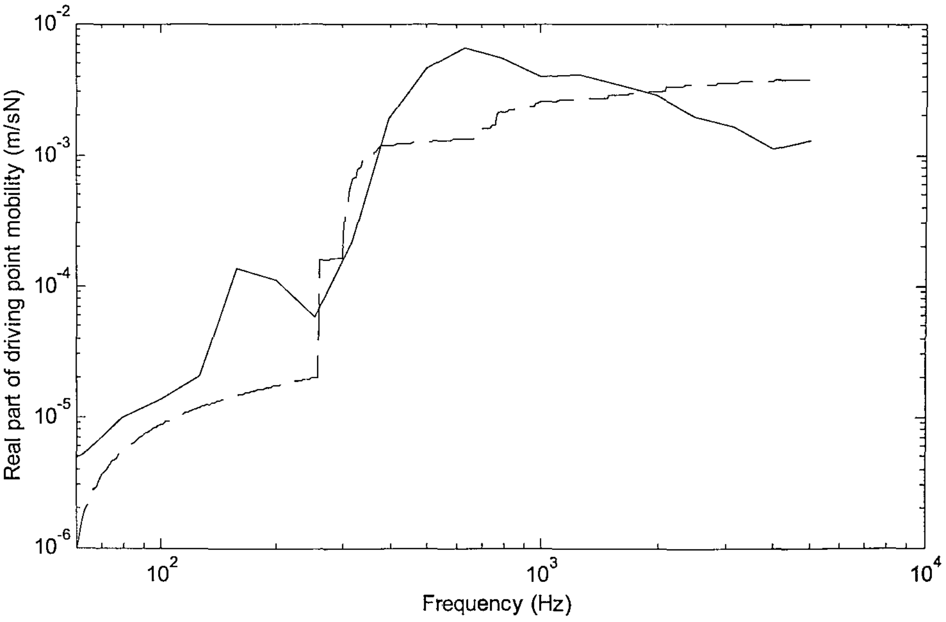

Figure 7.4 Real part of the driving point mobility of extruded plate.

—, measured for excitation on strip;- - -, equation (7.1)

Consider next a simply supported strip with dimensions 0.137 × 1.5 × 0.0026 m, which is similar to strip 4. A point force is applied at a position just off the centre, (x_0 = 0.07 m,

$y_0 = 0.8$ m). This is similar to the position in the measurements on strip 4. The driving point mobility is then calculated by [35]

$$Y(x_0, y_0) = \frac{4j\omega}{m''ab} \sum_{m,n=1}^{\infty} \frac{\sin^2(m\pi x_0/a)\sin^2(n\pi y_0/b)}{\omega_n^2(1+j\eta)-\omega^2} \tag{7.2}$$

where m'' is the mass per unit area of the strip, a, b are dimensions, m, n are indices of natural modes, η is the damping loss factor and ω_n is the nth natural mode.

For clarity and comparison, the driving point mobility of the corresponding infinite strip is also calculated. According to [35], the driving point mobility of an infinite strip having simple supports on two long edges can be given by[3]

$$Y(x_0, 0) = \frac{1}{2m''ac_B} \sum_{n=1}^{\infty} \left(\frac{1}{\sqrt{1-(n\pi/ka)^2}} - \frac{j}{\sqrt{1+(n\pi/ka)^2}} \right) \sin^2\left(\frac{n\pi x_0}{a}\right) \tag{7.3}$$

where a is the width of the strip, k is the wavenumber and c_B is the phase speed of the bending wave. The damping can be introduced by using the complex wavenumber $k = (1-j\eta/4)$.

Figure 7.5 presents the result of the modulus of the driving point mobility for the finite and infinite strips. The damping loss factors 0.1 and 0.01 are used for the finite strip and 0.01 is used for the infinite strip. Figure 7.6 presents the real part for the corresponding results. Note that, for frequencies below the first cut-on frequency, the curves for the infinite strip in the both figures are not distinguishable from the corresponding finite strip having the damping loss factor 0.01. The effect of the cut-on frequency is clearly seen for the infinite strip from the phase and the real part. It is noted that the modulus of the measured mobility above 500 Hz agrees well with both infinite strip and finite strip with the damping loss factor of 0.1. For frequencies above 500 Hz the response of the strip is resonance-controlled. This suggests the value 0.1 of the damping loss factor could be a reasonable estimate of the real damping. The measured data above 3 kHz is less reliable because the excitation force is reduced due to the stinger.

---

[3] Reference [35] gives the expression of an infinite strip with guided boundary conditions only, which has a similar form to equation (7.3) but replacing the sine function by the cosine with n starting from 0.

It is interesting to note the real part of the finite strip result with the damping loss factor of 0.01 agrees well with the measured real part. However, this cannot be a proof to suggest a damping loss factor than 0.1 for the panel. The peak at 500 Hz is likely the actual first cut-on frequency. The first cut-on frequency from the measurements is higher than the simply supported strip. This is because the actual boundary conditions across the strip are stiffer than simple supports as seen in Chapter 3. This higher cut-on frequency can lead to the lower measured mobility modulus at low frequencies. At low frequency, the response of the strip is also influenced by global modes of the extruded panel.

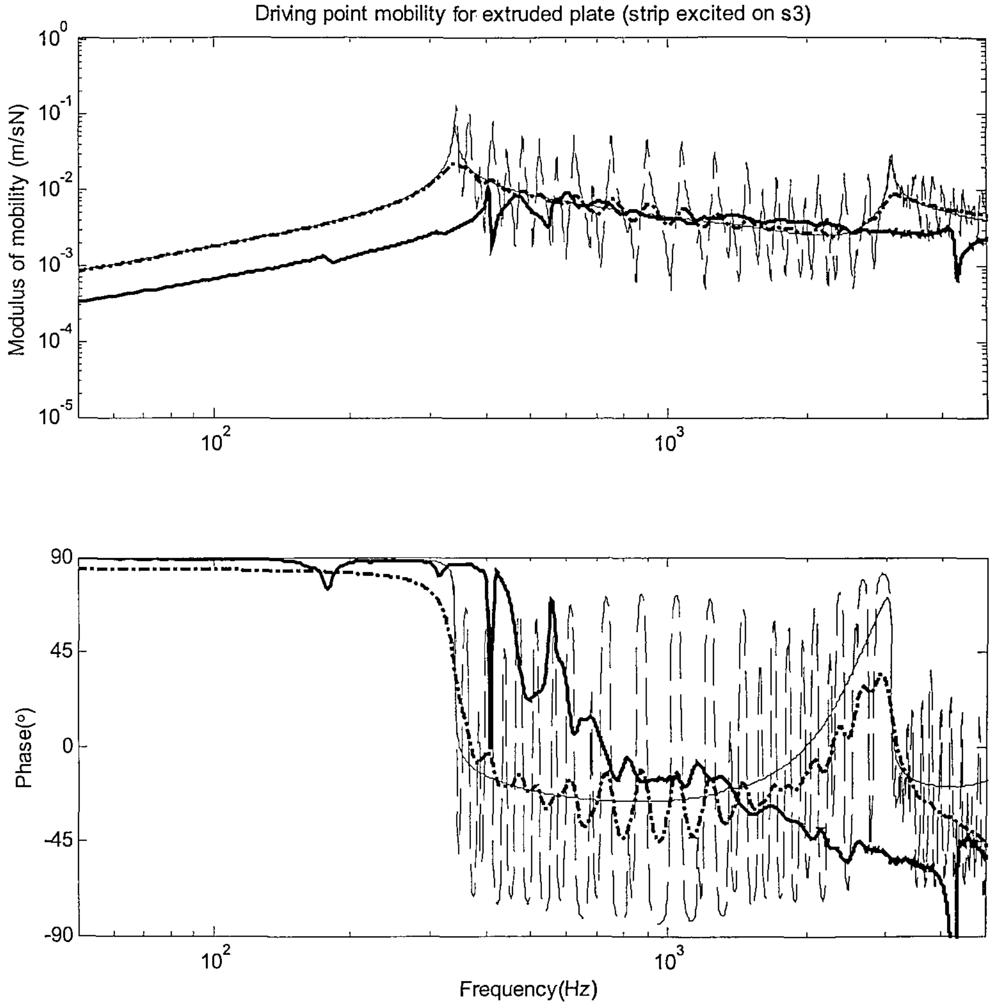

Figure 7.5. Modulus of the measured driving point mobility and calculated for the simply supported finite and infinite strip. — infinite simply supported strip (η = 0.01), – – finite simply supported strip (η = 0.01), ·— finite simply supported strip (η = 0.1), thick — measured on a strip.

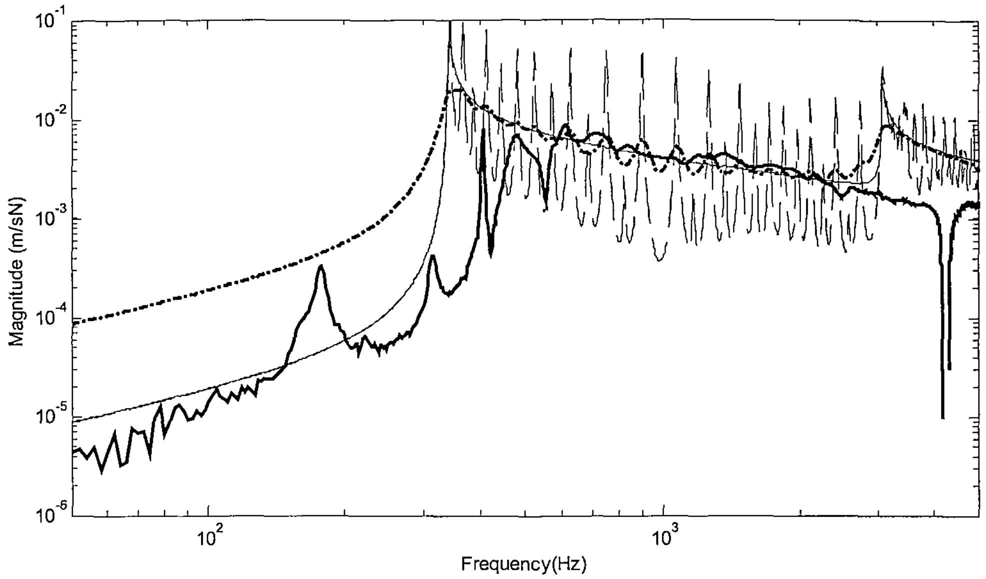

Figure 7.6. Real part of the measured driving point mobility and calculated for the simply supported finite and infinite strip. —— infinite simply supported strip (η = 0.01), – – finite simply supported strip (η = 0.01), ·— finite simply supported strip (η = 0.1), thick—— measured on a strip.

The experiments have shown that the spatially-averaged transfer mobility on the excited strip is higher than those on adjacent strips. This is shown in Figure 7.7 which presents spectra in one-third octave bands. For frequencies below 300 Hz, all strips appear to have the same average velocity. This is because the vibration is dominated by the global behaviour of the structure. Above 300 Hz, strip 4, which is directly excited by the shaker, has an averaged velocity that is about 20dB higher than the other strips, except for strip 3. This shows the localisation of response. Although the localisation has not yet been investigated quantitatively, it is seen that the amplitude decays rapidly away from the excitation region. The localisation should be distinguished from the attenuation of the response due to energy absorption by damping. Damping is important in limiting the overall response. However, localisation will occur even in the case of vanishing damping. Because the undamped panel is not available, the effect of localisation cannot be fully demonstrated on a damped panel at this stage. However, the measured results from the excitation applied on the joints (presented in a later section) will give additional evidence because the localisation disappears in that case.

It is noted that the average mobility of strip 3 (for excitation on strip 4) is higher than that of strip 5 while both are adjacent to strip 4. If this were to be investigated in detail, it would require that the boundary conditions between strips be modelled in detail. Also, strip 3 has a width more similar to strip 4 than strip 5. A similar problem of the propagation of plate flexural waves through reinforcing beams on beam-plate systems was investigated by Heckl [59] and Ungar [98]. It was shown there that there are discrete frequencies at which transmission occurs though the ribs (beams). Since extruded plates are designed with irregular geometry and mass on the joints, it is difficult to model the wave propagation for two adjacent strips specifically. Moreover, in practice, vibration engineers would like a relatively simple model or method which would enable them to understand broad features of the vibration distribution and transmission within extruded plates. For these reasons the wave transmission from a strip to its adjacent strip has not been investigated theoretically here.

Figure 7.8 presents a bar graph to represent the average transfer mobility in three one-third octave frequency bands for each strip on a dB scale. The reference mobility is 10^{-6}m/sN. 10^{-4} m/sN corresponds to 40 dB. This gives a general picture of the spatial distribution of the response for the plate. In the 200 Hz band, the plate is dominated by global motion so that all strips vibrate with a similar amplitude. Strips 2 and 6 even have larger amplitude because of the free boundary conditions. In the 500 Hz band, strip 4 has a larger mobility than the other strips. The same holds for the 2.5 kHz band where the localisation is even greater.

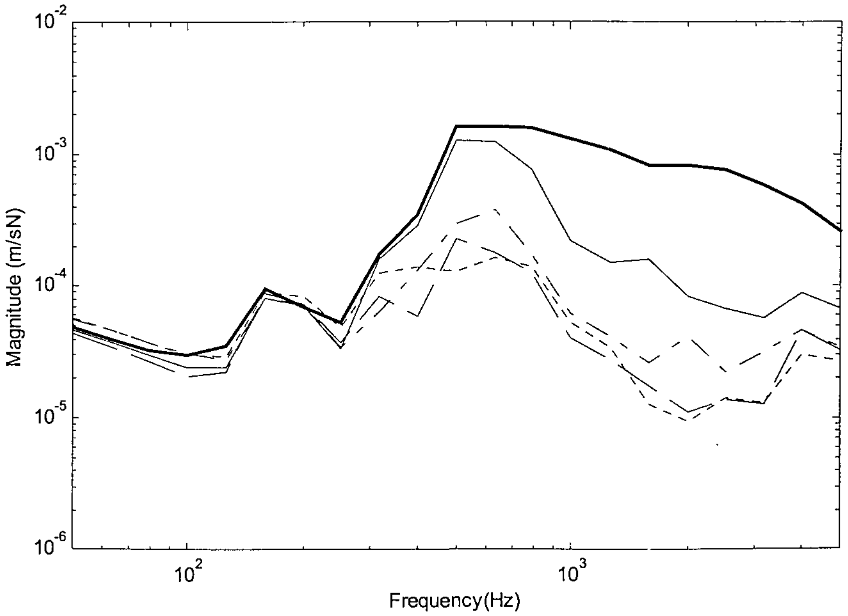

Figure 7.7. Spatially-averaged transfer mobility for each strip. Thick —, strip 4 (excited); —, strip 3, – –, strip 2; –·–, strip 5; ···, strip 6.

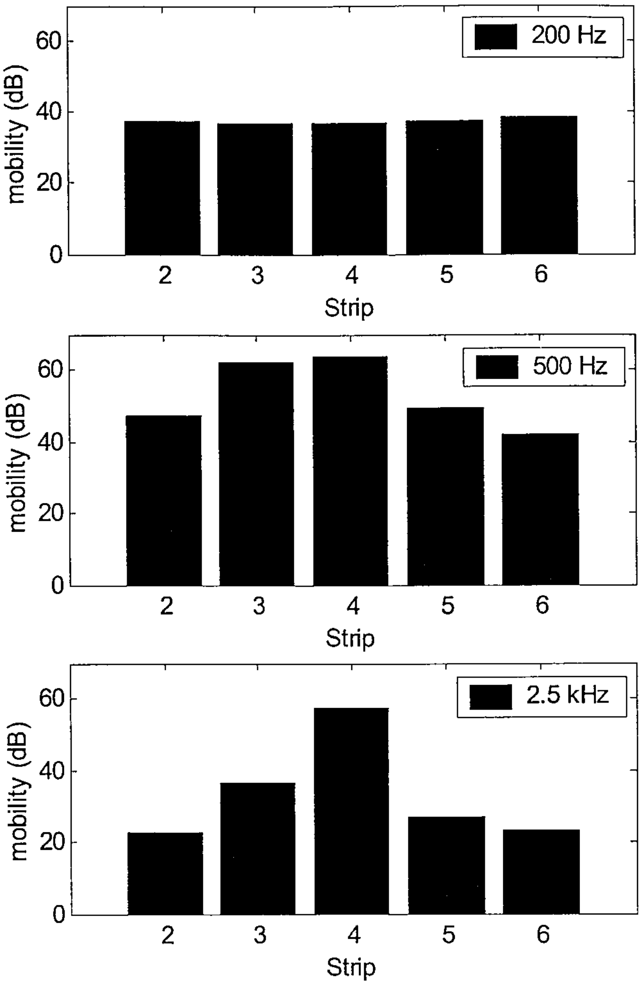

Figure 7.8. Distribution of the transfer mobility over strips. Strip 4 was excited. (dB Ref 10^{-6}m/sN)

Figure 7.9 presents the spatially-averaged transfer mobility for each strip with the excitation applied on strip 2. It is again seen that global vibration is dominant at frequencies below 300 Hz. At frequencies below about 500 Hz, both strips 3 and 4 have a peak. A similar peak was seen in the measurements above for excitation applied on strip 4, as shown in Figure 7.7. Due to the effect of localisation, strip 3, that is adjacent to the excitation strip 2, vibrates at a much lower level than strip 2 for frequencies above 500 Hz. Other more distant strips have even lower vibration levels. This is shown in a bar graph in Figure 7.10. In the 200 Hz band, all strips vibrate with a similar amplitude. For the 1 kHz and 2.5 kHz bands, a big drop occurs in the mobility from strip 2 to strip 3. From strip 3 to strip 6, there is a mild decay across the extruded plate of the average mobility. This is believed to be due to the damping effect.

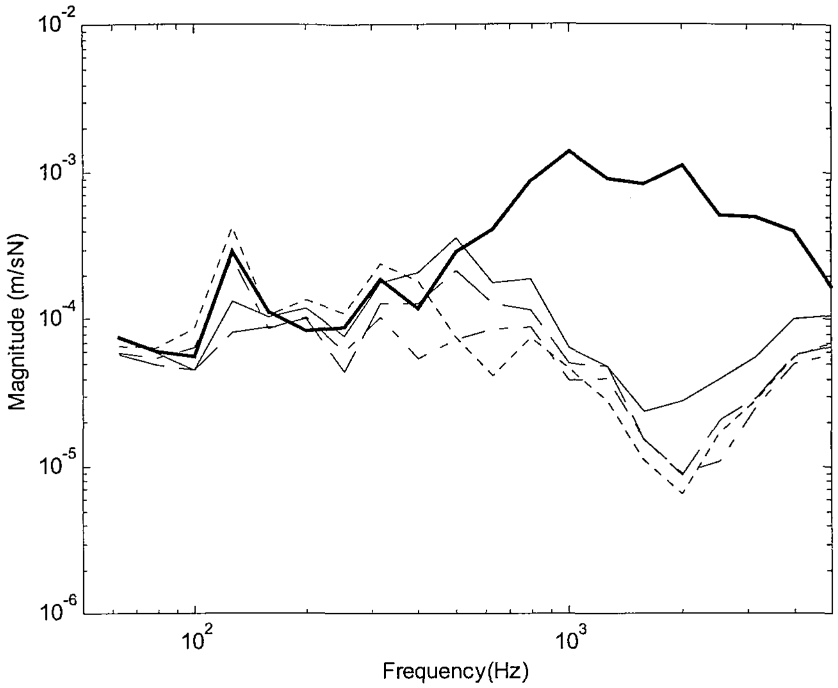

Figure 7.9. Spatially averaged mobility for each strip. Thick——, strip 2 (excited); ——, strip 3, – –, strip 4; —·—, strip 5; ···, strip 6.

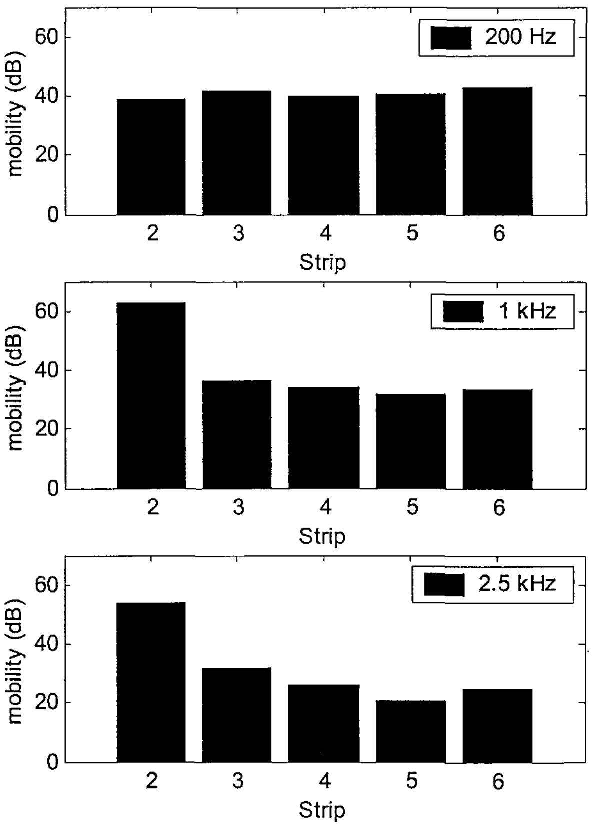

Figure 7.10. Distribution of the transfer mobility over strips. Strip 2 was excited. (dB Ref 10^{-6}m/sN)

The spatially averaged transfer mobilities of all strips on the excitation side and the opposite side are presented in Figure 7.11. It can be seen that, for frequencies above 400 Hz, the average velocity on the excitation side is much higher than that on the opposite side. The average velocities for the two sides are similar for frequencies below 400 Hz. This shows that the global vibration is dominant at low frequencies. The average velocity at those points located on stiffeners for the two sides is also presented in Figure 7.11. It is almost equal to the average velocity on the strips in this frequency range. The response of the stiffeners, in this case, represents the vibration only from global motions.

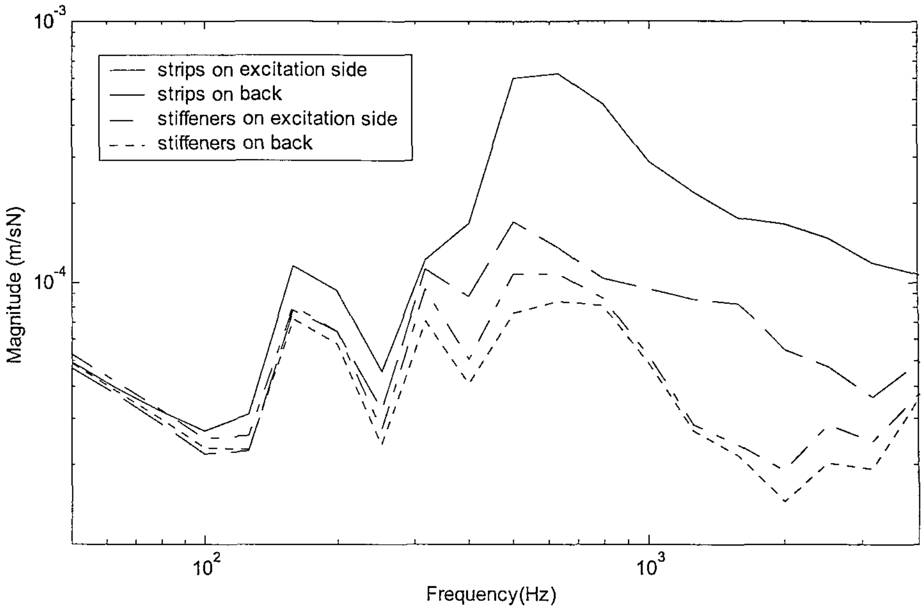

Figure 7.11 Spatially-averaged transfer mobility of the extruded plate for excitation point 3 on strip 4.

7.2.4 EXCITATION ON STIFFENERS

The mobility measurements have also been carried out for the driving points on stiffeners. The driving point mobility is presented in Figure 7.12. The plate behaves like a mass for frequencies below 110 Hz, which corresponds to an anti-resonance. With functions provided by the Scanning Laser Vibrometer, the vibration pattern of the panel can be observed to identify the mode shape of the resonance. The first twisting mode for the free panel occurs at 130 Hz. More importantly, it is found that the first bending mode occurs around 180 Hz.

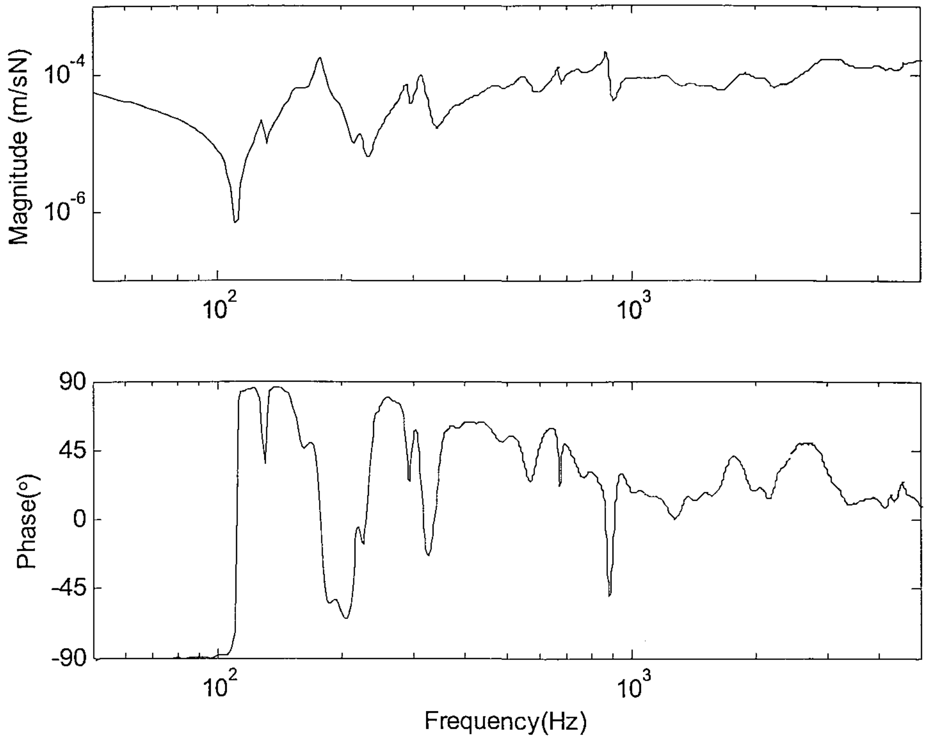

Figure 7.12. Driving point mobility of extruded plate at excitation point 6 on stiffener 4.

The real part of the measured driving point mobility is compared with the result calculated from equation (7.1) in Figure 7.13. It can be seen that the thick plate model (see Chapter 4) gives a good approximation. It is also noted that the real part of the driving point mobilities on strips (Figure 7.4) are about a factor of up to 100 higher than those on stiffeners.

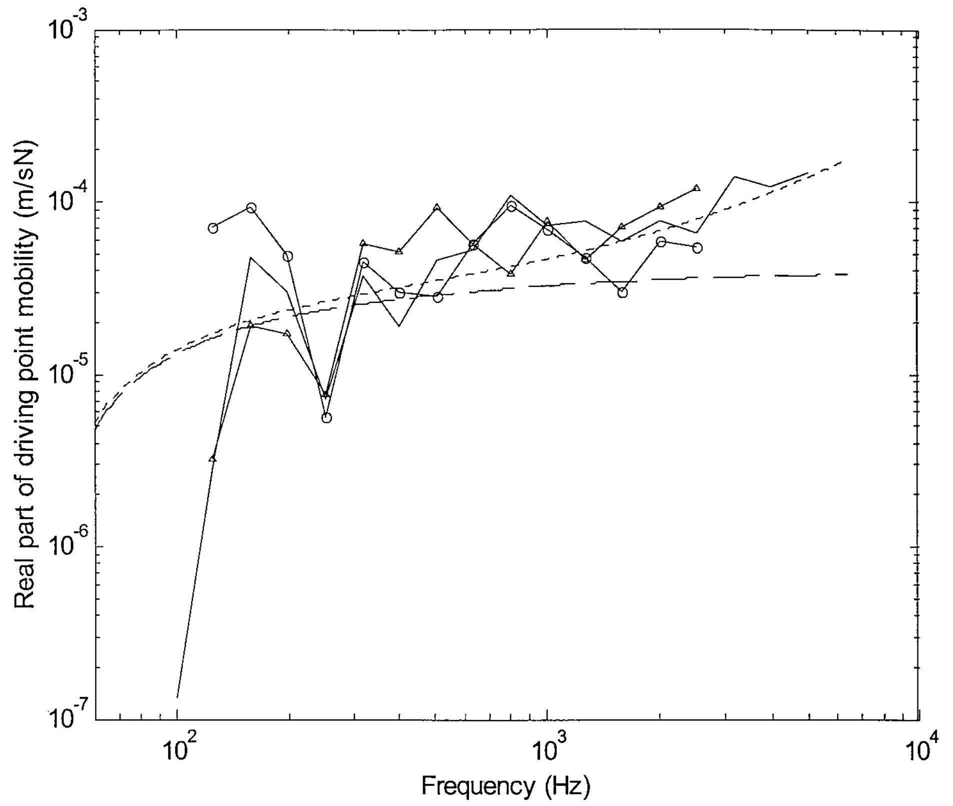

Figure 7.13. Real part of the driving point mobility for excitation positions on stiffeners.
—, excitation position 6; –Δ–, excitation position 5; –o–, excitation position 4;
——, equation (7.1) by thin plate model; ······, equation (7.1) by thick plate model.

The spatially-averaged mobilities for each strip on the excitation side are presented in Figure 7.14. It can be seen that all strips have amplitudes of the same order of magnitude. However the amplitude of strip 2 at frequencies above 400 Hz is lower than the rest. Strip 2 is located farthest from the driving point. It is therefore assumed that the damping effects cause the vibration decay, and the localisation of the response seen in the measurements for the excitation on strips does not occur in this case.

The spatially-averaged transfer mobilities of the strips and stiffeners for each side of the extruded plate are presented in Figure 7.15. All data are represented using one-third octave bands. For frequencies below 400 Hz, the average velocity of strips and stiffeners have very similar amplitudes. Between 400 Hz and 1 kHz, the average velocity of strips on the excitation side is higher than that on the opposite side. However above 1 kHz the average velocity is similar on the strips on both sides and on the stiffeners.

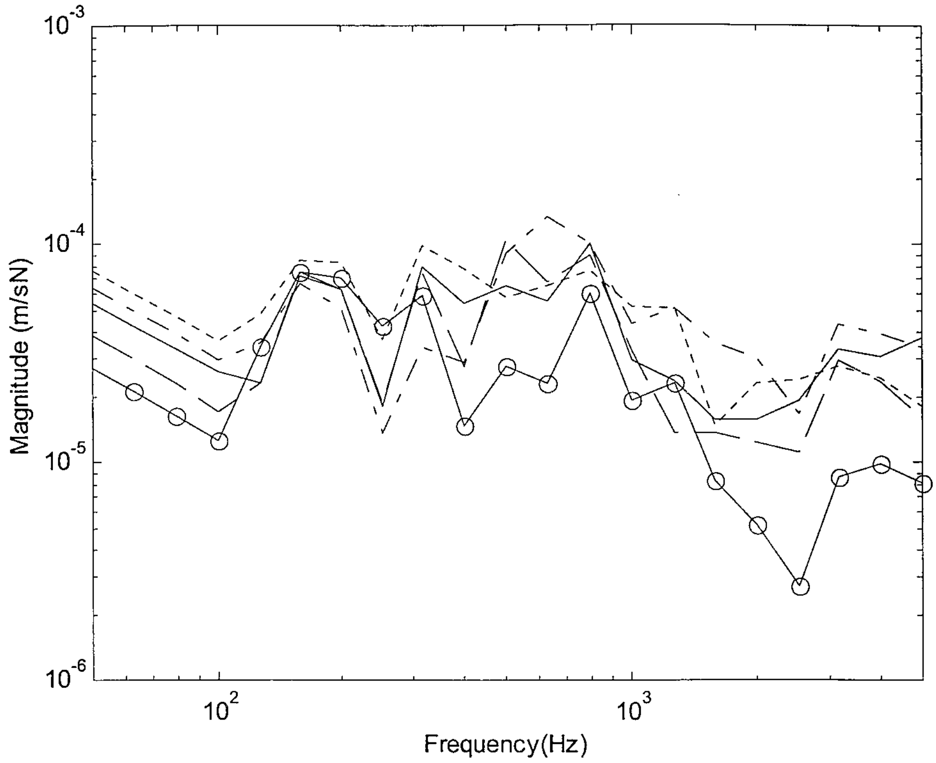

Figure 7.14. Spatially averaged transfer mobility for each strip of the extruded plate under the excitation on stiffeners. —, strip 4 (close to driving point); –o–, strip 2, – –, strip 3; ·—·, strip 5 (close to driving point); ···, strip 6.

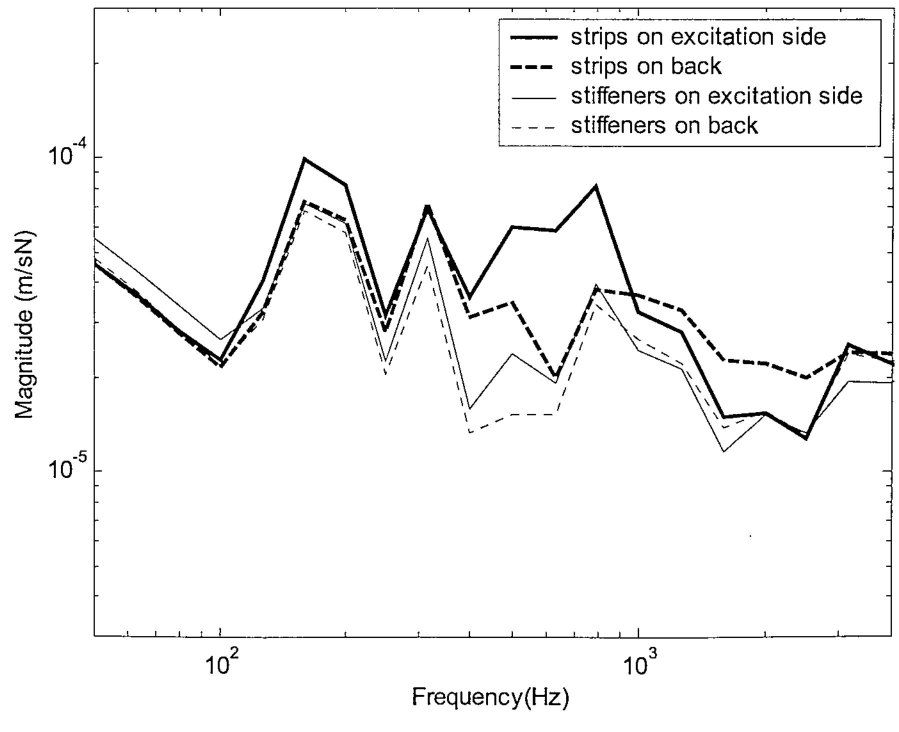

Figure 7.15. Average transfer mobility of the extruded plate for excitation point 6 on stiffener 4.

7.2.5 MEASUREMENT OF THE MODAL DAMPING

The modal damping of the extruded panel is determined experimentally using appropriate methods. When damping is light, the oscillation decay curve method is normally used. For this method, it is required that the structure vibrates freely. This is normally implemented by switching off the source or using a hammer. The structure is excited at resonance with a sine wave force applied with a shaker. A record is taken of the decaying vibration on a logarithmic recorder which displays the logarithm ($\log_{10}$) of the peak amplitude against time [74]. As long as a record of adequate length can be obtained, this method can be used. However, with moderate and heavier damping, the oscillation decay method becomes difficult to use because there is insufficient reverberant vibration field. For the extruded panel studied in this work, the damping is quite heavy so that alternative methods have to be used.

When the structure is in the steady-state under random forcing, the response in the frequency region close to a resonance frequency is predominately that of the resonance. The half-power bandwidth method can be used in this case to determine the modal damping [74]. At low frequency, the response of the extruded panel is dominated by the global modes, which are clearly seen in Figure 7.12. Therefore, the half-power bandwidth method is used to determine the damping loss factor for global modes.

At high frequency (above the cut-on frequency), the response of the panel is dominated by local modes of strips. However, the resonances cannot easily be distinguished from each other (see Figure 7.5) due to the high damping and high modal density. Therefore, a measurement of decay with distance is used to determine the damping loss factor for local modes. Because the structure is two-dimensional, the geometric attenuation should also influence the measured response at a position far from the driving point. However, this is overcome by the localization phenomenon at the forced strip. The driven strip behaves like a one-dimensional structure. The decay measurement is therefore carried out only on the forced strip.

7.2.5.1 Damping of global modes

The half-power bandwidth method is used to determine the damping loss factor at two global resonances. The two resonances at 177 Hz and 312 Hz are taken from the driving point mobility on the stiffener, as shown in Figure 7.12. The damping loss factor is calculated using

$$\eta = \frac{\Delta\omega}{\omega_n} \tag{7.4}$$

where $\Delta\omega$ is the bandwidth corresponding to a 3 dB decrease from the maximum amplitude and ω_n is the natural frequency.

For the resonance at 178 Hz, shown in Figure 7.16, the modal damping loss factor of 0.045 is obtained while for the resonance at 312 Hz as shown in Figure 7.17, 0.044 is obtained. These two values match each other very well.

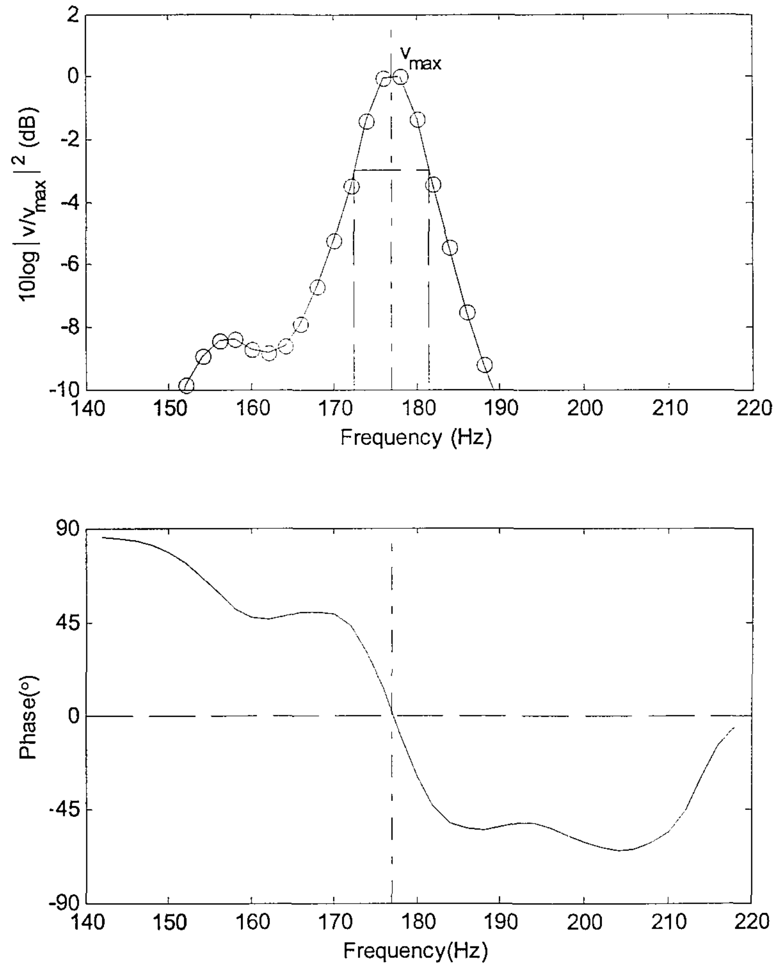

Figure 7.16. Use of half-power bandwidth method to determine the damping loss factor at 177 Hz resonance.

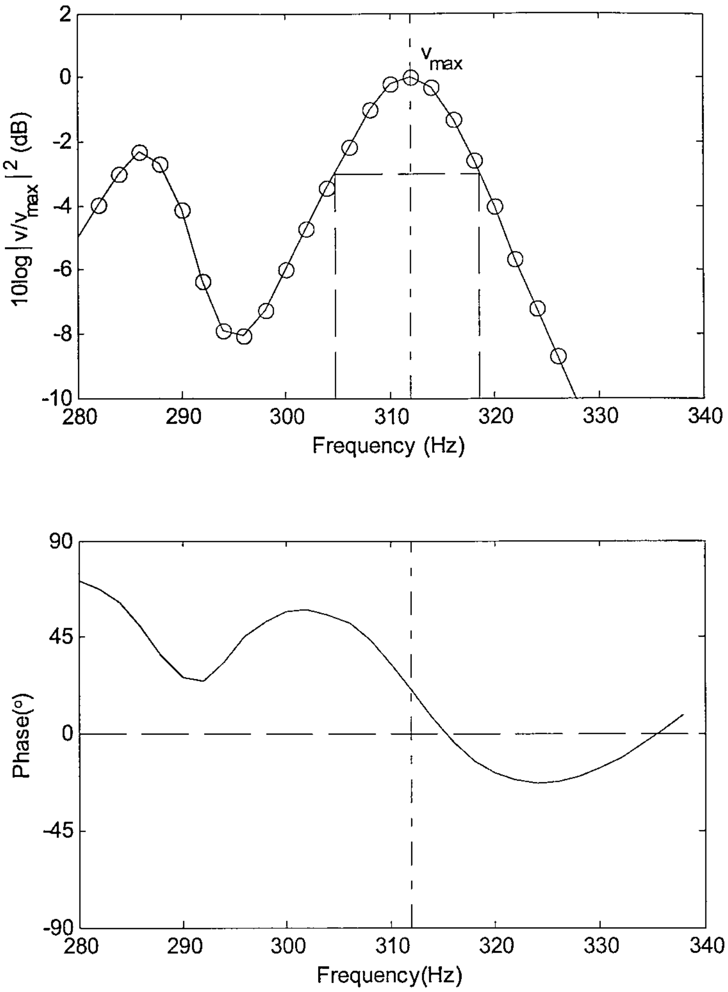

Figure 7.17. Use of half-power bandwidth method to determine the damping loss factor at 312 Hz resonance.

7.2.5.2 Damping of local modes

The attenuation of vibration with distance due to the damping effect has been measured. This can further be used to determine the damping loss factor, normally, in one-third octave frequency bands. Measurement positions were chosen at 2, 4, 8, 12, 16, 24, 32, 48 and 64 cm from the driving point (on strip 4) along the strip. This is shown in Figure 7.18.

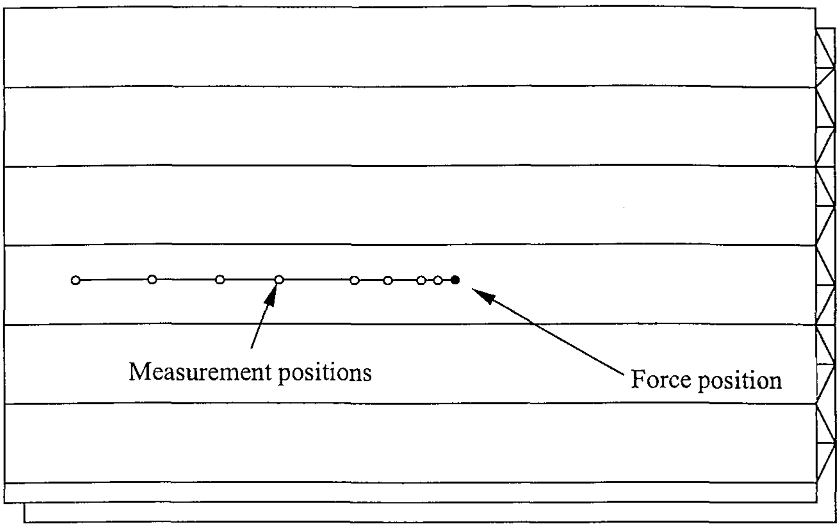

Figure 7.18. Sketch showing the measurement positions for the damping loss factor.

The transfer mobility was measured to derive the reduction in vibration level. Assuming bending waves, the damping loss factor is calculated from [35]

$$\eta = \frac{\Delta \lambda}{13.6} \tag{7.5}$$

where Δ represents the reduction of mobility in decibels per unit length, λ is the wavelength at the central frequency of the corresponding frequency band, assumed to be that of bending waves in an aluminium plate of thickness 2.6 mm. It should be noted that the above equation is not valid for frequencies below the cut-on frequency. This is because the response of the strip is stiffness controlled and there are only evanescent waves.

The attenuation of vibration with distance in different one-third octave bands is presented in Figure 7.19. For frequency bands lower than 500 Hz, the measured data is less reliable for deriving the damping loss factor due to the influence of the mode shape of global vibration and the fact that this is below the cut-on frequency. For example in the band of 200 Hz shown, the rapid decay of vibration within 0.1 m from the driving point is due to the evanescent waves since there are no propagating bending waves below the cut-on frequency. The vibration is controlled by the stiffness of the strip (see also the point mobility in Figure 7.3). Effects of global modes become more significant and they have a different wavelength as well in equation (7.5). This can be seen from the minor attenuation between 0.1 m and 0.32 m.

The reduction of mobility in decibels per unit length is obtained by a linear regression procedure for each frequency band. In this process the data for the measurement positions at the driving point, the points at 2 cm and 4 cm from the driving point are not used as these can be affected by near-field waves and by geometric attenuation. Figure 7.20 as an example shows the derived linear attenuation with distance. The slope of the straight line corresponds to the reduction of mobility in decibels per unit length. The damping loss factors in all frequency bands have been calculated. These are listed in Table 7.2 and plotted in Figure 7.21. The result in most bands is between about 0.1 and 0.25. The variance of these results should be understood to be due to certain measurement errors, which eventually affect the slope of the calculated vibration attenuations. At 500 Hz, the predicted wavelength on the strip is 0.23 m. However, the measurement results may still be affected by the cut-on frequency which is quite close to this frequency. The value of 0.4 at 500 Hz is therefore suspected not to represent the real damping value.

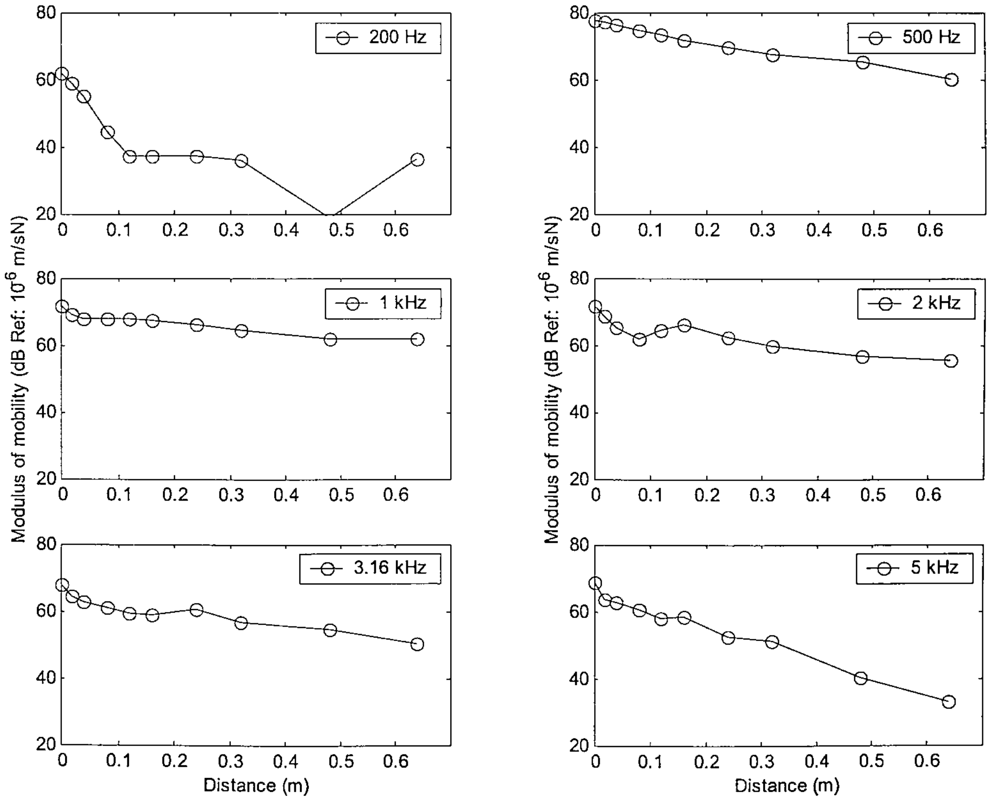

Figure 7.19. Attenuation of vibration with distance on extruded plate, measured along strip.

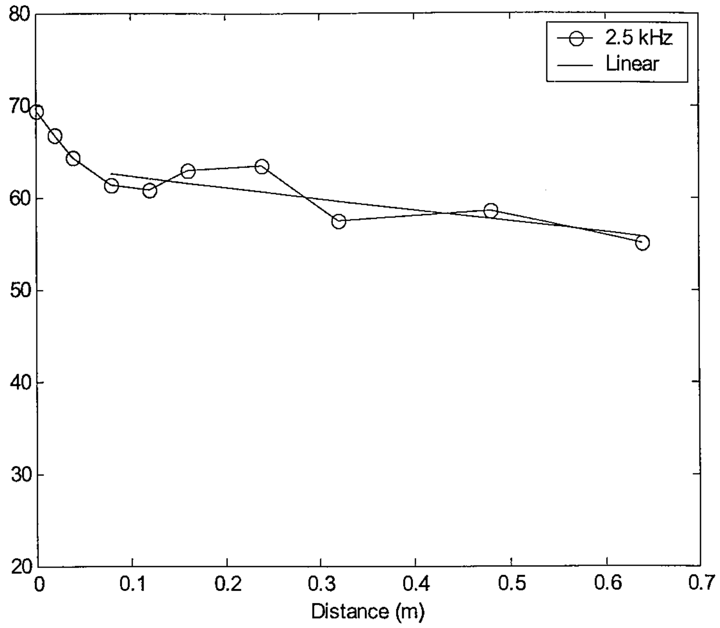

Figure 7.20. Linear regression of measured vibration to derive the damping loss factor (2.5 kHz).

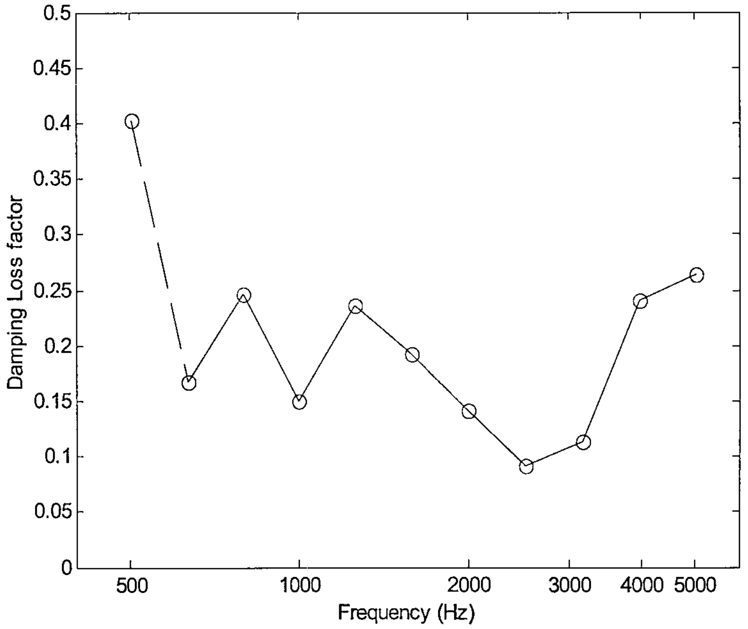

Figure 7.21 Measured damping loss factors in a strip.

The attenuation of vibration along a strip is compared with that across strips (strip 2 excited). This is respectively presented in Figure 7.22 for 1 kHz, Figure 7.23 for 2.5 kHz and Figure 7.24 for 3.16 kHz. It can be seen from these figures that the attenuation due to the damping acts similarly in both directions, along and across strips. Except for the big drop from the excited strip to the adjacent one in the direction across strips, the slopes of the curves in the two directions are similar. This also shows the localisation phenomenon on the extruded plate. This gives increased confidence in the results derived using decay measurements. As the geometric decay may still affect the results a little, it is safer to use a damping loss factor smaller than the value listed in Table 7.2.

It should be noted that the vibrations across strips increase a bit at the most distant strip (corresponding to a distance of about 0.6 m). This is because the spatially-averaged response was used for each strip. The strip along the edge of the panels vibrates more strongly due to the free boundary conditions in the measurements.

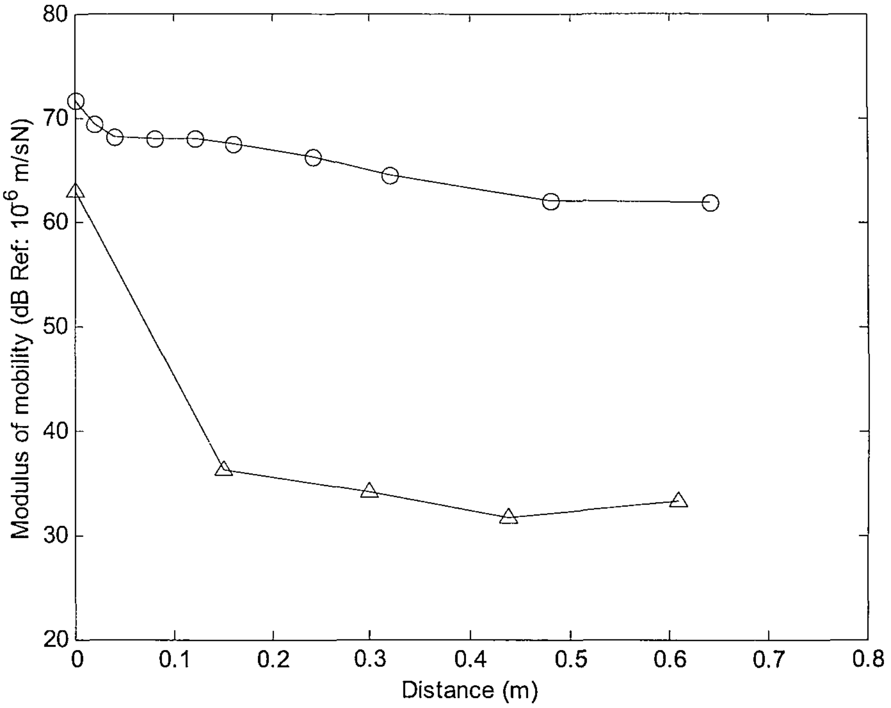

Figure 7.22. Comparison of the attenuation of vibration along strip and across strip (1 kHz). –o–, along strip; –Δ–, across strip.

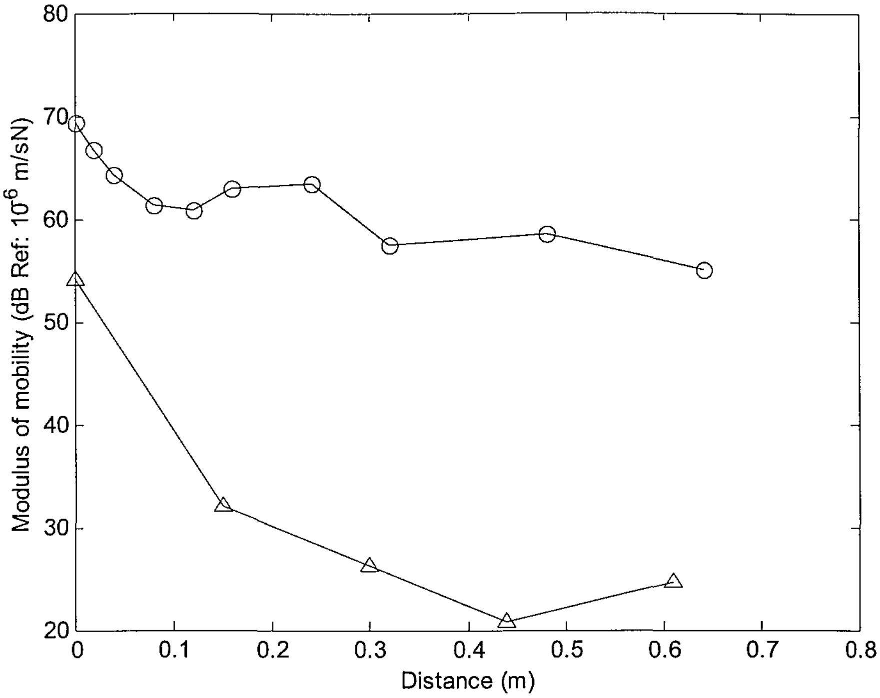

Figure 7.23. Comparison of the attenuation of vibration along strip and across strip (2.5 kHz).

–o–, along strip; –Δ–, across strip.

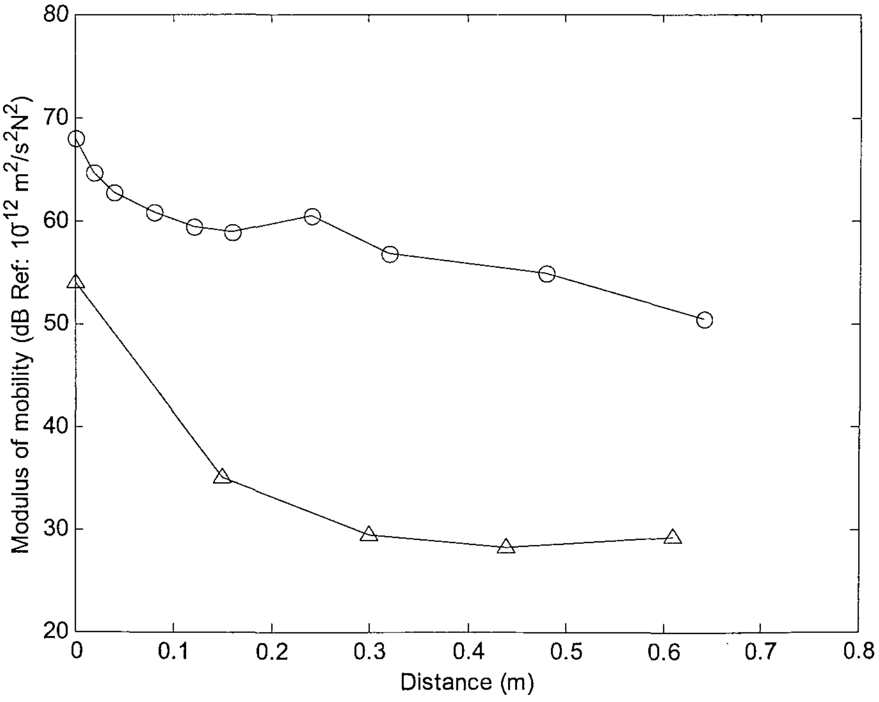

Figure 7.24. Comparison of the attenuation of vibration along strip and across strip (3.16 kHz).

–o–, along strip; –Δ–, across strip.

Table 7.2. Measured damping loss factors in a strip

Frequency band (Hz)	Damping loss factor
500	0.40
630	0.17
800	0.25
1k	0.15
1.25k	0.23
1.6k	0.19
2k	0.14
2.5k	0.09
3.15k	0.11
4k	0.24
5k	0.26

7.3 RADIATION EFFICIENCY MEASUREMENTS

7.3.1 THEORETICAL BACKGROUND

The method measuring the radiation efficiency is based on the reference [99]. The sound power radiated by a vibrating structure is related to its surface velocity by

$$W_{rad} = \rho_0 c \sigma S \left\langle \overline{v^2} \right\rangle \tag{7.6}$$

where ρ_0 is the density of air, c is the speed of sound in air, S is the surface area of the structure, σ is the radiation efficiency and $\left\langle \overline{v^2} \right\rangle$ is the spatially-averaged mean-square velocity of the structure normal to the surface. If equation (7.6) is normalised by the mean-square force applied to the structure $\overline{F^2}$, it becomes

$$\frac{W_{rad}}{\overline{F^2}} = \rho_0 c \sigma S \left\langle |Y|^2 \right\rangle \tag{7.7}$$

where Y is the transfer mobility from the excitation point to a point on the surface.

In order to obtain the radiation efficiency, it is necessary to perform two sets of measurements. The first consists of the spatially-averaged transfer mobility $\left\langle |Y|^2 \right\rangle$ for some excitation point. The second is a measurement of the radiated sound power normalised to the input mean square force for the same excitation point.

The power radiated into a room can be obtained by measuring the spatially-averaged sound pressure in the room $\left\langle \overline{p^2} \right\rangle$, away from the walls. This can be normalised to the mean-square force to give

$$\frac{W_{rad}}{\overline{F^2}} = \frac{\overline{S\alpha}}{4\rho_0 c} \left\langle \frac{\overline{p^2}}{\overline{F^2}} \right\rangle \tag{7.8}$$

where $\overline{S\alpha}$ is the room absorption.

Suppose that, instead of the spatially-averaged pressure in the room, the pressure p_F is measured at a location close to the wall. It is usual to avoid locations near the walls, but in the present case it is assumed that this restriction is not enforced. The pressure near to a wall is higher than the spatially-averaged value by an amount C_{rad}, which is the ratio of the radiation resistance of the source at that location to that in the free field. The spatially-averaged pressure should then be replaced by $\overline{p_F^2}/C_{rad}$:

$$\frac{W_{rad}}{\overline{F^2}} = \frac{\overline{S\alpha}}{4\rho_0 c C_{rad}} \frac{\overline{p_F^2}}{\overline{F^2}} \tag{7.9}$$

Using the principle of reciprocity, the ratio between the radiated pressure p_2 at location 2 and the force F_1 applied to the structure at location 1 is the same as that between the velocity response v_1 of the structure at location 1 and the volume velocity Q_2 of a source at location 2 that causes it:

$$\frac{p_2}{F_1} \equiv \frac{v_1}{Q_2} \tag{7.10}$$

Applying this to equation (7.9),

$$\frac{W_{rad}}{\overline{F^2}} = \frac{\overline{S\alpha}}{4\rho_0 c C_{rad}} \frac{\overline{p_F^2}}{\overline{F^2}} = \frac{\overline{S\alpha}}{4\rho_0 c C_{rad}} \frac{\overline{v_Q^2}}{\overline{Q^2}} \tag{7.11}$$

In practice, the volume velocity Q is not measured directly, but is deduced from a sound power measurement. For a compact source located in a free field with a mean-square volume velocity $\overline{Q^2}$, the radiated sound power is given by

$$W_Q = \rho c \overline{Q^2} \frac{k^2}{4\pi} \qquad (7.12)$$

where k is the wavenumber, $k = \omega/c$. For a source that is not in a free field, a correction is required, which is identical to C_{rad}, the ratio of the radiation resistance of the source to that in the free field. Hence,

$$W_Q = \rho c \overline{Q^2} \frac{k^2}{4\pi} C_{rad} \qquad (7.13)$$

The mean-square volume velocity $\overline{Q^2}$ is then given by

$$\overline{Q^2} = \frac{4\pi W_Q}{\rho_0 c C_{rad} k^2} = \frac{4\pi}{\rho_0 c C_{rad} k^2} \frac{S\bar{\alpha}}{4\rho_0 c} \left\langle \overline{p_Q^2} \right\rangle = \frac{S\bar{\alpha}\pi}{\rho_0^2 \omega^2 C_{rad}} \left\langle \overline{p_Q^2} \right\rangle \qquad (7.14)$$

Substituting equation (7.14) into (7.11),

$$\frac{W_{rad}}{\overline{F^2}} = \frac{S\bar{\alpha}}{4\rho_0 c C_{rad}} \frac{\overline{v_Q^2} \rho_0^2 \omega^2 C_{rad}}{S\bar{\alpha}\pi \left\langle \overline{p_Q^2} \right\rangle} = \frac{\overline{a_Q^2}}{\left\langle \overline{p_Q^2} \right\rangle} \frac{\rho_0}{4\pi c} \qquad (7.15)$$

where $\overline{a_Q^2}$ is the mean square acceleration of the structure due to excitation by the sound source and $\left\langle \overline{p_Q^2} \right\rangle$ is the spatially averaged mean square sound pressure in the room during the operation of the source. It will be noted that neither the absorption of the room nor the factor C_{rad} appear in this equation. The actual source and its volume velocity are unimportant provided that a diffuse field is generated.

Equation (7.10), and hence equation (7.15) apply for single frequencies. They cannot be used for an average over a frequency band unless the spectrum of $\overline{Q^2}$ (and by implication the spectrum of $\overline{F^2}$) is constant over each frequency band. Similarly, it is only possible to average over a number of source positions if $\left\langle \overline{p_Q^2} \right\rangle$ is the same in each case, in which case

$$\frac{W_{rad}}{\overline{F^2}} = \frac{\left\langle \overline{a_Q^2} \right\rangle}{\left\langle \overline{p_Q^2} \right\rangle} \frac{\rho_0}{4\pi c} \qquad (7.16)$$

where $\left\langle \overline{a_Q^2} \right\rangle$ is averaged over the source (loudspeaker) positions and $\left\langle \overline{p_Q^2} \right\rangle$ is averaged over microphone positions.

Hence from equation (7.7), the radiation efficiency is given by

$$\sigma = \frac{\left\langle \overline{a_Q^2} \right\rangle}{\left\langle \overline{p_Q^2} \right\rangle \left\langle |Y|^2 \right\rangle 4\pi S c^2} \tag{7.17}$$

Since the measurements are carried out for an unbaffled condition, the surface area S should be twice that of one side, $2ab$, to account for the total area vibrating. $<|Y^2|>$ is the spatially averaged transfer mobility to points on both sides of the panel from the chosen forcing point. It is also important that the ratio of two power spectra is measured and not a transfer function between p_Q and a_Q as these will be poorly correlated due to reverberation.

7.3.2 EXPERIMENTAL ARRANGEMENT

The measurements were made in the ISVR reverberant chamber, which has mean edge lengths 9.15 m × 6.25 m × 6.10 m, volume 348 m^3 and surface area 302 m^2. The plate was suspended on the frame and measurements made at a number of locations in the chamber. One loudspeaker was placed in the corner of the chamber and driven with continuous random noise generated from an HP analyser. This covered the frequency range 0 Hz to 6.4 kHz. A B&K microphone of type 4134 attached to the end of a B&K rotating microphone boom of type 3923 was used to measure a spatial average of the sound pressure in the chamber. The microphone signal was amplified using a B&K Measuring Amplifier of type 2610. One B&K type 4374 accelerometer was used to measure the response at locations on the panel corresponding to the excitation positions in the mobility measurements (Section 7.2). The acceleration signal was amplified using a B&K charge amplifier type 2635.

Measurements were made for two loudspeaker source positions and three positions of the panel within the chamber. For each pair of loudspeaker and panel positions, the sound pressure spectrum in the chamber and acceleration spectrum on the panel were recorded as narrow-band spectra. A Hanning window was used in the frequency analysis. A resolution of 4 Hz was used.

7.3.3 RESULTS

Figure 7.25 presents the average sound pressure for different source and panel positions. This shows a fairly constant level was achieved between 100 Hz and 3150 Hz. Due to the loudspeaker response the sound pressure drops at high frequencies. The acceleration of the extruded plate (at the strip excitation position) to acoustic excitation is presented in Figure 7.26.

After combining the results of the spatially averaged mobility, the radiation efficiency was calculated in one-third octave bands according to equation (7.17). This is presented in Figure 7.27 for the three different excitation positions on strips and one on the stiffener. It can be seen that the radiation efficiency tends to unity at frequencies above 4 kHz. For frequencies below this range, the radiation efficiency is smaller than unity, although for excitation on the stiffener it is unity for frequencies above 1 kHz.

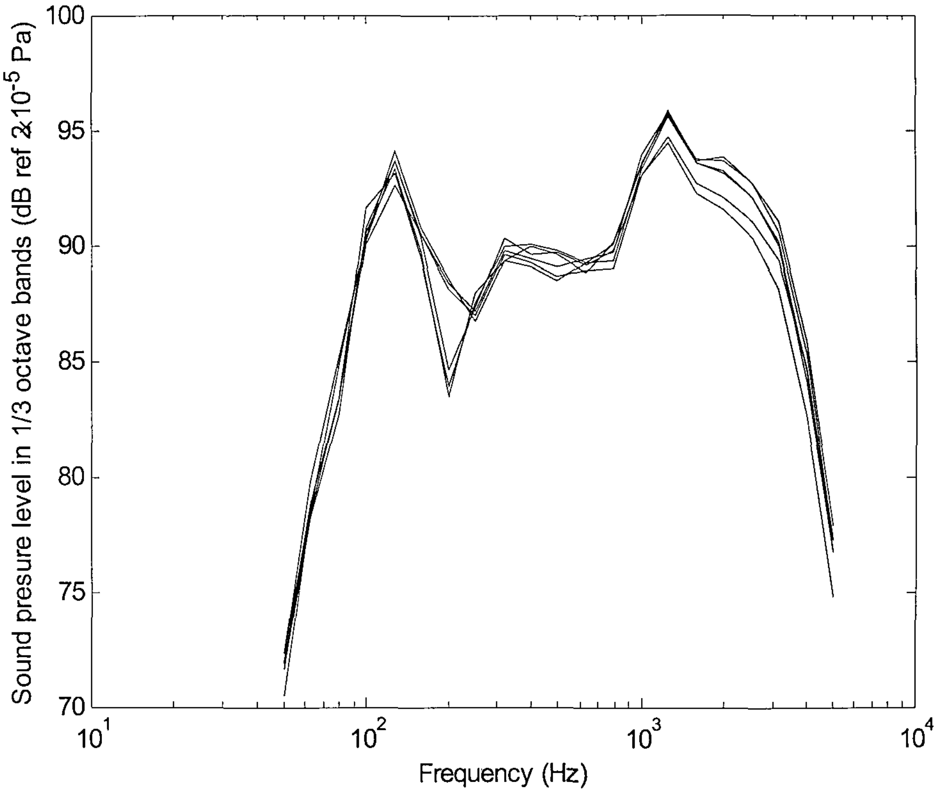

Figure 7.25. Sound pressure spectrum in the reverberation room for each source and panel position.

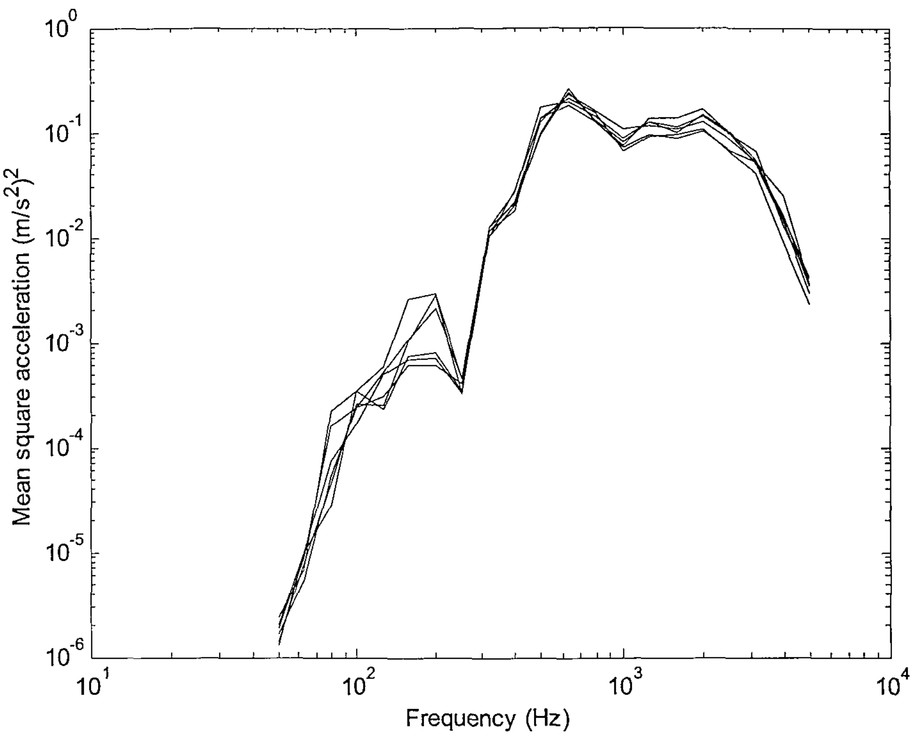

Figure 7.26. Acceleration due to acoustic excitation for each source and panel position.

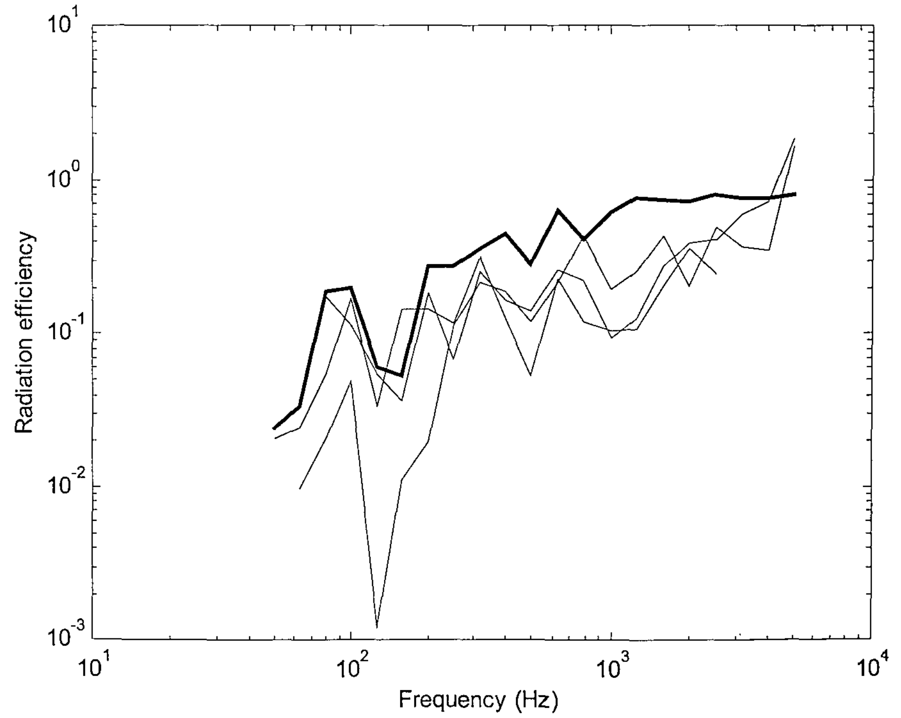

Figure 7.27. Measured radiation efficiency for three excitation positions on strips (thin line) and one excitation on a stiffener (thick line).

The radiation efficiency of the extruded plate is also predicted using the simple model described in Chapter 5. In this model, the sound radiation from the local vibration of strips was assumed to consist only of that from the strip on which the excitation point was located. Therefore the radiation from the local vibration of each strip will be weighted by the ratio of its area to the whole surface area of the panel. This is given by equation (7.18)

$$\sigma = \frac{\overline{W}_{global} + \overline{W}_{local}}{\rho c S \left\langle \overline{u^2} \right\rangle} = \frac{\sigma_g \left\langle \overline{u_g^2} \right\rangle + \left\langle \overline{u_l^2} \right\rangle \sum_i \frac{S_i}{S} \sigma_i}{\left\langle \overline{u_g^2} \right\rangle + \left\langle \overline{u_l^2} \right\rangle} \tag{7.18}$$

where u_g is the velocity due to global modes, u_l is the velocity due to local modes, σ_i and S_i are the radiation efficiency and area corresponding to ith strip on the outer plate, σ_g is the radiation efficiency of global modes and S is the surface area of the extruded panel. For this the measured velocities u_g and u_l are used.

In Figure 7.28, this predicted radiation efficiency is compared with the measured result for excitation on a strip. The spatially averaged velocities for global and local vibration used in the prediction are taken from the mobility measurements (section 7.2). For frequencies above 300 Hz, the predicted curve matches the measured one reasonably well. The model based on the baffled simply supported plate will cause a considerable overestimate for frequencies below the first natural frequency as the measurements are of an unbaffled panel. In the present measurements, this happens at frequencies below 100 Hz. In the prediction the effects due to unbaffled edges have been taken into account in σ_g according to corrected expressions [100]. Compared with a baffled plate, the radiation efficiency below the critical frequency for an unbaffled plate is given by

$$\sigma_{unb} = C_{plate} \left(C_{corner} \sigma_{corner,b} + C_{edge} \sigma_{edge,b} \right) \tag{7.19}$$

where σ_{unb} represents the radiation efficiency of the unbaffled plate, $\sigma_{corner,b}$ and $\sigma_{edge,b}$ are the radiation efficiencies for the corner and edge modes of a baffled plate. $\sigma_{edge,b}$ has been given in equation (5.28c) and $\sigma_{corner,b}$ is given by [45]

$$\sigma_{corner,b} = \frac{8}{\pi^4} \left(\frac{\lambda_c^2}{S} \right) \times \begin{cases} \left(1-2\alpha^2\right) \Big/ \left(\alpha \left(1-\alpha^2\right)^{1/2} \right), & \alpha^2 < 1/2 \\ 0, & \alpha^2 \geq 1/2 \end{cases} \tag{7.20}$$

The parameter C_{plate} is a plate correction that accounts for the effect of inertial flows that surround the plate at low frequencies where acoustic wavelength exceeds the dimensions of the plate. C_{corner} and C_{edge} are the local corrections that account for the effect on radiation from corner and edge modes at higher frequencies due to localized inertial flows near the plate perimeter. They are given in reference [100] respectively by

$$C_{corner}=\frac{1}{2}\left[\frac{(16/3)(\pi\varepsilon\alpha)^2}{1+(16/3)(\pi\varepsilon\alpha)^2}\right] \tag{7.21}$$

$$C_{corner}=\frac{1}{2}\left[\frac{2\pi^4(\varepsilon\alpha)^2}{1+2\pi^4(\varepsilon\alpha)^2}\right] \tag{7.22}$$

$$C_{plate}=\frac{53f^4S^2/c^4}{1+53f^4S^2/c^4} \tag{7.23}$$

where ε is a proportionality factor determined empirically. Here $\varepsilon = 0.5$ is used.

For frequencies between 100 and 300 Hz, there is quite a large discrepancy, with a big dip at 125 Hz. This is believed to be due to the effects of fluid flow around the plate at the first mode of the free plate, which causes certain cancellations to sound radiation. The first mode of the free plate consists of twisting in which opposite corners move in phase. This mode will have quite a low radiation efficiency, corresponding to 4 dipoles, one at each corner. This mode occurs at 128 Hz. Such a mode is not included in the theoretical model which assumes modes of a simply supported plate, although the effect of unbaffled edges are included.

Figure 7.29 presents the comparison between predicted and measured radiation efficiency of the extruded panel for excitation on a stiffener. For frequencies above 700 Hz, the predicted curve matches the measured one reasonably well. The low radiation efficiency at the first mode 128 Hz is again seen as a dip in the measured curve. The disagreement at frequencies between 200 Hz and 700 Hz of ±5dB is not so easy to explain. Measurement error is unlikely to be responsible; for example background noise was found to be 50 dB below the measured levels. Assumptions in the model that may not correspond to reality are (i) the cut-on frequencies for local modes (222 and 242 Hz in the model for the two sides and about 500 Hz in the measurements); (ii) the local modes are assumed to consist of motion of a single strip whereas motion of adjacent strips also occurs. The damping of the panel will also have an influence on the radiation of the local modes; it has been assumed as 0.1 which corresponds to measurements in Section 7.2.5.2.

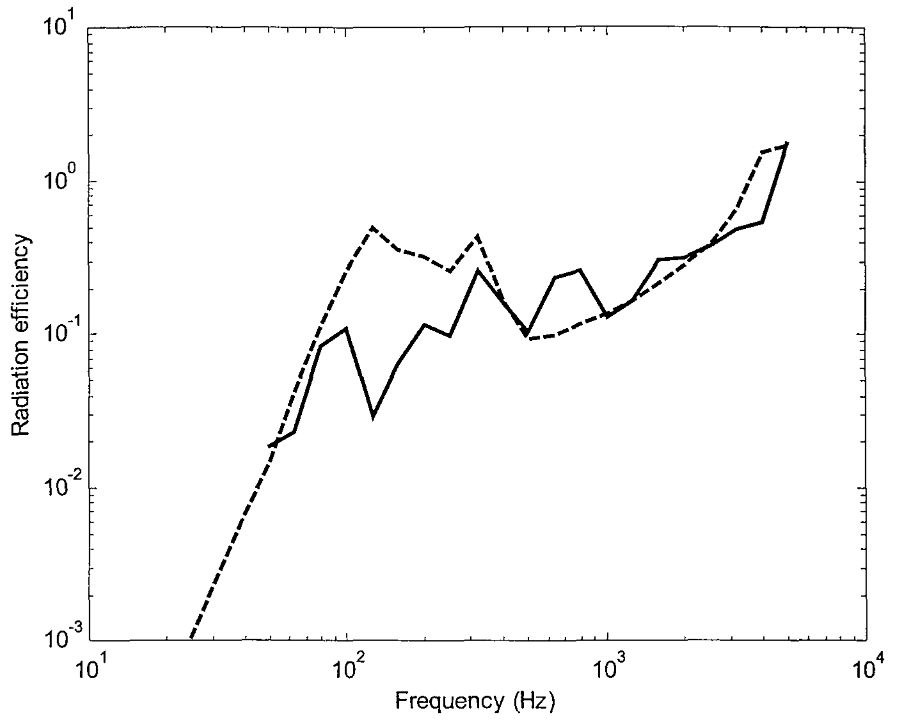

Figure 7.28. Predicted and measured radiation efficiency of extruded plate for excitations on a strip. —, measured; – – –, predicted.

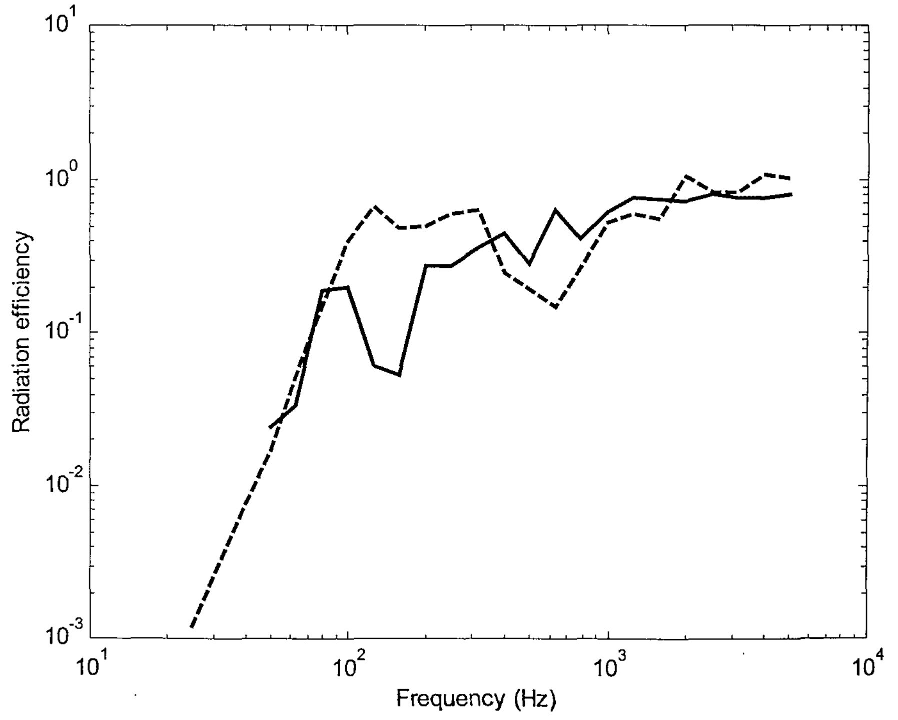

Figure 7.29. Predicted and measured radiation efficiency of extruded plate for excitation on a stiffener. —, measured; – – –, predicted.

7.4 CONCLUSIONS

The response of a sample extruded panel under a point excitation has been measured. At low frequencies, typically below 400 Hz, the panel vibrates in global modes while the vibration is dominated by localised modes of the strips at higher frequencies. The driving point mobility has been investigated for excitation positions either on 'strips' or 'stiffeners'. The driving point mobility on strips is controlled by the individual strip that is excited. The driving point mobility on stiffeners is controlled by global modes and is considerably lower than that on strips in the high frequency region.

The transfer mobility at many positions over the panel surface was used to obtain the spatially-averaged mobility. It has been shown that, for excitation on a strip, the average response of the panel on the excitation side is higher than on the other side; the response of the strip under excitation is about 20 dB higher than other strips; the response of the strips is generally higher than that of stiffeners.

The half-power bandwidth method has been used to determine the modal damping loss factors at low frequency for global modes. The propagation attenuation of vibration with distance due to the damping effect has been measured along the driven strip at higher frequencies. The damping loss factors in one-third octave bands have been derived for the local modes.

The radiation efficiency of the sample panel under unbaffled conditions has been measured using a reciprocal test method. Results have been obtained corresponding to excitation positions at strips and stiffeners. The results are compared with predictions from the model described in Chapter 5. It is found that the predictions agree with the measured results in most frequency bands. The difference found at the first mode is believed to be due to the cancellation caused by the fluid flow under the unbaffled conditions; this twisting mode is not accounted for in the model, but would not be present in a vehicle.

8 SEA MODEL FOR EXTRUDED PANELS

8.1 INTRODUCTION

It has been shown in Chapter 2 that SEA can be used to calculate the sound transmission of a panel between two acoustic cavities. For simple systems, such as the single-leaf panel used in Chapter 2, SEA does not offer advantages over conventional methods. However, for more complicated panels, such as double walls, SEA allows an analysis of the individual transmission paths through system, which cannot be readily achieved by conventional methods [73]. In this Chapter an SEA model will be presented to calculate the behaviour for extruded panels. This model is extended from the three-subsystem SEA model described in Chapter 2. Meanwhile, the models obtained in previous chapters for the modal density, the radiation efficiency and coupling between global and local modes will be introduced to represent extruded panels as groups of SEA subsystems. The result for mechanical excitation will be compared with measurements from the previous chapter. Moreover, the result of the sound transmission loss will be compared with experimental data obtained from a vehicle manufacturer on a large sample of the same panel used in Chapter 7 [101].

8.2 FIVE-SUBSYSTEM SEA MODEL

Consider a system consisting of an extruded panel between two acoustic cavities, Figure 8.1. One cavity can correspond to the underfloor cavity and one to the interior cavity of the vehicle. They can also represent the two rooms of a transmission suite. The key issue here is how to construct an SEA model for the extruded panel. Since it has been seen that the vibration energy of extruded plates is distributed in the global modes of the whole panel and local modes dominated by individual strips, the extruded panel is first divided into three subsystems: one representing the global modes and two separate subsystems representing local modes on the two sides of the panel. Therefore the SEA model includes five subsystems. Figure 8.1 shows the coupling between these subsystems.

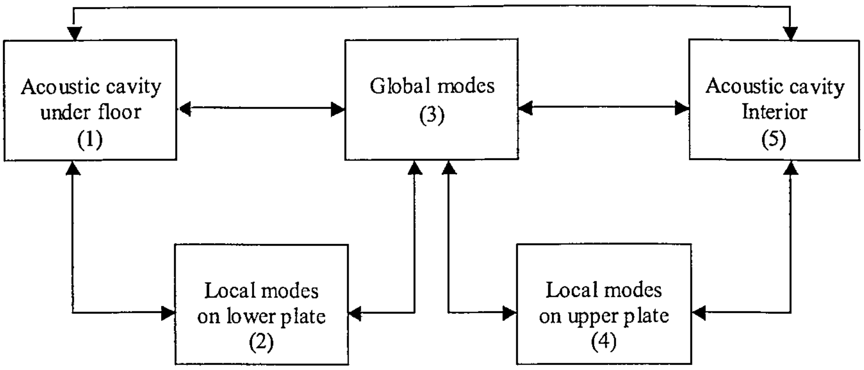

Figure 8.1. SEA block diagram for extruded plate

There are four types of coupling within this SEA model:

a) non-resonant sound transmission between two cavities through the extruded plate;
b) coupling between the cavities and global modes;
c) coupling between the cavities and local modes;
d) coupling between the global modes and local modes.

It is assumed here that there is no direct coupling between the local modes on the two sides of the extruded panel, either through the air or foam between them or through the connecting ribs. The latter connection is assumed to act through the global modes of the structure.

The non-resonant coupling between the two cavities through the extruded panel depends on the mass per unit area of the panel. The coupling loss factor can be calculated using equation (2.17) together with equations (2.18) to (2.20). The total mass per unit area of the extruded panel should be used in equation (2.20) to calculate the transmission loss under normally incident sound waves, and this is converted to a field incidence result using equation (2.19).

The coupling between the cavities and the global modes is the same as that described in Chapter 2. The coupling loss factor from global modes to the cavity can be obtained using equation (2.12). The counterpart of this, the coupling loss factor from the cavity to the global modes, can be given by making use of the consistency relationship, equation (2.16). The radiation efficiency of the global modes was given in Chapter 5.

The method to obtain the coupling between the cavities and the local modes is similar to that for the global modes. For the coupling loss factor from local modes to the cavity, the radiation efficiency of local modes is needed. This has already been studied in Chapter 5 in terms of the radiation efficiency of strips. From equation (5.62), which gives the averaged radiated power from local modes for all possible excitation points, the radiation efficiency of local modes can be expressed by

$$\sigma_l = \frac{\overline{W}_{local}}{\rho c S \left\langle \overline{u_l^2} \right\rangle} = \frac{1}{S} \sum_i S_i \sigma_i \tag{8.1}$$

The coupling loss factor from global modes to local modes is calculated using equation (6.27). The consistency relationship can be used to obtain the coupling loss factor from local to global modes.

8.2.1 MODAL DENSITIES

The dimensions of the two cavities are taken to be 5.8×6.0×7.0 m for the sending cavity and 5.5×6.0×7.0 m for the receiving cavity, corresponding to the transmission suite used for measurements [101]. The modal density *n(f)* of the two cavities is calculated using equation (2.15) and shown in Figure 8.2.

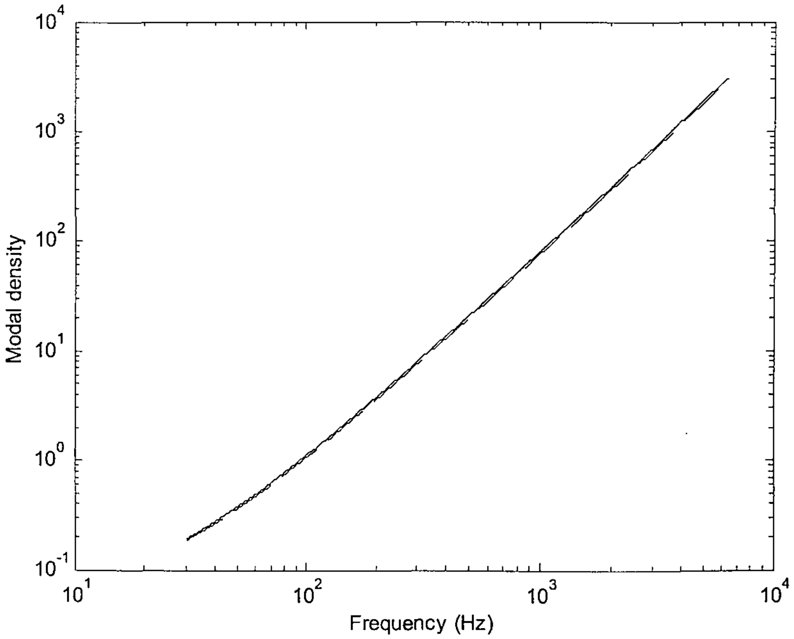

Figure 8.2. Modal densities of cavities. — sending room, – – – receiving room.

The extruded panel studied for acoustic transmission in this Chapter is aluminium of dimensions 3.37×3.0×0.07 m, where the length along the extrusion is 3 m. For mechanical excitation the dimensions are 1.5×1.0×0.07 m as in Chapter 7. The subsystem of global modes (subsystem 3) is described using an equivalent plate model for the whole panel. The mass per unit area for the global modes is 43 kg/m^2. The equivalent bending stiffness B_{xy} calculated using equation (4.59) is 5.18×10^5 m^4.

The local modes of the strips adjacent to the sending room are allocated as subsystem 2 while those adjacent to the receiving room form subsystem 4. This division of subsystems for the extruded panel is illustrated in Figure 8.3. Subsystems 2 and 4 can be described as an aluminium plate of dimensions 3.37×3×0.0026 m with a number of constraints (stiffeners) dividing them into strips. Due to the different layout of the constraints on the two sides of the extruded panel, the modal densities of subsystems 2 and 4 are a slightly different from each other at low frequencies.

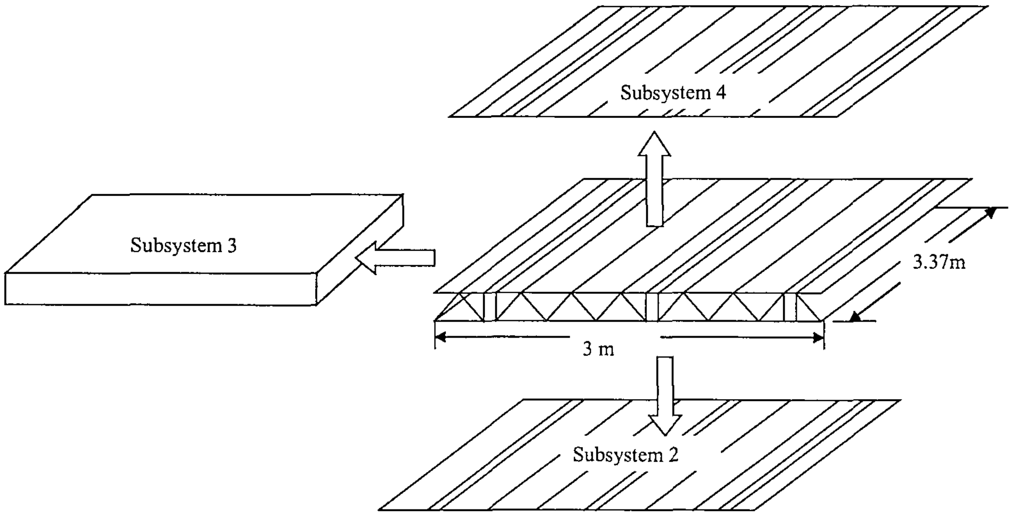

Figure 8.3 SEA subsystems of extruded panels

The modal densities of global and local modes are presented in Figure 8.4. The modal density of global modes (subsystem 3) is calculated using thick plate theory. The modal densities of local modes are calculated using simply supported thin plates. The first local mode on the side of the sending room occurs at 222 Hz while the first one on the receiving room side at 242 Hz. The wider a strip, the lower the first mode. Below these first modes subsystems 2 and 4 are omitted from the model. The modal density of local modes on the side of the sending room is higher than that on the side of the receiving room for frequencies below 1 kHz. At higher frequencies, the modal densities of the two local mode subsystems are similar to each other.

The actual boundary conditions of strips are known from Chapter 3 to be somewhere between simple supports and fully fixed. For the fully fixed strips, the first resonance frequencies are predicted as 503 Hz and 547 Hz for the sending and receiving side respectively. So the actual modal density of the local mode subsystem would be lower than the one predicted using simple supports. Due to these uncertain constraints, it will be also possible that the local modes start to appear at a higher frequency for a strip having a boundary condition that is close to the fully fixed condition.

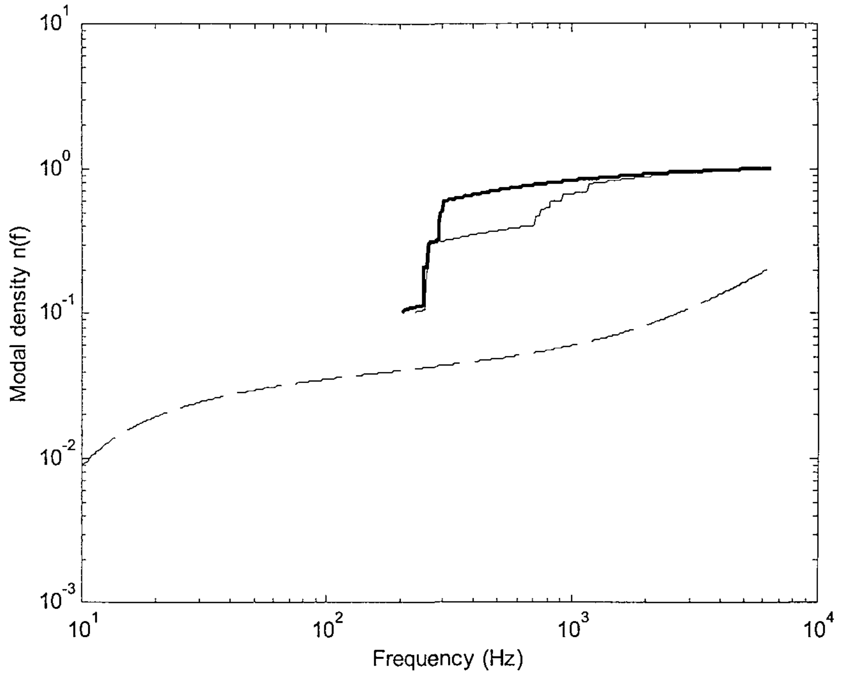

Figure 8.4 Modal densities of subsystems 2, 3 and 4. —subsystem 2 local modes (lower); — subsystem 4 local modes (upper); – – subsystem 3 global modes.

8.2.2 COUPLING LOSS FACTORS

8.2.2.1 Coupling between global modes and cavity

The radiation efficiency of the global modes is shown in Figure 8.5. The critical frequency is 170 Hz. The coupling loss factor from global modes to the cavity is shown in Figure 8.6. As the two cavities are similar, the coupling loss factor is similar for each. By using the consistency relationship, the coupling loss factor from the cavity to the global modes is also obtained and is presented in Figure 8.6.

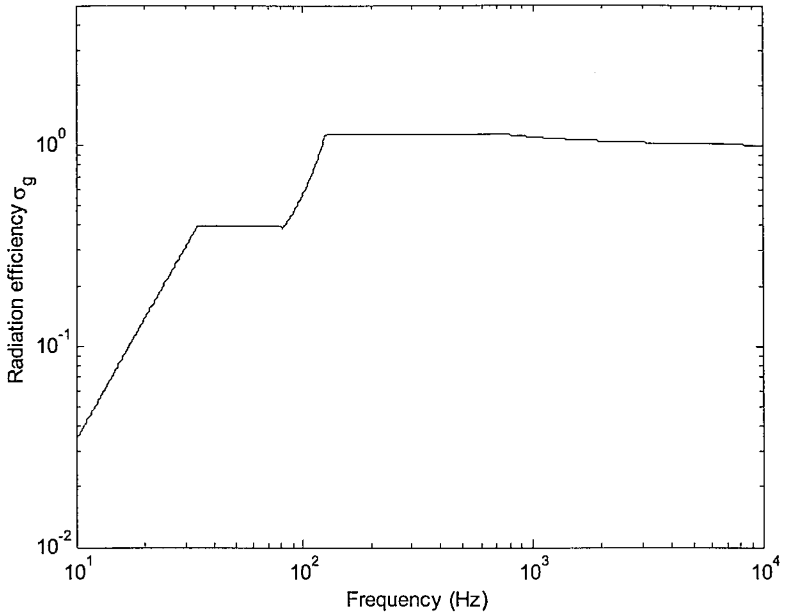

Figure 8.5. Radiation efficiency of global modes.

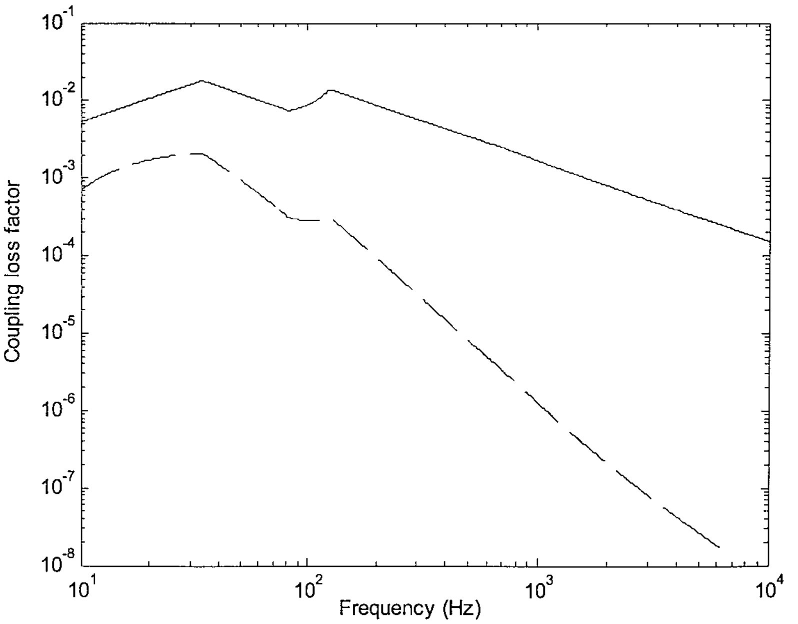

Figure 8.6. Coupling loss factor from global modes to cavity —; from cavity to global modes – –.

8.2.2.2 Coupling between local modes and cavity

The average radiation efficiencies of subsystems 2 and 4 are calculated using equation (8.1) and the results are shown in Figure 8.7. A damping loss factor of 0.1 is used. The radiation efficiency of subsystem 4 is higher than that of subsystem 2 for frequencies between the first resonance and the critical frequency. This is because some strips on the receiving side of the panel are very narrow and their aspect ratio is smaller than the critical aspect ratio. As seen in Chapter 5, the dip on the radiation efficiency curve between the first and second cut-on frequency will not occur for strips whose aspect ratio is smaller than the critical aspect ratio. This does not happen for the sending side of the panel. Alternatively, this can be simply explained by the number of the line constraints on the panel. According to Maidanik [45], the line constraint increases the perimeter terms for the frequencies below the critical frequency.

The difference between the radiation efficiencies of the two sides of the panel leads to different coupling loss factors from the local mode subsystems to the cavity. The coupling loss factors from local modes to the respective cavity are shown in Figure 8.8. Note, however, that they are not used below the first local resonance frequency of the corresponding subsystem. The coupling loss factors from the two cavities to local modes are calculated using the consistency relationship, and are shown in Figure 8.9.

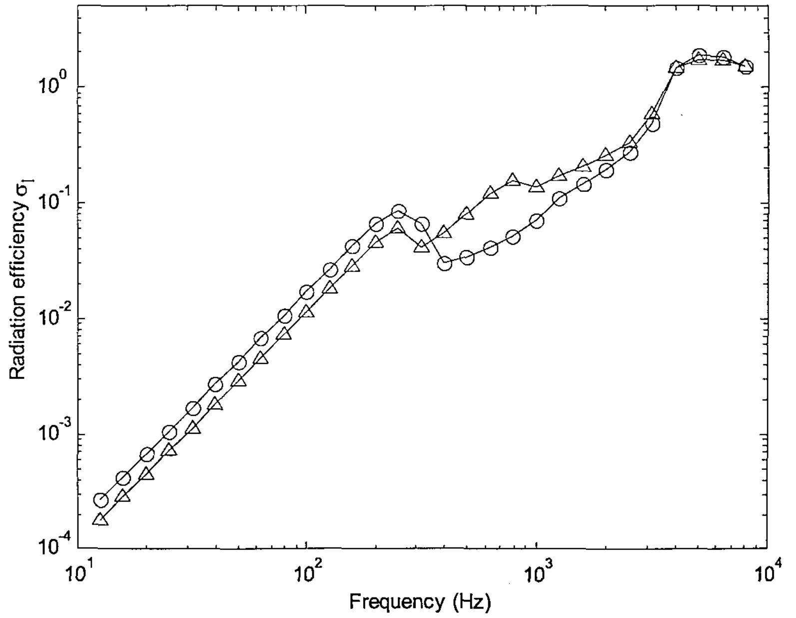

Figure 8.7. Radiation efficiency of local modes (η = 0.1). –o– subsystem 2; –Δ– subsystem 4.

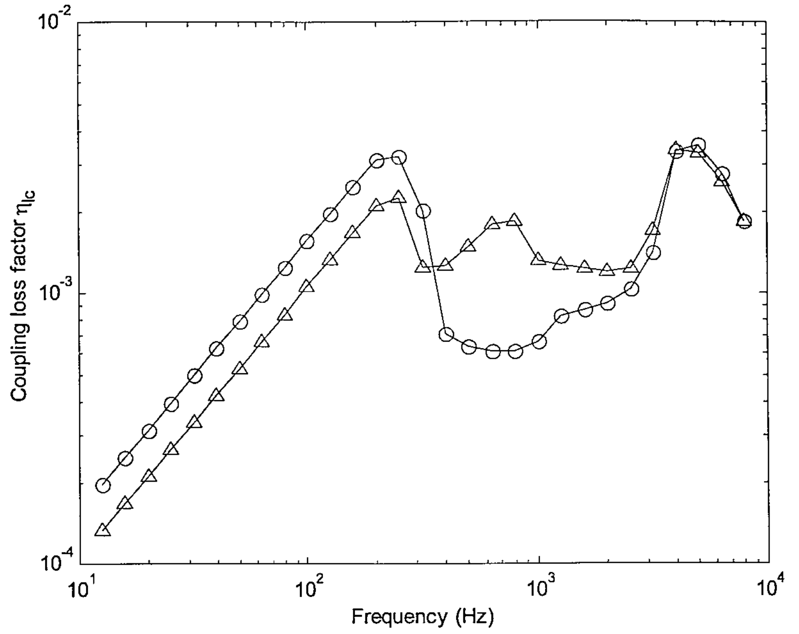

Figure 8.8. Coupling loss factors from local modes to cavity (η = 0.1).

–o– subsystem 2; –Δ– subsystem 4.

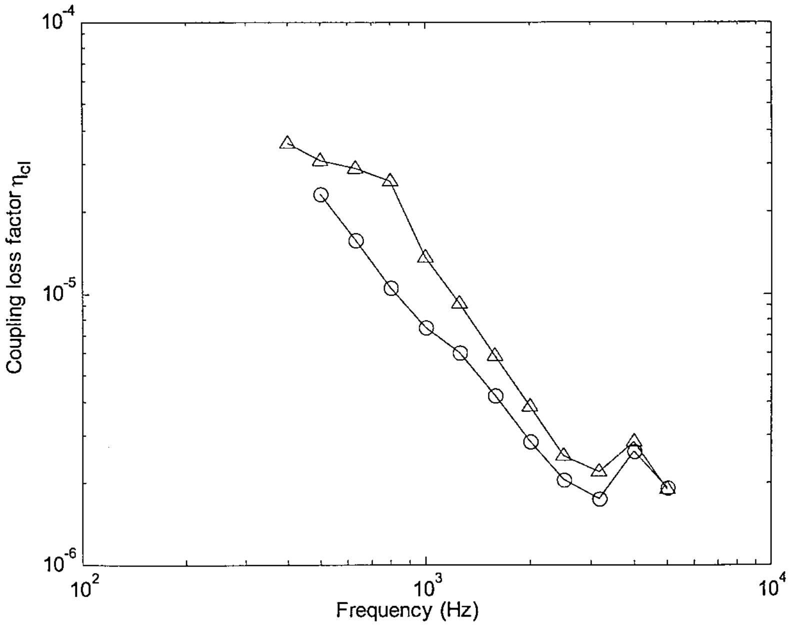

Figure 8.9. Coupling loss factors from cavity to local modes.

–o– sending room to subsystem 2; –Δ– receiving room to subsystem 4.

8.2.2.3 Coupling between global and local modes

The coupling loss factors between global and local modes are shown in Figure 8.10.

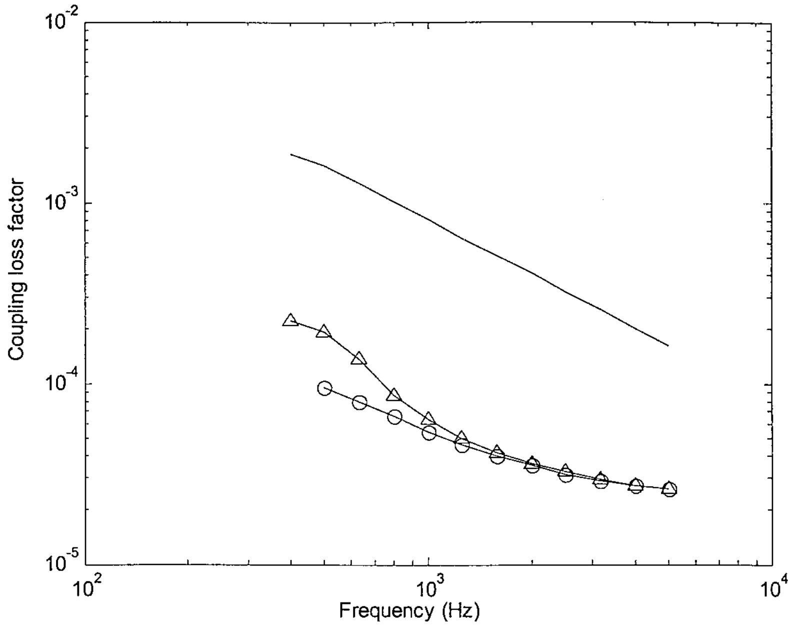

Figure 8.10. Coupling loss factors between global and local modes. —— from global to local modes; –o– from subsystem 2 to global modes; –Δ– from subsystem 4 to global modes.

8.2.3 DAMPING LOSS FACTORS

A damping loss factor of 0.045 is used for the global modes in all frequency bands. For local modes, it is assumed to be 0.1 in all frequency bands. The absorption coefficient in the source room is arbitrarily chosen as a constant value of 0.03 whereas that in the receiving room is used from experimental data (supplied by Bombardier [101]) as shown in Figure 8.11. The reverberation time T_{60} from experimental data is shown in Figure 8.12. The reverberation time and absorption coefficients are related by equation (2.8). Using equation (2.7), the damping loss factors in the two cavities can be obtained, and these are shown in Figure 8.13.

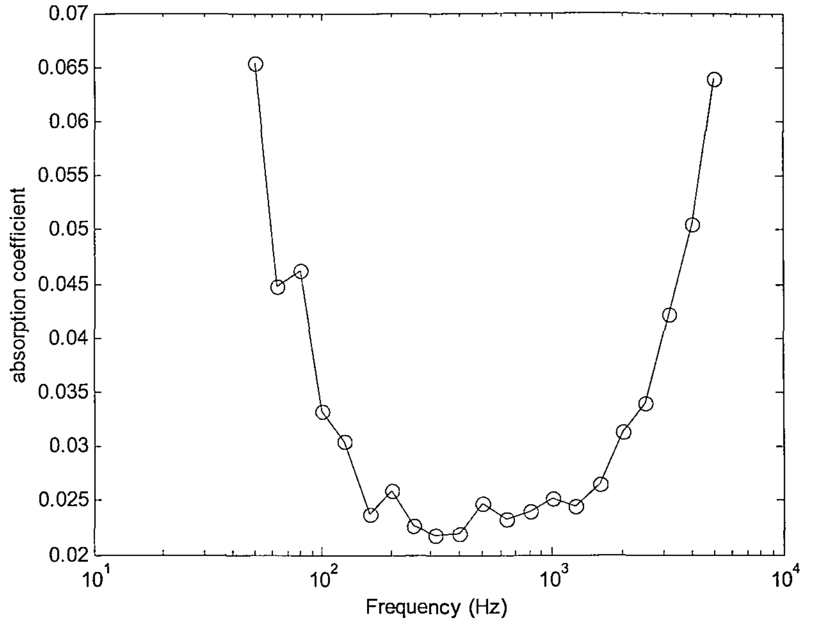

Figure 8.11. Absorption coefficient of walls in the receiving room.

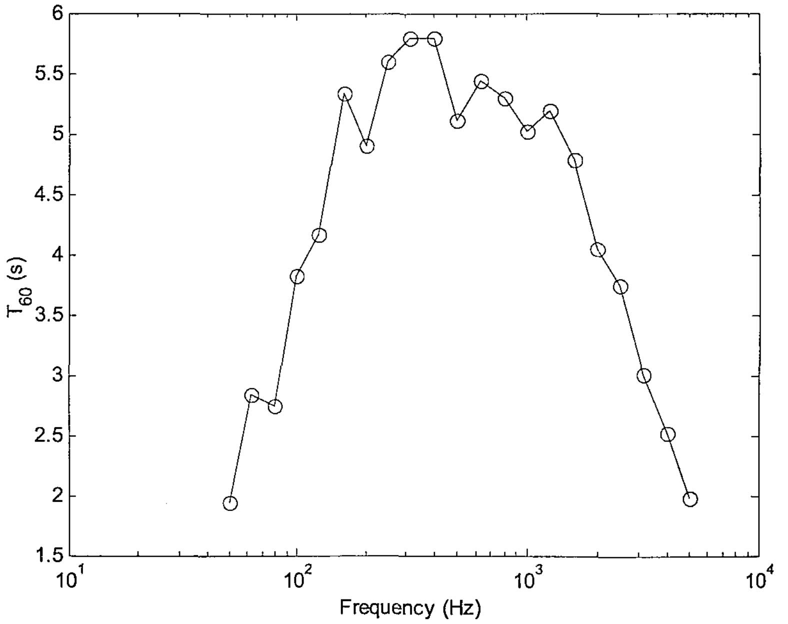

Figure 8.12. T_{60} of the receiving room.

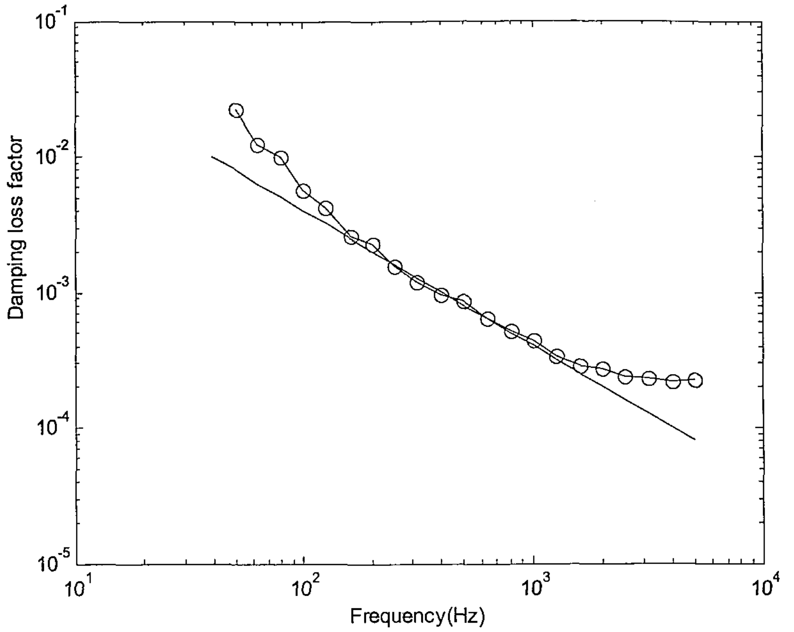

Figure 8.13. Damping loss factors of two cavities. —— source room; –o– receiving room.

8.2.4 MECHANICAL EXCITATIONS

The case in which the panel is excited by a point force introduced by a shaker, as studied in Chapter 7, can be used to check the validity of the above SEA model. This is investigated by checking whether it gives reasonable predictions of the response of the extruded panel under mechanical excitation. The response of the extruded panel under the point force excitation has been measured and the results have been presented in Chapter 7. In the sense of SEA, the average response under random forces (rain on the roof) is needed. In practice, this is achieved by randomly choosing a number of driving points on the structure. The experimental data provide six force positions. Here, only the results of three excitation positions on the strips are used. This is because the force positions on the strips can excite both global and local modes very well.

The average responses on either side of the panel correspond to the total response contributed from global and local modes. The response on the stiffeners corresponds to the global modes only. The measured driving point mobility and force can be used to give the input power for the extruded panel. However, this input power should be divided into two portions: one corresponds to the global mode subsystem and other to the local mode subsystem. Here, their modal densities are used to determine the ratio of the division. This can be expressed by

$$W_{in,2} = W_{in} \frac{n_2}{n_2 + n_3} \tag{8.2}$$

$$W_{in,3} = W_{in} \frac{n_3}{n_2 + n_3} \tag{8.3}$$

where n_2, n_3 represent the modal densities of subsystems 2 and 3.

The total input power W_{in} is given by

$$W_{in} = \overline{F^2}\,\mathrm{Re}(Y) \tag{8.4}$$

where $\overline{F^2}$ is the mean square force.

Here, the input power per unit force squared is used. In other words, the value of the input power is equal to the value of the real part of the driving point mobility. The response predicted using the SEA model then corresponds to the spatially averaged transfer mobility. Figure 8.14 shows the input power for the point force excitation from the measurement studied in Chapter 7. For frequencies below 400 Hz, there is no input power into the local modes subsystem since there are no local modes at all. Above 400 Hz, most power goes to the local modes.

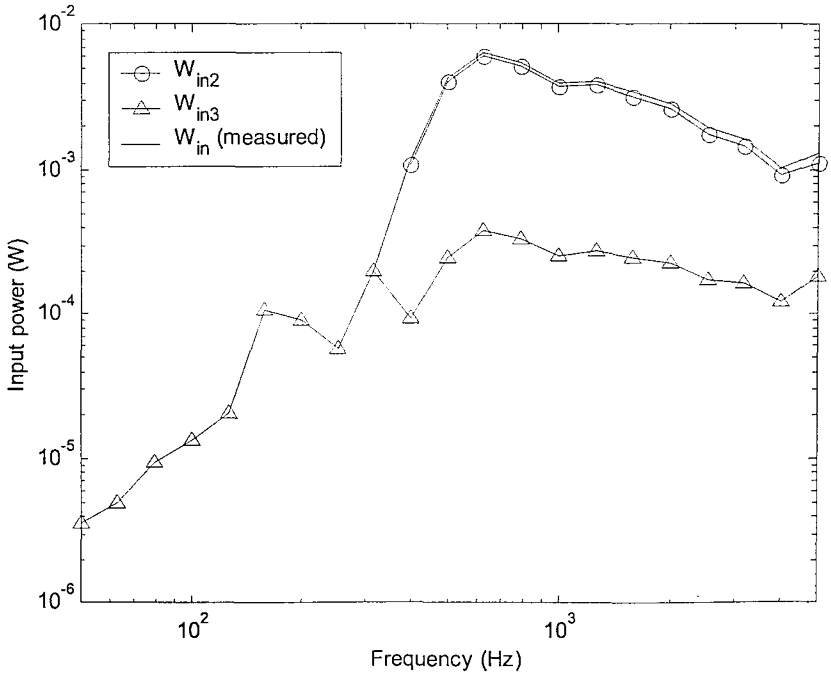

Figure 8.14. Input power under mechanical excitation.

The interest here is to see whether the SEA model can give a reasonable prediction for the response on the other side of the panel. The results from the SEA calculations are presented in Figure 8.15. It can be seen that the predicted vibration level of the sending room side agrees with the measured response very well. The predicted response of the global modes also agrees with the measured response on the stiffeners quite well. However, the predicted response of the receiving room side has a very similar level to that of the global modes. The measured results are 4 to 8 dB higher than those for the global modes. This shows that this five-subsystem SEA model cannot give good predictions of the response of the panel under the mechanical excitations. The level difference cross the panel is presented in Figure 8.16, which confirms this.

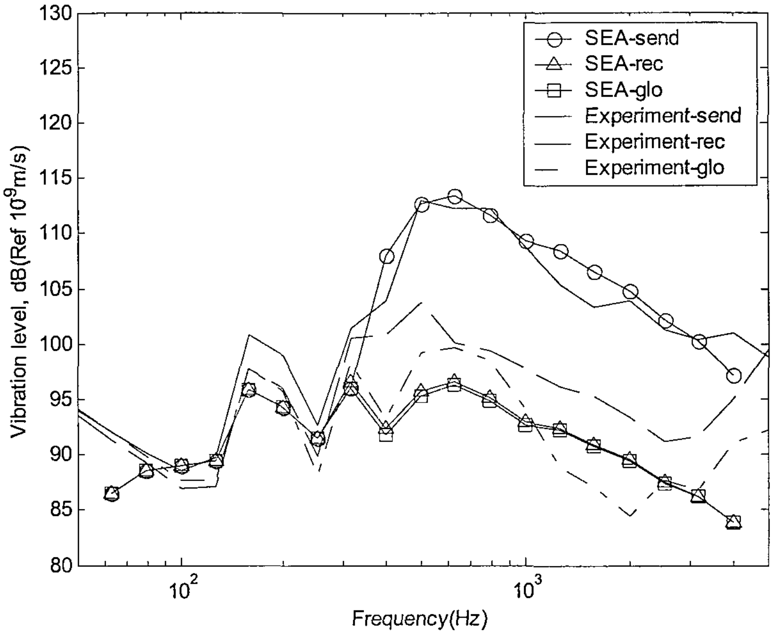

Figure 8.15. Predicted vibration levels of the extruded panel using 5 subystem SEA model for mechanical excitations on strips.

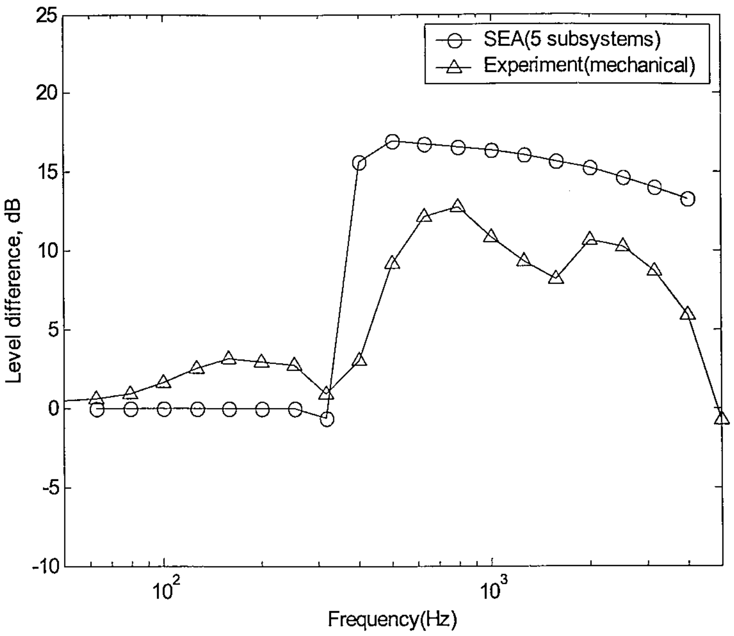

Figure 8.16. Vibration level difference of the two sides of the extruded panel.

The SEA model consisting of 5 subsystems cannot predict the response of extruded panels appropriately. In the five-subsystem model, the local modes on the two sides are assumed to have no direct coupling between them. Their coupling is assumed to act through the global modes of the structure. However, this mechanism does not provide good results. This could be due to unknown problems associated with the coupling model described in Chapter 6 which is based on a simple two-dimensional model, in which all beam segments are assumed to be independent of each other. The validation of this model for the coupling between the global and local modes is also limited to the two-dimensional FEM model with a damping value lower than that used in the current SEA model. The model will be refined in Section 8.3 below, but first the results for acoustic excitation are presented.

8.2.5 SOUND TRANSMISSION LOSS

The response of the extruded panel to acoustic excitation is predicted with this five-subsystem model. The predicted sound pressure levels in the two rooms are presented in Figure 8.17. The predicted sound pressure for the source room is the same as that from experimental data. This is obtained by adjusting the input power into the source room. The predicted sound pressure level in the receiving room is lower than the measured one for most frequency bands. An acceptable prediction of the sound pressure in the receiving room is only found for frequencies below 315 Hz. The sound transmission loss calculated using the above SEA model based on equation (2.21) is shown in Figure 8.18. For comparison, the transmission loss found by the normal incidence mass law equation (2.20) is also plotted. It can be seen that the five-subsystem SEA model overestimates the sound transmission loss of the extruded panels at high frequencies by up to 20 dB.

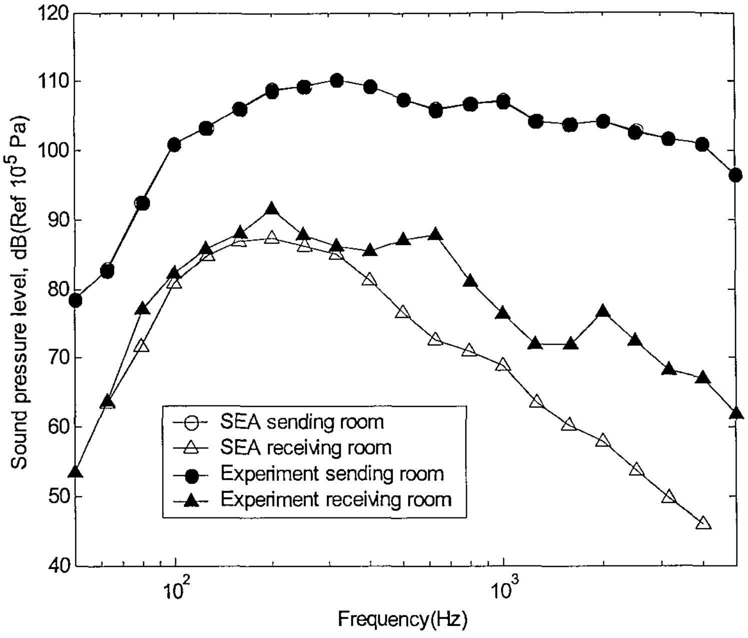

Figure 8.17. Sound pressure levels in the sending and receiving room.

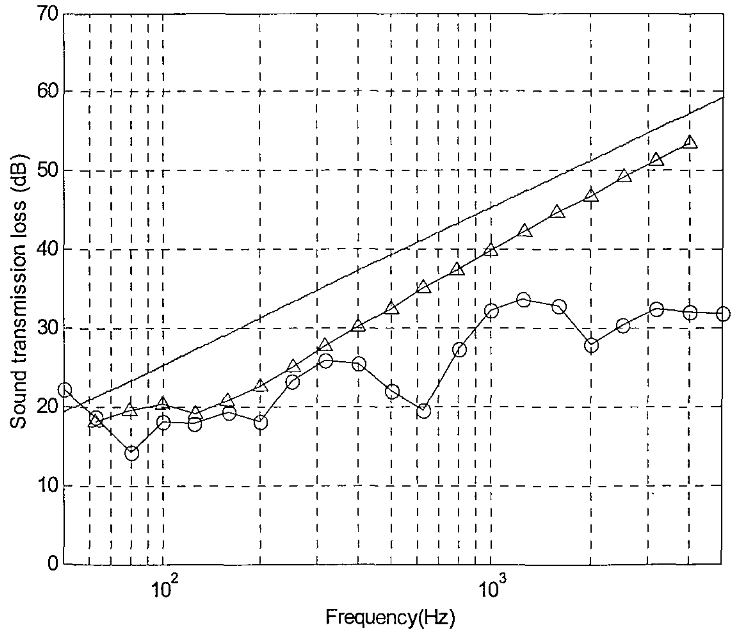

Figure 8.18. Sound transmission loss. — mass law; –o– experiment; –Δ– SEA model.

The predicted vibration levels of the two sides of the panel are presented in Figure 8.19 and compared with the measured results. It can be seen that the predicted vibration levels on the two sides of the panel are similar to the measured results for frequencies below 250 Hz. For this frequency region the vibration of the panel is dominated by global modes. The SEA model gives a reasonable estimate at low frequencies.

The local modes become dominant for frequencies above 250 Hz from the measured vibration levels. The predicted vibration level for both the local modes subsystem adjacent to the source room (subsystem 2) and that adjacent to the receiving room (subsystem 4) are much lower than the measured results. The vibration of subsystem 4 has a similar level to that of the global modes in all frequency bands. The predicted vibration level difference across the extruded panel is compared with the measured results in Figure 8.20. The measured difference between the two sides of the panel is approximately 5 dB for frequencies above 500 Hz. For the band of centre frequency 400 Hz, the measured vibration level of the receiving side is 10 dB higher than that of the sending side. This is possibly because the local modes on the receiving room side occur at lower frequencies than those on the source room side. There is no difference in the predicted vibration level on the two sides of the panel for frequencies below 400 Hz. Generally, the SEA model overestimates the vibration difference for the local modes on the two sides of the panel at high frequencies.

Clearly, this five-subsystem model cannot give a good prediction of the response of the panel under acoustical excitation. Therefore a reasonable prediction of the sound transmission loss has not been achieved. The higher vibration on the receiving side panel that is measured will lead to a higher sound transmission than that is predicted.

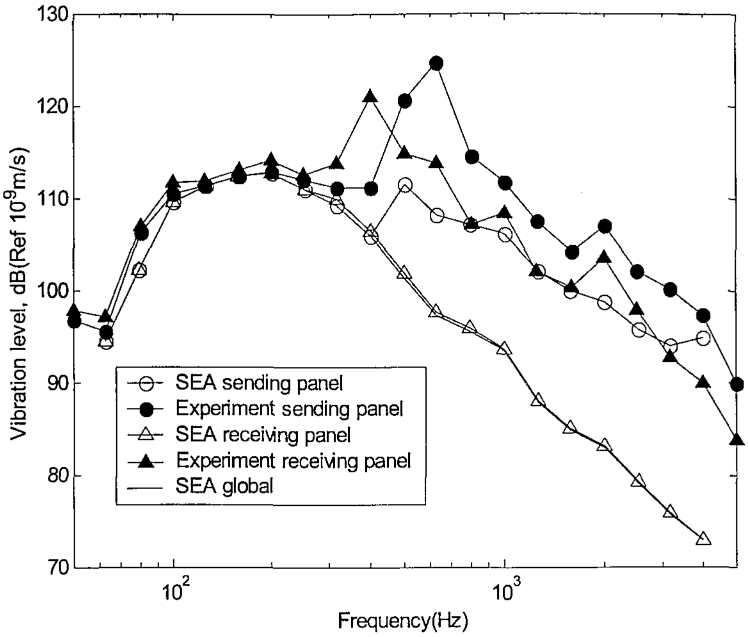

Figure 8.19. Predicted and measured vibration level of the extruded plate for the acoustical excitation. (five-subsystem model.)

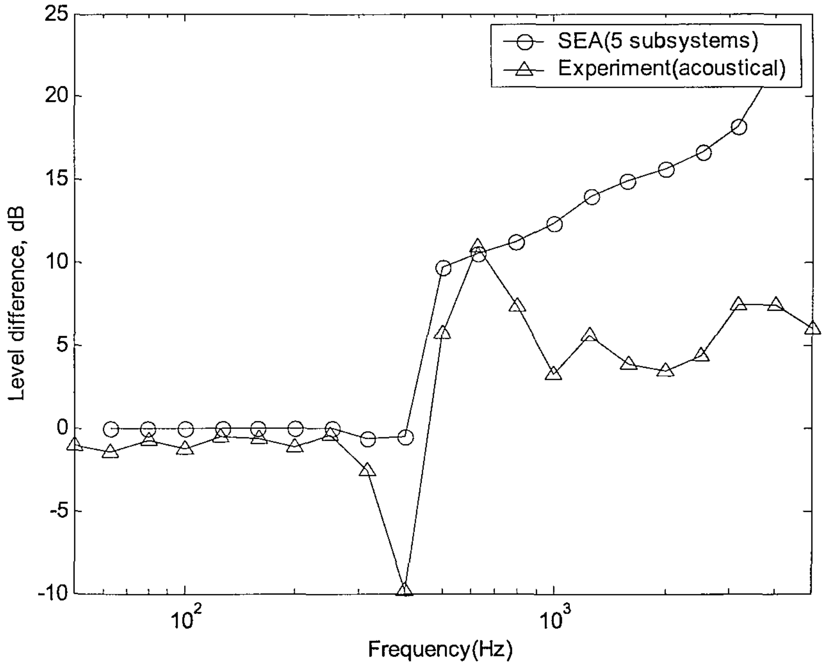

Figure 8.20. Vibration level difference of the two side of the extruded panel predicted using five-subsystem SEA model.

8.3 SIX-SUBSYSTEM SEA MODEL

In the five-subsystem SEA model, the two local mode subsystems are indirectly coupled through the global mode subsystem. In this section, their direct coupling is also considered.

8.3.1 COUPLING BETWEEN LOCAL MODES THROUGH AIR

The coupling between the two outer plates of the extruded panel through air can be considered using the theory for the analysis of the sound transmission through a double-leaf partition [87]. In the present analysis for the extruded panel, for the purpose of simplification, only the air between two outer plates is considered and the intermediate ribs and foam are not included in the analysis. For the case of the normal incidence plane waves acting on an unbounded double-leaf partition, the air between the two plates acts as a spring of stiffness per unit area $s' = \rho c^2 / d$. When the acoustic damping, and the damping and stiffness of the plates are neglected, the ratio of the vibration of the two leaves is given by

$$\frac{\mathbf{v}_{rec}}{\mathbf{v}_{send}} = \frac{\rho c^2 / d}{-\omega^2 \rho_s h + \rho c^2 / d} \tag{8.5}$$

where d is the distance between two leaves, $\mathbf{v}_{rec}$ and $\mathbf{v}_{send}$ represent the complex velocity amplitudes of the receiving side and sending side plates.

The vibration level of the receiving side plate due to the coupling through the air is calculated using equation (8.5) and is plotted in Figure 8.21. The measured vibration for the sending side of the panel in the sound transmission is used (see Figure 8.19) in this calculation. For comparison, the result predicted from the previous five-subsystem SEA model and the result from the measurement for the acoustical excitation are also plotted. It has been shown in the previous section that, for the case of the coupling through the global modes, the vibration on the sending side of the panel was actually underestimated. However, the vibration on the receiving side obtained from this underestimated vibration on the sending side is still higher than that obtained through air coupling. It can hence be seen that the coupling through the air will have negligible effect compared with the coupling through the global modes. Therefore, the mechanism of the coupling through air between two outer plates can be neglected from the SEA model.

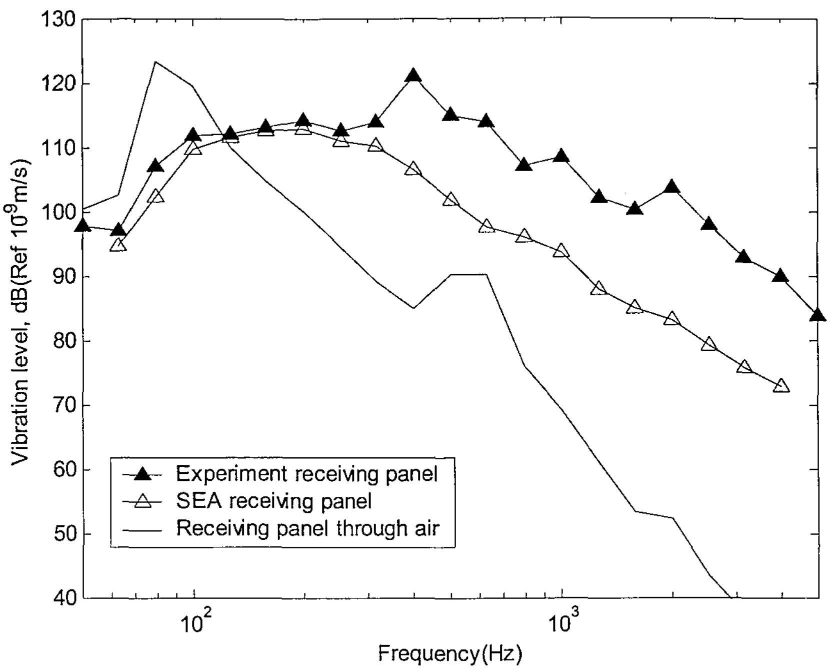

Figure 8.21 Vibration of the receiving plate due to the coupling through air, compared with results from five subsystem SEA model and TL measurement.

8.3.2 COUPLING BETWEEN LOCAL MODES

The intermediate connecting ribs between the two face plates can act as a bridge to connect the two local mode subsystems on the two sides of the extruded panel. These connecting ribs can be considered as subsystem 6 also consisting of local modes, in addition to the 5 subsystems used in the previous section. Local modes on the two sides both couple to the connecting ribs by bending waves. This forms a route for vibration energy to be transmitted from one side of the panel to the other. Figure 8.22 shows the illustration of this SEA model for extruded panels.

The intermediate connecting ribs are also coupled with the global modes. Here, their coupling is treated in the same way as the coupling between two the outer local mode subsystems and the global modes described in the previous five-subsystem model, although the intermediate ribs are not in the same geometric formation as two outer plates. Certainly, this is a simplified approximation. It is noted that, when considering the coupling between the intermediate subsystem and the global modes, the vertical ribs should not be taken into account since the global bending wave will not interact with their local bending waves. However, for coupling between the local modes of the two outer plates and the intermediate ribs, these vertical ribs should be taken into account. This difference can be represented by using different modal densities for the intermediate ribs in the two cases.

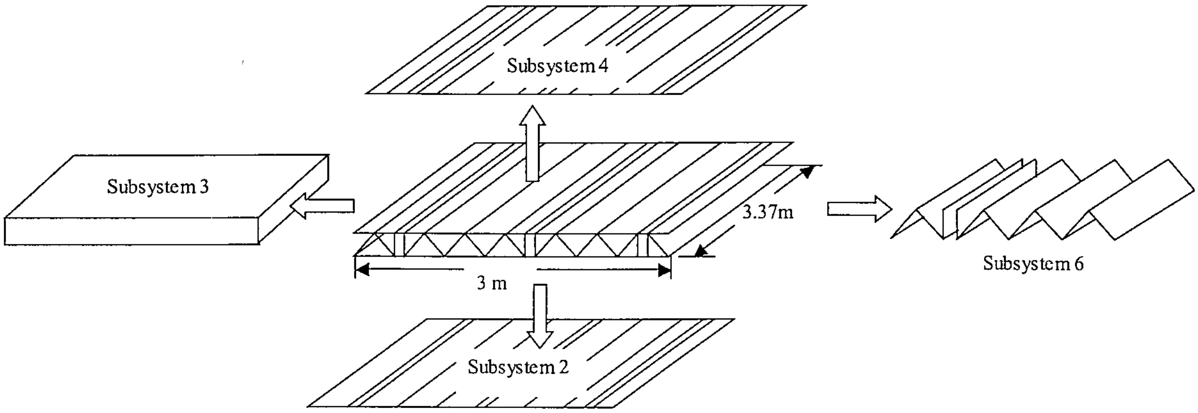

Figure 8.22. SEA four-subsystem model for extruded panels.

In extruded panels, the joints connecting the intermediate ribs and two face plates have two basic forms: 'T' joint and '_V_' joint. Coupling between the three local mode subsystems occur through the interaction of waves at these junctions. The structure can normally support bending waves, longitudinal waves and transverse shear waves. The most important wave is the bending wave for the present interest. Here, only the coupling of bending waves between local modes is considered. The coupling loss factor between local mode subsystems is related to the transmission coefficient of waves between two plates. This can be given by

$$\eta_{12} = \frac{Lc_{g1}\tau_{12}}{\pi\omega S_1} \tag{8.6}$$

where L is the joint length, c_{g1} is the group velocity on the source plate 1, τ_{12} is the transmission coefficient and S_1 is the area of plate 1.

For a joint where two or more plates are connected together, the bending wave incident on the joint will generate waves on all other plates. In the SEA model, each plate is modelled as a separate subsystem. The coupling loss factor from one plate to another can be determined using equation (8.6). Craik [73] gives expressions for the transmission coefficients for various joints. These can be used to determine the coupling loss factor between the three local mode subsystems for the extruded panel.

The extruded panel can be considered to be made from a combination of many structures, each of which has a similar form and consists of a number of strip plates as shown in Figure 8.23. The typical structure is plotted in solid lines. Plates 1 and 6 correspond to the local modes on the source room side. Plates 2 and 3 form the intermediate local modes. Plate 4, 5 and 7 form the local modes on the receiving room side. The coupling between local modes on the face plate and the intermediate local modes can be obtained by working on the typical structure shown in solid lines in Figure 8.23.

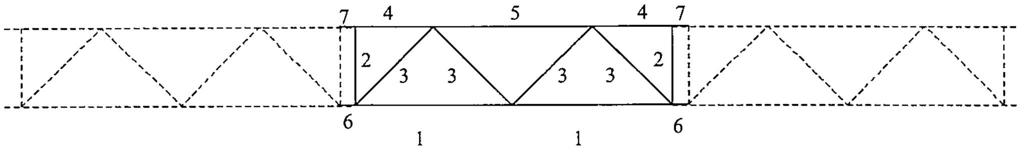

Figure 8.23. SEA model of the joints for the coupling between local modes of extruded panels.

The power flow from the local modes on the source room side to the intermediate local modes consists of contributions of: each plate 1 to one plate 2 and three plates 3; each plate 6 to one plate 2 and one plate 3. This is given by

$$W_{s\to i} = 2\left(E_1 + E_6\right)\omega\eta_{si} = 2E_1\omega(\eta_{12} + 3\eta_{13}) + 2E_6\omega(\eta_{62} + \eta_{63}) \tag{8.7}$$

where η_{12} and η_{13} represent the coupling loss factors from plate 1 to plate 2 and 3. η_{62} and η_{63} represent the coupling loss factors from plate 6 to plate 2 and 3. η_{si} is the coupling loss factor from the local modes on the source room side to the intermediated local modes.

Using the assumption of energy equipatition that assumes the same response for all the intermediate plates (as they have the same thickness), equation (8.7) can be written as

$$W_{s\to i} = m_s\left\langle\overline{v_s^2}\right\rangle\omega\eta_{si} = 2m_1\left\langle\overline{v_s^2}\right\rangle\omega\left(\eta_{12} + 3\eta_{13}\right) + 2m_6\left\langle\overline{v_s^2}\right\rangle\omega\left(\eta_{62} + \eta_{63}\right) \tag{8.8}$$

where m_s is the mass of the all outer plates, m_1 and m_6 are mass of plates 1 and 6 respectively and $\left\langle\overline{v_s^2}\right\rangle$ is the spatially averaged mean square velocity of the sending side plates. Because each plate has the same thickness, the coupling loss factor from the local modes on the source room side to intermediate local modes can therefore given by

$$\eta_{si} = \frac{l_1(\eta_{12} + 3\eta_{13}) + l_6(\eta_{62} + \eta_{63})}{l_1 + l_6} \tag{8.9}$$

In a similar manner, the power flow from intermediate local modes to the local modes on the source room side can be given by

$$P_{i \to s} = E_i \omega \eta_{is} = 2E_2 \omega(\eta_{21} + \eta_{26}) + 2E_3(3\eta_{31} + \eta_{36}) \tag{8.10}$$

The coupling loss factor from intermediate local modes to the local modes on the source room side can be given by

$$\eta_{is} = \frac{l_2(\eta_{21} + \eta_{26}) + l_3(3\eta_{31} + \eta_{36})}{l_2 + 2l_3} \tag{8.11}$$

where l_2 and l_3 are the length of the plate 2 and 3.

The coupling loss factors between the plates 1, 2, 3 and 6 can be determined using equation (8.6), provided the transmission coefficients are available. According to Craik [73], the transmission coefficient for a cross joint should be used. Equation (8.12), together with parameters presented in Table 8.1, is used to calculate the transmission loss R_{12} of the joint, which is related to the transmission coefficient by equation (8.13).

$$R_{12} = 20\log\left(\left(\frac{\chi}{A}\right)^{1/2} + \left(\frac{A}{\chi}\right)^{1/2}\right) + B + \frac{C}{\chi} + D\log\left(1 + \frac{1}{\chi^4}\right) \qquad (\chi \geq 1) \tag{8.12}$$

$$R_{12} = 10\log\left(\frac{1}{\tau_{12}}\right) \tag{8.13}$$

where the variables χ and ψ are defined as

$$\chi = \frac{k_2}{k_1} = \frac{c_{L1}h_1}{c_{L2}h_2} \tag{8.14}$$

and

$$\psi = \frac{B_2 k_2^2}{B_1 k_1^2} = \frac{c_{L2}h_2\rho_{s2}}{c_{L1}h_1\rho_{s1}} \tag{8.15}$$

For the present case, all plates have the same material and thickness and hence $\chi = 1$ and $\psi = 1$. Then the transmission coefficient for a cross joint $\tau_{cross} = 0.0838$. After some algebraic manipulations, the coupling loss factors between the local mode subsystem on the source side and the intermediate rib subsystem are given by

$$\eta_{si} = \frac{6c_g \tau_{cross}}{\omega\pi\left(l_1 + l_6\right)} \tag{8.16}$$

$$\eta_{is} = \frac{6c_g \tau_{cross}}{\omega\pi\left(2l_3 + l_2\right)} \tag{8.17}$$

It is also obvious to note that the consistency relationship holds between above equations, as the respective modal densities are proportional to the length.

Table 8.1. Parameters for calculating random incident transmission loss, R_{12}, for various joints. (Craik [73])

Joint	A	B	C	D
Cross 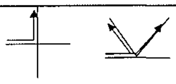	ψ	4.0153	0.2535	1.5600
Tee 	$\psi/2$	1.0050	0.2535	1.5600
TeeC 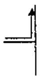	2ψ	1.0050	0.2535	1.5600
Corner 	ψ	- 2.0053	0.2535	1.5600

Using a similar analysis, the coupling loss factor from intermediate local modes to the local modes on the receiving room side is given by

$$\eta_{ir} = \frac{l_2\left(\eta_{24} + \eta_{27}\right) + 2l_3\left(\eta_{34} + \eta_{35}\right)}{l_2 + 2l_3} \tag{8.18}$$

The coupling loss factor from the local modes on the receiving room side to the intermediate local modes is given by

$$\eta_{ri} = \frac{2l_4\left(\eta_{42} + 2\eta_{43}\right) + 4l_5\eta_{53} + 2l_7\eta_{72}}{l_5 + 2l_4 + 2l_7} \tag{8.19}$$

Coupling loss factors η_{34}, η_{43}, η_{35} and η_{53} can be determined using the transmission coefficient for a cross joint. The coupling loss factor η_{24}, η_{27} should be used the corresponding expressions for a 'TeeC' joint while η_{72}, η_{42} for a 'Tee' joint. In the present case, $\tau_{Tee} = \tau_{TeeC} = 0.149$ is found. Eventually, the coupling loss factors between the intermediate local modes and local modes on the receiving side are given by

$$\eta_{ir} = \frac{c_g\left(2\tau_{TeeC} + 4\tau_{cross}\right)}{\omega\pi\left(l_2 + 2l_3\right)} \tag{8.20}$$

$$\eta_{ri} = \frac{c_g\left(4\tau_{Tee} + 8\tau_{cross}\right)}{\omega\pi\left(l_5 + 2l_4 + 2l_7\right)} \tag{8.21}$$

It can also be noted that the consistency relationship holds.

Using equations (8.16), (8.17), (8.20) and (8.21), the coupling loss factors between local modes subsystems of the extruded panel are calculated and presented in Figure 8.24. For frequencies below 500 Hz, coupling loss factors are zero as there are no local modes.

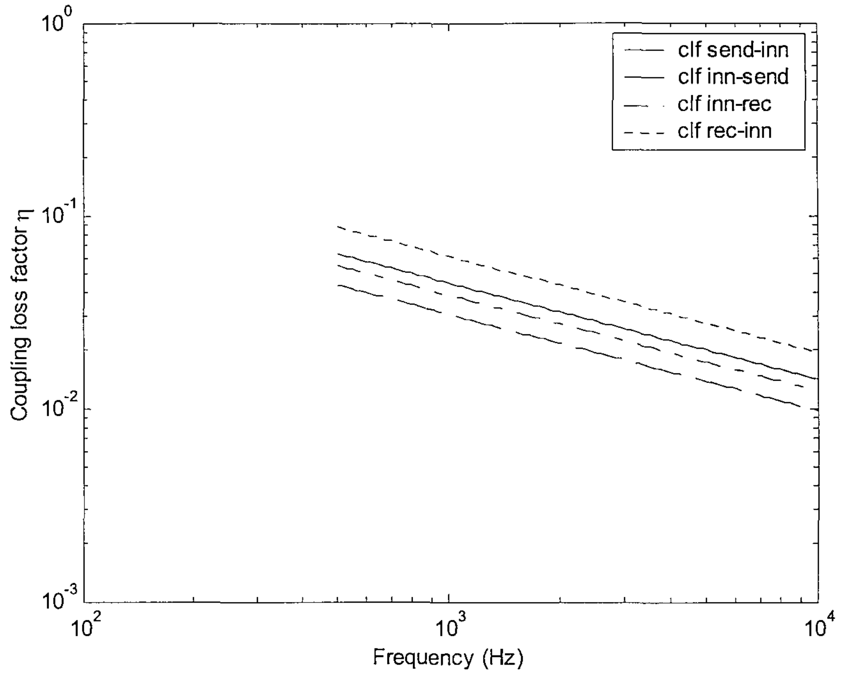

Figure 8.24. Coupling loss factors between local modes.

8.3.3 MECHANICAL EXCITATION

For the mechanical excitations, the predicted panel response is presented in Figure 8.25. It is noted that not only the predicted responses of the source side and global modes agree well with the measured results, but also those of the receiving side. The response of the receiving side is well predicted after the intermediate rib subsystem was introduced into the SEA model. The vibration level difference across the panel is shown in Figure 8.26. Compared with the result from the five-subsystem SEA model, the level difference across the panel is now reasonably well estimated.

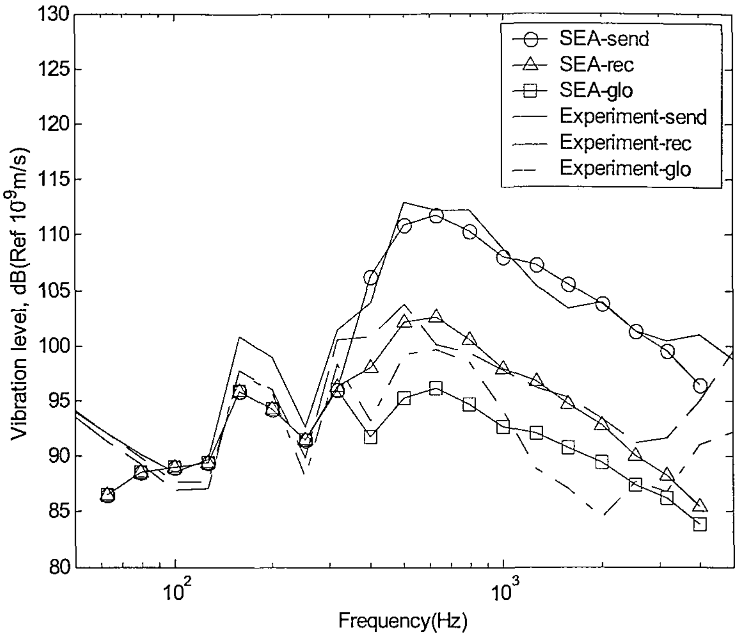

Figure 8.25. Predicted vibration levels of the extruded panel using 6 subystem SEA model for mechanical exciations.

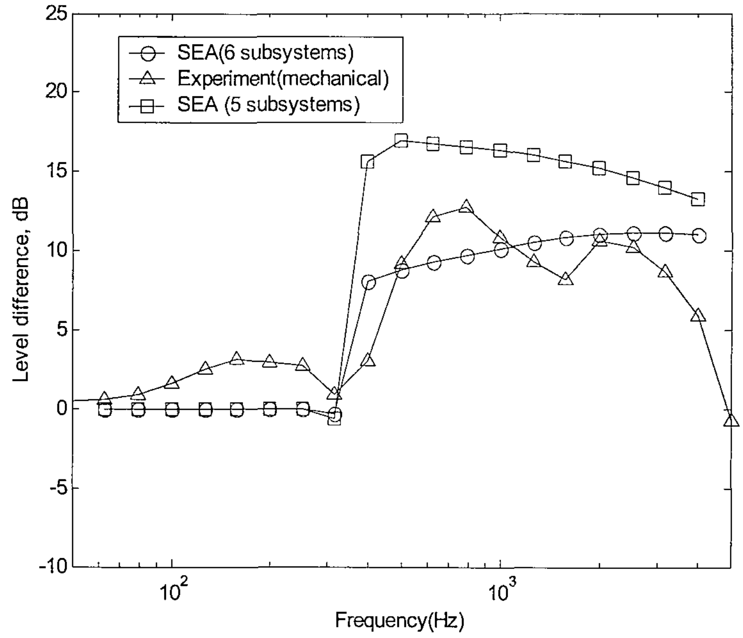

Figure 8.26. Vibration level difference cross the panel for mechanical excitations.

8.3.4 SOUND TRANSMISSION LOSS

The response of the extruded panel under acoustical excitation is predicted using this six-subsystem SEA model in a similar manner as for the five-subsystem SEA model. The predicted sound pressure levels in the two rooms are presented in Figure 8.27. Again, the sound pressure level in the receiving room is underestimated for frequency bands above 315 Hz. There is not a significant improvement compared with the result from the five-subsystem SEA model. This can be seen in the sound transmission loss presented in Figure 8.28.

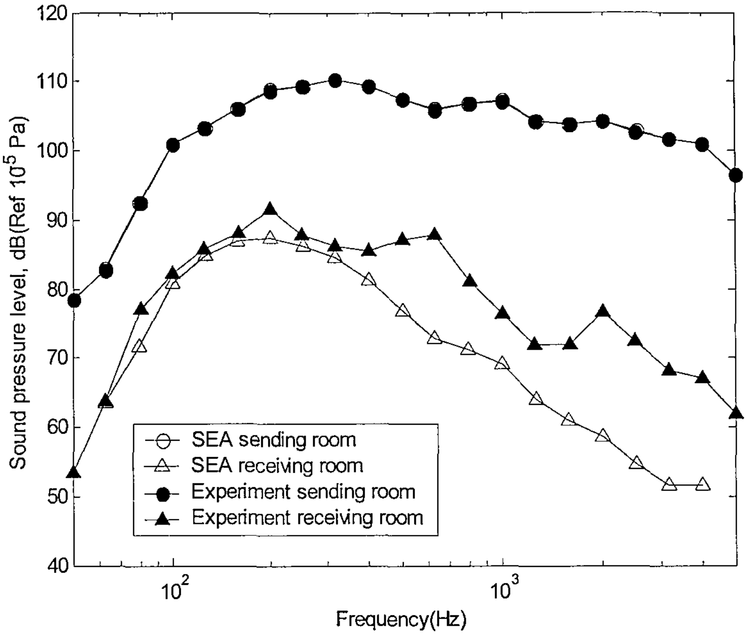

Figure 8.27. Sound pressure levels in two rooms predicted using six-subsystem SEA model.

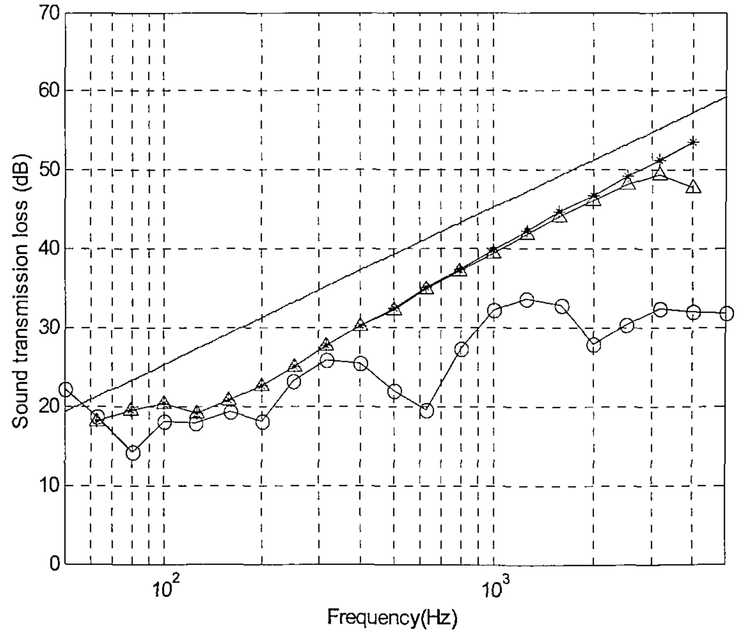

Figure 8.28. Sound transmission loss predicted from SEA.

— mass law; –o– experiment; –Δ– 6 subsystems SEA model, –*– 5 subsystems SEA model.

The predicted response of the panel is compared with the measured one in Figure 8.29. For frequencies below 250 Hz the SEA model gives a reasonable estimate, as before. Due to adding the intermediate local mode subsystem, the response of the local modes on the source room side and the receiving room side increase a bit (compared with Figure 8.19). The vibration level on the receiving room side is higher than that of global modes. However, it is clear that the underestimate of the pressure in the receiving room is due to the underestimated vibration on this side of the panel.

The six-subsystem SEA model still overestimates the vibration difference for the local modes on the two sides of the panel although by about 5 dB less than the result from the five-subsystem SEA model. This is shown in Figure 8.30.

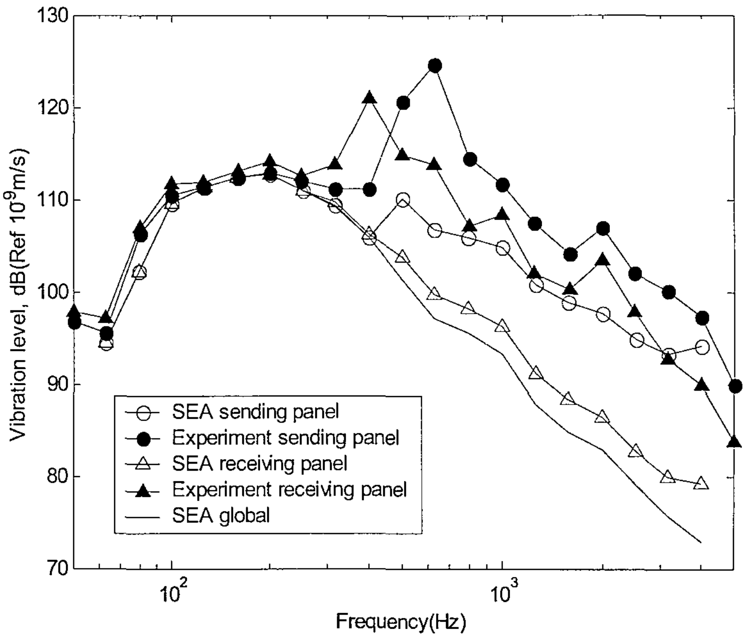

Figure 8.29. Predicted and measured vibration level of the extruded plate for the acoustical excitation.

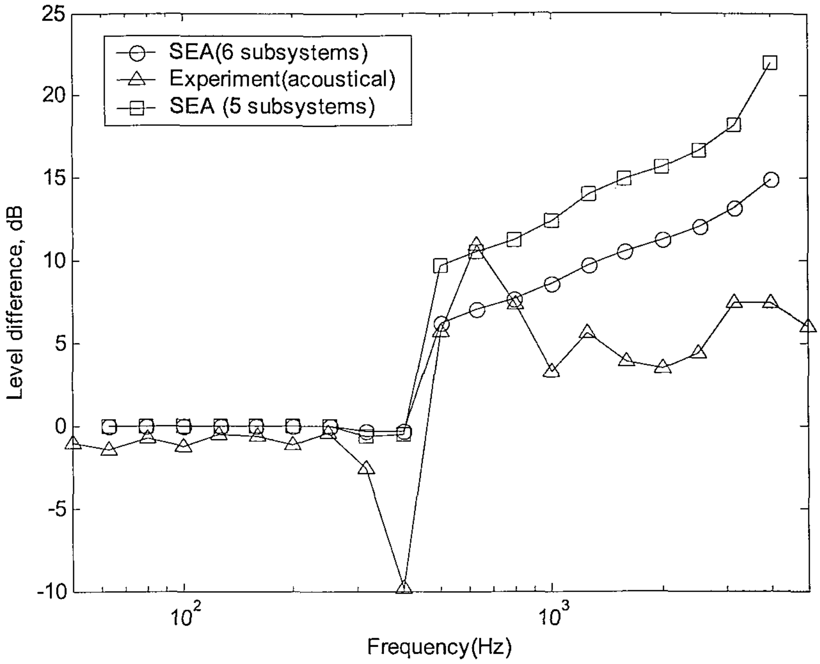

Figure 8.30. Vibration level difference of the two side of the extruded panel predicted using 6 subsystem SEA model.

8.4 DISCUSSIONS

8.4.1 NON-RESONANT VIBRATION

From the above analysis, it can be noted that the vibration level on both sides of the panel is underpredicted. Although the six-subsystem model gives reasonable results for the global vibration and the vibration level difference across panel, it underpredicts the response of the local modes. To understand the possible reason of this underprediction, it is worth checking the vibration of the panel due to the non-resonant vibration.

The response of a finite panel to the sound field can be considered as the contributions from two components: (i) the response of the corresponding infinite panel; (ii) the response due to the interference from the actual boundaries. The latter corresponds to the free bending waves travelling at their natural frequencies, so called resonant vibrations. In the SEA, only the vibration of resonant modes is taken into account. Below the critical frequency of the panel, the vibration of the panel excited by the sound field may be more controlled by the contribution of the first kind response mentioned above. The panel actually vibrates under the forced condition and is mass-controlled due to the contribution of those modes that have their resonance frequencies well below the excitation bands. This forced vibration can make the panel radiate sound efficiently to the air on the other side. Only for lightly damped panels, the resonant vibration can be dominant below the critical frequency.

By analogy with the concept of the radiation efficiency, the panel forced by plane sound waves always have radiation efficiencies equal to or larger than unity. This radiation efficiency is dependent only on angle of incidence and given by [75]

$$\sigma_{non} = \frac{1}{\sqrt{1-\sin^2\theta}} \tag{8.22}$$

where σ_{non} denotes the radiation efficiency of the panel forced by plane waves and θ is the incident angle.

The transmitted sound power W_t through this mechanism is given by

$$W_t = W_i \tau_{field} \tag{8.23}$$

where $W_i = \dfrac{\left\langle \overline{p_1^2} \right\rangle S}{4\rho c}$ is the incident power and τ_{field} is the field-transmission coefficient that is given by equation (2.19)(a) . It can be easily shown that equation (8.23) is equivalent to

$$W_t = E_1 \omega \eta_{15} \tag{8.24}$$

where η_{15} is the coupling loss factor between two cavities through the panel. The transmitted power W_t can also be related to the forced vibration $\left\langle \overline{v_{non}^2} \right\rangle$ and radiation efficiencies σ_{non} by

$$W_t = \rho c S \sigma_{non} \left\langle \overline{v_{non}^2} \right\rangle \tag{8.25}$$

Considering for simplicity the normal incidence only ($\sigma_{non} = 1$), the maximum of the non-resonant vibration can be found by

$$\left\langle \overline{v_{non}^2} \right\rangle = \frac{W_i \tau_{field}}{\rho c S} = \frac{\left\langle \overline{p_1^2} \right\rangle \tau_{field}}{4\rho^2 c^2} \tag{8.26}$$

The non-resonant vibration calculated using equation (8.26) also excites the motion of the local modes due to the global non-resonant vibration. For comparison, it is presented together with the global vibration predicted from the SEA model in Figure 8.31. It is shown that the non-resonant vibration is much lower than the resonant vibration. It can hence be concluded that the non-resonant vibration can be neglected (apart from its effect in sound transmission).

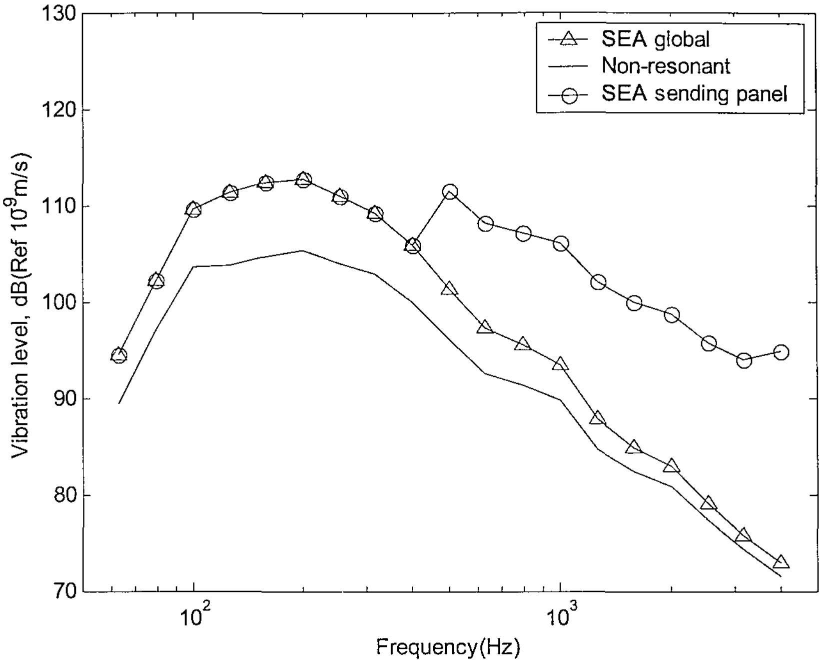

Figure 8.31 Comparison of resonant and non-resonant vibration of the panel.

8.4.2 RADIATION EFFICIENCY

The underprediction of the response of the two outer plates at frequencies dominated by local modes may also suggest that the actual radiation efficiency for the case of acoustical excitation is higher than that used in the SEA models. Using the vibration level measured in the experiments of sound transmission loss, together with the radiation efficiency measured for mechanical excitations in Chapter 7, the sound pressure level in the receiving room can be predicted. The power radiated from the panel into the receiving room is given by

$$W_{45} = \rho c A \sigma_{rec} \left\langle \overline{v_{rec}^2} \right\rangle \tag{8.27}$$

If the power transmitted back from the receiving room to the panel is neglected, the radiated power is equal to the dissipated power in the receiving room. This gives

$$W_{45} = \omega E_5 \eta_5 \tag{8.28}$$

Then the energy E_5 can be obtained to give the sound pressure in the receiving room. Figure 8.32 shows the result from this calculation. The measured radiation efficiency shown in Figure 7.28 is used. The sound pressure level in the receiving room calculated in this way is still lower than the measured one in the whole frequency range. The underestimate at high frequencies suggests that the effective radiation efficiency in the case of acoustical excitation is higher than that measured for the case of mechanical excitation. The underestimate occurs also for frequencies below 315 Hz. This is largely because the measured radiation efficiency was taken for an unbaffled panel, for which a relatively low radiation efficiency was obtained at low frequencies. For the present purpose to understand the underestimate of the SEA result, only results above 315 Hz are of interest.

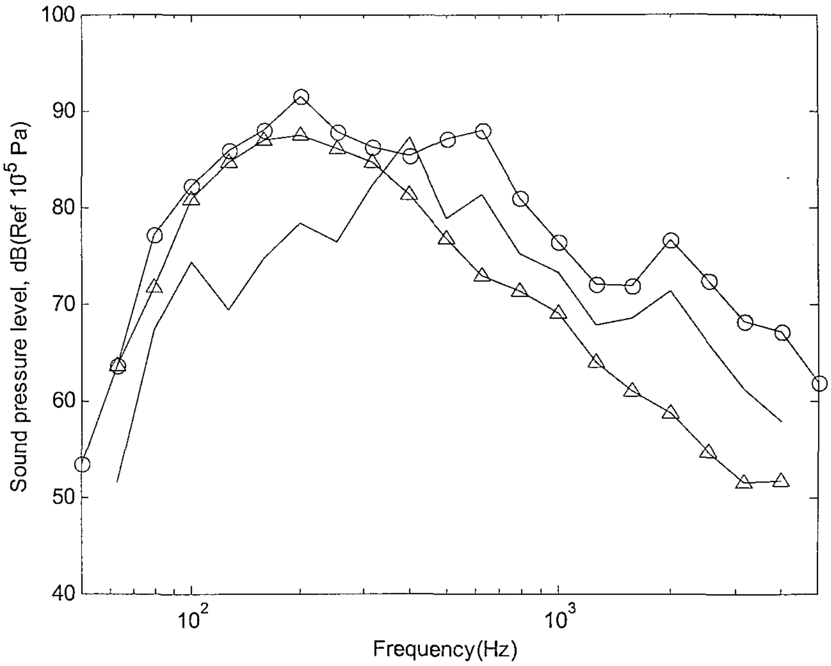

Figure 8.32 Sound pressure level (—) in the receiving room calculated using the measured radiation efficiency from Chapter 7 and measured vibration level from the sound transmission loss measurement [101], compared with sound pressure level (–o–) in the TL measurements and prediction from six-subsystem SEA model (–Δ–).

8.4.3 EFFECT OF DAMPING LOSS FACTOR

The damping loss factors for the local modes also have significant influence on the results of SEA models. For a lightly damped panel, the vibration is mainly controlled by the resonant response. In this case, the radiation efficiency of the local mode subsystems will decrease for frequencies between the first resonance and the critical frequency. If the value of the damping loss factors used for the local mode subsystems is reduced from 0.1, the sound transmission loss at frequencies above 315 Hz will decrease. Figure 8.33 shows the radiation efficiency of the two local mode subsystems for a damping loss factor $\eta = 0.01$. Compared with the corresponding results for the case of $\eta = 0.1$ (see Figure 8.7), the radiation efficiency of the sending panel decreases much more than that of the receiving panel. The reason why the radiation efficiency of the receiving panel is not so sensitive to the damping value is because its radiation efficiency is more controlled by the very narrow strips, which have γ smaller than the limiting value given by equation (5.51). For these very narrow strips, the corner modes do not exist between the first and the second cut-on frequency. An alternative way to understand the insensitivity to the damping of the radiation efficiency of the receiving panel is that those very narrow strips have very high first cut-on frequencies (about 800 Hz). Below the first cut-on frequency, the radiation efficiency is independent of the damping.

As a result of the decrease of the radiation efficiencies, the coupling loss factors from the local mode subsystem to the cavities also decrease, as shown in Figure 8.34. It can be seen that a quite large drop occurs on the curve of the coupling loss factor for the local mode on the sending panel. It is also noted that the assumption of weak coupling is satisfied for the use of the value 0.01 for the damping loss factors.

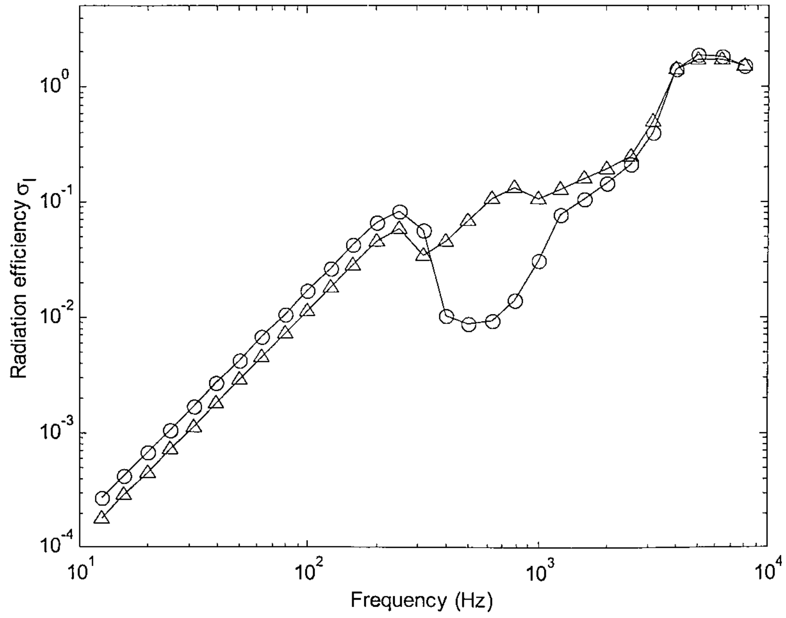

Figure 8.33 Radiation efficiency of local modes ($\eta = 0.01$). –o– subsystem 2; –Δ– subsystem 4.

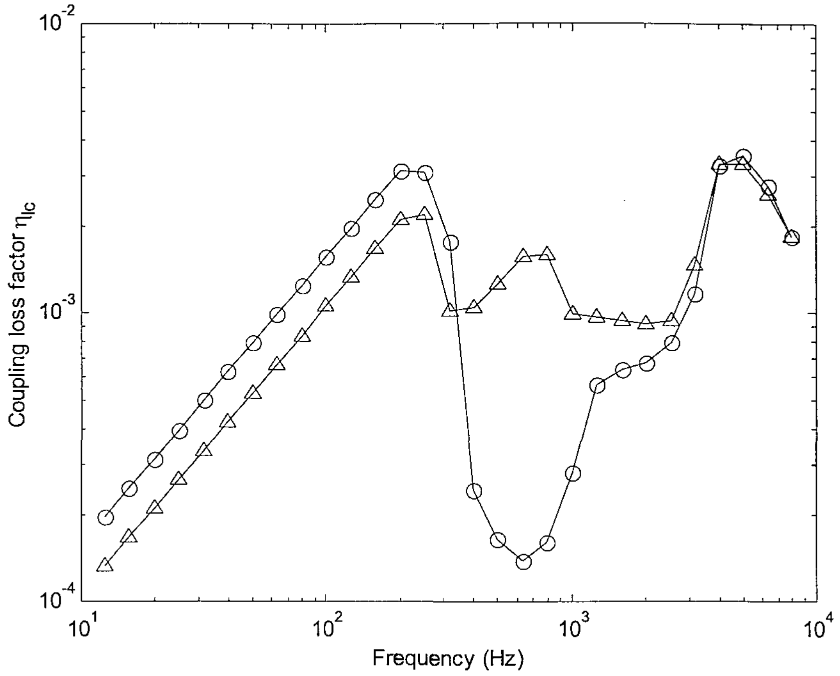

Figure 8.34 Coupling loss factors from local modes to cavity (η = 0.01). –o– subsystem 2; –Δ– subsystem 4.

Figure 8.35 presents the results obtained using values of 0.1, 0.01 and 0.001 for the damping loss factors of local modes. It can be seen that the transmission loss decreases as the damping loss factor decreases. The result of the case of the damping loss factor 0.001 is much closer to the experimental result. However, it must be pointed out that the weak coupling does not hold for the local mode subsystems for such small damping loss factors. The coupling loss factors from the local mode subsystems to the cavities for the damping loss factor 0.001 are not too much different from the result for the case of the damping loss factor 0.01 in Figure 8.34. Then it turns out that the coupling loss factors in most frequency bands are higher than the damping loss factors.

The vibration level differences across the panel using different damping loss factors are also shown in Figure 8.36. From these results, it appears that a damping loss factor slightly higher than 0.01 can give the best prediction of the level difference. However, if compared with the measured result in the case of mechanical excitations, this certainly underestimates the level difference (see Figure 8.26).

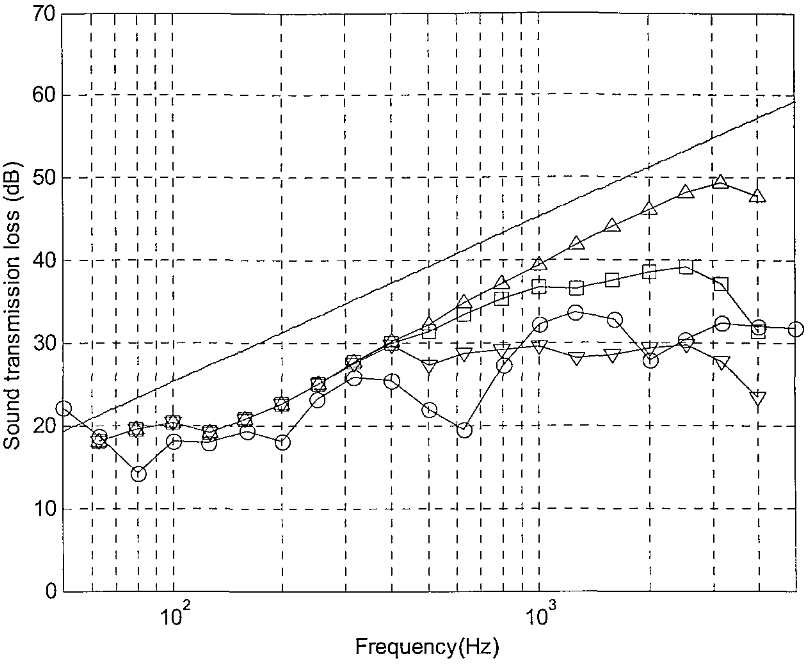

Figure 8.35 Sound transmission loss predicted using different damping loss factor for local mode subsystems. –Δ–, $\eta = 0.1$; –□–, $\eta = 0.02$; –∇–, $\eta = 0.01$; –o–, measurement

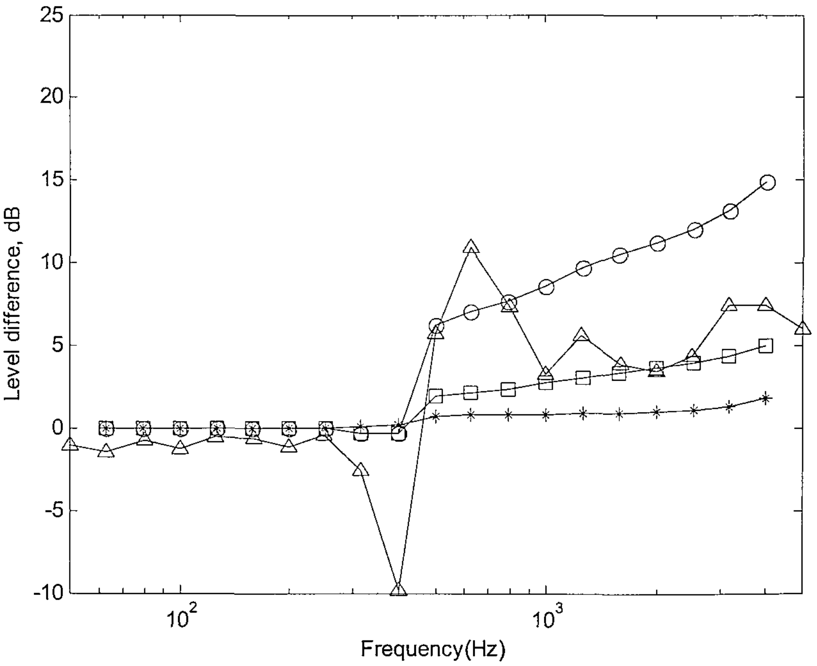

Figure 8.36 Vibration level difference of the two sides of the extruded panel predicted using 6 subsystem SEA model with different damping loss factors for the local mode subsystems. –Δ–, measurement; –*–, $\eta = 0.001$; –□–, $\eta = 0.01$; –o–, $\eta = 0.1$.

8.5 CONCLUSIONS

The response of extruded panels under acoustical and mechanical excitation has been predicted using SEA models. The initial SEA model for the panel consists of 3 subsystems: one global mode subsystem and two local mode subsystems representing two outer plates. The vibration on the receiving side of the panel is transmitted though the coupling between the global modes and local modes. However, the vibration level difference across the panel cannot be well predicted using this model. For the case of acoustical excitation, the vibration levels on the two sides of the panel are underestimated. The sound transmission loss for the acoustical excitation is therefore overestimated. For mechanical excitation, the predicted results have good agreements for the local modes on the source side and global modes. The response of the receiving side is underestimated.

A more complicated SEA model for the extruded panel has been established by introducing the intermediate rib subsystem. This allows the vibration energy to be transmitted from the source side to the receiving side through the coupling between local modes as well. For the case of mechanical excitation, the response of the panel is well predicted. The vibration level difference across the panel has a reasonable prediction. However, for the case of acoustical excitation, the vibration has still been underestimated for both sides of the panel. This underestimation of the vibration of the panel leads to an overprediction of the sound transmission loss. The reason for the higher amplitude of the response of the extruded panel is not clear.

The damping of the extruded panel used in the SEA analysis is based on the experiments studied in Chapter 7. The value of the damping loss factor for the extruded panels has a significant influence on the predicted results. To obtain better understanding of the predicted results from the SEA model, more accurate damping values are required. Using a more reliable damping loss factor, the coupling mechanism between subsystems can then be verified. The actual radiation efficiency for case of acoustical excitation appears higher than that measured for mechanical excitation. This also has effects on the response of the panel. Therefore, a more accurate model for the radiation efficiency under acoustical excitation is also required.

Certainly, damping and coupling loss factors determine the energy distributions among subsystems. An inappropriate use of any one of them could lead to poor predictions. So far, it is clear that further work is required to obtain better understanding the sound transmission loss of extruded panels. The SEA technique has shown potential for dealing with this problem but requires refinement.

9 CONCLUSIONS

The vibroacoustic behaviour of extruded panels has been investigated in the present work. The aim of this thesis is to establish an SEA modelling approach for extruded panels. In order to model the interior noise of railway vehicles using the SEA technique, the extruded panel must be represented in terms of SEA subsystems. To cope with this problem, characteristics of the structural vibration, radiation and sound transmission of extruded panels must be understood and modelled. Under this aim, a number of problems have been addressed, some of which have been investigated in detail. The concluding remarks are summarised in this Chapter.

The bending waves of extruded panels are the only wave form of interest in the present work. At low frequency, the panel bends in global motion of the whole structure. This corresponds to long wavelengths across the panel, which are controlled by the global modes. The global modes are represented by the mass and bending stiffness of the whole structure. At high frequency, the motion of the panel is dominated by the local mass and stiffness, which represents local modes. The local modes correspond to short wavelengths.

Modal density is a crucial parameter to represent the subsystem in an SEA model. For basic structures such as a rod, a beam or a plate, the expressions have been available for many decades. However, for complicated structures, such as extruded panels, no reliable theoretical expressions are available for their modal densities. While it is possible to use FEM to calculate modal densities, as done here, this is numerically inefficient and is inconsistent with the use of a broad-brush tool such as SEA. Therefore it is desirable to obtain simple approximations for the modal density of such panels, both to give increased computational efficiency and fundamental understanding of the problem. For this purpose, the investigation of the mode count and modal density of the structure has formed one of the primary subjects of the present thesis. The conclusions obtained from this part of the work are summarised in section 9.1.

The radiation efficiency of extruded panels is required for modelling their coupling with the surrounding air. For this reason, the radiation of an extruded panel has been modelled based on the studies of the radiation of rectangular plates and strips, using a modal summation approach. The primary conclusions of this part of the study are summarised in section 9.2.

Extruded panels are built with a double skin and intermediate connecting ribs. This causes the response on the one side of the panel to be different from that on the other side, under mechanical or acoustic excitation. Coupling loss factors between global modes and local modes, and between local mode subsystems themselves, are hence crucial for the application of SEA to extruded panels. This various couplings have been developed. Given the coupling loss factors and modal densities, the SEA models have been established for extruded panels. The predicted results from these models have been compared with experimental results for both mechanical and acoustical excitation. The conclusions from the SEA modelling for extruded panels are given in section 9.3.

9.1 MODE COUNT AND MODAL DENSITY

The mode count of one- and two-dimensional structural systems has been investigated. A simple relationship has been shown between the mode count and the boundary conditions for one-dimensional systems. For bending vibrations, a sliding constraint adds to the mode count by $-1/4$, a simple support condition by $-3/4$ and a fixed boundary constraint by -1 compared with a free boundary. For longitudinal vibrations, a fixed boundary constraint adds to the mode count by $-1/2$. For more general boundary conditions, here in particular a point mass and a point spring, the boundary condition effect on the mode count is frequency dependent.

For multi-beam systems in a single line, the mode count of the system can be estimated by taking the mode count of a long beam without any extra constraints and substracting the sum of the constraint coefficients. An intermediate constraint has the same effect on the average mode count of a one-dimensional system as the same type of constraint applied at an end.

Line constraints have systematic effects on the mode count of a two-dimensional system. The effect depends on the type of the boundary condition, as well as the geometric and material properties of the system. The results follow on from those for the same type of boundary in a one-dimensional system. Approximate theoretical expressions have been obtained to estimate the mode count of a two-dimensional system. The results from these estimated formulae have shown the limitation of the commonly used formula, in which the effects of the boundary conditions are neglected.

For a composite two-dimensional system, an intermediate line constraint has the same effect on the mode count as the equivalent constraint applied on an edge. The average mode count of such a composite system can be estimated by taking that of the system without intermediate constraints and substracting the product of the number of constraints, the constraint effect δ_{BC} and the term kL/π, where k is the structural wavenumber and L is the length of the constrained edges.

Theoretical expressions for the modal density of a two-dimensional system have been obtained that include boundary effects. The modal density of a rectangular plate is a frequency-dependent parameter, which depends on geometric information and the dispersion relation of the plate under consideration. However, at high enough frequency, the modal density tends to a constant value, which is determined only by the area of the plate and dispersion relation and is independent of the boundary conditions.

Although in practice it is not possible to analyse in detail all the various combinations of boundary conditions, the analyses for the most basic boundary conditions presented in this thesis are expected to provide enough general insight to permit some sorts of complicated structure comprising many small beams or plates to be dealt with in applications of SEA.

9.2 SOUND RADIATION

The radiation efficiency of plates has been investigated by using the modal summation approach. The radiation efficiency is calculated by considering the average over all possible point force excitation positions. Cross-modal terms do not arise in this averaged radiation efficiency. These averaged radiation efficiency results show the limitations of previous formulae by Maidanik [45] for a plate when it has a large aspect ratio. It has been shown that its radiation efficiency below the fundamental frequency is proportional to the square of the shortest edge length rather than the area of the plate. For frequencies between the fundamental natural frequency and the cut-on of modes involving a whole wavelength deformation across the strip, the radiation from the strip can be considered to be equivalent to the radiation of two monopoles each of size $a \times \lambda_y/4$ where λ_y is the wavelength along the length of the strip. The near-field radiation from the forcing point in this frequency region is proportional to the damping loss factor. It is found that the dependence on the damping loss factor of the near-field radiation efficiency for the strip is approximately twice that for the rectangular plate with moderate aspect ratio. Finally, an approximate model for calculating the radiation efficiency of a strip has been presented.

Based on the results from the modal summation approach, it is found that the maximum average radiation efficiency expressed in one-third octave bands increases in proportion to $(k_c a)^{1/4}$ for $k_c a > 3$, not $(k_c a)^{1/2}$ as given by Leppington [50]and Maidanik [45], where k_c is the wavenumber at the critical frequency and a is the shorter edge of the plate. For $k_c a < 3$, the maximum radiation efficiency tends to a constant value between 1.2 and 1.3, depending on the aspect ratio, but no longer occurs at the critical frequency.

9.3 SEA MODELLING FOR EXTRUDED PANELS

Models of the mode count and modal density for both two-dimensional and three-dimensional representation of an aluminium extrusion have been proposed based on the studies of the boundary effects on the mode count. The modes are divided into global modes and local modes. Approximate theoretical expressions have been developed to estimate the mode count and modal density for extruded panels. The results from these models have shown fairly good agreement with those from FE models. Generally, the predicted modal density has better agreement than the mode count. The actual boundary conditions between strips in reality are normally unknown and have been shown to be between simply supported and fixed conditions. It is therefore natural that variance occurs in the predictions if using a constant δ_{BC}. However, this variance compared with the FE model should be understood in terms of statistical variance, which is acceptable in utilization of SEA. It is therefore seen that the proposed model fairly successfully allows extruded panels to be represented using global parameters in terms of SEA subsystems. Moreover, a better physical understanding of the characteristics of extruded panels has been achieved.

Measurements of the response of a sample extruded panel excited by the point force has been implemented. At low frequencies, typically below 400 Hz, the panel vibrates purely in global modes while the vibration is dominated by localised modes of strips at higher frequencies. The driving point mobility has been investigated for excitation positions either on 'strips' or 'stiffeners'. The driving point mobilities on strips are controlled by the individual strip that is excited. The driving point mobility on stiffeners is controlled by global modes and is considerably lower than that on the strips in the high frequency region.

The transfer mobility at many positions over the panel surface was used to obtain the spatially-averaged mobility. It has been shown that, for excitation on a strip, the average response of the panel on the excitation side is higher than that on the other side; the response of the strip under excitation is about 20 dB higher than other strips; the response of the strips is also generally higher than that of stiffeners. These measurement results have furthermore confirmed the possibility to use the proposed modal densities to represent the extruded panels.

The half-power bandwidth method has been used to determine the modal damping loss factors at low frequency for global modes. The attenuation of vibration with distance due to the damping effect has been measured along the driven strip at higher frequencies. The damping loss factors in one-third octave bands have been derived for the local modes from these results.

Modelling the radiation of the extruded panel becomes more difficult because it requires the vibration distribution on the surface of the structure in detail. In practice, the average radiation efficiency is normally of interest. Classical work in this field can only cope with simple and basic structures such as a beam or a plate. A modal summation approach has been used to study the radiation of rectangular plates and strips. The principle of average radiation efficiency has been then applied to extruded panels. An approximate expression has been developed for the average radiation efficiency of extruded panels. This can also give the radiation efficiency for global modes and local modes separately to allow the coupling loss factor between extruded panels and cavities to be modelled in the SEA model.

The radiation efficiency of the sample panel under unbaffled conditions has been measured using a reciprocal test method. Results have been obtained corresponding to excitation positions at strips and stiffeners. The results have been compared with predictions from the proposed analytical model. It has been found that the predictions agree with the measured results in most frequency bands.

SEA models consisting of three and four subsystems to represent extruded panels have been proposed in the last part of this thesis. For the three subsystem model, the extruded panels are represented by a global mode subsystem, a local mode subsystem on the source side and a local mode subsystem on the receiving side. There is no direct coupling between the local mode subsystems; their coupling is through the global modes. The coupling between global modes and local modes has been modelled for a velocity input due to the global waves under the assumption that the local modes of each strip are uncorrelated. For the four subsystem model, the intermediate ribs form another local mode subsystem, which can couple with both local mode subsystems on the source and receiving side. The coupling loss factor between local modes has been modelled using standard expressions for various structure joints.

For mechanical excitation, both SEA models can fairly well predict the responses of global modes and the source side local modes. However, it has been found that the response of the local modes on the receiving side cannot be predicted correctly without including the intermediate local mode subsystem. The four subsystem model gives a good estimate of the response on the receiving side of the panel. The vibration level difference across panels can be well predicted.

To predict the sound transmission loss, two cavity subsystems have been added to form two SEA models. Unfortunately, the predicted results overestimate the transmission loss from measurements. Basically, both SEA models underestimate the response of the panel on both sides for frequencies above 400 Hz. For frequencies below 400 Hz, the SEA models give reasonable predictions of the response of the panel and the sound transmission loss. It has been found that even the model including the intermediate local mode subsystem overestimates the vibration level difference across panels by about 5 to 10 dB. It has also been noted that the vibration level difference across panels for acoustical excitation is about 5 dB higher than that for mechanical excitation at high frequency.

9.4 FUTURE WORK

The primary tasks implemented in this thesis are concerned with modelling the vibroacoustic behaviour of aluminium extrusions used in railway vehicles. The SEA model for extruded panels proposed in the present work has shown a good performance for the case of mechanical excitation. Although the agreement with measurements for the response of extruded panel under acoustical excitation is more limited, a first step has been made to achieve the long-term goal that is to be able to model the interior noise of railway vehicles. For this goal, obviously, more work is needed to be identified and be carried out.

There is always a gap between predictions and reality. It is believed that a good model can only be established based on the deep understanding of the fundamental mechanisms involved. The SEA method was developed from studies on two oscillators. A number of assumptions were made to extend the conclusion into complicated systems in practice. The global parameters such as modal density and loss factor should be derived based on rigorous analyses or experiments. Without these, confidence in an SEA application can never be obtained. The present work has addressed some general topics in the field of noise and vibration for the purpose of application of SEA. This has allowed a simplified and efficient analytical model to be established. This also reflects, to a certain extent, the philosophy of SEA, which is using global parameters to represent complicated systems. However, to model extruded panels in terms of SEA successfully, the present work is not adequate to reveal every aspect involved.

The concept of the spatially averaged response, which is one of the greatest physical importance, has been used throughout the present work to allow the principle of mode orthogonality to be used. The spatially averaged mean square velocity is again averaged over all possible excitation positions rather than dealing with a specific excitation positions. The result from this second averaging process is that the response to a point excitation depends only on the global parameters such as the total mass, the damping, frequency and the excitation force. For the radiation of a structure, the cross mode effect is also eliminated. However, for extruded panels, the intermediate ribs do have to be taken into account although they can never be under excitation in reality. Therefore, strictly speaking, the orthogonality principle does not hold in this averaging process.

When the radiation of extruded panels was modelled, it was assumed that the vibration is localised to the strip excited directly by the point force. This eventually leads the simplest approximation that the radiation from local modes is determined by a weighted single strip. This might not be true in reality. If strips vibrate in phase, the radiation efficiency of extruded panel will increase; if strips vibrate out of phase, the radiation will decrease. For this reason, it is inadequate to use this approximation to model the response of the panel to acoustic excitation. This is probably the reason the SEA model could not predict the sound transmission appropriately. Therefore, in the future, more detailed study is essential to reveal the distribution of vibration under both mechanical and acoustic excitations.

It is desirable to develop a more advanced analytical model for an undamped panel so that the response of the panel can be predicted. Certainly, FEM or BEM can be helpful in the validation or numerical experiments. The Dynamic Stiffness Method or Spectral Finite Element Method could be considered to model extruded panels either in two-dimensions or three-dimensions. The computational efficiency should also be considered.

The structural damping in extruded panels has not been investigated sufficiently. The damping has a significant effect on the energy distribution and wave propagation. The vibration measurement carried out in the present work is for a fully damped section of a real floor. Experiments on an undamped panel are definitely necessary in the future. This will not only reveal the effects of the damping but also help in the work of theoretical modelling in the future, by allowing wavenumbers and mode localisation to be studied.

SEA has shown its potential in modelling extruded panels. More modelling work and parameter studies are required in the future. For the final aim to model the interior noise using SEA technique, some questions have been identified. At this stage, it can be expected that further progresses in modelling interior noise of railway vehicles can be achieved if appropriate research can be carried out in this area.

(This page is intended as empty)

REFERENCES

1. N. J. Shaw 1990 *MSc Thesis Heriot-Watt University, Edinburgh* The predition of railway vehicle internal noise using statistical energy analysis techniques.

2. P. Geissler and D. Neumann 1999 *Proceedings of the 1999 ASME Design Engineering Technical Conference, Las Vegas, Nevada.* 563-570. Modelling extruded profiles for railway coaches using SEA.

3. T. Kohrs 2002 *Diploma Thesis Institut fur Technische Akustik - TU Berlin* Structural acoustic investigation of orthotropic plates.

4. K. A. Cunefare and B. S. Dater 2003 *Journal of Computational Acoustics.* **11**, 115-137. Structural acoustic optimization using the complex method.

5. S. Marburg, H. J. Beer, J. Gier, H. J. Hardtke, R. Rennert, and F. Perret 2002 *Journal of Sound and Vibration.* **252**, 591-615. Experimental verification of structural-acoustic modelling and design optimization.

6. S. P. Engelstad, K. A. Cunefare, E. A. Powell, and V. Biesel 2000 *Journal of Aircraft.* **37**, 165-171. Stiffener shape design to minimize interior noise.

7. A. R. Mohanty, B. D. St Pierre, and P. Suruli-Narayanasami 2000 *Applied Acoustics.* **59**, 1-17. Structure-borne noise reduction in a truck cab interior using numerical techniques.

8. S. Marburg and H. J. Hardtke 2002 *Finite Elements in Analysis and Design.* **38**, 737-754. A general concept for design modification of shell meshes in structural-acoustic optimization - Part II: Application to a floor panel in sedan interior noise problems.

9. S. Marburg 2002 *Archives of Computational Methods in Engineering.* **9**, 291-370. Developments in structural-acoustic optimization for passive noise control.

10. P. W. Eade and A. E. J. Hardy 1977 *Journal of Sound and Vibration.* **51**, 401-415. Railway vehicle internal noise.

11. R. H. Lyon 1975 *Statistical Energy Analysis of Dynamical Systems.* Cambridge, MA MIT.

12. R. Bickerstaffe, P. W. Eade, A. E. J. Hardy, S. Peters, and B. Woodward 1975 *Journal of Sound and Vibration.* **43**, 265-272. An analysis of railway vehicle acoustics.

13. A. E. J. Hardy and R. R. K. Jones 1989 *Proc Instn Mech Engrs.* **203**, 79-85. Control of the noise environment for passengers in railway vehicles.

14. A. E. J. Hardy 1999 *Proc Instn Mech Engrs*. **213**, 173-180. Railway passengers and noise.

15. K. De. Meester and L. Hermans 1996 *Inter Noise, Liverpool*. 2895-2902. High frequency experimental statistical energy modelling of a high speed train: Measurement strategy, model derivation and model application.

16. N. Lalor 1990 *ISVR Technical Report* **No 182.** Practical consideration for the measurement of internal and coupling loss factors on complex structures.

17. N. Lalor 1996 *Sound and Vibration*. **January**, 16-20. Statistical energy analysis and its use as an NVH analysis tool.

18. A. Fages and G. Borello 1996 *ISMA21-Noise and Vibration Engineering, Leuven, Belgium*. 163-169. Use of SEA to reduce the noise in the driver's cabin of a TGV high speed train.

19. K. de.Meester, L. Hermans, K. Wyckaert, and N. Cuny 1996 *ISMA21-Noise and Vibration Engineering, Leuven, Belgium*. 151-161. Experimental SEA on a highspeed train carriage.

20. G. Borello 1998 *EURO-NOISE*, 183-188. Prediction and control of structure borne noise transfers in vehicles using SEA.

21. U. Orrenius and R. Enblom 2001 *Inter Noise 2001, The Hague, Netherlands*. Acoustic optimization of car-body structures: Weight efficient setting of subsystem requirements.

22. U. Orrenius and U. Stegemann 2003 *Proceedings of the Vibro-Acoustic users conference, Leuven, Belgium*. Development and validation of a SEA model of a metro rail car.

23. U. Stegemann 2002 *MSc Thesis* Development and validation of a vibro-acoustic model of a metro rail car using Statistical Energy Analysis (SEA).

24. Vibro-acoustic Sciences 2001 *Theory & QA for AutoSEA2*. San Diego. Vibro-Acoustic Science.

25. D. Backstrom 2001 *MSc Thesis KTH Stockholm* Analysis of the sound transmission loss of train partitions.

26. D. Backstrom and U. Orrenius 2002 *Proc. ISMA 2002, Leuven, Belgium*. 783-788. A model for transmission loss calculations of floor and wall constructions of railway carbodies.

27. S. Bruhl, P. Faulhaber, and M. Grunewald 2000 *Proceedings of the First International AutoSEA Users Conference, San Diego, CA*. AutoSEA2 studies on generic lightweight structures.

28. C. Pezerat and J. L. Guyader 2003 *EURO-NOISE, Naples, Italy*. Analytical modelling of extruded plates.

29. R. Courant and D. Hilbert 1953 *Methods of Mathematical Physics*. New York Interscience Publishers.

30. V. V. Bolotin 1984 *Random Vibrations of Elastic Systems*. The Hague Martinus Nijhoff.

31. I. Elishakoff 1975 *Journal of the Acoustical Society of America*. **57**, 361-369. Distribution of natural frequencies in certain structural elements.

32. F. D. Hart and K. C. Shah 1971 *NASA Contractor Report* **CR-1773.** Compendium of modal densities for structures.

33. M. Heckl 1962 *Journal of the Acoustical Society of America*. **34**, 1553-1557. Vibrations of point-driven cylindrical shells.

34. J. P. D. Wilkinson 1967 *Journal of the Acoustical Society of America*. **43**, 245-251. Modal densities of certain shallow structural elements.

35. L. Cremer, M. Heckl, and E. E. Ungar 1988 *Structure-borne Sound*. Berlin Springer-Verlag. Second edition.

36. R. S. Langley 1996 *Journal of the Acoustical Society of America*. **99**, 3481-3487. The modal density of anisotropic structural components.

37. R. H. Lyon and R. G. DeJong 1995 *Theory and Application of Statistical Energy Analysis*. London Butterworth-Heinemann.

38. P. M. Morse and R. H. Bolt 1944 *Reviews of Modern Physics*. **16**, 69-150. Sound waves in rooms.

39. D. Y. Maa 1939 *Journal of the Acoustical Society of America*. **10**, 235-238. Distribution of eigentones in a rectangular chamber at low frequency range.

40. G. M. Roe 1941 *Journal of the Acoustical Society of America*. **13**, 1-7. Frequency distribution of normal modes.

41. E. Bogomolny and E. Hugues 1998 *Physical Review*. **57**, 5404-5424. Semiclassical theory of flexural vibrations of plates.

42. P. Bertelsen, C. Ellegaard, and E. Hugues 2000 *The European Physical Journal B*. **15**, 87-96. Distribution of eigenfrequencies for vibrating plates.

43. D. G. Vasil'ev 1987 *Transactions of Moscow Mathematics Society*. **49**, 173-245. Asymptotics of the spectrum of a boundary value problem.

44. Lord Rayleigh 1945 *The Theory of Sound*. Dover, New York. 2nd ed.

45. G. Maidanik 1962 *Journal of the Acoustical Society of America*. **34**, 809-824. Response of ribbed panels to reverberant acoustic fields.

46. C. E. Wallace 1972 *Journal of the Acoustical Society of America*. **51**, 946-952. Radiation resistance of a rectangular panel.

47. M. C. Gomperts 1974 *Acustica.* **30**, 320-327. Radiation from rigid baffled rectangular plates with general boundary conditions.

48. M. C. Gomperts 1977 *Acustica.* **37**, 93-102. Sound radiation from baffled, thin, rectangular plates.

49. M. Heckl 1977 *Acustica.* **37**, 155-166. Radiation from plane sound sources.

50. F. G. Leppington, E. G. Broadbent, and K. H. Heron 1982 *Proceedings of the Royal Society of London Series A- Mathematical Physical and Engineering Sciences.* **382**, 245-271. The Acoustic Radiation Efficiency of Rectangular Panels.

51. E. G. Williams 1983 *Journal of the Acoustical Society of America.* **73**, 1520-1524. A Series Expansion of the Acoustic Power Radiated from Planar Sources.

52. W. L. Li 2001 *Journal of Sound and Vibration.* **245**, 1-16. An analytical solution for the self- and mutual radiation resistances of a rectangular plate.

53. I. L. Ver and C. I. Holmer 1971 *Noise and Vibration Control.* McGraw-Hill, New York. (L. L. Beranek, ed.).

54. S. D. Snyder and N. Tanaka 1995 *Journal of the Acoustical Society of America.* **97**, 1702-1709. Calculating Total Acoustic Power Output Using Modal Radiation Efficiencies.

55. W. L. Li and H. J. Gibeling 2000 *Journal of Sound and Vibration.* **229**, 1213-1233. Determination of the mutual radiation resistances of a rectangular plate and their impact on the radiated sound power.

56. W. L. Li and H. J. Gibeling 1999 *Journal of Sound and Vibration.* **220**, 117-133. Acoustic radiation from a rectangular plate reinforced by springs at arbitrary locations.

57. K. Michishita, K. Sakagami, M. Morimoto, and U. P. Svensson 2000 *Applied Acoustics.* **61**, 45-63. Sound radiation from an unbaffled elastic plate strip of infinite length.

58. K. Sakagami, K. Michishita, M. Morimoto, and Y. Kitamura 1998 *Applied Acoustics.* **55**, 181-202. Sound radiation from a baffled elastic plate strip of infinite length with various concentrated excitation forces.

59. M. Heckl 1961 *Journal of the Acoustical Society of America.* **33**, 640-651. Wave propagation on beam-plate systems.

60. G.L.Lamb 1961 *Journal of the Acoustical Society of America.* **33**, 628-633. Input impedance of a beam coupled to a plate.

61. R. M. Grice and R. J. Pinnington 2000 *Journal of Sound and Vibration.* **230**, 825-849. A method for the vibration analysis of built-up structures, part I: Introduction and analytical analysis of the plate- stiffened beam.

62. R. M. Grice and R. J. Pinnington 2000 *Journal of Sound and Vibration*. **230**, 851-875. A method for the vibration analysis of built-up structures, part II: Analysis of the plate-stiffened beam using a combination of finite element analysis and analytical impedances.

63. L. Ji, B. Mace, and R. J. Pinnington 2003 *10th International Congress of Sound and Vibration, Stockholm, Sweden*. 1075-1082. A mode-based approach to the vibration analysis of coupled long- and short-wavelength subsystems.

64. R. S. Langley and P. Bremner 1999 *Journal of the Acoustical Society of America*. **105**, 1657-1671. A hybrid method for the vibration analysis of complex structural-acoustic systems.

65. C. Soize 1993 *Journal of the Acoustical Society of America*. **94**, 849-865. A Model and Numerical-Method in the Medium Frequency-Range for Vibroacoustic Predictions Using the Theory of Structural Fuzzy.

66. M. Strasberg and D. Feit 1996 *Journal of the Acoustical Society of America*. **99**, 335-344. Vibration damping of large structures induced by attached small resonant structures.

67. A. D. Pierce, V. W. Sparrow, and D. A. Russell 1995 *Journal of Vibration and Acoustics-Transactions of the Asme*. **117**, 339-348. Fundamental Structural-Acoustic Idealizations for Structures with Fuzzy Internals.

68. R. H. Lande, R. S. Langley, P. J. Shorter, and J. Woodhouse 2003 *10th International Congress of Sound and Vibration, Stockholm, Sweden*. 1083-1090. Statistical energy analysis of a built-up structure excited through its stiffening members.

69. F. J. Fahy 1982 *Statistical Energy Analysis*. Chapter 7 in *Noise and Vibration* by R.G.White and J.G.Walker. Chichester, West Sussex, England. Ellis Horwood Ltd.

70. H. G. Davies and M. A. Wahab 1981 *Journal of Sound and Vibration*. **77**, 311-321. Ensemble Averages of Power Flow in Randomly Excited Coupled Beams.

71. P. W. Smith Jr 1980 *Journal of Sound and Vibration*. **46**, 343-353. Random response of identical one-dimensional coupled systems.

72. P. W. Smith Jr 1979 *Journal of the Acoustical Society of America*. **65**, 695-698. Statistical models of coupled dynamical systems and transition from weak to strong coupling.

73. R. J. M. Craik 1996 *Sound Transmission through Buildings using Statistical Energy Analysis*. Aldershot, England Gower Publishing Limited.

74. D. J. Mead 1998 *Experimental measurement of the modal damping*. Chapter 2.7 in *Passive Vibration Control*. Chichester, West Sussex, England. John Wiley & Sons Ltd.

75. L. L. Beranek 1971 *Noise and Vibration Control*. McGraw-Hill, Inc.

76. F. J. Fahy 1969 *Journal of Sound and Vibration.* **10**, 490-512. Vibration of containing structures by sound in the contained fluid.

77. F. J. Fahy 1970 *Journal of Sound and Vibration.* **13**, 171-194. Response of a cylinder to random sound in the contained fluid.

78. R. S. Langley 1992 *Journal of Sound and Vibration.* **159**, 483-502. A wave intensity technique for the analysis of high frequency vibrations.

79. S. A. Hambric 1990 *Journal of Vibration and Acoustics-Transactions of the Asme.* **112**, 542-549. Power Flow and Mechanical Intensity Calculations in Structural Finite-Element Analysis.

80. C. Simmons 1991 *Journal of Sound and Vibration.* **144**, 215-227. Structure-Borne Sound-Transmission Through Plate Junctions and Estimates of Sea Coupling Loss Factors Using the Finite-Element Method.

81. C. R. Fredo 1997 *Journal of Sound and Vibration.* **199**, 645-666. A SEA-like approach for the derivation of energy flow coefficients with a finite element model.

82. K. Shankar and A. J. Keane 1997 *Journal of Sound and Vibration.* **201**, 491-513. Vibrational energy flow analysis using a substructure approach: The application of receptance theory to FEA and SEA.

83. J. A. Steel and R. J. M. Craik 1994 *Journal of Sound and Vibration.* **178**, 553-561. Statistical Energy Analysis of Structure-Borne Sound- Transmission by Finite-Element Methods.

84. W. S. Park 2003 *PhD Thesis University of Southampton, Highfield, Southampton, England.* The sources of variability in the statistical energy analysis of two rectangular plates.

85. R. S. Langley 1989 *Journal of Sound and Vibration.* **135**, 319-331. Application of the dynamic dtiffness method to the free and forced vibrations of aircraft panels.

86. A. Ratka and N. Schneider 2002 *Procedings ISMA, Leuven, Belgium.* Development of a simulation tool for internal and external noise caused by rail bound vehicles.

87. F. J. Fahy 1985 *Sound and Structural Vibration: Radiation, Transmission and Response.* London Academic Press.

88. M. J. Crocker and A. J. Price 1969 *Journal of Sound and Vibration.* **9**, 469-486. Sound transmission using Statistical Energy Analysis.

89. D. J. Mead 1994 *Journal of Sound and Vibration.* **171**, 695-702. Waves and Modes in Finite Beams - Application of the Phase- Closure Principle.

90. D. J. Mead 1975 *Journal of Sound and Vibration.* **40**, 1-18. Wave propagation and natural modes in periodic systems: I. Mono-coupled systems.

91. D. J. Mead 1975 *Journal of Sound and Vibration*. **40**, 19-39. Wave propagation and natural modes in periodic systems:II Multi-coupled systems, with and without damping.

92. R. S. Langley 1994 *Journal of Sound and Vibration*. **172**, 491-511. On the Modal Density and Energy-Flow Characteristics of Periodic Structures.

93. R. S. Langley 1991 *Journal of Sound and Vibration*. **145**, 261-277. An Elastic Wave Technique for the Free-Vibration Analysis of Plate Assemblies.

94. W. Leissa 1969 *Vibration of Plates*. Washington, D.C. National Aeronautics and Space Administration.

95. S. P. Timoshenko and S. Woinowsky-Krieger 1959 *Theory of Plate and Shells*. McGraw-Hill. 2nd Edition.

96. R. D. Mindlin 1951 *Journal of Applied Mechanics*. 31-38. Influence of rotatory inertia and shear on flexural motions of isotropic, elastic plates.

97. M. Heckl 1960 *Acustica*. **10**, 109-115. Untersuchungen an orthotropen platten.

98. E. Ungar 1961 *Journal of the Acoustical Society of America*. **33**, 633-639. Transmission of plate flexural waves through reinforcing beams; Dynamic stress concentrations.

99. D. J. Thompson, I. Back, and A. N. Thite 2002 *ISVR Contract Report* **02/15.** Measurements of sound radiation by a steel valve cover.

100. C. H. Oppenheimer and S. Dubowsky 1997 *Journal of Sound and Vibration*. **199**, 473-489. A radiation efficiency for unbaffled plates with experimental validation.

101. U. Orrenius 2003 Bombardier Transportation, Private Communication.

APPENDIX A

- **Ten subsystem SEA model**

A more advanced ten-subsystem SEA model is presented here. Table A.1 shows a list of the subsystems and the coupling among them. The dominant noise transmission into the interior cavity comes from three types of transmission: (i) the non-resonant sound transmission from the under-floor cavity through the floor, walls, windows and the roof; (ii) resonant sound transmission from the under-floor cavity through the floor, walls windows and the roof; (iii) radiation from vibrations of the floor, walls, windows and the roof. The first type of transmission can be well modelled using the 'mass law' (equation (2.20)). Modelling the resonant sound transmission involves the study of interactions between structures and fluid. This interaction can normally be represented using the radiation efficiency of the structure. Modelling the third type of transmission requires investigations of the coupling between structures. To use an SEA model to predict the interior noise level, all these transmission paths will eventually be expressed using coupling loss factors. Together with the damping loss factors of each subsystem, the total energy of each subsystem can be calculated after introducing the input powers and hence the spatially-averaged response can be obtained. The input power for this SEA model will be an acoustic input to the under-floor cavity and a mechanical excitation from the bogies to the floor.

In the SEA model of reference [22], the exterior of the vehicle was divided into 10 cavities. The assumption of diffuse field was made for each of these cavities. This is not valid as a free field condition holds in reality.

In the present ten-subsystem model, the problem of modelling the space outside the vehicle is by-passed using a modified non-resonant coupling between the under-floor cavity and the interior cavity. The non-resonant transmission from the under-floor cavity to the interior cavity can be considered via the floor, the walls and the roof. The power flow of this transmission can be expressed by

$$\begin{aligned} P_{31} &= \omega\eta_{31(2)}E_3 + \omega\eta_{31(4)}E_3C_4 + \omega\eta_{31(6)}E_3C_6 \\ &= \omega\left[\eta_{31(2)} + \eta_{31(4)}C_4 + \eta_{31(6)}C_6\right]E_3 \end{aligned} \tag{A.1}$$

where $\eta_{31(i)}$ means the coupling loss factor from subsystem 3 to subsystem 1 via *i*th subsystem. C_4 and C_6 are the coefficients used to describe the sound propagation decay from the under floor cavity to the walls and roof. So the coupling loss factor from the under- floor cavity to the interior cavity can be given by

$$\eta_{31} = \eta_{31(2)} + \eta_{31(4)}C_4 + \eta_{31(6)}C_6 \tag{A.2}$$

The decay due to the sound propagation around the outside of the vehicle also affects the coupling loss factor from the under-floor cavity to the walls and roof. The coupling loss factor from the under-floor cavity to the walls is expressed by

$$P_{34} = \omega\eta_{34}E_3 = \omega\eta'_{34}E_3C_4 \tag{A.3}$$

where η'_{34} is the coupling loss factor without the decay of the sound in the field.

The case of the roof can be considered similarly by

$$\eta_{36} = \alpha_6\eta'_{36} \tag{A.4}$$

where η'_{36} is the coupling loss factor without the decay of the sound in the field.

It has been emphasized that the key issue in this thesis is not to address how to decompose the whole vehicle into subsystems and how to implement this SEA model to predict the interior noise. The discussion regarding the justification of the ten-subsystem model for the whole vehicle will not be addressed in the later content.

Table A.1 Subsystems used in 10-subsystem SEA model

Subsystems		Number	1	2	3	4	5	6	7	8	9	10
		Name	Interior cavity	Floor	Underfloor cavity	Walls (2)	Transverse beam (2)	Roof	Windows	Sole bars(2)	Interior bulkhead+doors	Vestibules
Number	Name	Type	Cavity	Ribbed plate	Cavity	Ribbed plate	Beam	Curved plate	Plate	Beam	Plate	Cavity
1	Interior cavity	Cavity	▨	1	2++	1	_	5	1	_	1	2
2	Floor	Extruded plate	1	▨	1	-	4	_	_	4	3	1
3	Underfloor cavity	Cavity	2++	1	▨	1*	6	1*	1*	6	_	2+
4	Walls (2)	Extruded plate	1	-	1*	▨	_	3	7	4	3	1
5	Transverse beam (2)	Beam	_	4	6	_	▨	_	_	8	_	_
6	Roof	Curved plate	5	_	1*	3	_	▨	_	_	3	5
7	Windows	Plate	1	_	1*	7	_	_	▨	_	_	_
8	Sole Bars (2)	Beam	_	4	6	4	8	_	_	▨	_	_
9	Interior bulkhead+doors	Plate	1	3	_	3	_	3	_	_	▨	1
10	Vestibules	Cavity	2	1	2+	1	_	5	_	_	1	▨

Coupling types

1 = plate and cavity
2 = cavity through plate to cavity
3 = plate to plate (normal)(include curved plate)
4 = beam flexural to plate flexural (line connection)
5 = curved plate to cavity
6 = beam to cavity
7 = plate to plate (parallel)
8 = beam to beam (normal)
2+ = including interconnection, doors and windows
2++=including walls, windows and roof
* = modified under considering sound decay

APPENDIX B

The natural modes and mode count for a single beam with different boundary conditions are listed in Table B.1. The mode count is calculated by

$$N = \frac{kL}{\pi} + \delta_{BC}$$

where $\delta_{BC} = 1 - \delta_L - \delta_R$. δ_L and δ_R are shown in Table 3.1.

Table B.1 Natural modes and mode count of single beam system

Boundary conditions	*Frequency equation*	δ_L	δ_R	δ_{BC}	*Mode count* N
Free-free	$kL = (n - \frac{3}{2})\pi$	0	0	1	$\frac{kL}{\pi} + 1$
Free-sliding	$kL = (n - \frac{5}{4})\pi$	0	1/4	3/4	$\frac{kL}{\pi} + \frac{3}{4}$
Free-pinned	$kL = (n - \frac{3}{4})\pi$	0	3/4	1/4	$\frac{kL}{\pi} + \frac{1}{4}$
Free-fixed	$kL = (n - \frac{1}{2})\pi$	0	1	0	$\frac{kL}{\pi}$
Sliding-sliding	$kL = (n - 1)\pi$	1/4	1/4	1/2	$\frac{kL}{\pi} + \frac{1}{2}$
Sliding-pinned	$kL = (n - \frac{1}{2})\pi$	1/4	3/4	0	$\frac{kL}{\pi}$
Sliding-fixed	$kL = (n - \frac{1}{4})\pi$	1	1/4	-1/4	$\frac{kL}{\pi} - \frac{1}{4}$
Pinned-pinned	$kL = n\pi$	3/4	3/4	-1/2	$\frac{kL}{\pi} - \frac{1}{2}$
Pinned-fixed	$kL = (n + \frac{1}{4})\pi$	3/4	1	-3/4	$\frac{kL}{\pi} - \frac{3}{4}$
Fixed-fixed	$kL = (n + \frac{1}{2})\pi$	1	1	-1	$\frac{kL}{\pi} - 1$

APPENDIX C

Leissa [94] gives a comprehensive collection of solutions for natural frequencies of rectangular plates. The boundary conditions considered for a rectangular plate may be a combination of simple supports (SS), clamped (C) or free (F). There are six possible distinct sets of boundary conditions along either x- or y-direction. For a plate in the coordinate system illustrated in Figure 4.1, they are

a) simply supported at $x = 0$ and $x = a$;
b) clamped at $x = 0$ and $x = a$;
c) free at $x = 0$ and $x = a$;
d) clamped at $x = 0$ and simply supported at $x = a$;
e) free at $x = 0$ and simply supported at $x = a$;
f) clamped at $x = 0$ and free at $x = a$.

and similarly for constraints at $y = 0$ and $y = b$.

The natural frequencies are given by

$$\omega^2 = \frac{\pi^4 D}{a^4 m''}\left\{G_x^4 + G_y^4\left(\frac{a}{b}\right)^4 + 2\left(\frac{a}{b}\right)^2\left[\nu H_x H_y + (1-\nu) J_x J_y\right]\right\} \tag{C.1}$$

where a and b are the dimensions of the rectangular plate, D is the flexural rigidity, m'' is the mass per unit area, G_x, H_x and J_x are functions determined from Table C.1. The quantities G_y, H_y and J_y are obtained from Table C.1 by replacing x by y and m by n.

The indicators m and n are seen to be the number of nodal lines parallel to the y- and x-axes, respectively, including the boundaries as nodal lines, except when the boundary is free.

Table C.1. Frequency coefficients in equation (C.1)

Boundary conditions at		m	G_x	H_x	J_x
$x=0$	$x=a$				
SS	SS	2, 3, 4, …	$m-1$	$(m-1)^2$	$(m-1)^2$
C	C	2	1.506	1.248	1.248
		3, 4, 5, …	$m-\frac{1}{2}$	$\left(m-\frac{1}{2}\right)^2\left[1-\frac{2}{\left(m-\frac{1}{2}\right)\pi}\right]$	$\left(m-\frac{1}{2}\right)^2\left[1-\frac{2}{\left(m-\frac{1}{2}\right)\pi}\right]$
F	F	0	0	0	0
		1	0	0	$12/\pi^2$
		2	1.506	1.248	5.017
		3, 4, 5, …	$m-\frac{1}{2}$	$\left(m-\frac{1}{2}\right)^2\left[1-\frac{2}{\left(m-\frac{1}{2}\right)\pi}\right]$	$\left(m-\frac{1}{2}\right)^2\left[1+\frac{6}{\left(m-\frac{1}{2}\right)\pi}\right]$
C	SS	2, 3, 4, …	$m-\frac{3}{4}$	$\left(m-\frac{3}{4}\right)^2\left[1-\frac{1}{\left(m-\frac{3}{4}\right)\pi}\right]$	$\left(m-\frac{3}{4}\right)^2\left[1-\frac{1}{\left(m-\frac{3}{4}\right)p}\right]$
F	SS	1	0	0	$3/\pi^2$
		2, 3, 4, …	$m-\frac{3}{4}$	$\left(m-\frac{3}{4}\right)^2\left[1-\frac{1}{\left(m-\frac{3}{4}\right)\pi}\right]$	$\left(m-\frac{3}{4}\right)^2\left[1+\frac{3}{\left(m-\frac{3}{4}\right)\pi}\right]$
C	F	1	0.597	−0.0870	0.471
		2	1.494	1.347	3.284
		3, 4, 5, …	$m-\frac{1}{2}$	$\left(m-\frac{1}{2}\right)^2\left[1-\frac{2}{\left(m-\frac{1}{2}\right)\pi}\right]$	$\left(m-\frac{1}{2}\right)^2\left[1+\frac{2}{\left(m-\frac{1}{2}\right)\pi}\right]$